HARVARD UNIVERSITY
Graduate School of Arts and Sciences

DISSERTATION ACCEPTANCE CERTIFICATE

The undersigned, appointed by the

Division of Medical Sciences

Program in Neuroscience

have examined a dissertation entitled

Ultrastructural insights into mammalian cutaneous mechanoreceptors

presented by Qiyu Zhang

candidate for the degree of Doctor of Philosophy and hereby certify that it is worthy of acceptance.

Signature: _____

Typed Name: Dr. Rachel Wilson

Signature: _____

Typed Name: Dr. Chenghua Gu

Signature: Bradford Lowell
Bradford Lowell (May 4, 2021 13:38 EDT)

Typed Name: Dr. Bradford Lowell

Signature: David I Hughes
David I Hughes (May 4, 2021 16:11 GMT+1)

Typed Name: Dr. David Hughes

Date: April 19, 2021

Ultrastructural insights into mammalian cutaneous mechanoreceptors

A dissertation presented

by

Qiyu Zhang

to

The Division of Medical Sciences

in partial fulfillment of the requirements

for the degree of

Doctor of Philosophy

in the subject of

Neurobiology

Harvard University

Cambridge, Massachusetts

April 2021

Dissertation Advisor: David D. Ginty Qiyu Zhang

Ultrastructural insights into mammalian cutaneous mechanoreceptors

Abstract

Cutaneous mechanoreceptors are a morphologically and functionally diverse class of primary sensory neurons in mammals that transduce mechanical stimuli acting on the skin into electrical impulses. These neurons reside in trigeminal ganglia and dorsal root ganglia and form pseudounipolar axons, of which one branch innervates the skin and the other innervates the spinal cord dorsal horn and brainstem, where it forms synapses with second-order neurons. Although substantial progress has been made in characterizing the anatomical and physiological properties of mechanoreceptors, the mechanotransduction mechanisms within endings in the skin and the organizational logic of synapses in the spinal cord remain poorly understood. To gain insight into these two questions, I used electron microscopy (EM) in conjunction with mouse genetic tools to investigate the ultrastructural properties of mechanoreceptors and their associated glia in the skin as well as primary afferent synapses in the spinal cord. I generated an optimized peroxidase, dAPEX2, and created a collection of genetically encoded EM reporters that are robust, versatile, and suitable for multiplexed labeling and volume EM reconstructions. Using these EM reporters, I first investigated the ultrastructural properties of sensory axon central branches in the spinal cord dorsal horn, identifying distinct ultrastructural features of previously inaccessible C-fiber subtypes. In addition, I have initiated a large-scale EM reconstruction of the spinal cord dorsal horn, which is enabling visualization and characterization of spinal cord circuit motifs. In the skin, genetic EM labeling has revealed insights into the ultrastructural basis of different physiological response properties of two mechanoreceptor subtypes that innervate Meissner corpuscles, a mechanosensory end organ in the glabrous skin. Moreover, three-dimensional EM reconstructions of hair follicle afferents and Meissner corpuscle afferents using focused ion beam-scanning EM have revealed common ultrastructural features of these distinct end organs, leading to new models to explain mechanisms of mechanotransduction in the skin.

Table of Contents

Acknowledgements

I would like to thank my thesis advisor Dr. David Ginty for all the mentorship and guidance throughout my graduate school. His scientific acumen and approach to research questions are inspiring and serve as an outstanding model for me as a scientist. At the same time, he also ensures that I have access to resources I need and is committed to my success. Without his support and dedication, this project truly would not have been possible.

I would like to thank my collaborator Dr. David Paul for his immense knowledge in molecular biology and neuroscience, and always being patient when teaching me experimental techniques. In addition, it is always fun to chat with him and learn about how much scientific experiments have changed over the years.

I would like to thank my collaborator Dr. Annie Handler for spearheading the skin electron microscopy project together and contributing both conceptually and experimentally. I am also grateful for the technicians and undergraduate students who worked with me over the years: Stuart Cattel, Nusrat Africawala, Bartianna Brown, Rebecca Plumb, Brianna Sanchez, Madiha Kabeer, and Nicholas Cao. Their hard work allows the team to be highly productive.

I would like to thank my collaborators Dr. Wei-Chung Lee, Dr. Jeff Lichtman, Dr. Harald Hess, Dr. C. Shan Xu, Song Pang, Dr. Tri Nguyen, Dr. Richard Schalek, Dr. Ciara Bolger, and Dr. Yuelong Wu for enabling us to pursue scientific questions with cutting-edge electron microscopy techniques and providing us with exceptional insights. I would also like to thank the Harvard Medical School Electron Microscopy Facility, Boston Children's Hospital Mouse Gene Manipulation Core, and Boston Children's Hospital Viral Core for their technical support.

I would like to thank my dissertation advisory committee members Dr. Rachel Wilson, Dr. Wade Regehr, Dr. Matthew Pecot, and Dr. Lisa Goodrich for their scientific advice and feedback over the years. I would also like to thank my student advisory committee member Dr. Rick Born for his support.

I would like to thank all current and former Ginty Lab members for making the lab both an intellectually stimulating environment and a friendly home. In particular, I would like to thank Mark Springel and Aniqa Tasnim for being great colleagues and friends and making graduate school an enjoyable experience.

I would like to thank the Quan family for their support through the Stuart H.Q. & Victoria Quan Fellowship.

Finally, I would like to thank my family for their unwavering love and support through this long journey.

List of Figures and Tables

Chapter 1. Introduction

The somatosensory system is important for organisms to perceive and react to multiple modalities of stimuli that are important for the survival and reproduction of the individuals. Cutaneous mechanosensation, the sense of touch, is a major component of the somatosensory system, which provides us rich information emanating from the skin. The mammalian primary somatosensory neurons are commonly categorized based on their conduction velocities and adaptation properties. In addition, they can also be divided based on response thresholds into low-threshold mechanoreceptors (LTMRs), which detect innocuous touch, and high-threshold mechanoreceptors (HTMRs), which detect noxious mechanical stimuli. These mechanoreceptors reside in the dorsal root ganglia (DRG) and trigeminal ganglia, and have pseudounipolar axons, with one axonal branch innervating the skin and another axonal branch innervating the central nervous system (Abraira and Ginty, 2013; Zimmerman et al., 2014). Thus, mechanoreceptors transduce tactile stimuli acting upon the skin into electrical signals that are transmitted to the central nervous system (CNS).

Mechanoreceptor subtypes and their functions

Aβ-mechanoreceptors have a conduction velocity of 30-75 m/s (~ 15 m/s in mouse). These neurons are heavily myelinated, and possess neurofilaments in their cell bodies and axons. A small portion of Aβ-mechanoreceptors are Aβ-HTMRs, which are mostly free nerve endings. Based on their adaptation properties, Aβ-LTMRs can be further divided into slowly adapting type I (Aβ SAI-LTMR), slowly adapting type II (Aβ SAII-LTMR), rapidly adapting type I (Aβ RAI-LTMR) and rapidly adapting type II (Aβ RAII-LTMR). In glabrous (hairless) skin, which is found mostly on hands and feet, or paws of rodents, Aβ SAI-LTMR endings associate with Merkel cells in the basal layer of the epidermis, and are activated by skin indentation. These neurons have high sensitivity and small receptive fields, which is thought to allow discrimination of fine textures. Aβ SAII-LTMR endings in glabrous skin are best tuned to skin stretch, have some proprioceptor characteristics, and are believed to innervate Ruffini corpuscles. However, while Aβ SAII-LTMR-like neurons are commonly found in mammals, Ruffini corpuscles are not found in the skin

of certain species such as rodents, raising the question of what the anatomical correlates of Aβ SAII-LTMR endings are in these species. Aβ RAI-LTMR endings are tuned to detect light touch and low-frequency vibration on the skin, and these neurons associate with Meissner corpuscles, which reside within dermal papillae. Aβ RAII-LTMR endings innervate Pacinian corpuscles, and are highly sensitive to high-frequency vibrations and pressure (Abraira and Ginty, 2013; Zimmerman et al., 2014) (**Fig. 1.1a**). Pacinian corpuscles can be found in the deep dermis and the hypodermis, as well as in the periosteum and the mesentery. In hairy skin, Aβ SAI-LTMR endings are associated with Merkel cells, as in the glabrous skin, and a distinguishing feature of these hairy skin Aβ SAI-LTMR endings is that the Merkel cell-neurite complex clusters into touch domes at the epidermis-dermis junction surrounding guard hairs in mice. Aβ SAII-LTMR fibers are also found in the hairy skin, although the anatomical correlates are also unknown. Aβ RAI-LTMR endings form lanceolate endings around guard, awl and auchene hairs. Hairy skin Aβ RAI-LTMR fibers are tuned to detecting hair follicle deflections, with extensive variations in receptive field size across the body (Abraira and Ginty, 2013; Zimmerman et al., 2014). Finally, Aβ field-LTMRs form circumferential endings around all types of hair follicles outside of the lanceolate endings. They have rapid to intermediate adaptation properties, are highly sensitive to skin strokes and have large receptive fields (Bai et al., 2015) (**Fig. 1.1b**).

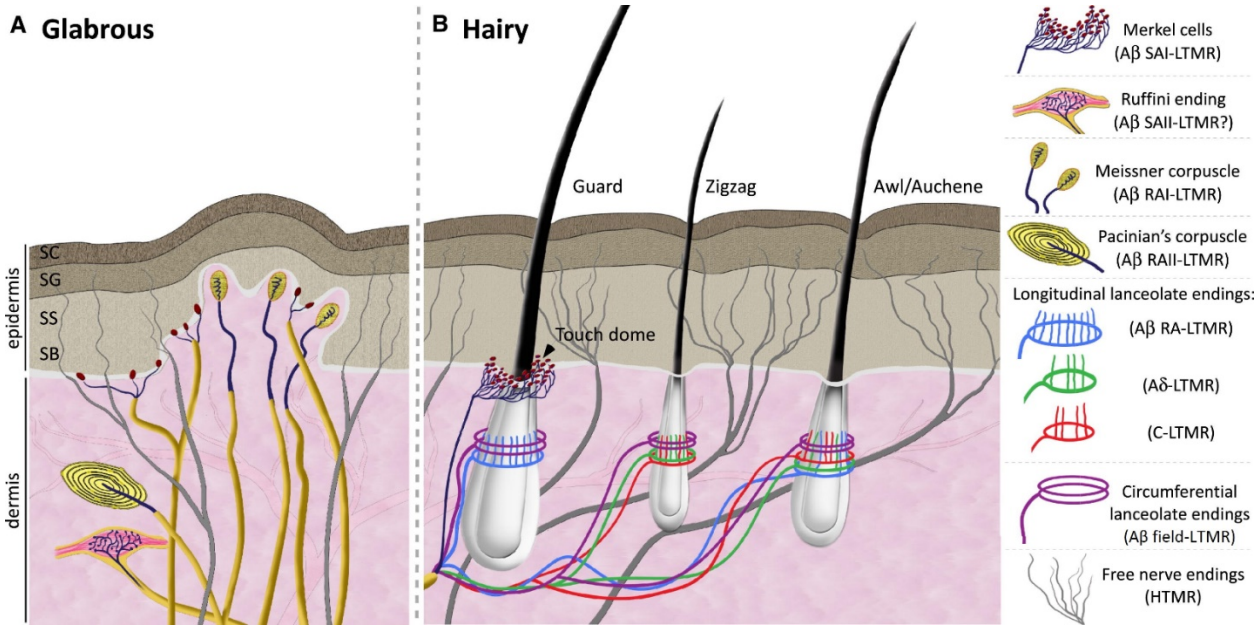

Figure 1.1. Organization of cutaneous receptors in the skin

(**a**) Glabrous skin.

(**b**) Hairy skin.

SC, stratum corneum; SG, stratum granulosum; SS, stratum spinosum; SB, stratum basalis.

Adapted from Abraira and Ginty, 2013.

Aδ-mechanoreceptors have a conduction velocity of 2-30 m/s (~ 5 m/s in mice). Their myelination is thinner than Aβ-mechanoreceptors, and they contain neurofilaments in their cell bodies but not their axon terminals. Aδ-HTMRs innervate both glabrous and hairy skin and respond to both noxious mechanical and thermal stimuli; most of these are free nerve endings that do not associate with any particular structures. In the hairy skin, however, Aδ-HTMRs can form circumferential endings around hair follicles, and respond well to hair pulling (Ghitani et al., 2017). These neurons are thought to mediate the fast and well localized pain. Aδ-LTMRs are present in the hairy skin, and associate with awl, auchene and zigzag hairs as lanceolate endings. They are rapidly adapting to static hair deflections, and have extremely low mechanical thresholds, making them the most sensitive mechanoreceptors in the skin. The receptive fields of Aδ-LTMRs are highly consistent in shape and size across the body (Abraira and Ginty, 2013). One interesting property of Aδ-LTMRs is that they exhibit direction selectivity, responding more strongly to rostral hair deflections than caudal deflections. This direction selectivity results from asymmetrical innervations of hair follicles by Aδ-LTMRs, which are enriched on the caudal side of the hair follicles (Rutlin et al., 2014) (**Fig. 1.1**).

C-mechanoreceptors have a conduction velocity of 0.5-2 m/s and are the largest group of DRG neurons. These neurons are unmyelinated and do not contain neurofilaments. The majority of C-fibers are nociceptors, which innervate glabrous and hairy skin as free nerve endings. C-HTMRs respond to noxious mechanical stimuli but not thermal stimuli. Nociceptors can be further categorized as peptidergic nociceptors, which express substance P and/or calcitonin gene-related peptide (CGRP) and innervate the basal region of epidermis, and nonpeptidergic nociceptors, which do not express these neuropeptides and innervate a more superficial layer of epidermis (Abraira and Ginty, 2013). These neurons are thought to mediate the slow and poorly localized pain. Additionally, a large population of unmyelinated neurons

are classified as C-LTMRs. These neurons constitute of 5-30% of all DRG neurons, depending on the DRG axial level, making them the largest population of LTMRs. C-LTMRs form lanceolate endings around awl, auchene and zigzag hairs (Li et al., 2011), and there are also recent reports of their existence in human glabrous skin at low densities (Watkins et al., 2021). They respond to light touch, gentle stroking and rapid cooling, and are hypothesized to mediate pleasant touch (Li et al., 2011; McGlone et al., 2014; Watkins et al., 2021) (**Fig. 1.1**).

One important question regarding cutaneous mechanoreceptors is how mechanical stimuli activate different subtypes with distinct tuning properties and adaptation properties. While there are significant differences in the molecular profiles and electrophysiological properties between different subtypes of mechanoreceptors, these differences do not always provide satisfactory explanations for their tuning properties and adaptation properties seen in response to mechanical stimuli. As an example, sustained current injections into the somata of Aβ RAI-LTMRs result in repeated firing of high frequencies with little adaptation, while similar current injections into the somata of Aβ SAI-LTMRs yield only a few spikes at the onset of the current steps (Zheng et al., 2019). On the other hand, the morphological and functional features of end organs in the skin can also have profound influences on the response properties of mechanoreceptors. One example is that decapsulating Aβ RAII-LTMRs innervating Pacinian corpuscles by removing lamellar cell wrappings causes the receptor potential to change from rapidly adapting to slowly adapting, which can then be restored by adding artificial lamellar wrappings (Loewenstein and Mendelson, 1965). Finally, different subtypes of mechanoreceptors also express different mechanosensitive channels. LTMRs mainly rely on Piezo2 for mechanotransduction (Ranade et al., 2014), while HTMRs often express TRP channels (Ranade et al., 2015). Different channel gating thresholds may allow different subtypes to be tuned to different force amplitudes and tile the force space.

In addition, most naturalistic stimuli activate more than one type of mechanoreceptors. For example, stroking the hairy skin activates Aβ field-LTMRs, all LTMRs associated with lanceolate endings, and Aβ SAI-LTMRs. Pinching will activate HTMRs as well as LTMRs. Thus, ensembles of neuronal activities encode the different features of any given stimulus and allow us to distinguish different complex tactile

stimuli (Abraira and Ginty, 2013). Losing peripheral tactile processing capabilities can have dramatic consequences on touch perception. For example, patients with SCN9A channelopathy, where nonsense mutations result in truncated α-subunits of $Na_V1.7$, nociceptors, including HTMRs, do not have normal central neurotransmitter release. These patients have congenital insensitivity to pain, but otherwise they have normal perception of light touch and pressure. Since these patients perceive noxious mechanical stimuli as innocuous stimuli and not painful, they do not avoid harmful stimuli and usually have wounds and bruises all over their bodies (Cox et al., 2006). On the other hand, abnormal crosstalk between noxious and innocuous touch can lead to mechanical allodynia, which is a debilitating pathological condition where light touch is perceived as painful and usually caused by nerve injury. These examples highlight the fact that concurrent neuronal activities need to be properly integrated by higher centers to give rise to normal touch percepts. Understanding how tactile inputs are processed is crucial to understanding how the nervous system utilizes multiple somatosensory inputs to generate appropriate outputs.

Integration of tactile information

All primary somatosensory neurons innervate the dorsal horn of the spinal cord, which serves as the first integration center for tactile information (Brown, 1981). The spinal cord contains multiple populations of morphologically, physiologically and neurochemically distinct interneurons and projection neurons. Based on cytoarchitecture, Rexed (1952) divided the spinal cord grey matter into ten laminae. The dorsal horn consists of laminae I-VI. While early studies used intracellular recordings and cell fillings (Brown, 1981; Sugiura et al., 1986), histochemical methods (Light and Perl, 1979a, b; Scheibel and Scheibel, 1969), or immunohistochemical staining (Alvarez et al., 1993; Gibson et al., 1981) to identify the locations of primary afferent terminals in the dorsal horn, recent studies have used genetic labeling strategies to label most types of mechanoreceptor endings in the dorsal horn (Bai et al., 2015; Li et al., 2011; Luo et al., 2009; Vrontou et al., 2013; Zylka et al., 2005). Aδ- and C-peptidergic nociceptors predominantly innervate the dorsal most laminae of the spinal cord, lamina I and outer lamina II (Brown, 1981; Gibson et al., 1981; Todd, 2010), though Aδ-HTMRs also innervate laminae V and X (Light and Perl, 1979b). C-

nonpeptidergic nociceptors innervate dorsal inner lamina II (II_{id}) (Vrontou et al., 2013; Zylka et al., 2005). On the other hand, C-LTMRs innervate ventral inner lamina II (II_{iv}) (Li et al., 2011). Aδ-LTMRs innervate laminae II_{iv}-III (Li et al., 2011), and Aβ-LTMRs innervate laminae II_{iv}-V, depending on the subtype (Bai et al., 2015; Li et al., 2011). Different types of LTMRs from the same patch of skin form a dorsal-ventrally shaped column of axonal innervation, indicating a high level of somatotopy and perhaps providing a structural basis for integration (Li et al., 2011). Finally, descending cortical inputs from the somatosensory cortex also heavily innervate the dorsal horn (Abraira et al., 2017; Brown, 1981), although they are conspicuously absent in laminae II_o-II_{id} (Abraira et al., 2017). This innervation pattern is summarized in **Fig. 1.2**.

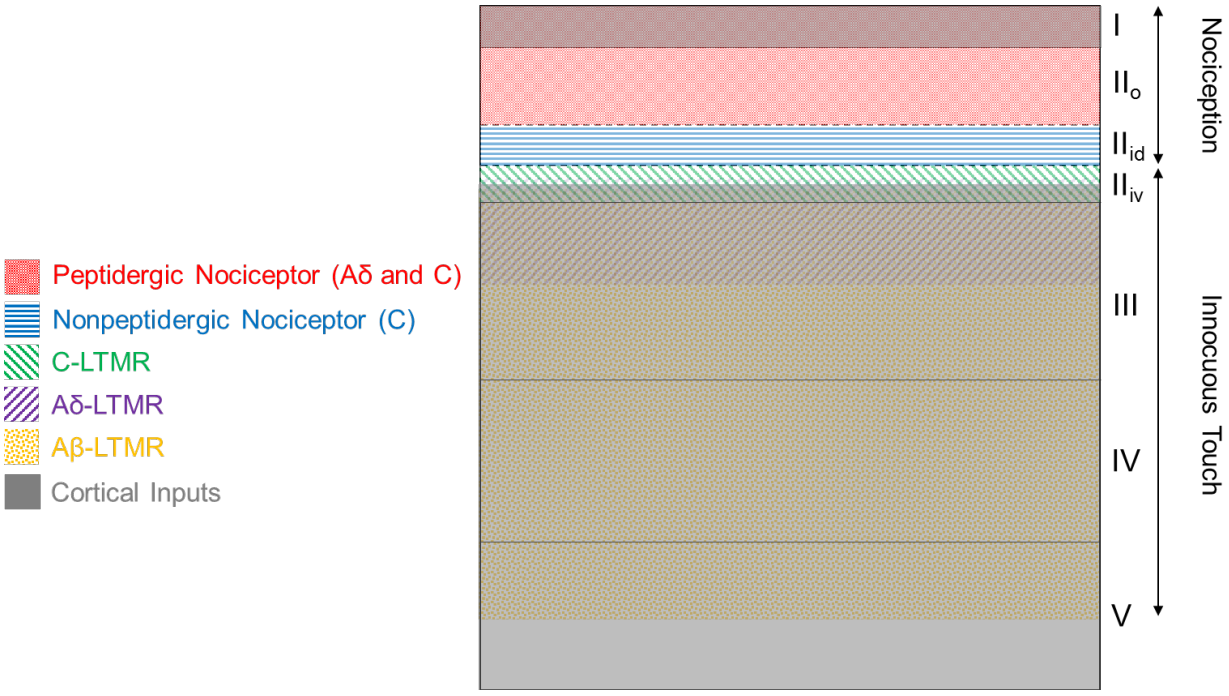

Figure 1.2. Cutaneous mechanoreceptor and cortical innervations of the dorsal horn

Approximate innervation zones of each major type of cutaneous mechanoreceptors and cortical neurons. In general, unmyelinated afferents synapse in the region dorsal to myelinated afferents, and nociceptors synapse in the region dorsal to LTMRs. Therefore, there is a sharp anatomical boundary between nociceptive inputs (laminae I-II_{id}) and innocuous inputs (laminae II_{iv}-V).

Most Aβ-mechanoreceptors possess an additional axonal branch that ascends the dorsal column to synapse within the cuneate nucleus or gracile nucleus (collectively called the dorsal column nuclei). However, all other types of mechanoreceptors do not have direct projections to higher brain centers, and therefore relay information to projection neurons in the spinal cord. Three major projection pathways for tactile stimuli are present in the dorsal horn: the postsynaptic dorsal column (PSDC) pathway, spinocervical tract (SCT) and anterolateral tracts (ALT). PSDC projection neurons are located in the deep dorsal horn (laminae IV and V) and project to dorsal column nuclei via the dorsal column. The majority of PSDC neurons respond to both innocuous and noxious mechanical stimuli, while ~ 20% respond exclusively to innocuous stimuli. A small population of PSDC neurons (~ 6%) respond only to noxious stimuli. Several types of Aβ-mechanoreceptors, both glabrous and hairy skin types, and type I_a muscle afferents form monosynaptic contacts onto PSDC neurons (Abraira and Ginty, 2013; Abraira et al., 2017; Maxwell et al., 1985). On the other hand, PSDC neurons receive only polysynaptic connections from Aδ-LTMRs (Abraira et al., 2017). Even though PSDC neurons have defined receptive fields, they lack modality specificity, suggesting that they relay integrated tactile information from the dorsal horn (Uddenberg, 1968). Additionally, PSDC projection neurons also receive inhibitory GABAergic and glycinergic interneuron inputs (Abraira et al., 2017; Maxwell et al., 1995). Thus, the PSDC pathway may be a major output for integrated tactile information from the dorsal horn. SCT neurons are located in laminae III and IV, and project to the lateral cervical nucleus near C1 and C2. SCT neurons can also be divided into three groups: low-threshold, wide-dynamic-range, and high-threshold, the proportions of which are similar to those of PSDC neurons. Unlike PSDC neurons, however, SCT neurons respond only to hair follicle movements and not activation of hairy Aβ SAI-LTMR afferents nor glabrous skin innervating neurons. SCT neurons receive monosynaptic inputs from Aβ- and Aδ-hair follicle afferents, as well as local interneurons, and serve as a hub for integrated hair follicle stimulus information (Abraira and Ginty, 2013; Brown, 1981). ALT projection neurons are located mainly in laminae I and V, and transmit nociceptive, temperature and crude touch information. The main targets of the ALT are ventral posterolateral nucleus in the thalamus, lateral parabrachial nucleus in the brainstem, caudal ventrolateral medulla and periaqueductal gray. ALT projection neurons are thought to convey both discriminative and affective aspects of pain. Most types of nociceptors have direct or indirect inputs onto these projection

neurons, making them the main nociception pathway (Todd, 2010). In addition, some ALT projection neurons respond to both LTMR inputs and nociceptor inputs, and are therefore wide-dynamic-range projection neurons (Choi et al., 2020; Naim et al., 1998). It is possible that C-LTMRs also send information through the ALT, rather than the PSDC pathway or the SCT, consistent with the hypothesis that they convey affective touch information (Sewards and Sewards, 2002). However, there are also recent reports in humans showing that sensation of pleasant stimuli are still present after anterolateral cordotomy, suggesting that C-LTMR information may ascend through pathways other than the ALT (Marshall and McGlone, 2020; Marshall et al., 2019). Recently, it has been shown that ALT projection neurons can be divided into different subtypes (Browne et al., 2019), and molecularly distinct populations of ALT projection neurons with distinct but overlapping innervation patterns carry painful versus mixed tactile stimuli information (Choi et al., 2020). In all, multiple ascending pathways for integrated tactile stimulus information exist in the spinal cord, suggesting that population coding mechanisms, rather than strictly labeled lines, are used for the transmission of somatosensory information (Ma, 2010). However, much is still unknown about the organization, function or behavioral significance of these projection pathways due to lack of genetic access to these populations and detailed knowledge of their synaptic connections.

Dorsal horn interneurons are an important component of tactile information processing and integration and can be divided into different populations based on anatomical, electrophysiological, and molecular profiles (Abraira et al., 2017; Graham and Hughes, 2020). Interneurons in lamina II, which is proposed to be the location of the gate for pain perception (Melzack and Wall, 1965), are the most extensively studied. Most neurons in lamina II are interneurons, although dendrites of projection neurons in other laminae also penetrate lamina II. Both excitatory and inhibitory interneurons are present, and ~ 30% of lamina II neurons are GABAergic (Polgar et al., 2013). Additionally, glycine is also used as an inhibitory transmitter in the spinal cord, and glycine colocalizes with GABA in many cells in laminae I-III (Brown, 1981; Polgar et al., 2013; Todd, 2010; Todd and Sullivan, 1990). The major form of inhibition in the spinal cord dorsal horn is postsynaptic inhibition, accounting for ~ 97% of all inhibitory synapses, which is mediated through axodendritic, axosomatic, and dendrodendritic synapses (Duncan and Morales, 1978). Postsynaptic

inhibition uses both GABA and glycine as the neurotransmitter (Todd, 2010). In addition, two specialized forms of synaptic organization in the spinal cord, axoaxonic and dendroaxonic inhibitory synapses from interneurons onto primary afferents, mediate presynaptic inhibition. The inhibitory neuron releases GABA, which opens $GABA_A$ receptors and causes a depolarization of the primary afferent, due to the elevated chloride reversal potential in primary afferents. This depolarization reduces the amplitude of the action potential, likely by inactivation of voltage-dependent sodium channels and/or shunting, and thus reduces calcium influx and transmitter release from primary afferents. The classical mode of primary afferent depolarization (PAD) involves a trisynaptic circuit: activation of primary afferents leads to activation of excitatory interneurons, which in turn synapse onto inhibitory interneurons and causes the release of GABA. Recent evidence suggests that a more direct disynaptic pathway in which primary afferents directly synapse on inhibitory interneurons, which in turn synapse on primary afferents, also exists (Hochman et al., 2010). Another form of presynaptic inhibition characterized recently uses glutamate to activate NMDA receptors, which is evoked by activation of Aδ- and C-fibers (Zimmerman et al., 2019). Glycine, on the other hand, appears to not be involved in presynaptic inhibition (Todd, 1996). In addition, descending pathways modulate primary afferent activity via PAD, which is also mediated by one or more unidentified populations of interneurons (Rudomin and Schmidt, 1999). Besides modulating the activity of primary afferents, some populations of interneurons relay information from primary afferents to projection neurons. For example, glutamatergic central cells in lamina II receive direct inputs from C-nociceptors, and synapse onto glutamatergic vertical cells in the same lamina, which receive direct inputs from Aδ-nociceptors. The vertical cells then synapse onto lamina I projection neurons (Lu and Perl, 2005). Recent efforts in our lab to identify genetically defined populations dorsal horn interneurons yielded 11 different populations (Abraira et al., 2017). Broadly speaking, all identified interneuron populations receive inputs from multiple subtypes of LTMRs in additional to corticospinal neurons (Abraira et al., 2017). Nonetheless, some levels of specificity do exist, especially for C-LTMRs, which form monosynaptic inputs to only four of the 11 populations (Abraira et al., 2017). Despite this appreciation of interneuronal diversity and connectivity, we still lack detailed knowledge of how primary afferents are connected to these interneuron and projection neuron populations on the cellular level rather than the population level.

Understanding the precise connectivity in the dorsal horn circuitry will lay the foundation for understanding how tactile information is processed in the CNS.

Circuit mapping with electron microscopy in the dorsal horn

Electron microscopy (EM) is an effective method for studying synaptic connectivity in the nervous system, due to its high spatial resolution. It allows us not only to see structural synapses in the nervous systems but also characterize types of synapses based on the ultrastructural features, such as the classical categorization into asymmetric and symmetric synapses, which correspond to excitatory and inhibitory synapses, respectively (Gray, 1959; Peters et al., 1991). A classic example of the utility of EM is in defining the connectome of *C. elegans*, which was obtained by serial EM reconstruction (Jarrell et al., 2012; White et al., 1986). These findings provided crucial insights into the organization of the entire light touch circuit of *C. elegans* and how it connects to motor circuits to mediate avoidance behaviors (Chalfie et al., 1985). The *C. elegans* circuit map provides a prime example on how knowledge of synaptic connectivity can inform circuit functions, and it provides a framework for functionally testing circuit models. Recently, the connectome of *D. melanogaster* brain was completed (Scheffer et al., 2020; Zheng et al., 2018), and a full EM volume of the ventral nerve cord was also acquired (Phelps et al., 2021). Similar efforts to generate connectomes are underway for the mouse brain (Kasthuri et al., 2015; Morgan et al., 2016; Motta et al., 2019). It is likely that EM circuit mapping has the potential to solve the synaptic connectivity map of the spinal cord dorsal horn and thus shed light on the logic of the tactile information processing.

Previous EM studies of the dorsal horn revealed that complex synaptic structures called synaptic glomeruli are a prominent ultrastructural feature of the dorsal horn (**Fig. 1.3**). In each of these glomeruli, there is one axon surrounded by multiple neuronal profiles. The axon in the center is called the central axon, and the neuronal profiles surrounding the central axon are called peripheral profiles. These dorsal horn glomeruli are reminiscent of glomeruli in the cerebellum and thalamus. This glomerular organization is prevalent in lamina II and III, while rare in lamina I and deeper laminae (Ribeiro-da-Silva and Coimbra,

1982). The peripheral profiles in glomeruli include axons, dendrites, vesicle-containing dendrites, and glial processes (Ribeiro-da-Silva et al., 1985). Based on the morphology of the central terminal, dorsal horn glomeruli can be divided into four types: Ia, Ib, IIa and IIb (**Fig. 1.3**) (Ribeiro-da-Silva, 2004; Ribeiro-da-Silva and Coimbra, 1982; Ribeiro-da-Silva et al., 1985; Ribeiro-da-Silva et al., 1989). Type Ia glomeruli have unmyelinated central axons, are found in lamina II, and do not contain substance P or CGRP. The central axon has a dark appearance and a small number of mitochondria. Dendroaxonic synapses from peripheral vesicle-containing dendrites onto the central axon are common in type Ia glomeruli, as are axoaxonic synapses from peripheral axons onto the central axon (Ribeiro-da-Silva et al., 1985). Type Ib glomeruli are similar to type Ia glomeruli except that central axons contain substance P and/or CGRP, have multiple large dense core vesicles, are surrounded by fewer peripheral profiles, and receive very few dendroaxonic and axoxonic synapses (Ribeiro-da-Silva et al., 1989). Type IIa glomeruli have myelinated central axons and are found in ventral lamina II and dorsal lamina III. The central axon has more mitochondria than type I and lacks neurofilaments. Axoaxonic synapses from peripheral axons are more common than type I but fewer dendroaxonic synapses are found. Moreover, the central axon has a higher density of synapses onto peripheral dendrites (Ribeiro-da-Silva et al., 1985). Finally, type IIb glomeruli are similar to type IIa glomeruli except that central axons have neurofilaments and are found in dorsal lamina III (Ribeiro-da-Silva et al., 1985).

Multiple studies have been conducted to determine the identities of dorsal horn glomerular synaptic profiles. Central axons of glomeruli were found to undergo degeneration after dorsal root rhizotomy, indicating their primary afferent origin (Ralston and Ralston, 1979). This finding was extended by bulk labeling of primary afferents for EM investigation with horseradish peroxidase (HRP), in which all of the central axons were shown to be of primary afferent origin (Cruz et al., 1991). Moreover, most primary afferents innervating lamina II_i form synaptic glomeruli (Cruz et al., 1991). HRP fills have been used to examine the ultrastructure of primary afferents after intracellular recording so that physiological responses and receptive fields can be correlated with anatomical features. Using this technique, Aδ-LTMR terminals were shown to form type IIa glomeruli (Rethelyi et al., 1982). Similarly, Aβ-LTMR terminals form type IIb glomeruli (Ralston et al., 1984; Watson, 2003; Watson et al., 2002). There appear to be minor

morphological differences between the synaptic organizations of type IIb glomeruli formed by different subtypes of Aβ-LTMRs (Maxwell and Réthelyi, 1987). Type Ia and type Ib glomeruli are most likely formed by C-fibers based on their unmyelinated appearance and their anatomical locations. However, due to difficulties in obtaining high-quality neuronal fills of C-fibers, there is limited information on the functional correlates of these types of glomeruli. Presumably C-nonpeptidergic nociceptors form type Ia glomeruli, and type Ib glomeruli are inferred to be C-peptidergic nociceptors based on their expression of neuropeptides determined by immuno-EM (Ribeiro-da-Silva et al., 1989). Since sensory neurons only form central axons in glomeruli, peripheral profiles must be from non-sensory origins. Indeed, almost all of the peripheral axons and the majority of vesicle-containing dendrites are found to be GABAergic and/or glycinergic, consistent with an interneuronal origin. Based on the neurotransmitter profiles, there may be multiple populations of interneurons giving rise to presynaptic axons (Todd, 1996; Watson, 2003; Watson et al., 2002). One recent study used immuno-EM to demonstrate that parvalbumin (PV) interneurons form axoaxonic synapses onto central axons in glomeruli (Hughes et al., 2012), and these neurons are implicated in tactile allodynia (Boyle et al., 2019). On the other hand, only a small population of dendrites without vesicles are found to be GABAergic or glycinergic (Todd, 1996; Watson, 2003; Watson et al., 2002). Based on immuno-EM, one candidate for these latter neurons is the protein kinase C gamma (PKCγ) interneurons (Neumann et al., 2008), which have been shown to be involved in neuropathic pain (Malmberg et al., 1997). Another candidate is the PSDC projection neurons, which have been shown using HRP fills to be postsynaptic in glomerular structures (Bannatyne et al., 1987).

One potential advantage of having a glomerular configuration is that it may provide an efficient way of organizing complex computational machinery. Complex synaptic interactions such as dyadic and triadic synaptic interactions are common in dorsal horn glomeruli. Representative forms of dyadic and triadic interactions in dorsal horn glomeruli are shown in **Fig. 1.3**. The most common form of triadic interaction involves a peripheral axon synapsing onto both a central axon and a dendrite that is postsynaptic to the central axon. This allows the interneuron to exert both presynaptic and postsynaptic inhibition with regard to the primary afferent. The other potential advantage is allowing the primary afferent to broadcast its information to multiple neurons effectively, which may be a predominant function for Type Ib glomeruli,

where presynaptic inhibitory axoaxonic synapses are rare (Ribeiro-da-Silva et al., 1989). Therefore, synaptic glomeruli are structurally suited as information processing hubs, and may be the key organizing structures underlying tactile information integration in lamina II_i.

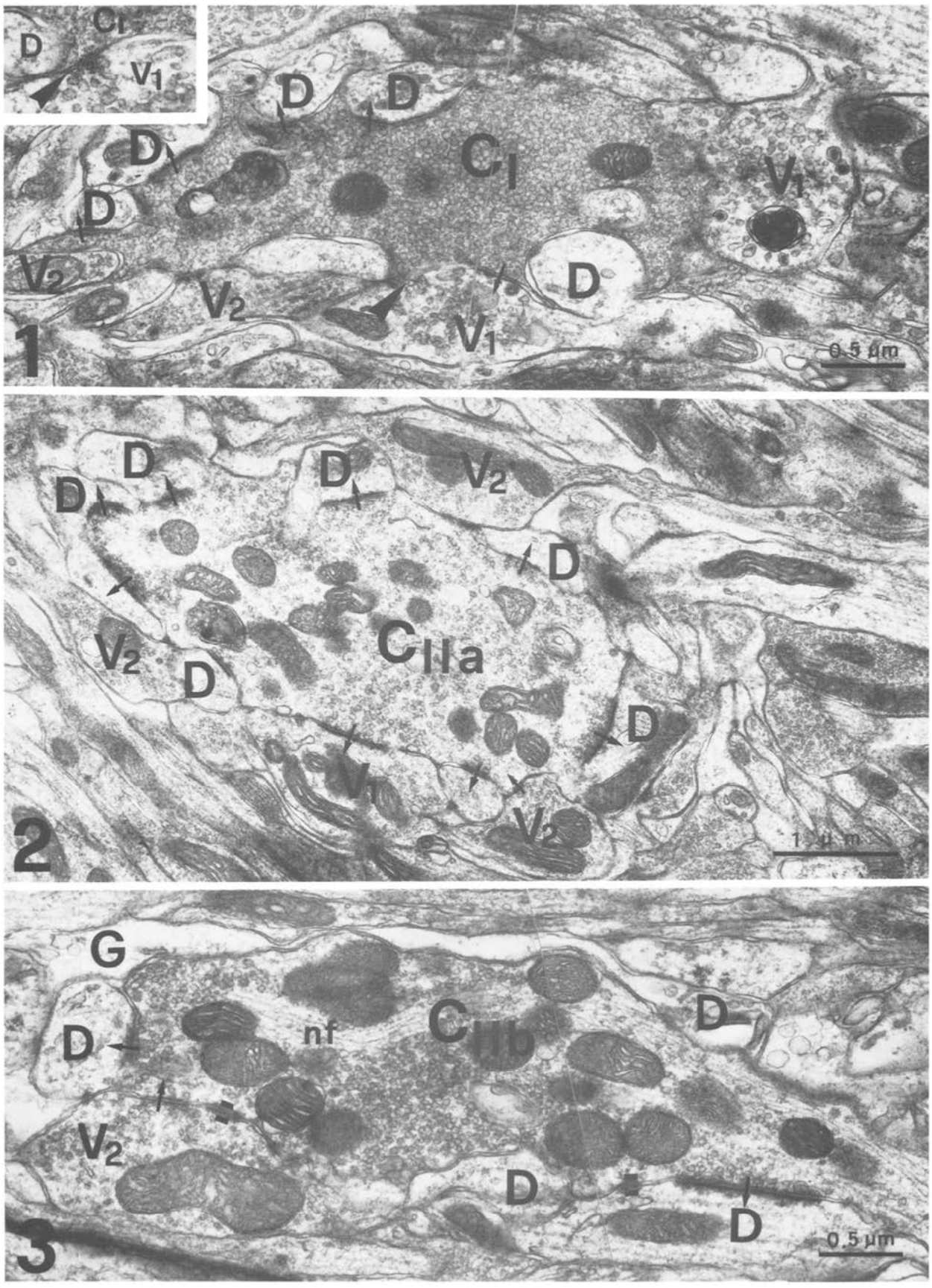
D
Ct
V1
D
D
D
D
C1
V1
D
V2
V2
D
V1
1
0.5 µm
D
D
D
V2
D
V2
D
CIIa
D
V1
V2
2
1 µm
G
D
nf
CIIb
D
V2
D
D
3
0.5 µm

Figure 1.3. Ultrastructural features of synaptic glomeruli

C_I: central axon of type I glomerulus, C_{IIa}: central axon of type IIa glomerulus, C_{IIb}: central axon of type IIb glomerulus, D: dendrites, V_1: vesicle-containing dendrites, V_2: axons, G: glial processes.
Reproduced from Ribeiro-da-Silva et al., 1985.

Even though synaptic glomeruli were identified in 1970s, very little is known about the function and significance of this organization, and how tactile information is integrated and processed in the dorsal horn. This is mainly due to two reasons: 1) the anatomical details of the circuits are not well established, and the identities of the synaptic profiles are largely unknown; and 2) there have been few genetic tools for independently manipulating the various components of synaptic glomeruli. Recent advances in EM technology, especially automatic sectioning and wider imaging fields, have allowed collecting larger-scale EM datasets, which can greatly facilitate circuit mapping (Kasthuri et al., 2015; Phelps et al., 2021; Xu et al., 2017; Zheng et al., 2018). With these improvements in EM data collection, reconstructing large datasets becomes one of the main bottlenecks for connectivity studies, and new automatic and semi-automatic segmentation tools are being actively developed (Berning et al., 2015; Funke et al., 2019; Januszewski et al., 2018). In the meanwhile, genetically defined populations of primary sensory neurons, dorsal horn interneurons and projection neurons that are electrophysiologically, morphologically and neurochemically distinct have been delineated with the generation of multiple mouse Cre and Flp recombinase driver lines (Abraira et al., 2017; Bai et al., 2015; Choi et al., 2020; Li et al., 2011; Luo et al., 2009; Rau et al., 2009; Vrontou et al., 2013). The ability to label and visualize different genetically defined populations of neurons under EM will allow us to conduct electrophysiological and behavioral investigations informed by connectivity frameworks gleaned from EM, which will serve as the foundation for understanding the processing of information in the first integration center for tactile information.

Ultrastructural features of cutaneous mechanosensory end organs

Five major types of cutaneous mechanosensory end organs have been described in mammals: Merkel cell complexes, which are innervated by Aβ SAI-LTMRs; Ruffini corpuscles, which may be innervated by

Aβ SAII-LTMRs; Meissner corpuscles, which are innervated by Aβ RAI-LTMRs; Pacinian corpuscles, which are innervated by Aβ RAII-LTMRs; and hair follicles, which are innervated by Aβ-, Aδ-, and C-LTMRs, depending on the type of hair follicles (Zimmerman et al., 2014). HTMRs have also been reported to innervate some of these end organs (Pare et al., 2001). The high spatial resolution of EM proved to be instrumental in understanding the detailed anatomical features of the cutaneous mechanosensory end organs.

Merkel cell complexes involve Aβ SAI-LTMR endings closely associated with Merkel cells near the epidermis-dermis junction (**Fig. 1.4a**). Under EM, Merkel cells are seen to be anchored to keratinocytes in the epidermis by desmosomes, and frequently extend long cytoplasmic profiles devoid of organelles or cytoskeletons into the epidermis. SAI axons are sandwiched between Merkel cells and lamellar cells on the apical side and the basal side, respectively. In addition, dense-core vesicles are often seen on the axon-facing side of Merkel cells, and synapse-like structures are seen between Merkel cells and Aβ SAI-LTMR axons (Iggo and Muir, 1969). These structures have been variously reported to be serotonergic and/or adrenergic synapses from Merkel cells to Aβ SAI-LTMR axons (Chang et al., 2016; Hoffman et al., 2018), and the loss in Piezo2 in Merkel cells leads to a large reduction in Aβ SAI-LTMR response during the static phase of mechanical stimuli (Woo et al., 2014), suggesting that this close association plays an important functional role.

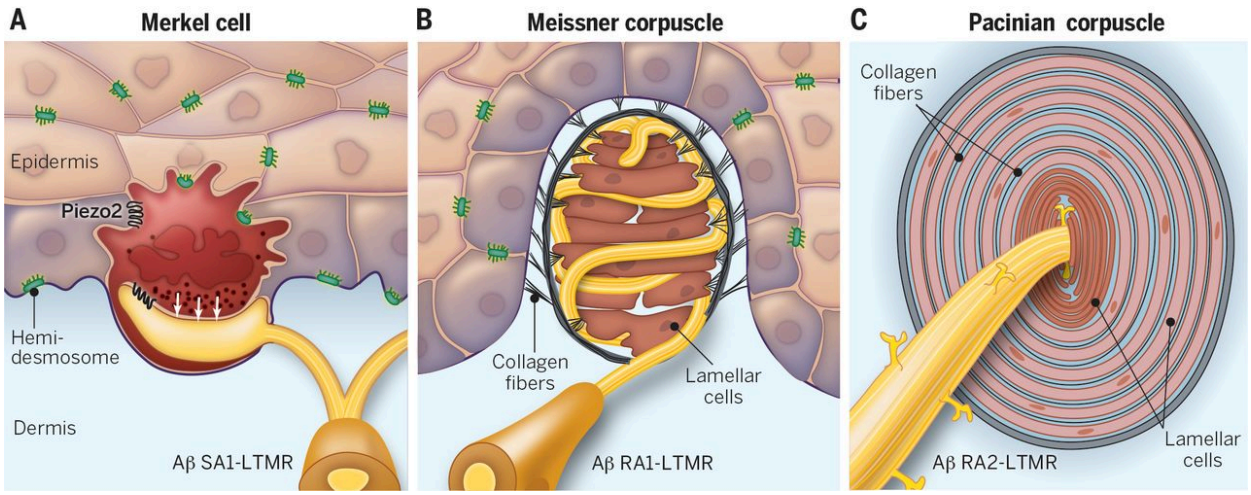

Figure 1.4. Structures of murine glabrous end organs

(**a**) Merkel cell.

(**b**) Meissner corpuscle.

(**c**) Pacinian corpuscle.

Reproduced from Zimmerman et al., 2014.

Ruffini corpuscles are relatively understudied due to their scarcity in rodents. Unlike humans, in rodents there has been no report of Ruffini corpuscles in the skin. However, they can be found frequently in the periodontal ligaments (Byers, 1985; Takahashi-Iwanaga et al., 1997). EM studies show that Ruffini endings are embedded within collagen matrix with different orientations, but they are often separated from the collagen matrix by multiple layers basal laminae (Byers, 1985; Takahashi-Iwanaga et al., 1997). The Ruffini corpuscle endings contain single axons encased by single Schwann cell processes on two sides, and numerous axon protrusions extend out between the gaps of Schwann cell sheaths (Byers, 1985; Takahashi-Iwanaga et al., 1997). In addition, long profiles of Schwann cells sandwiching the axon can be seen in the terminal portions of the endings (Takahashi-Iwanaga et al., 1997). One prominent ultrastructural feature of the terminal Schwann cell profiles is the abundance of caveolae, which tend to be more concentrated on the axon-facing side (Takahashi-Iwanaga et al., 1997). It has also been reported that these periodontal Ruffini endings can have rapidly to intermediate adapting response profiles (Linden et al., 1994; Millar et al., 1989).

Meissner corpuscles are located in the apex of dermal papillae of the glabrous skin, which are long invaginations of the dermis into the epidermis (**Fig. 1.4b**). On the ultrastructural level, multiple lamellae of Schwann cell processes are seen to wrap around Aβ RAI-LTMR axonal profiles and leave gaps where axon protrusions extend out. Collagen fibers of different orientations fill the space between lamellar cells, which also have numerous caveolae (Ide, 1976), and the corpuscle is wrapped around by a few capsule cells. In addition, it has been reported that different subtypes of C-HTMRs also innervate Meissner corpuscles within distinct zones in the corpuscle (Pare et al., 2001), which may correspond to the unmyelinated fibers seen under EM (Ide, 1976).

Pacinian corpuscles are not found in the dermis of rodents, unlike humans, but are abundant within the periosteum surrounding bones. They are large and elongated with a bulb-like ultraterminal structure at the end (**Fig. 1.4c**). EM studies reveal dense, regular, but thin lamellar wrappings, five to ten times more numerous than that of Meissner corpuscles, surrounding the central axon in the terminal region (Pease and Quilliam, 1957). Caveolae are less frequently present in these thin lamellae. A cleft in the lamellar wrappings can be seen in the terminal region, and axonal protrusions are present in the cleft (Pease and Quilliam, 1957). This organization quickly breaks down in the ultraterminal region, where the central axon is much more enlarged and contains densely packed mitochondria. The number of lamellar wrappings in the ultraterminal region is usually a tenth of that in the terminal region, and the shape of the central axon is much less regular. Axons frequently bulge out from lamellar wrappings, and numerous axonal protrusions can be seen (Spencer and Schaumburg, 1973). This distinction in ultrastructure in the terminal region versus the ultraterminal region may indicate that they serve different functions for Aβ RAII-LTMR activation.

Hair follicles usually have two types of morphologically distinct axonal innervations: lanceolate endings and circumferential endings (**Fig. 1.5**). The former type consists of Aβ RAI-LTMRs, Aδ-LTMRs, and C-LTMRs, while the latter type consists of Aβ field-LTMRs and Aδ Circ-HTMRs (Abraira and Ginty, 2013; Bai et al., 2015; Ghitani et al., 2017; Zimmerman et al., 2014). Lanceolate endings are closer to the hair shaft than circumferential endings (**Fig. 1.5a**). Intriguingly, EM studies show that lanceolate endings are embedded in longitudinally oriented collagen fibers, while circumferentially endings are embedded in circumferentially oriented collagen fibers (**Fig. 1.5b**). This ordered organization of collagen matrix is not observed in other end organs, suggesting that it may play a unique role in the activation of hair follicle afferents. Both lanceolate endings and circumferential endings have single layers of Schwann cell sheaths, with gaps, axon protrusions and caveolae similar to the other end organs (Li and Ginty, 2014; Takahashi-Iwanaga, 2000). In addition, adherens junctions can frequently be seen between the axon and Schwann cell processes in lanceolate endings (Kaidoh and Inoue, 2008).

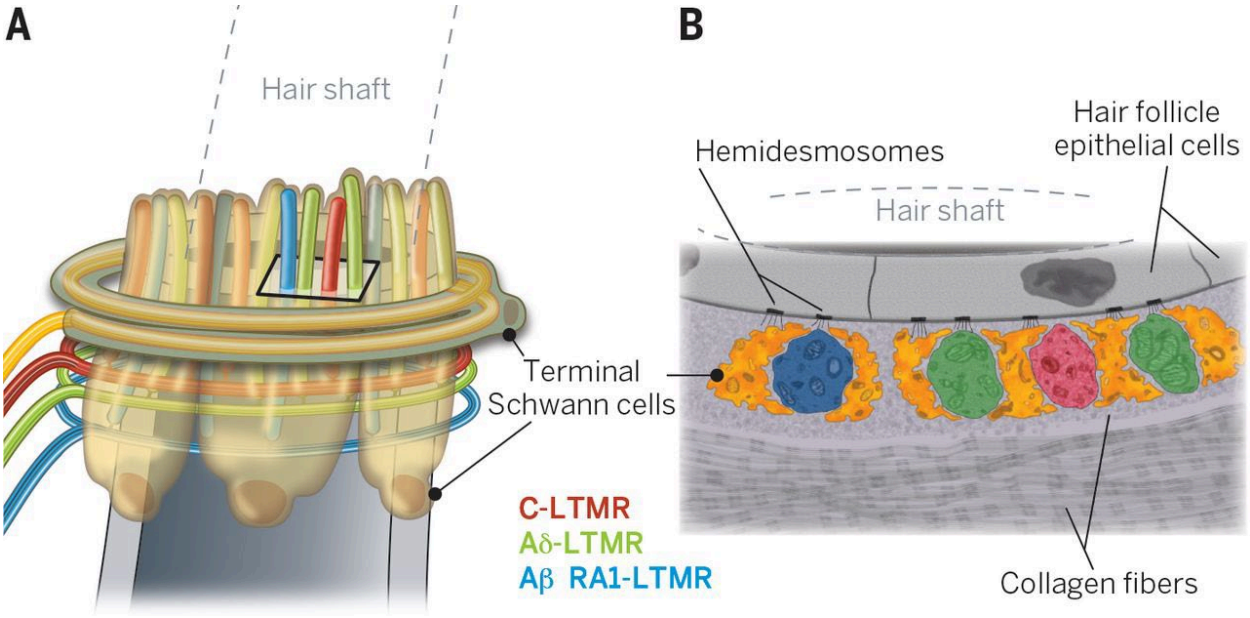

Figure 1.5. Structure of murine hair follicles

(**a**) Overall organization of hair follicle afferents and associated Schwann cells.

(**b**) Example ultrastructural features seen in hair follicles.

Reproduced from Zimmerman et al., 2014.

The commonalities and differences between these end organs raise the question of how these ultrastructural features may contribute to the mechanical activation of mechanoreceptors by physiological stimuli. In addition, the exact localization of mechanosensitive channels, such as Piezo2, in these end organs is unknown. A three-dimensional appreciation of the ultrastructure of mechanosensory end organs will be highly informative for answering these questions.

Summary

While substantial progress has been made to understand how different subtypes of mechanoreceptors function together to generate touch percepts, our knowledge of how their anatomical features ultimately enable their functions is rudimentary. In my dissertation work, I will first present efforts to generate a toolkit for genetic labeling and visualization of different cell types under EM. I will then present findings where I applied this technique to study the ultrastructural features of mechanoreceptors in both the spinal

cord dorsal horn and the skin. The combination of molecular genetic tools and high-throughput EM has allowed us to gain ultrastructural insights into cutaneous mechanoreceptors, thereby enabling the next generation of structure-function investigations of tactile sensory organs.

Chapter 2. Development of Genetically Encoded Electron Microscopy Reporters for Multiplexed Labeling

This chapter is expanded from the paper previously published as: Zhang, Q., Lee, W.-C. A., Paul, D. L. & Ginty, D. D. Multiplexed peroxidase-based electron microscopy labeling enables simultaneous visualization of multiple cell types. *Nature Neuroscience* 22, 828-839 (2019).

Abstract

Electron microscopy (EM) is a powerful tool for circuit mapping, but identifying specific cell types in EM datasets remains a major challenge. Here we describe a technique enabling simultaneous visualization of multiple, genetically identified neuronal populations so that synaptic interactions between them can be unequivocally defined. We present 15 AAV constructs and six mouse reporter lines for multiplexed EM labeling in the mammalian nervous system. These reporters feature dAPEX2, which exhibits dramatically improved signal compared to previously described ascorbate peroxidases. By targeting this enhanced peroxidase to different subcellular compartments, multiple orthogonal reporters can be simultaneously visualized and distinguished under EM using a protocol compatible with existing EM pipelines. Proof-of-principle double and triple EM labeling experiments demonstrated synaptic connections between primary afferents, descending cortical inputs, and inhibitory interneurons in the spinal cord dorsal horn. Our multiplexed peroxidase-based EM labeling system should therefore greatly facilitate analysis of connectivity in the nervous system.

Introduction

Precise patterns of synaptic connectivity are central to nervous system function, and thus a major ongoing effort of neuroscience research is defining detailed maps of synaptic interactions throughout the nervous system. Currently, the main strategies for visualizing synaptic connectivity rely on light microscopy (LM) and electron microscopy (EM). With advances in molecular genetic approaches, specific

neurons and their synapses can be genetically labeled for visualization using both microscopic approaches. However, while multiplexed labeling strategies are readily implemented in LM, a practical system for multiplexed labeling in EM is not available. Thus, it has not been possible to fully combine the power of molecular genetics with EM, which could greatly facilitate efforts towards defining patterns of synaptic connectivity in the nervous system.

Several LM techniques have been developed to investigate synaptic connections between different neuronal populations. With fluorescence microscopy, spectrally separated fluorescent proteins can be localized to pre- or postsynaptic structures to identify synaptic partners (Daigle et al., 2018; Zhu et al., 2018), and more complex approaches such as GRASP, where signals are only detected at synapses with both pre- and postsynaptic partners expressing specific marker proteins, have also been developed (Feinberg et al., 2008; Martell et al., 2016). However, the resolution of LM is limited by diffraction, and the sizes of synaptic structures are typically below the LM resolution limit. Recently, super-resolution microscopy (Dani et al., 2010) and expansion microscopy (Karagiannis and Boyden, 2018) have been used to address this problem, however achieving the resolution necessary for visualizing fine neurites and synaptic structures is not always possible. Furthermore, fluorescence-based LM methods selectively label particular proteins; surrounding, unlabeled neuropil and intracellular compartments are not visible. Thus, many important contextual details relevant to neuronal circuitry are discarded.

EM remains the only unbiased method for comprehensively resolving the different components of synapses and structurally identifying synaptic partners. Recent advances in EM sectioning and imaging methods have made large-scale reconstructions and connectomics possible, leading to the generation of comprehensive maps of synaptic connectivity (Hildebrand et al., 2017; Kasthuri et al., 2015; Zheng et al., 2018). Despite these major advances, EM-derived connectome data can be difficult to place into a functional context because the molecular and physiological identities of pre- and postsynaptic partners generally cannot be determined. Long-range projection neurons whose axons can span nearly the entire body suffer particularly from this issue as they are particularly difficult to trace across many sections. For EM visualization, approaches using genetically expressed peroxidases and miniSOG afford a powerful

strategy to label defined neuronal populations, including projection neurons, providing identity information for one of the two synaptic partners (Atasoy et al., 2014; Joesch et al., 2016; Leal-Ortiz et al., 2008; Li et al., 2010; Schikorski et al., 2007; Shu et al., 2011). A greater challenge, however, is to simultaneously label multiple defined neuronal populations for EM analysis, which is necessary to establish the identities of pre- and postsynaptic partners as well as the convergence of multiple synapses onto common targets. Unlike fluorescence microscopy, commonly used EM imaging techniques do not permit multiplexed labeling by spectral separation. In single sections, this issue could be addressed with immuno-EM or energy-filtered transmission EM (EFTEM) with spectral resolution (Adams et al., 2016); in volumes created from serial images, this could be addressed with correlated light and electron microscopy (CLEM) using multiple fluorescence channels, and recent advances allow high-accuracy tracking of single axons (Drawitsch et al., 2018) and immunostaining with ultrastructural preservation (Fang et al., 2018). However, a technique that works well with both single sections and volumes that is versatile and simple to implement is still lacking.

To circumvent this technical challenge, we have developed tools for double, triple and higher order EM labeling by targeting peroxidase reporters to distinct cellular compartments. A previous report using double peroxidase labeling in *Drosophila* successfully enabled simultaneous visualization of two labeled cell types, however synaptic ultrastructure could not be visualized in this previous report and therefore synapse identification was not possible (Lin et al., 2016). The multiplexed EM labeling strategy reported here works exceptionally well with conventional EM pipelines with minimal modification, and provides simultaneous, unequivocal identification of pre- and postsynaptic neurons in EM volumes. We report the generation of a multiplexed EM labeling toolkit comprised of single Cre-recombinase-dependent, Flp-recombinase-dependent, and Cre-and-Flp-dual-recombinase-dependent mouse lines, as well as an array of adeno-associated virus (AAV) vectors that allow versatile multiplexed EM labeling. This multiplexed EM labeling toolkit should facilitate efforts to define patterns of synaptic connectivity throughout the mammalian nervous system.

Results

Optimization of a peroxidase for EM labeling in the mammalian nervous system

To explore the suitability of peroxidases for multiplexed EM labeling of neurons in mice, we began by testing previously described peroxidase reporter constructs (**Supplementary Table 2.1**). We first focused on defining ultrastructural features and synaptic partners of primary somatosensory neurons, whose cell bodies reside in dorsal root ganglia (DRG) and axonal projections extend peripherally into the skin and internal organs, and centrally into the spinal cord and brainstem. DRG neurons could be efficiently transduced (>90%) by neonatal AAV9 intraperitoneal (IP) injection, with small-diameter DRG neurons generally expressing AAV-delivered transgenes at higher levels than large-diameter neurons (Machida et al., 2013) (**Supplementary Fig. 2.1**). A small number of spinal cord and cortical neurons were also transduced (data not shown). While two previously described plasma membrane-targeted horseradish peroxidase (HRP) constructs, HRP-TM (Rhee et al., 2013) and mHRP (Li et al., 2010), labeled the membranes of transduced HEK293T cells (HRP-TM shown in **Supplementary Fig. 2.2a, b**), neither resulted in detectable staining of DRG axonal projections within the spinal cord following AAV9 delivery via IP injection (data not shown). Moreover, injections of the same constructs with the AAV1 capsid into the neocortex resulted in expression levels detectable by LM (**Supplementary Fig. 2.2c**), but surprisingly failed to yield detectable labeling by EM (**Supplementary Fig. 2.2d**). We speculate that the discrepancy occurred because the LM signal reflects the summation of staining throughout a thick vibratome section, but the staining was too diffuse to be visualized in EM of a single ultrathin section. A plasma membrane-targeted HRP construct, HRP-DsRed-GPI (Han et al., 2012; Lin et al., 2016), which worked well in *Drosophila* neurons, failed to traffic to the plasma membrane of cells in mouse cortex (data not shown). A construct targeting synaptic vesicles, VAMP2-HRP (Atasoy et al., 2014), which could be visualized in mouse hypothalamic neurons, labeled only one or two vesicles per terminal under the fixation and sample preparation conditions used in conventional EM pipelines. We also tested constructs expressing APEX2, an enhanced soybean ascorbate peroxidase (APX) that is less catalytically active than HRP, but is functional when expressed in cytosolic environments, unlike HRP (Lam et al., 2015). After transduction of neonatal DRG neurons by IP injection of AAV9 containing a mitochondrial-matrix-targeted APEX2

construct, mito-V5-APEX2 (Hung et al., 2016), transverse spinal cord sections were stained for peroxidase activity. Axons of small-diameter neurons, which terminate in superficial laminae of the spinal cord dorsal horn, were strongly labeled (**Fig. 2.1a**, black arrow), but axons of large-diameter neurons, which terminate in deeper laminae, exhibited low or undetectable labeling. The poor labeling of DRG axon terminals in the deep dorsal horn was not due to lack of transduction or failure of mito-V5-APEX2 expression in large-diameter DRG neurons, as mitochondrial labeling of both large- and small-diameter neuronal somata in the DRG was observed (data not shown). One possible explanation for the lack of deep dorsal horn staining is the relatively lower expression levels in the large-diameter neurons. Taken together, these results indicate that the performance of existing peroxidase constructs is strongly influenced by differences in the systems used for testing, including cell type, species of origin of those cells and sample preparation methods. Therefore, we attempted to optimize reporters and labeling conditions to visualize long-range axon projections for ultrastructural synaptic analyses in mice.

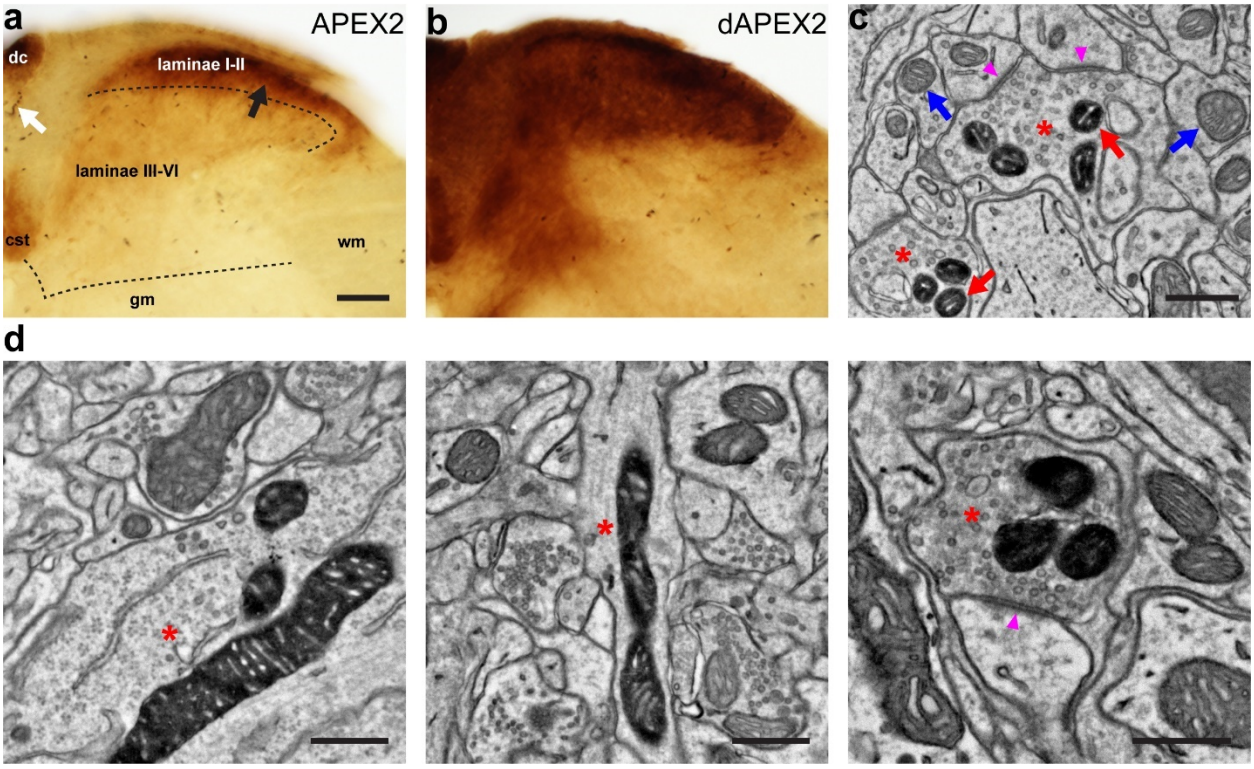

Figure 2.1. dAPEX2 is a sensitive reporter for visualizing axons of long projection neurons with EM

(**a**) LM image of the spinal cord dorsal horn after systemic transduction of AAV9-mito-V5-APEX2. Black arrow: staining from mito-V5-APEX2. Laminae I-II has much stronger staining than laminae III-VI. White arrow: endogenous peroxidase activity from erythrocytes. dc: dorsal column, cst: corticospinal tract, gm: grey matter, wm: white matter. n = 4 animals and experiments.
(**b**) LM image of the spinal cord dorsal horn after systemic transduction of AAV9-Matrix-dAPEX2. Note the robust staining in laminae III-VI with Matrix-dAPEX2 and generally increased staining levels compared to mito-V5-APEX2. n = 6 animals and experiments.
(**c**) EM image of the spinal cord dorsal horn after systemic transduction of AAV9-Matrix-dAPEX2. Asterisks: labeled axon terminals. Red arrows: labeled mitochondria. Blue arrows: unlabeled mitochondria. Arrowheads: synapses made by the labeled axon terminals. Note that ultrastructural details of the labeled neurons are not obscured by staining products. n = 3 animals and experiments.
(**d**) EM images of a cortical layer 5 neuron labeled using Tg(Rbp4-Cre)KL100 and AAV1-DIO-Matrix-dAPEX2 (asterisks). (Left) Soma of a labeled neuron. (Middle) Dendrite of a labeled neuron. (Right) Corticospinal axon in the spinal cord dorsal horn of a cortical layer 5 neuron labeled using Tg(Rbp4-Cre)KL100. Arrowhead: synapse made by the labeled neuron. n = 2 animals and experiments.
Scale bars: **a, b**: 100 μm, **c, d**: 0.5 μm.

In the process of creating APEX2 from APX, two residues (K14 and E112) at the dimeric interface were mutated to increase monomericity, thereby avoiding the concern that incorporation of a dimerizing peroxidase into a fusion protein could potentially induce mislocalization or alter function in an unexpected way (Lam et al., 2015; Martell et al., 2012). However, the mutations also decreased signal levels in tissue culture cells, possibly from lowered heme affinity and thermal stability (Lam et al., 2015; Martell et al., 2012). We reasoned that dimerization of APEX2 should not be problematic to achieve our goal of directing peroxidase reporters to different subcellular compartments. Thus, we introduced the native residues to the dimeric interface of APEX2, presumably enhancing heme affinity and thermal stability, and designated the resultant protein dAPEX2, for dimeric APEX2, although dimerization was not directly tested. Matrix-dAPEX2, which has the same sequence as mito-V5-APEX2 except for the replacement of APEX2 with dAPEX2, was packaged into AAV9 and used for IP injection to test its activity. We found that

Matrix-dAPEX2 exhibits substantially increased staining intensity (**Fig. 2.1b**) compared to mito-V5-APEX2 (**Fig. 2.1a**). The dorsal horn was intensely and evenly stained along the dorsoventral axis with Matrix-dAPEX2, mirroring the efficiency of DRG somata labeling. Axons containing labeled mitochondria (**Fig. 2.1c**, red arrows) in the dorsal horn could be clearly visualized in EM and easily distinguished from those containing unlabeled mitochondria (**Fig. 2.1c**, blue arrows). We also systematically investigated peroxidase reaction conditions and sample preparation strategies to determine optimal procedures for detecting the dAPEX2 catalyzed reaction product by EM (see **Methods** and **Supplementary Fig. 2.3-2.5**). These simple, optimized conditions do not require detergent extraction of the sample and include concentrations of glutaraldehyde appropriate for excellent specimen preservation, allowing dAPEX2 to be used for investigating the ultrastructural properties of labeled neurons and their long-range projections.

Mitochondria are ideal for EM labeling in neurons because they are abundant in somata, dendrites, axons and axon terminals. In addition, ultrastructural details of mitochondrial-labeled cells are more clearly visualized than those of cells labeled with a cytosolic reporter, because the spread of the peroxidase reaction product is limited by the mitochondrial membrane. This feature is crucial when ultrastructural details such as cytosolic electron density and synaptic vesicle morphology are of interest. To test the utility of EM labeling of long-range projection neurons using Matrix-dAPEX2, we performed cortical injections of a Cre-dependent AAV1-DIO-Matrix-dAPEX2 into the Tg(Rbp4-Cre)KL100 mouse line, which restricts expression to cortical layer 5 pyramidal tract and inter-telencephalic corticofugal neurons (Gerfen et al., 2013). Robust labeling was observed in the cell body (**Fig. 2.1d**, left panel), dendrites (**Fig. 2.1d**, middle panel) and corticospinal terminals in the dorsal horn of the cervical spinal cord (**Fig. 2.1d,** right panel). Therefore, a recombinase-dependent, mitochondrial-matrix-targeted dAPEX2 AAV construct, used in conjunction with genetic tools to selectively label neuronal subtypes, enables neuronal-subtype-specific visualization of the ultrastructural properties of axonal terminals and their synaptic arrangements by EM.

Simultaneous visualization of multiple genetically defined populations using peroxidase constructs targeted to different subcellular compartments

The finding that targeting dAPEX2 to the mitochondrial matrix can enable comparisons between the synapses of sensory neuron subtypes suggested that simultaneously targeting peroxidases to distinct subcellular compartments in two or more genetically defined neurons would allow for visualization of their synaptic relationships. To generate new peroxidase reporters targeted to distinct subcellular compartments abundant in axons and dendrites for multiplexed EM labeling, we tested dAPEX2 or HRP fused to targeting motifs for the plasma membrane, microtubules, mitochondrial intermembrane space (IMS), peroxisomes, synaptic vesicles (SV), and endoplasmic reticulum (ER) (**Supplementary Table 2.1**). These peroxidase constructs were tested in HEK293T cells and in mice by IP or cortical AAV injections (**Supplementary Table 2.1**). This testing yielded four additional constructs useful for multiplexed EM labeling: untagged, soluble dAPEX2, which labels the cytosol and nucleus (**Fig. 2.2a**), ER-dAPEX2, which includes an N-terminal Igκ signal sequence and a C-terminal KDEL ER retention sequence and labels the ER (**Fig. 2.2b**), IMS-dAPEX2, which contains the localization signal from LACTB and labels the mitochondrial IMS (**Fig. 2.2c**), and SV-HRP, a fusion protein of synaptophysin and HRP, which labels the lumen of synaptic vesicles (**Fig. 2.2d**). EM signals from dAPEX2, Matrix-dAPEX2, ER-dAPEX2, and IMS-dAPEX2 could be readily observed in neuronal somata, dendrites, and short axons, while SV-HRP could be observed only in axon terminals (in all figures, red arrows indicate labeled structures and blue arrows indicate unlabeled equivalents). Signals from dAPEX2, Matrix-dAPEX2, IMS-dAPEX2 and SV-HRP, but very little from ER-dAPEX2 (data not shown), were also observed in terminals of long-range axonal projections, which in mice can reach several centimeters in length (**Fig. 2.2**). In addition to neurons in the cerebral cortex, spinal cord and DRG shown here, some of these constructs were also shown to effectively label neurons in the cerebellum (Laurens Witter, Chong Guo, Wade Regehr, unpublished data) and the hippocampus (Ee-Lynn Yap, Michael Greenberg, unpublished data). It is noteworthy that in any given plasma-membrane-enclosed profile, all mitochondria are either labeled or unlabeled (100.0 ± 0.0%, mean ± SD, n = 30 profiles for both Matrix-dAPEX2 and IMS-dAPEX2), implying that the penetrance for matrix and IMS labeling in transduced cells is 100%, which is useful for registering profiles across different sections. The same is likely true for cytosolic and ER labeling because the cytosol and ER are largely continuous compartments where dAPEX2 can freely diffuse. SV-HRP labeled vesicles constituted

19.6 ± 12.4% (mean ± SD, n = 30 profiles) of the total synaptic vesicles in labeled presynaptic profiles. Expression of these constructs did not lead to increased mortality, or gross behavioral, anatomical or cytological abnormalities, with the exception of IMS-dAPEX2, which induced mitochondrial aggregation when expressed at very high levels but not at the levels employed in this study (see **Supplementary Table 2.1**). Therefore, these five orthogonal dAPEX2 and HRP constructs are excellent candidates for further development of a multiplexed EM labeling system for mice.

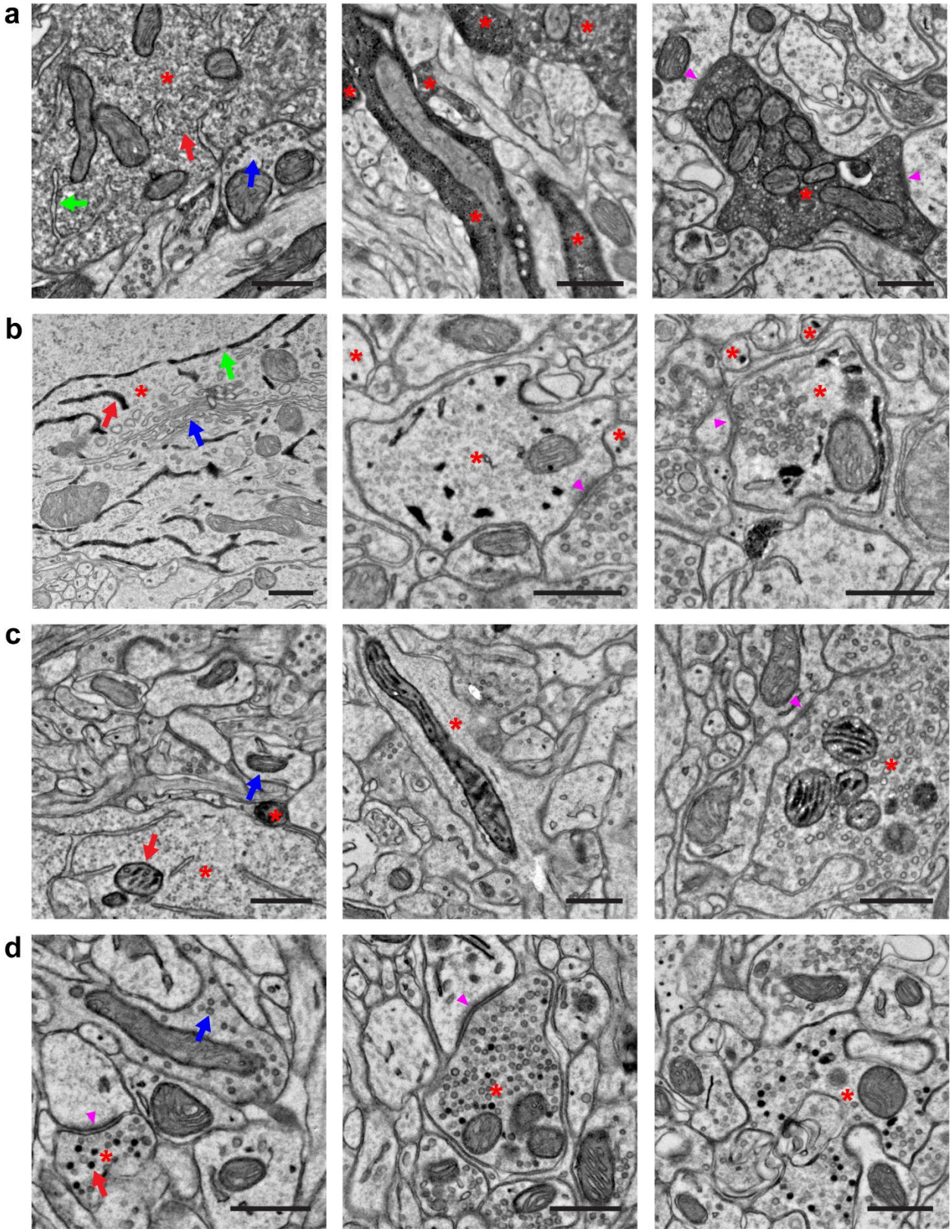
a
b
c
d

Figure 2.2. Peroxidase constructs targeted to different subcellular compartments for multiplexed EM labeling

(**a**) EM images showing localization of dAPEX2. Asterisks: labeled neurons. Staining in the cytoplasm is often not uniform and can appear granular. (Left) Soma of a cortical layer 5 neuron labeled using Tg(Rbp4-Cre)KL100. Red arrow: labeled cytoplasm. Blue arrow: unlabeled cytoplasm. Note that membrane-limited organelles, such as ER (green arrow), mitochondria, and Golgi apparatus, can usually be distinguished in stained cells. (Middle) Dendrites of cortical layer 5 neurons labeled using Tg(Rbp4-Cre)KL100. (Right) Axon of a primary sensory neuron in the spinal cord dorsal horn after AAV9 systemic transduction. Arrowheads: synapses made by the labeled neuron. n = 2 animals and experiments for each condition.

(**b**) EM images showing localization of ER-dAPEX2. Asterisks: labeled neurons. (Left) Soma of a cortical layer 5 neuron labeled using Tg(Rbp4-Cre)KL100. Red arrow: labeled ER. Blue arrow: unlabeled Golgi apparatus. Note that nuclear envelope is labeled as expected and nuclear pores (green arrows) are clearly visible, unobscured by the reaction product. (Middle) Inhibitory interneurons in the dorsal horn labeled using *Slc32a1*$^{IRES\text{-}Cre}$. Arrowhead: a synapse received by an inhibitory interneuron. (Right) Inhibitory interneurons in the spinal cord dorsal horn labeled using *Slc32a1*$^{IRES\text{-}Cre}$. Arrowhead: a synapse made by an inhibitory interneuron. Note that identification of small ER profiles can be difficult and only clearly identified profiles are marked. n = 2 animals and experiments for each condition.

(**c**) EM images showing localization of IMS-dAPEX2. Asterisks: labeled neurons. (Left) Soma of a cortical layer 5 neuron labeled using Tg(Rbp4-Cre)KL100. Red arrow: labeled mitochondrion. Blue arrow: unlabeled mitochondrion. Preservation of the full extent of IMS staining is not always achieved, potentially due to difficulty in sectioning dense heavy metal labeling, however this usually does not hinder identification of stained mitochondria. (Middle) Dendrite of cortical layer 5 neuron labeled using Tg(Rbp4-Cre)KL100. (Right) Axon in the spinal cord dorsal horn after AAV9 systemic transduction. Arrowhead: synapse made by the labeled neuron. n = 2 animals and experiments for each condition.

(**d**) EM images showing localization of SV-HRP. Asterisks: labeled neurons. Not every vesicle in transduced cells is stained. (Left) Corticocortical axon of a cortical layer 5 neuron labeled using Tg(Rbp4-Cre)KL100. Red arrow: labeled vesicle. Blue arrow: unlabeled vesicle. Arrowhead: synapse made by the

labeled neuron. (Middle) Corticospinal axon in the spinal cord dorsal horn of a cortical layer 5 neuron labeled using Tg(Rbp4-Cre)KL100. Arrowhead: synapse made by the labeled neuron. (Right) Axon in the spinal cord dorsal horn after AAV9 systemic transduction. n = 2 animals and experiments for each condition.

Scale bars: 0.5 μm.

To simultaneously label multiple genetically defined neuronal populations for synapse analysis, we used orthogonal expression systems. Currently, Cre, Flp and Dre recombinases, as well as transcription factors such as tTA/rtTA are used for directed expression of reporter genes in mice, with Cre and Flp recombinases being most widely used. Specific neuronal populations can also be targeted anatomically using AAV injections or by taking advantage of the different tropisms of AAV capsids (Castle et al., 2016). Therefore, we constructed constitutively expressed as well as Cre- and Flp-recombinase-dependent AAV vectors for dAPEX2, Matrix-dAPEX2, ER-dAPEX2, IMS-dAPEX2, and SV-HRP (**Table 2.1**). To address the utility of these AAV constructs for multiplexed EM labeling, we employed two different genetic strategies. For the first strategy, we crossed the Tg(Rbp4-Cre)KL100 mouse line with the *Pvalb*$^{T2A\text{-}FlpO}$ line, which expresses FlpO in fast spiking cortical interneurons, including basket and chandelier cells (Madisen et al., 2015). We performed cortical injections of Cre-dependent AAV1-DIO-ER-dAPEX2 and Flp-dependent AAV1-FDIO-Matrix-dAPEX2 into Tg(Rbp4-Cre)KL100; *Pvalb*$^{T2A\text{-}FlpO}$ neonates. Cells with ER labeling (**Fig. 2.3a**, red asterisks) and mitochondrial matrix labeling (**Fig. 2.3a**, green asterisks) were easily observed and distinguished, and since neither dAPEX2 reporter obscures ultrastructural details, identification of synapses was straightforward. EM analysis revealed Pvalb^{+} neuron to Rbp4^{+} neuron synapses that were typically perisomatic and symmetric (**Fig. 2.3a**, arrowheads), consistent with prior electrophysiological and EM studies (Hu et al., 2014). For a second test, we used *Slc32a1*$^{IRES\text{-}Cre}$ mice, in which Cre is expressed in all inhibitory neurons (Vong et al., 2011), and *Avil*^{FlpO} mice, in which FlpO is expressed in all primary somatosensory neurons (Ling Bai, D.D.G., unpublished data). AAV9-FDIO-IMS-dAPEX2 was delivered by IP injection into *Slc32a1*$^{IRES\text{-}Cre}$; *Avil*^{FlpO} neonates followed by a dorsal horn injection of AAV1-DIO-Matrix-dAPEX2 at P11-P12. This resulted in robust labeling of dorsal horn inhibitory interneurons, identified by peroxidase staining of their mitochondrial matrix (**Fig. 2.3b,** red

asterisks), and somatosensory neuron terminals, identified by staining of their mitochondrial IMS (**Fig. 2.3b**, green asterisks). In this case, axodendritic synapses from primary afferents onto dorsal horn inhibitory interneurons and axoaxonic synapses from inhibitory interneurons onto primary afferents were readily seen (**Fig. 2.3b**, arrowheads). The latter type of synapse is believed to underlie presynaptic inhibition, an important mechanism for central control of somatosensory input (Rudomin and Schmidt, 1999).

Table 2.1. List of AAV constructs

AAV Construct	Recombinase Control	Addgene Plasmid #
pAAV-dAPEX2	None (constitutive)	117173
pAAV-DIO-dAPEX2	Cre-dependent	117174
pAAV-FDIO-dAPEX2	Flp-dependent	117175
pAAV-Matrix-dAPEX2	None (constitutive)	117176
pAAV-DIO-Matrix-dAPEX2	Cre-dependent	117177
pAAV-FDIO-Matrix-dAPEX2	Flp-dependent	117178
pAAV-IMS-dAPEX2	None (constitutive)	117179
pAAV-DIO-IMS-dAPEX2	Cre-dependent	117180
pAAV-FDIO-IMS-dAPEX2	Flp-dependent	117181
pAAV-ER-dAPEX2	None (constitutive)	117182
pAAV-DIO-ER-dAPEX2	Cre-dependent	117183
pAAV-FDIO-ER-dAPEX2	Flp-dependent	117184
pAAV-SV-HRP	None (constitutive)	117185
pAAV-DIO-SV-HRP	Cre-dependent	117186
pAAV-FDIO-SV-HRP	Flp-dependent	117187

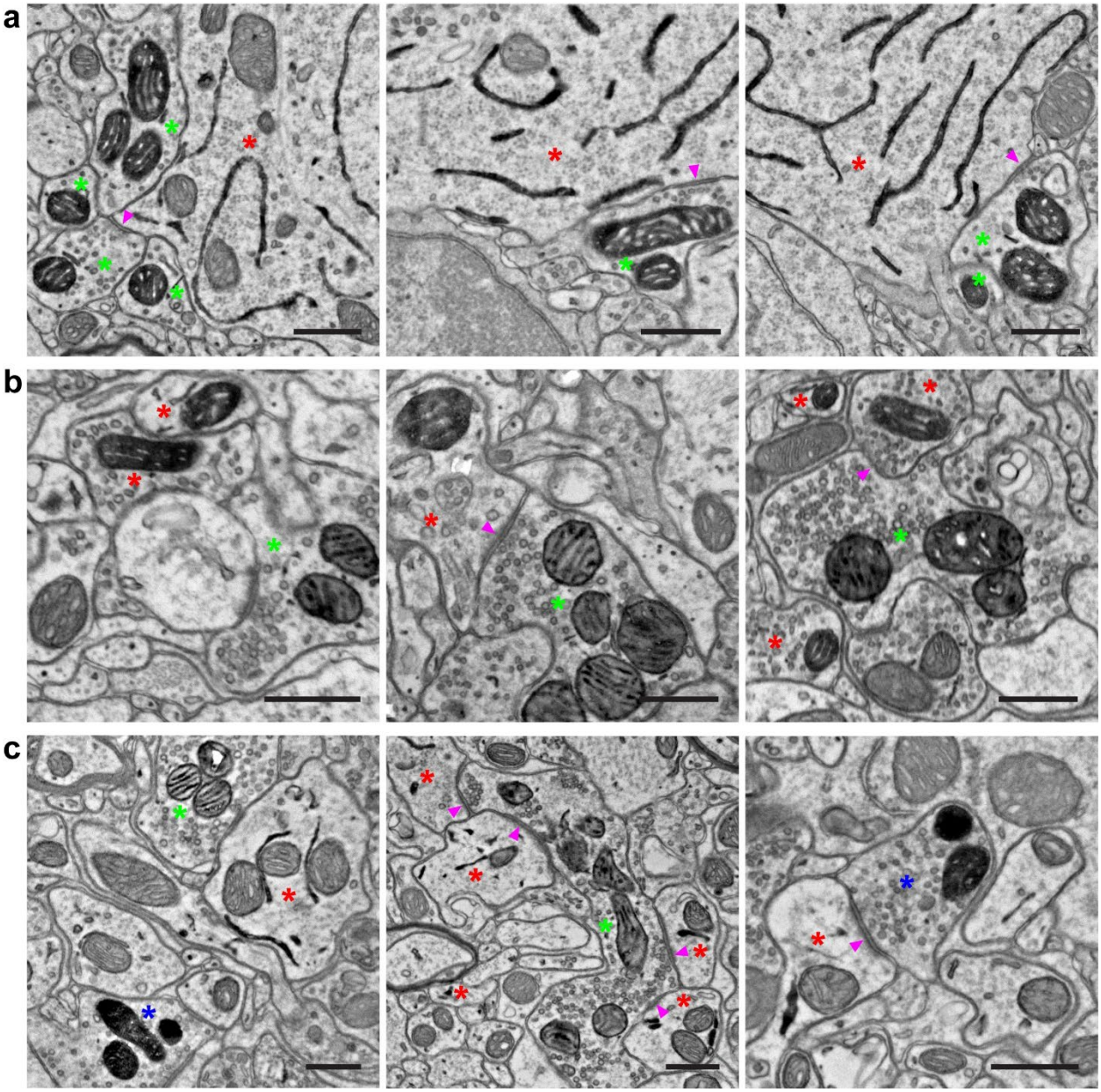

Figure 2.3. Double and triple EM labeling using orthogonal peroxidase reporter constructs

(**a**) EM images showing double labeling of cortical layer 5 pyramidal neurons (ER) using Tg(Rbp4-Cre)KL100 and AAV1-DIO-ER-dAPEX2 (red asterisks), and fast-spiking GABAergic interneurons (mitochondrial matrix) using *Pvalb*$^{T2A\text{-}FlpO}$ and AAV1-FDIO-Matrix-dAPEX2 (green asterisks). Note the symmetric perisomatic synapses made by fast-spiking interneurons onto layer 5 pyramidal neurons (arrowheads). n = 4 animals and experiments.

(**b**) EM images showing double labeling of spinal cord dorsal horn inhibitory interneurons (mitochondrial matrix) using *Slc32a1*$^{IRES\text{-}Cre}$ and AAV1-DIO-Matrix-dAPEX2 (red asterisks), and primary somatosensory afferents (mitochondrial IMS) using *Avil*^{FlpO} and AAV9-FDIO-IMS-dAPEX2 (green asterisks). Arrowheads: an axodendritic synapse from a primary somatosensory afferent to an inhibitory interneuron (Middle) and an axoaxonic synapse from an inhibitory interneuron to a primary somatosensory afferent (Right). n = 3 animals and experiments.

(**c**) EM images showing triple labeling of dorsal horn inhibitory interneurons (ER) using *Slc32a1*$^{IRES\text{-}Cre}$ and AAV1-DIO-ER-dAPEX2 (red asterisks), primary somatosensory afferents (mitochondrial IMS) using *Avil*^{FlpO} and AAV9-FDIO-IMS-dAPEX2 (green asterisks), and corticospinal inputs (mitochondrial matrix) using cortical injections of AAV1-Matrix-dAPEX2 (blue asterisks). (Left) All three stains can be clearly visualized and distinguished in the same field of view. (Middle) A primary somatosensory afferent making axodendritic synaptic contacts onto inhibitory interneurons (arrowheads). Note the numerous synaptic contacts made by the primary somatosensory afferent, which is characteristic of the central axons of glomeruli. (Right) A corticospinal axon making an axodendritic synapse onto an inhibitory interneuron (arrowhead). This type of simple synaptic arrangement is typical of corticospinal inputs. n = 2 animals and experiments.

Scale bars: 0.5 μm.

To address the feasibility of simultaneously labeling three neuronal populations, we used *Slc32a1*$^{IRES\text{-}Cre}$; *Avil*^{FlpO} mice, and injected AAV9-FDIO-IMS-dAPEX2 IP to label primary afferents, AAV1-DIO-ER-dAPEX2 into the dorsal horn to label spinal cord inhibitory interneurons, and AAV1-Matrix-dAPEX2 into the cortex to label descending corticospinal neurons. Each of the three labeled structures, ER (**Fig. 2.3c**, red asterisks), mitochondrial IMS (**Fig. 2.3c**, green asterisks), and mitochondrial matrix (**Fig. 2.3c**, blue asterisks), respectively, were clearly visualized and distinguished from the other two structures in the spinal cord dorsal horn by EM. Consistent with previous reports (Abraira et al., 2017; Ribeiro-da-Silva and Coimbra, 1982; Valtschanoff et al., 1993), primary afferents (green asterisks) often form glomerular synapses, while corticospinal axons (blue asterisks) mainly form simple synaptic interactions. In addition,

inhibitory interneurons (red asterisks) represent a large fraction of all postsynaptic partners for both types of long-range inputs into the dorsal horn.

In order to investigate whether these reporters can be used for multiple labeling in volume EM, we serially sectioned one of the spinal cord dorsal horn samples used for **Fig. 2.3b**, and imaged a volume of 35 x 24 x 2 µm. These two labels could be readily seen throughout the volume and did not cause any issue in montaging or alignment. We used this volume to reconstruct a primary afferent (green) and two inhibitory interneuron profiles (axon in light red and dendrite in dark red) where synaptic interactions were seen (**Fig. 2.4a, b** and **Supplementary Video 2.1 and 2.2**). We also determined the discriminability of the two mitochondrial labels using this image volume. Two annotators independently categorized all the mitochondria as either matrix-labeled, IMS-labeled, or unlabeled in a volume of 12 x 8 x 2 µm, and then the annotations were compared. Of the 325 mitochondria annotated, 319 had matching annotations (98.2%), and only six mitochondria had mismatching annotations (1.8%) (**Fig. 2.4c**). Of the six mismatching annotations, one was a matrix-labeled vs. IMS-labeled mismatch, one was a matrix-labeled vs. unlabeled mismatch, and four were IMS-labeled vs. unlabeled mismatches. Three of the IMS-labeled vs. unlabeled mismatches resulted from human error during annotation. This indicates that the two mitochondrial labels are readily distinguishable from each other. Because the three other orthogonal labels are targeted to different organelles, they are even more easily distinguished from each other and the two mitochondrial labels, and the few mismatches for the volume annotated here for mitochondrial matrix vs. mitochondrial IMS thus likely represents a worst-case scenario.

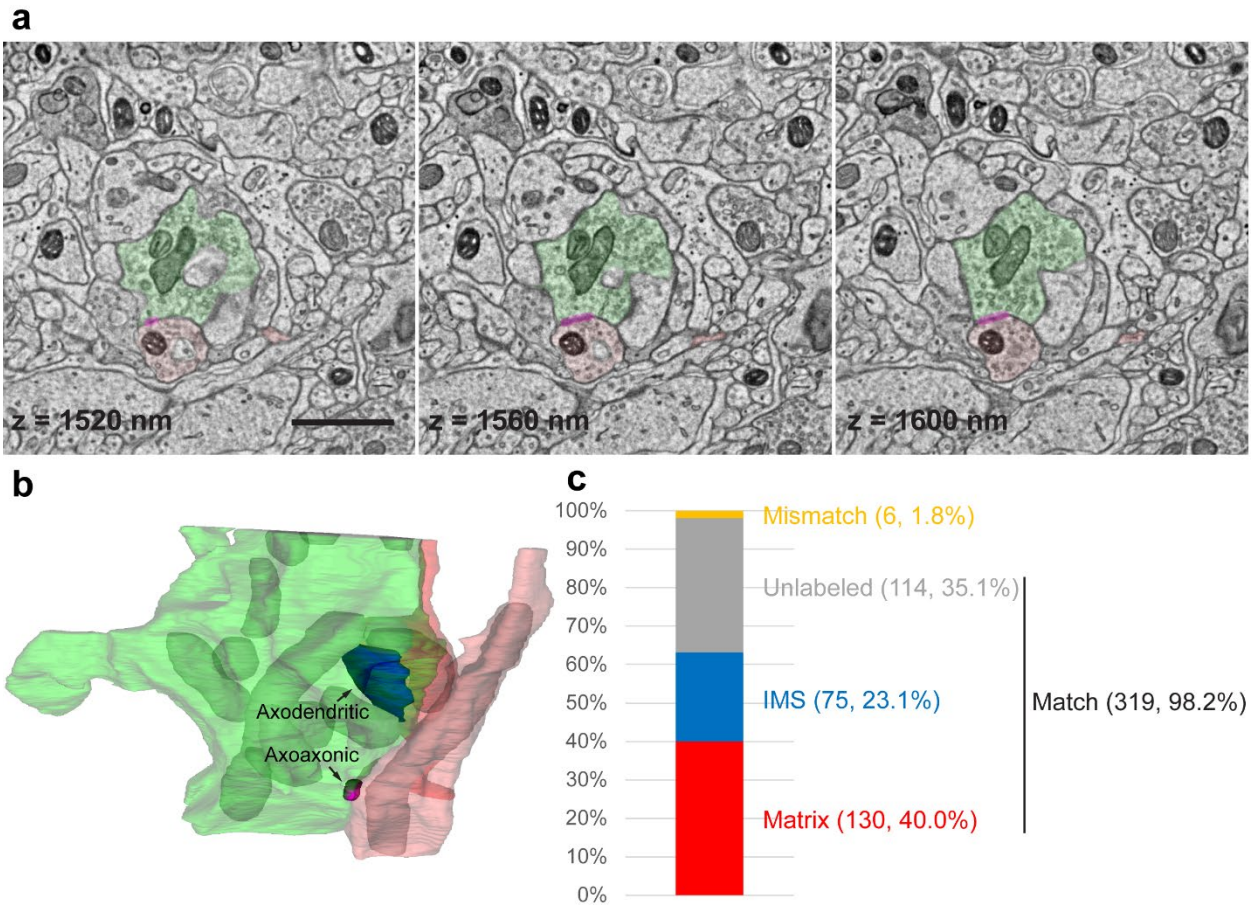

Figure 2.4. Multiplexed peroxidase labeling in volume EM

(**a**) Three consecutive sections from one of the samples shown in **Fig. 2.3b** in which spinal cord dorsal horn inhibitory interneurons (mitochondrial matrix) were labeled using *Slc32a1*$^{IRES\text{-}Cre}$ and AAV1-DIO-Matrix-dAPEX2 (axon in light red and dendrite in dark red), and primary somatosensory afferents (mitochondrial IMS) were labeled using *Avil*^{FlpO} and AAV9-FDIO-IMS-dAPEX2 (green). Magenta overlay: axoaxonic synapse between an inhibitory interneuron and the primary afferent. The z coordinates from the top of the volume are noted on each image. Scale bar: 1 µm. See also **Supplementary Video 2.1**.

(**b**) The 3D reconstruction of the same primary afferent and inhibitory interneuron profiles. Labeled mitochondria (grey) and an axodendritic synapse between the primary afferent and an inhibitory interneuron (blue) are additionally reconstructed. See also **Supplementary Video 2.2**.

(**c**) Level of concordance between independent annotations of mitochondria (matrix-labeled, IMS-labeled, or unlabeled) in a volume of 12 x 8 x 2 µm by two annotators. The numbers of each category as well as their proportions of the total number of mitochondria are indicated in parentheses. The three categories

Matrix, IMS, and Unlabeled all contain matching annotations, while the Mismatch category contains mismatching annotations.

Therefore, labeling with orthogonal EM reporters provides a versatile approach to investigate complex synaptic interactions in both single sections and volumes. In all, the fifteen AAV peroxidase reporter constructs (**Table 2.1**), used with orthogonal recombinase-dependent expression systems and anatomically defined injections, allow simultaneous double, triple, and possibly higher order EM labeling to visualize and define synaptic arrangements in complex neuropils.

Generation and characterization of mouse lines encoding orthogonal EM reporters

To complement the use of the AAV peroxidase reporter constructs and increase the versatility of the multiplexed peroxidase EM labeling strategy, we next generated mouse lines that conditionally express two of the dAPEX2 reporters. These mouse reporter lines can be used in conjunction with the AAV peroxidase reporter vectors for multiplexed EM labeling, and for many applications will be preferable to AAV vectors. For example, mouse reporter lines may be superior if: 1) AAVs lead to variable levels of expression due to variability of transduction; 2) recombinases must be expressed during embryonic development to successfully label a particular neuronal type; or 3) complex surgeries are required to inject AAVs into target regions, which may be technically challenging or result in tissue damage. Thus, mouse lines that conditionally express dAPEX2 reporters in defined neuronal subtypes should enable a diverse range of single or multiplexed EM labeling applications.

We first generated Cre- and Flp-dual-recombinase-dependent reporter lines for both Matrix-dAPEX2 and ER-dAPEX2 (**Fig. 2.5a**). The targeting strategy employed a dual-recombinase-dependent expression cassette with an artificial CAG promoter (Madisen et al., 2015) preceding the dAPEX2 reporters knocked into the *Gt(ROSA)26Sor* (*ROSA26*) locus for ubiquitous tissue expression. The frt-STOP-frt and loxP-STOP-loxP cassettes enable Flp- and Cre-dependent expression, respectively (Madisen et al., 2015). Mice carrying these knock-in alleles, termed *ROSA26*$^{DR\text{-}Matrix\text{-}dAPEX2}$ and *ROSA26*$^{DR\text{-}ER\text{-}dAPEX2}$, were

generated and tested for recombinase-dependent reporter expression by cortical injection of AAV1-Cre, AAV1-FlpO, or a mixture of both. AAV1-tdTomato was co-injected to mark the injection site and evaluate viral transduction. We found no peroxidase activity from dAPEX2 in the cortex of mice injected with AAVs lacking recombinases, AAV1-Cre alone, or AAV1-FlpO alone (**Fig. 2.5b, c**, left three panels), demonstrating tight control of reporter expression by each of the STOP cassettes. On the other hand, co-injection of AAV1-Cre and AAV1-FlpO resulted in strong peroxidase activity from dAPEX2 in the brains of *ROSA26*$^{DR\text{-}Matrix\text{-}dAPEX2}$ and *ROSA26*$^{DR\text{-}ER\text{-}dAPEX2}$ mice (**Fig. 2.5b, c**, rightmost panel), demonstrating high recombinase-dependent dAPEX2 expression from both reporter lines. Subsequently, single-recombinase-dependent reporter lines were generated by germline deletion of the appropriate STOP cassettes (**Table 2.2**). To determine whether dAPEX2 peroxidase levels in these mouse lines are sufficient for EM identification of labeled neurons, we prepared dual AAV-transduced cortical samples for EM analysis. Ultrathin sections revealed easily identifiable, correctly localized staining in both *ROSA26*$^{DR\text{-}Matrix\text{-}dAPEX2}$ (**Fig. 2.5d**) and *ROSA26*$^{DR\text{-}ER\text{-}dAPEX2}$ (**Fig. 2.5e**) mice.

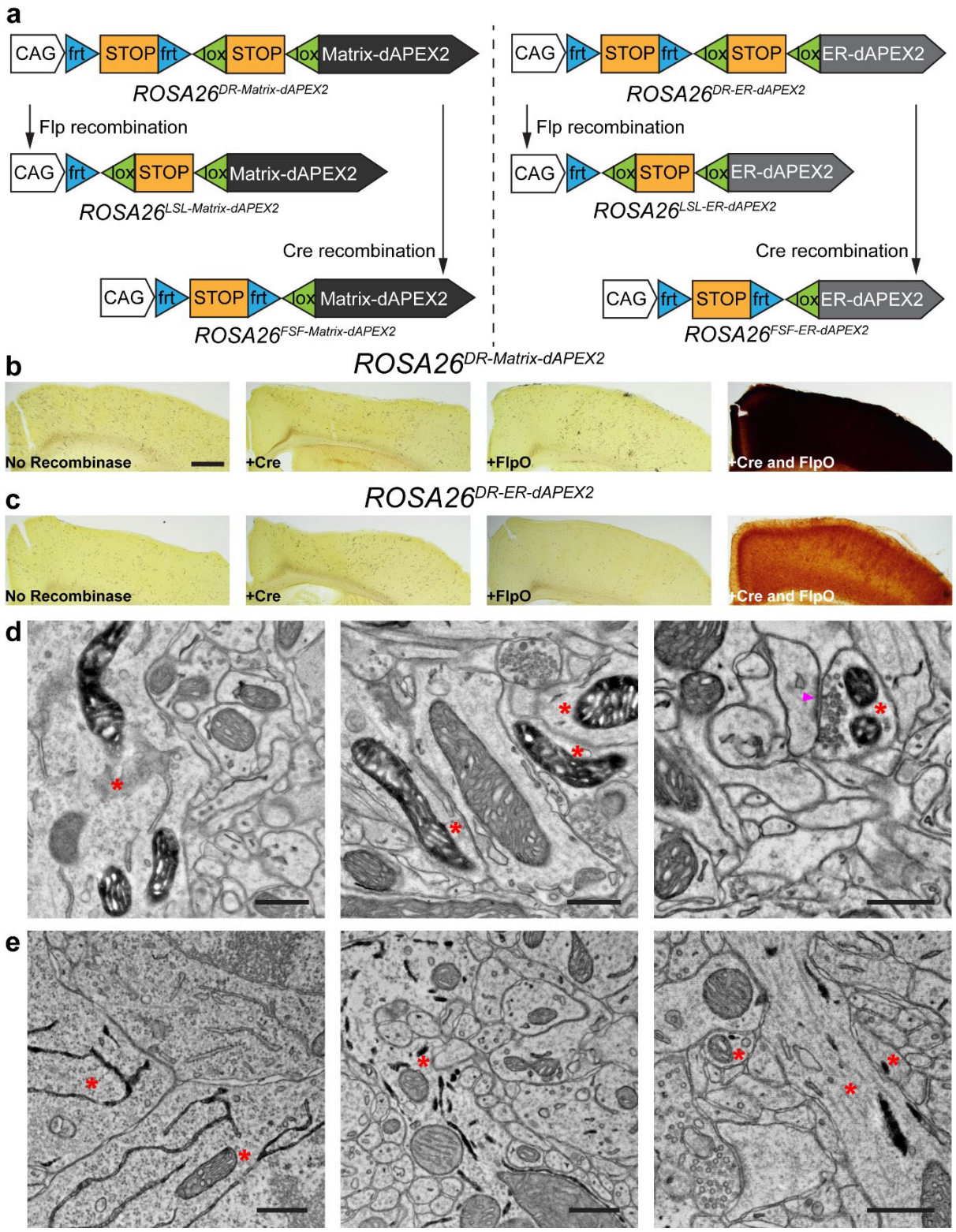

Figure 2.5. Generation of recombinase-dependent mouse dAPEX2 reporter lines

(**a**) Schematics showing overviews of the six mouse reporter lines. Single-recombinase-dependent lines were generated by germline deletion of one of the STOP cassettes.

(**b, c**) LM images showing cortical sections after injections of AAVs encoding various recombinases into dual-recombinase-dependent *ROSA26*$^{DR\text{-}Matrix\text{-}dAPEX2}$ (**b**) and *ROSA26*$^{DR\text{-}ER\text{-}dAPEX2}$ animals (**c**). Only endogenous peroxidase activity was observed when no recombinase, Cre alone, or FlpO alone was transduced (left three panels). dAPEX2 peroxidase staining was observed only following co-injection of Cre and FlpO viruses (rightmost panels).

(**d**) EM images from the cortex of a *ROSA26*$^{DR\text{-}Matrix\text{-}dAPEX2}$ animal co-transduced with Cre and FlpO. Asterisks: labeled neurons. Labeled mitochondria can be seen in soma, dendrites, and axons, consistent with results using AAVs to express peroxidase constructs. Arrowhead: synapse made by the labeled neuron. n = 4 animals and experiments.

(**e**) EM images of the cortex of a *ROSA26*$^{DR\text{-}ER\text{-}dAPEX2}$ animal co-transduced with Cre and FlpO. Asterisks: labeled neurons. Labeled ER can be seen in somata and dendrites, as expected. n = 4 animals and experiments.

Scale bars: **b, c**: 500 μm, **d, e**: 0.5 μm.

Table 2.2. List of mouse reporter lines

Mouse Line	Recombinase Control	JAX Stock #
ROSA26$^{DR\text{-}Matrix\text{-}dAPEX2}$	Cre-and-Flp-dual-dependent	032764
ROSA26$^{LSL\text{-}Matrix\text{-}dAPEX2}$	Cre-dependent	032765
ROSA26$^{FSF\text{-}Matrix\text{-}dAPEX2}$	Flp-dependent	032766
ROSA26$^{DR\text{-}ER\text{-}dAPEX2}$	Cre-and-Flp-dual-dependent	032767
ROSA26$^{LSL\text{-}ER\text{-}dAPEX2}$	Cre-dependent	032768
ROSA26$^{FSF\text{-}ER\text{-}dAPEX2}$	Flp-dependent	032769

Since labeling many neuronal populations and their projections requires intersectional genetic strategies, we investigated whether the *ROSA26*$^{DR\text{-}Matrix\text{-}dAPEX2}$ line can label long-range axonal projections in a dual-recombinase-dependent manner using mouse recombinase driver lines. For this, we generated

Scn10a^{Cre}; *Avil*^{FlpO}; *ROSA26*$^{DR\text{-}Matrix\text{-}dAPEX2}$ animals: *Scn10a*^{Cre} expresses Cre recombinase in virtually all C-fiber sensory neurons and a smaller number of medium-diameter lightly myelinated sensory neurons (Nassar et al., 2004; Shields et al., 2012), and *Avil*^{FlpO} expresses FlpO recombinase in all somatosensory neurons. By LM, strong staining in the superficial dorsal horn, as well as sparse labeling in the deep dorsal horn and dorsal column was observed, while no labeling of spinal cord neurons or the corticospinal tract was observed, as predicted (**Fig. 2.6a**, left panel). By EM, abundant labeled axon terminals (red asterisks) were observed in the superficial laminae of the dorsal horn (**Fig. 2.6a**, middle panel), as well as some myelinated axons and axon terminals in deeper laminae (**Fig. 2.6a**, right panel). Axon terminals of these long-range projection neurons could also be observed in the skin with LM (**Fig. 2.6b**, left panel), and labeled longitudinal lanceolate endings associated with hair follicles (**Fig. 2.6b**, middle panel) and free nerve endings (**Fig. 2.6b**, right panel) within the epidermis were seen under EM. We also tested whether C-LTMRs could be selectively labeled using this reporter line by generating *Th*$^{T2A\text{-}CreER}$; *Avil*^{FlpO}; *ROSA26*$^{DR\text{-}Matrix\text{-}dAPEX2}$ animals. Indeed, staining patterns consistent with C-LTMR labeling (Li et al., 2011) could be seen under LM (data not shown). Additionally, labeled axonal profiles with glomerular synapses were observed under EM (**Fig. 2.6c**). These findings demonstrate that the *ROSA26*$^{DR\text{-}Matrix\text{-}dAPEX2}$ mouse line works well for labeling long-range projections of genetically defined neuronal populations. Finally, we generated mice harboring the *Slc32a1*$^{IRES\text{-}Cre}$ and Cre-dependent *ROSA26*$^{LSL\text{-}ER\text{-}dAPEX2}$ alleles to label the ER in inhibitory interneurons throughout the nervous system. We observed correctly localized ER labeling in inhibitory neurons in cortex, spinal cord dorsal horn, and striatum, demonstrating the wide range of brain regions and neurons that could be visualized using this mouse line (**Fig. 2.6d**).

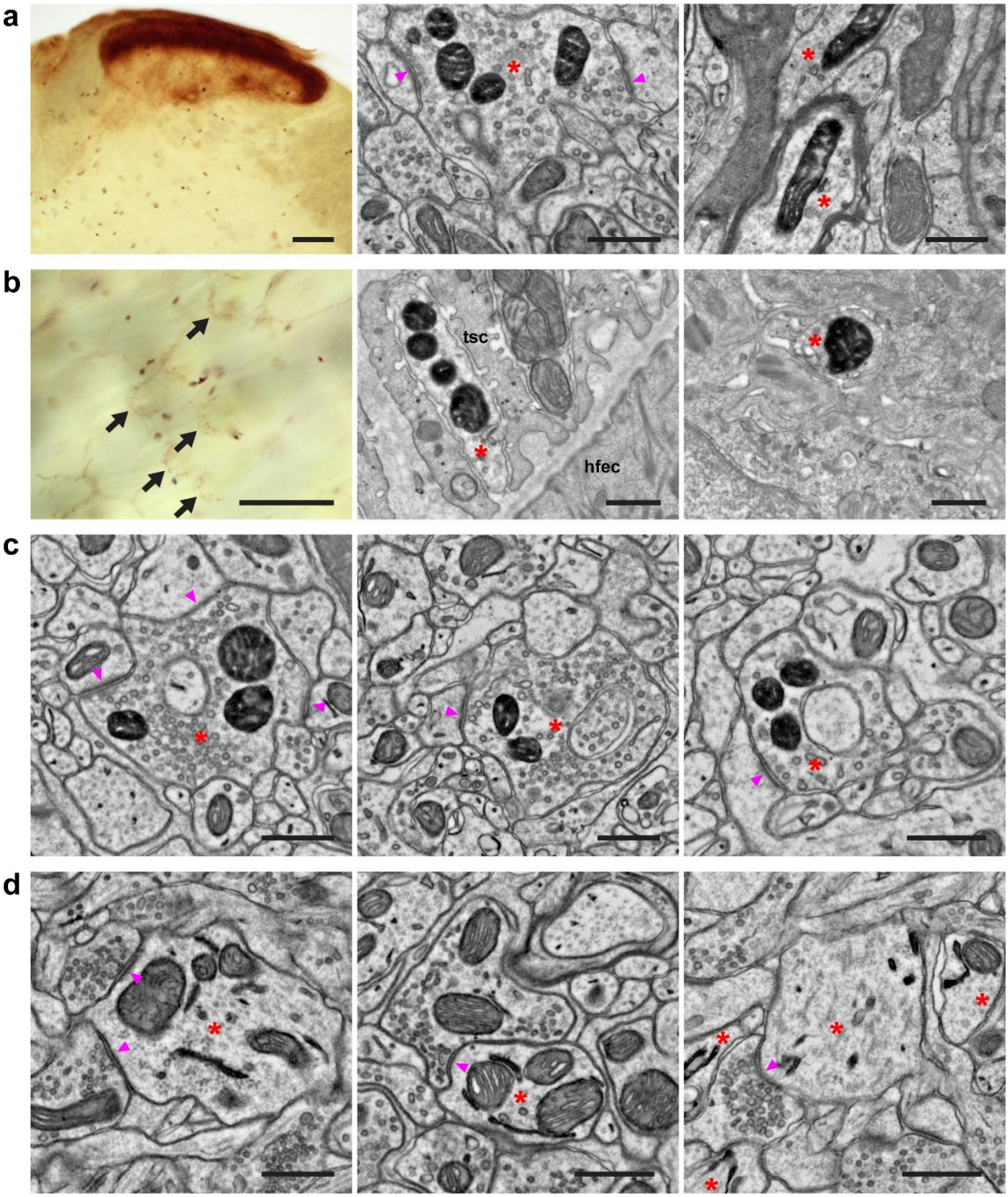

Figure 2.6. Mouse dAPEX2 reporter lines exhibit robust EM staining

(**a**) Spinal cord dorsal horn images from an *Scn10a*^{Cre}; *Avil*^{FlpO}; *ROSA26*$^{DR\text{-}Matrix\text{-}dAPEX2}$ animal. (Left) LM image showing the expected pattern of heavy labeling in superficial laminae and lighter labeling in deep

laminae expected from the expression of $Na_V1.8$ in both small- and a subset of large-diameter neurons. (Middle) EM image showing labeling in superficial laminae. Asterisk: labeled C-fiber axon terminal. Arrowheads: synapses made by the labeled C-fiber. (Right) EM image showing labeling in deep laminae. Asterisks: labeled axons. Note the myelination around one of the profiles. n = 2 animals and experiments.
(**b**) Skin images from an *Scn10a*^{Cre}; *Avil*^{FlpO}; *ROSA26*$^{DR\text{-}Matrix\text{-}dAPEX2}$ animal. (Left) LM image showing labeled lanceolate endings (arrows). Free nerve endings are also labeled but not visible in this focal plane. (Middle) EM image showing a labeled lanceolate ending (asterisk) around a hair follicle. tsc: terminal Schwann cell, hfec: hair follicle epithelial cell. (Right) EM image showing a labeled free nerve ending (asterisk) in the epidermis. n = 2 animals and experiments.
(**c**) EM images from a *Th*$^{T2A\text{-}CreER}$; *Avil*^{FlpO}; *ROSA26*$^{DR\text{-}Matrix\text{-}dAPEX2}$ animal treated with tamoxifen at P14 to label C-LTMRs. Asterisks: labeled C-LTMR terminals. Arrowheads: synapses made by labeled C-LTMRs. n = 2 animals and experiments.
(**d**) EM images from an *Slc32a1*$^{IRES\text{-}Cre}$; *ROSA26*$^{LSL\text{-}ER\text{-}dAPEX2}$ animal. Asterisks: labeled neurons. (Left) A dendrite of a cortical inhibitory interneuron. Arrowheads: synapses received by the labeled inhibitory interneuron. (Middle) A dendrite of a spinal cord dorsal horn inhibitory interneuron. Arrowhead: synapse received by the labeled inhibitory interneuron. (Right) Dendrites of striatal inhibitory neurons. Arrowhead: synapse received by a labeled inhibitory neuron. n = 2 animals and experiments.
Scale bars: **a**: (Left) 100 μm, (Middle and Right) 0.5 μm, **b**: (Left) 100 μm, (Middle and Right) 0.5 μm, **c, d**: 0.5 μm.

In addition, we generated mouse reporter lines using ER-HRP (dAPEX2 replaced with HRP in ER-dAPEX2) and SV-HRP in order to further expand the utility of this technique (**Table 2.3**). Since mouse reporter lines tend to express proteins at lower levels than AAV1 injected parenchymally, *ROSA26*$^{ER\text{-}HRP}$ lines allow more robust labeling and exhibit similar labeling appearances to *ROSA26*$^{ER\text{-}dAPEX2}$ lines (**Fig. 2.7a**). On the other hand, *ROSA26*$^{SV\text{-}HRP}$ mouse lines provide an axonal labeling tool (**Fig. 2.7b**) that can be used in conjunction with *ROSA26*$^{Matrix\text{-}dAPEX2}$ lines.

Table 2.3. List of additional mouse reporter lines

Mouse Line	Recombinase Control	JAX Stock #
ROSA26$^{DR\text{-}ER\text{-}HRP}$	Cre-and-Flp-dual-dependent	034748
ROSA26$^{LSL\text{-}ER\text{-}HRP}$	Cre-dependent	034746
ROSA26$^{FSF\text{-}ER\text{-}HRP}$	Flp-dependent	034750
ROSA26$^{DR\text{-}SV\text{-}HRP}$	Cre-and-Flp-dual-dependent	034749
ROSA26$^{LSL\text{-}SV\text{-}HRP}$	Cre-dependent	034747
ROSA26$^{FSF\text{-}SV\text{-}HRP}$	Flp-dependent	034745

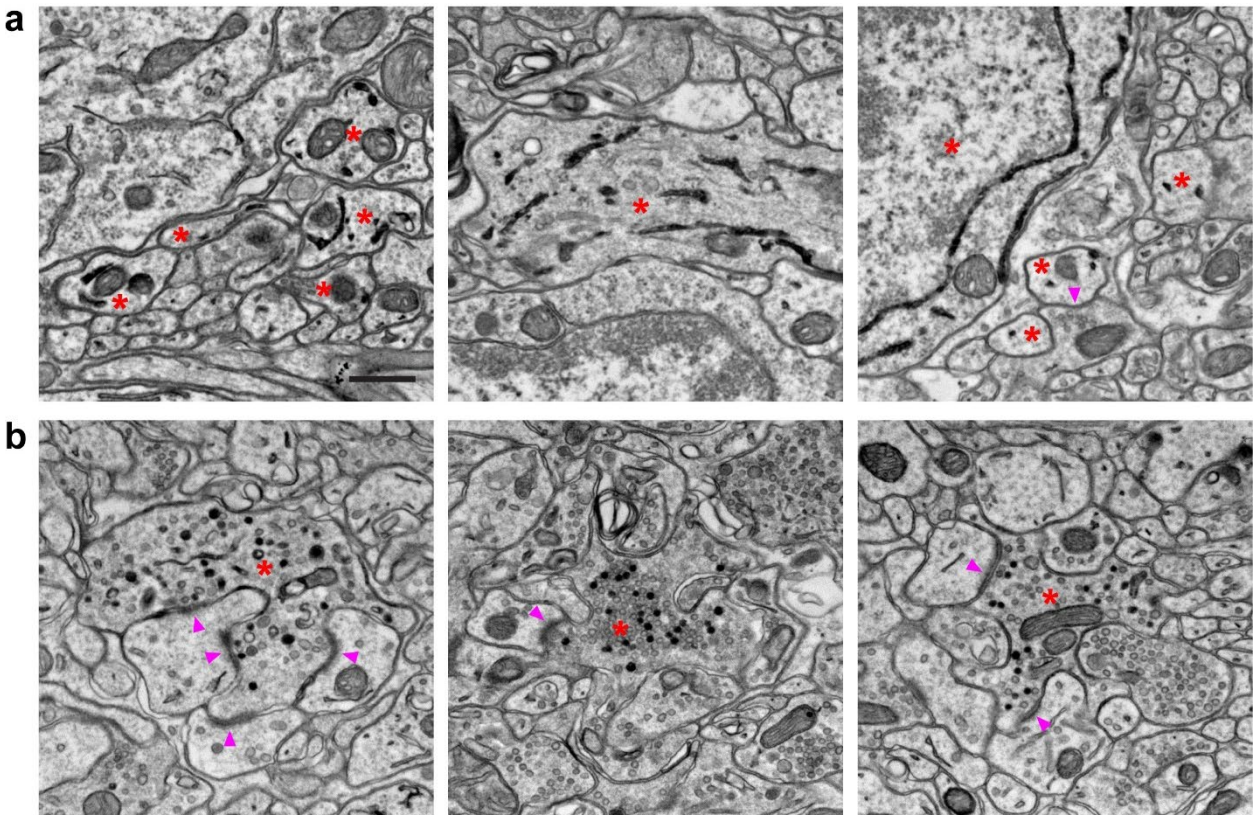

Figure 2.7. Additional mouse reporter lines for versatile labeling

(**a**) EM images from an *Slc32a1*$^{IRES\text{-}Cre}$; *ROSA26*$^{LSL\text{-}ER\text{-}HRP}$ animal. Asterisks: labeled spinal cord dorsal horn inhibitory neurons. Arrowhead: synapse received by a labeled inhibitory neuron. n = 2 animals and experiments.

(**b**) EM images from an *Scn10a*^{Cre}; *Avil*^{FlpO}; *ROSA26*$^{DR\text{-}SV\text{-}HRP}$ animal. Asterisks: labeled C-fiber terminals. Arrowheads: synapses made by labeled C-fibers. n = 2 animals and experiments.

Scale bar: 0.5 µm.

Discussion

Here we describe a multiplexed peroxidase-based labeling strategy for simultaneous visualization of multiple neuronal populations by EM. We also report six new dAPEX2 mouse reporter lines and 15 AAV peroxidase constructs that comprise a versatile toolkit for multiplexed labeling. These tools, which have been deposited into public repositories, can be used alone or in combination to define synaptic arrangements of complex neuropils in mammalian systems.

Historically, multiplexed labeling in EM has been a major challenge. One approach to multiplexed EM labeling is to use antibodies conjugated with different-sized gold particles for immuno-EM. While immuno-EM is valuable for providing information on protein localization, it is difficult to implement because many, if not most, epitopes are destroyed or rendered inaccessible by conventional EM specimen preparation. Furthermore, specimen preparations amenable to immuno-EM are poorly suited for preserving the ultrastructural details needed to identify pre- and postsynaptic structures. A more recent approach using EFTEM to achieve spectral separation for different stains, requires highly specialized equipment and long exposure times (Adams et al., 2016), and is unlikely to be feasible for most applications including large-scale reconstructions. CLEM has also been used to identify multiple neuronal populations in tissue volumes. Newly developed algorithms have enabled improved accuracy and allowed tracking projection axons in dense neuropils with multiple channels (Drawitsch et al., 2018). However, for small profiles such as axons, a relatively large EM volume (encompassing axonal lengths of 40-50 µm) and considerable amount of reconstruction at both LM and EM levels are required for the registration algorithms to identify matching profiles. This approach is time- and labor-intensive and cannot be performed routinely like single-section EM.

Our peroxidase-based multiplexed EM labeling tools take advantage of the simple fact that peroxidase staining can be restricted to distinct cellular compartments and thus the majority of peroxidase reporters

we described do not obscure ultrastructural features of cells such as synaptic vesicles, postsynaptic densities, and the cytoskeleton. These peroxidase reporters can be targeted to two, three, four or more cellular compartments, in different populations simultaneously, to address synaptic relationships between genetically defined neuronal populations. An additional key advantage of this approach is that minimal modifications to existing EM pipelines are required for implementation. Thus, in addition to single-section and serial-section transmission EM used here, multiplexed peroxidase EM labeling should also be compatible with serial block-face scanning EM, serial-section scanning EM, focused ion beam scanning EM, and X-ray microscopy (Joesch et al., 2016; Ng et al., 2016).

While previously reported peroxidase constructs have been shown to work well in tissue culture and in certain organisms, our findings suggest that many of these are not optimal for the mammalian nervous system. dAPEX2, described here, is more sensitive than APEX2 and can be used in any context where dimerization is tolerated. The improvement on peroxidase activity afforded by dAPEX2 proved critical for the generation of mouse reporter lines, in part because the commonly used ROSA26-CAG cassette typically expresses transgenes at lower levels than viral transduction methods with a concomitant reduction in the level of detection of genetically encoded reporters (Daigle et al., 2018).

The suite of peroxidase EM reporter constructs described here is highly versatile, and may be further increased by generating Dre-dependent and tTA-dependent dAPEX2 and HRP constructs for additional orthogonal driver channels, as well as constructing ΔG-rabies for trans-synaptic tracing. One exciting prospect will be to use the AAV and mouse line EM reporters with serial-section EM to obtain large-scale volume reconstructions for connectomics. Multiplexed EM labeling will reduce costs and efforts for data collection compared to approaches where each desired population is individually labeled, one-by-one, which requires collecting multiple datasets. In addition, the high penetrance of these reporters should facilitate the reconstruction process itself by providing a strong indicator of continuity between profiles in cases where intervening EM sections are omitted or lost. It is likely that more efficient reconstruction algorithms can be developed based on peroxidase labeling. Another potentially valuable use of these peroxidase reporters is functional CLEM. Previous studies used fluorescent calcium indicators *in vivo* to

assess functional properties of neurons and then identified their synaptic connections ultrastructurally (Bock et al., 2011; Briggman et al., 2011; Lee et al., 2016). One could envision multicolor *in vivo* calcium imaging of different neuronal populations, while using orthogonal peroxidase labeling to identify these neuronal populations in EM, through the use of bicistronic vectors such as Matrix-dAPEX2-IRES-jGCaMP7s and ER-dAPEX2-IRES-jRGECO1a. In all, the 15 AAV constructs and six mouse reporter lines reported here for multiplexed EM labeling in the mammalian nervous system will enable advances in synaptic connectivity mapping with unequivocal genetic identification of synaptic partners.

Acknowledgements

We thank P. Kaeser, G. Fishell and members of the Ginty laboratory for discussions and comments on this manuscript, the Boston Children's Hospital Viral Core Facility for sharing AAV production reagents, E. Raviola, C. Bolger and the Harvard Medical School Electron Microscopy Facility for EM assistance, and the Boston Children's Hospital Mouse Gene Manipulation Core Facility for assistance in generating of mouse lines. We thank K. Deisseroth for providing the AAV expression vector and H. Zeng for providing the Ai65 targeting vector. This work was supported by NIH grants R35NS097344 (D.D.G.), RF1MH114047 (W.-C.A.L.), and U54HD090255 (Boston Children's Hospital Mouse Gene Manipulation Core Facility, Intellectual and Developmental Disabilities Research Center), and the Edward R. and Anne G. Lefler Center for Neurodegenerative Disorders (D.L.P. and D.D.G.). Q.Z. is a Stuart H.Q. & Victoria Quan Fellow at Harvard Medical School. D.D.G. is an investigator of the Howard Hughes Medical Institute.

Author Contributions

Q.Z., D.L.P. and D.D.G. conceived the study. Q.Z. and D.L.P. generated the AAV constructs and mouse lines. Q.Z. did the LM and EM experiments. W.-C.A.L. assisted with EM experiments and analysis. Q.Z. and D.L.P. quantified the EM volume. Q.Z., D.L.P. and D.D.G. wrote the paper, with input from W.-C.A.L.

Methods

All experiments using animals were conducted according to United States National Institutes of Health guidelines for animal research and were approved by the Institutional Animal Care and Use Committee at Harvard Medical School. All procedures were done at room temperature unless otherwise noted.
No statistical methods were used to pre-determine sample sizes but sample sizes are similar to those reported in previous publications (Atasoy et al., 2014). Sample assignment was not randomized. Data collection and analysis were not performed blind to the conditions of the experiments. All materials are available upon request.

Molecular cloning

DNA fragments were synthesized as IDT gBlocks Gene Fragments and/or oligonucleotides and amplified by PCR using Q5 Hot Start (New England Biolabs), and cloned into an AAV expression vector (Addgene plasmid # 20299) using In-Fusion HD (Takara Bio) or NEBuilder HiFi (New England Biolabs), replacing the FLEX-mCherry construct originally in the vector. Descriptions of all the constructs tested are listed in **Supplementary Table 2.1**. The constructs used for multiplexed EM labeling in the study are bolded in **Supplementary Table 2.1**. All constructs were verified using Sanger sequencing and maintained in NEB Stable *E. coli* (New England Biolabs). Plasmids generated in this study (**Table 2.1**) were deposited to Addgene.

Cell culture and transfection

HEK293T cells were maintained in DMEM (Thermo Fisher) supplemented with 10% FBS (Thermo Fisher), and split when confluency reached ~80% with trypsin/EDTA (Thermo Fisher). Transfections were carried out using polyethylenimine (PEI, linear, MW 25K, Polysciences) with PEI:DNA ratio of 4:1 at in PBS (pH 7.4) at ~50% confluency.

AAV production

AAV productions were carried out according to a previously described protocol (Deverman et al., 2016). Briefly, HEK293T cells were triply transfected with an AAV genome plasmid, a Rep/Cap plasmid of the desired serotype, and the pHelper plasmid using PEI. Cells were maintained for 5 days with media collection on day 3. Culture media were concentrated using polyethylene glycol (MW 8K, MilliporeSigma), and cells were digested using Salt Active Nuclease (ArcticZymes). The AAVs were further purified from the lysates using discontinuous iodixanol (MilliporeSigma) gradients, and finally diafiltrated using Amicon Ultra (100K NMWL, Millipore) with PBS with 0.001% Pluronic F-68 (Thermo Fisher). AAV titers were determined using qPCR as DNase-I-resistant viral genomes (vg). Typical final concentrations obtained for AAV1 were ~3×10^{13} vg/mL, and for AAV9 were ~3×10^{14} vg/mL.

Viral injections

For all injections Fast Green FCF dye (MilliporeSigma) was included to aid visualization.
For IP AAV9 injections, ~1×10^{12} vg was delivered through glass pipettes into P0-P1 animals after the animals were anesthetized with ice.

For all parenchymal AAV1 injections, viruses were diluted to final concentrations of 3×10^{12}-1×10^{13} vg/mL each before injection. 3-4 injections were made on different sites and 50-100 nL was injected at each site. For non-stereotactic cortical AAV1 injections, P1-P3 animals were anesthetized with ice, and viruses were injected into the cortex using glass pipettes directly through the skulls. For stereotactic cortical AAV1 injections, P21 animals were anesthetized with isoflurane, and viruses were injected into S1 forelimb area using glass pipettes through drilled holes in the skull. For spinal cord AAV1 injections, P12-P14 animals were anesthetized with isoflurane, and viruses were injected into the cervical spinal cord using glass pipettes directly through the meninges.

Immunohistochemistry and confocal imaging

Mice were transcardially perfused with Ames' medium (MilliporeSigma) containing heparin (MilliporeSigma) (oxygenated with 95% O_2, 5% CO_2, warmed to 37 °C) to remove blood, and then 4% paraformaldehyde (Electron Microscopy Sciences) in 0.1 M PB (pH 7.4, warmed to 37 °C). Tissues were dissected out and then post-fixed in the same fixative at 4°C overnight. After washing with PBS, tissues were cryoprotected using PBS containing 30% sucrose (MilliporeSigma) at 4°C overnight. Tissues were then embedded in OCT (Sakura Finetek) and frozen with dry ice. 25 µm sections were prepared using a Leica CM3050 S cryostat, and dried on slides for 30 min. Sections were rehydrated with PBS for 3x5 min, and then blocked with PBS containing 5% Normal Goat Serum (Vector Labs) and 0.1% Triton X-100 (MilliporeSigma) ("blocking solution") for 1 hour. Sections were then stained with primary antibodies diluted in blocking solution at 4°C overnight. Sections were washed with PBS containing 0.02% Tween-20 (MilliporeSigma) for 4x5 min, and then stained with secondary antibodies diluted in blocking solution at 4°C overnight. Sections were then washed with PBS containing 0.02% Tween 20 for 4x5 min, and mounted with Fluoromount-G (SouthernBiotech). Slides were imaged with a Zeiss LSM 700 laser scanning confocal microscope as Z-stacks. Maximum intensity projections were made, and image intensities were adjusted using Fiji/ImageJ.

Primary antibodies used were rabbit anti-DsRed polyclonal (1:500, Takara Bio, 632496) and mouse anti-NeuN, clone A60 (1:1000, Millipore, MAB377). Secondary antibodies used were goat anti-Rabbit IgG (H+L) highly cross-adsorbed, Alexa Fluor 546 (1:500, Thermo Fisher, A-11035) and goat anti-Mouse IgG1 cross-adsorbed, Alexa Fluor 488 (1:500, Thermo Fisher, A-21121). All antibodies were validated by manufacturers.

Mice

All mice used in the study are of mixed background.

Th$^{T2A\text{-}CreER}$ (JAX 025614) (Abraira et al., 2017) was used to label C-LTMRs. Tg(Rbp4-Cre)KL100 (MMRRC 037128) (Cui et al., 2013) was used to label layer 5 corticofugal neurons. *Slc32a1*$^{IRES\text{-}Cre}$ (JAX 028862) (Vong et al., 2011) was used to label all inhibitory neurons. *Pvalb*$^{T2A\text{-}FlpO}$ (JAX 022730) (Madisen et al., 2015) was used to label fast-spiking GABAergic cortical interneurons. *Avil*^{FlpO} (Choi et al., 2020) was used to label all somatosensory afferents. *Scn10a*^{Cre} (Nassar et al., 2004) was used to label all $Na_V1.8^+$ neurons.

Animals were sacrificed 2-3 weeks after AAV injections or tamoxifen administration, whichever came later (median P21, range P21-P35).

Tamoxifen administration

Tamoxifen (MilliporeSigma) was dissolved in ethanol (MilliporeSigma) to 10 mg/mL and then mixed with an equal volume of sunflower seed oil (MilliporeSigma). The mixture was vortexed, and ethanol was then removed under vacuum. The final solution was delivered to animals via IP injection.

Generation of mouse lines

DNA fragments were amplified by PCR using Q5 Hot Start and cloned into the targeting vector used to create the Ai65 mouse line (Madisen et al., 2015). In-Fusion HD or NEBuilder HiFi was used to replace the tdTomato coding sequences of the Ai65 tageting vector (Addgene plasmid # 61577) to generate *ROSA26*$^{DR\text{-}Matrix\text{-}dAPEX2}$, *ROSA26*$^{DR\text{-}ER\text{-}dAPEX2}$, *ROSA26*$^{DR\text{-}ER\text{-}HRP}$, and *ROSA26*$^{DR\text{-}SV\text{-}HRP}$ targeting vectors. Targeting vectors were linearized using KpnI-HF (New England Biolabs), and 129S4/SvJae ES cells (J1) were transfected for homologous recombination and selected using neomycin. ES cells harboring successful integrations were screened using long-range PCR for both 5'- and 3'-arms. Properly recombined and karyotypically normal ES cells were then injected into blastocysts to generate chimeras. Germline transmission of the targeted alleles was established to obtain F1 animals. For generation of mouse lines harboring the single-recombinase-dependent alleles, dual-recombinase-dependent

ROSA26$^{DR\text{-}Matrix\text{-}dAPEX2}$, *ROSA26*$^{DR\text{-}ER\text{-}dAPEX2}$, *ROSA26*$^{DR\text{-}ER\text{-}HRP}$, and *ROSA26*$^{DR\text{-}SV\text{-}HRP}$ mouse lines were crossed to the germline deleter lines EIIa-Cre (JAX 003724) (Lakso et al., 1996) and Actb-Flpe (JAX 005703) (Rodriguez et al., 2000) to excise the loxP-STOP-loxP and frt-STOP-frt cassettes, respectively. Mouse lines generated in this study (**Table 2.2**) were deposited to the Jackson Laboratory.

Determination of optimal staining conditions

Given the wide range of reaction conditions reported for peroxidase staining (Atasoy et al., 2014; Han et al., 2012; Joesch et al., 2016; Li et al., 2010; Martell et al., 2017), we systematically determined the optimal condition for peroxidase staining with dAPEX2 expressed in mice. We tested a range of hydrogen peroxide concentrations (0.0003% to 0.03%) as well as DAB concentrations (0.1 mg/mL to 1 mg/mL) (**Supplementary Fig. 2.3**). We found that 0.003% hydrogen peroxide gave the highest staining intensity regardless of the DAB concentration. Staining intensity observed under LM is positively correlated with DAB concentration, however we found that if the DAB concentration is too high staining artifacts could occur (**Supplementary Fig. 2.4**). Therefore, we determined 0.003% hydrogen peroxide and 0.3 mg/mL DAB to be the optimal concentrations for staining. We also found that including saponin during peroxidase staining (Atasoy et al., 2014) degraded ultrastructure (data not shown). Adding a sodium hydrosulfite reduction step as previously reported (Joesch et al., 2016) did not lead to any perceivable difference in EM (data not shown), and we speculate that this might be due to our use of a lower hydrogen peroxide concentration in comparison, which presumably did not oxidize the samples as much.

We noticed that when the peroxidase labeling density is extremely high, such as in the cortex after injection of large amounts of constitutive AAV1 vectors, staining penetration issues could occur. It appeared that this was due to local reactant depletion since a more sparsely labeled region in the same slice stained in the same well (e.g. the thalamus) did not have this issue. This issue was not apparent when labeling density was lower as was typical in most experiments. We recommend using thinner vibratome sections (e.g. 100 μm) when staining penetration is a concern.

We also determined the optimal EM sample preparation protocol that best preserves DAB staining while providing sufficient counterstaining for synapse analysis. The osmium-only protocol (see below for details) led to clear DAB staining but minimal contrast in membrane and synaptic density (data not shown), while the rOTO protocol yielded excellent contrast, spurious DAB staining artifacts could be seen with the Matrix-dAPEX2 construct (**Supplementary Fig. 2.5**). The rOTO protocol (see below for details) did not cause any issue with the ER-dAPEX2 construct and was successfully used in a double labeling experiment equivalent to that in **Fig. 2.3a** (**Supplementary Fig. 2.5c**), suggesting that rOTO is compatible with this technique when distinguishing the two mitochondrial constructs is not needed and heavy metal impregnation is desired. Therefore, we used a reduced osmium protocol (see below for details) which afforded a balance between the ability to distinguish DAB staining and section counterstaining contrast (**Supplementary Fig. 2.5**).

Electron microscopy

Mice were transcardially perfused with Ames' medium containing heparin (oxygenated with 95% O_2, 5% CO_2, warmed to 37 °C) to remove blood, and then with a buffer containing 0.15 M sodium cacodylate (Electron Microscopy Sciences) (pH 7.4) and 0.04% $CaCl_2$ (MilliporeSigma) (cacodylate buffer) with 2.5% glutaraldehyde (Electron Microscopy Sciences) and 2% paraformaldehyde (warmed to 37 °C). Tissues were dissected out and then post-fixed in the same fixative at 4°C overnight. Skin samples were first shaved and then the adipose layer beneath the dermis was removed. After washing tissues with cacodylate buffer, tissues were embedded in low-melting-point agarose (Thermo Fisher), and 100-200 µm sections were taken in cacodylate buffer using a Leica VT1000 S vibratome. Sections were washed 2x10 min with cacodylate buffer containing 50 mM glycine (MilliporeSigma), 1x10 min with cacodylate buffer, and then incubated in 1 mL of 3,3'-diaminobenzidine tetrahydrochloride hydrate (MilliporeSigma) (DAB; 0.3 mg/mL) in cacodylate buffer in the dark for 30 min. 10 µL of cacodylate buffer containing 0.3% H_2O_2 (MilliporeSigma) was then added to the DAB solution directly (final H_2O_2 concentration: 0.003%) to initiate the peroxidase reaction. The reaction was allowed to proceed in the dark for 1 hour, and sections were then washed with cacodylate buffer. Stained sections were then fixed with cacodylate buffer

containing 3% glutaraldehyde at 4°C overnight. Sections were washed with cacodylate buffer, followed by cacodylate buffer containing 50 mM glycine, and then cacodylate buffer. For reduced osmium staining (used for all figures unless otherwise noted), sections were osmicated in cacodylate buffer containing 1% osmium tetroxide (Electron Microscopy Sciences)/1.5% potassium ferrocyanide (MilliporeSigma) for 1 hour. Sections were then washed with ddH_2O, and stained in a solution containing 0.05 M sodium maleate (MilliporeSigma) (pH 5.15) and 1% uranyl acetate (Electron Microscopy Sciences) at 4°C overnight. After washing with ddH_2O, sections were dehydrated with an ethanol series followed by propylene oxide (Electron Microscopy Sciences). Sections were then infiltrated with 1:1 epoxy resin mix (LX-112, Ladd Research):propylene oxide at 4°C overnight. Finally, sections were embedded in epoxy resin mix and cured at 60°C for 48-72 hours.

For osmium-only staining, sections were processed as described above up to but not including the osmication step, and then osmicated with an aqueous solution containing 1% osmium tetroxide for 30 min, and washed with ddH_2O. Dehydration and embedding were done as described above.

For reduced-osmium-thiocarbohydrazide-osmium (rOTO) staining, sections were stained following a slightly modified previously reported protocol (Hua et al., 2015). Sections were processed as described above up to but not including the osmication step, and osmicated with cacodylate buffer containing 2% osmium tetroxide for 1 hour, and reduced in cacodylate buffer containing 2.5% potassium ferrocyanide for 1 hour, and then washed with ddH_2O. Then sections were incubated in a filtered aqueous solution containing 1% thiocarbohydrazide (Electron Microscopy Sciences) at 40°C for 15 min, and washed with ddH_2O. Sections were osmicated again with an aqueous solution containing 2% osmium tetroxide for 1 hour, and washed with ddH_2O. Then sections were incubated in a solution containing 0.05 M sodium maleate (pH 5.15) and 1% uranyl acetate overnight at 4°C. Sections were warmed to 50°C for 2 hours in the uranyl acetate solution and then washed with ddH_2O. Dehydration and embedding proceeded as described above.

For HEK293T cells, cells were fixed with cacodylate buffer containing 2.5% glutaraldehyde and 2% paraformaldehyde for 30 min, and washed with cacodylate buffer containing 50 mM glycine followed by cacodylate buffer. Peroxidase reactions were initiated with cacodylate buffer containing 0.003% H_2O_2 and 0.3 mg/mL DAB, and allowed to proceed for 15 min. Cells were then washed with cacodylate buffer and scraped off the plate. Scraped cells were then prepared for EM with the osmium-only staining protocol described above.

Samples were sectioned using a Leica EM UC7 ultramicrotome with Diatome diamond knives, and ultrathin sections (40 nm) were picked up on glow-discharged formvar/carbon films on slot grids (Ted Pella). For single sections, ultrathin sections were imaged using a JEOL 1200EX transmission electron microscope at 80 kV accelerating voltage and 10,000x nominal magnification with an AMT XR-611 CCD camera at a final pixel size of 1.84 nm. Micrographs were excluded from analysis if they were out-of-focus, had inappropriate background correction, or had debris or other artifacts obscuring the field of view. Images were adjusted with normalization using Fiji/ImageJ to enhance contrast.

For serial sections, 50 ultrathin sections were manually picked up and imaged using a JEOL 1200EX transmission electron microscope at 120 kV accelerating voltage and 2,500x nominal magnification with an XIMEA CB200MG-CM CMOS camera at a final pixel size of 4.26 nm. Sections 45-47 were lost during imaging. Images were adjusted with contrast limited adaptive histogram equalization using Fiji/ImageJ to reduce intensity variation across different imaging fields. Individual images were then elastically montaged and aligned using TrakEM2 (Cardona et al., 2012; Saalfeld et al., 2010; Saalfeld et al., 2012). Neuronal profiles, mitochondria and synapses were manually reconstructed using TrakEM2. For 3D visualization, arealists were interpolated using TrakEM2, and meshes were smoothed using ImageJ 3D Viewer to generate 3D models with smooth surfaces.

For quantification of discriminability of Matrix-dAPEX2 vs. IMS-dAPEX2, two annotators (Q.Z. and D.L.P.) independently categorized all the mitochondria in the volume as either matrix-labeled, IMS-labeled, or unlabeled based on the features of the staining derived from single labeling experiments. Then the level

of concordance was assessed by comparing the annotations, with the possible outcomes as matching matrix-labeled annotation, matching IMS-labeled annotation, matching unlabeled annotation, mismatching matrix-labeled vs. IMS-labeled annotation, mismatching matrix-labeled vs. unlabeled annotation, and mismatching IMS-labeled vs. unlabeled annotation. Objects on either surface of the volume were not quantified if they only spanned 3 or fewer sections. 12 objects were excluded from the analysis because at least one annotator could not ascertain whether they were mitochondria or not (for 10 of these 12 objects neither annotator could ascertain the identity of the object), because of the small size, obscuration by artifacts, or lack of internal ultrastructure.

Also see **Appendix 2** for a detailed staining protocol.

Bright-field light microscopy

Sections were processed as described above for electron microscopy up to but not including the osmication step. Then sections were dehydrated with a methanol (MilliporeSigma) series and cleared with 1:2 benzyl alcohol (MilliporeSigma)/benzyl benzoate (MilliporeSigma) (BABB). Cleared sections were mounted with BABB and imaged with an Olympus BX63 using 4x, 10x or 20x objectives. White balance was individually calibrated for each slide, and lighting and exposure times were controlled for all comparison groups.

Chapter 3. Large-scale Electron Microscopic Reconstruction of the Spinal Cord Dorsal Horn with Genetically Identified Neuronal Types

Part of this chapter is from the paper previously published as: Zhang, Q., Lee, W.-C. A., Paul, D. L. & Ginty, D. D. Multiplexed peroxidase-based electron microscopy labeling enables simultaneous visualization of multiple cell types. *Nature Neuroscience* 22, 828-839 (2019).

Richard Schalek performed all ATUM sectioning and wafer staining, contributed to wafer mapping, single-beam SEM imaging, and performed all MultiSEM imaging. Stuart Cattel and David Paul contributed to wafer making and mapping and single-beam SEM imaging. Yuelong Wu processed and aligned the MultiSEM images. Jeff Lichtman supervised the SEM experiments.

Ultrastructural characterization of genetically identified C-fiber subtypes

In order to define the dorsal horn projection patterns of molecularly defined subtypes of sensory neurons in large-scale EM reconstruction, we first investigated whether different the central terminals of subtypes have characteristic ultrastructural features. We applied Matrix-dAPEX2 labeling (Zhang et al., 2019) to a previously intractable problem: defining the ultrastructural properties of physiologically distinct populations of small-diameter, unmyelinated primary somatosensory neuronal axons, also known as C-fibers. These small-diameter neurons include nociceptors, thermoceptors, pruriceptors, and a subset of low-threshold mechanoreceptors (LTMRs) (Abraira and Ginty, 2013; Basbaum et al., 2009; Owens and Lumpkin, 2014; Smith and Lewin, 2009; Todd, 2010). Peripheral terminals of these subtypes are morphologically distinct (Abraira and Ginty, 2013; Owens and Lumpkin, 2014) but no structural difference in their central terminations have been described. Due to the fine caliber of C-fibers, adequate filling of these small-diameter neurons with HRP through recording pipettes to visualize their axonal projections to the spinal cord or periphery has proven to be a major challenge (Alvarez et al., 1993; Sugiura et al., 1986). To label select populations of C-fibers, Cre-dependent AAV9-DIO-Matrix-dAPEX2 was injected IP into $Th^{T2A\text{-}CreER}$ (Abraira et al., 2017), $Mrgprd^{Cre}$ (Rau et al., 2009), and $Mrgprb4^{Cre}$ (Vrontou et al., 2013) mouse lines,

which express CreER or Cre recombinase in three physiologically distinct nonpeptidergic C-fiber subtypes: C-LTMRs, Mrgprd$^+$ polymodal nociceptors, and Mrgprb4$^+$ afferents implicated in tactile sensation, respectively. This strategy allowed robust labeling of these different C-fiber populations, as indicated by LM (**Fig. 3.1a, c, e**) and EM (**Fig. 3.1b, d, f**) peroxidase labeling patterns. EM analysis of the spinal cord dorsal horn showed that each of the three classes of primary sensory neurons often forms synapses onto multiple postsynaptic dendrites (**Fig. 3.1b, d, f**, arrowheads), as the labeled axons (**Fig. 3.1b, d, f**, asterisks) were observed in complexes termed synaptic glomeruli (Ribeiro-da-Silva and Coimbra, 1982). Moreover, the terminals of each sensory neuron class receive abundant axoaxonic connections. Because the peroxidase reporter is confined to the mitochondrial matrix, we were able to observe ultrastructural features that distinguish the axon terminals of the three labeled sensory neuron populations, with synaptic vesicle morphology being the most apparent difference. While C-LTMRs mostly contain round, clear vesicles and lack clusters of vesicles, Mrgprd$^+$ polymodal nociceptors and Mrgprb4$^+$ afferents typically exhibit large, variably shaped dense-core vesicles and clusters of vesicles (**Fig. 3.1b, d, f**, green and yellow arrows). The ultrastructural features of C-LTMRs are consistent with those of type IIa glomeruli (Ribeiro-da-Silva and Coimbra, 1982), while the ultrastructural features of Mrgprd$^+$ polymodal nociceptors and Mrgprb4$^+$ afferents are consistent with those of type Ia glomeruli (Ribeiro-da-Silva and Coimbra, 1982). This is a somewhat surprising finding because C-fibers had been generally thought to form type I glomeruli (Ribeiro-da-Silva, 2004; Ribeiro-da-Silva and Coimbra, 1982; Ribeiro-da-Silva et al., 1985; Ribeiro-da-Silva et al., 1989) while type IIa glomeruli were believed to be formed by Aδ-fibers (Rethelyi et al., 1982), and suggests that the division between type I and type II glomeruli are along the functional division of nociceptors and LTMRs, rather than myelination patterns. These results are consistent with some previous EM studies using antibodies against VGLUT3 and HRP-conjugated IB4 (Gerke and Plenderleith, 2004; Larsson and Broman, 2019), but inconsistent with other EM studies using antibodies against TAFA4 and VGLUT3 (Kambrun et al., 2018; Salio et al., 2021), where C-LTMRs were reported to form type Ia glomeruli. Futher experiments using a *TAFA4^{CreER}* recombinase line with an EM reporter line may provide more clarity on this particular question.

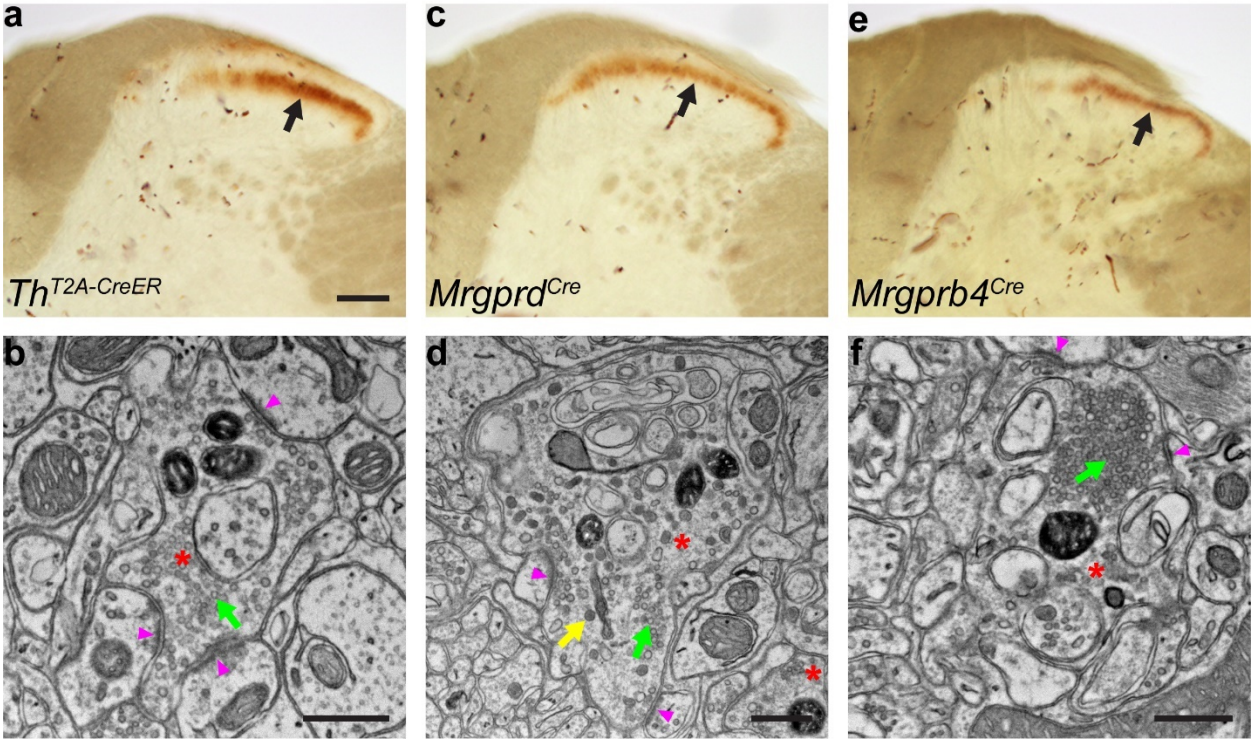

Figure 3.1. Different C-fiber subtypes have distinct ultrastructural features

(**a**) LM image of spinal cord dorsal horn from a *Th*$^{T2A\text{-}CreER}$ animal transduced with AAV9-DIO-Matrix-dAPEX2 and treated with tamoxifen from P14-21 to label C-LTMRs. Arrow: staining from labeled C-LTMR axons. n = 6 animals and experiments.

(**b**) EM image from the same animal in **a**. Asterisk: labeled C-LTMR axon terminal with round, clear vesicles (green arrow). Most C-LTMR axon terminals have only clear vesicles. Arrowheads: synapses made by the labeled C-LTMR terminal. n = 4 animals and experiments.

(**c**) LM image of spinal cord dorsal horn from an *Mrgprd*^{Cre} animal transduced with AAV9-DIO-Matrix-dAPEX2. Arrow: staining from labeled Mrgprd^{+} polymodal nociceptor afferents. n = 4 animals and experiments.

(**d**) EM image from the same animal in **c**. Asterisk: labeled Mrgprd^{+} polymodal nociceptor axon terminal. Unlike C-LTMRs, these neurons can exhibit both round, clear vesicles (green arrow) and large, variably shaped dense-core vesicles (yellow arrow). Arrowheads: synapses made by the labeled Mrgprd^{+} polymodal nociceptor axon terminal. n = 3 animals and experiments.

(**e**) LM image of spinal cord dorsal horn from an *Mrgprb4*^{Cre} animal transduced with AAV9-DIO-Matrix-dAPEX2. Arrow: staining from labeled Mrgprb4^{+} afferents. n = 4 animals and experiments.

(**f**) EM image from the same animal in **e**. Asterisk: labeled Mrgprb4$^+$ afferent axon terminal with a dense cluster of vesicles (green arrow), a configuration rarely seen in C-LTMRs, but often present in both Mrgprb4$^+$ and Mrgprd$^+$ afferents. Arrowheads: synapses made by the labeled Mrgprb4$^+$ afferent axon terminal. n = 3 animals and experiments.
Scale bars: **a, c, e**: 100 μm, **b, d, f**: 0.5 μm.

Dorsal horn sample preparation for large-scale EM reconstructions

Since much of the existing spinal cord morphological and electrophysiological data are from the lumbar spinal cord (Abraira et al., 2017; Grudt and Perl, 2002; Hughes et al., 2012; Koch et al., 2012; Wall et al., 1967; Woolf and King, 1990; Yasaka et al., 2010; Anda Chirila and Genelle Rankin, unpublished data), we chose the same region to acquire a large-scale EM reconstruction dataset. In order to have a reasonable chance of reconstructing volumes large enough to be of biological interest but small enough to be achievable with current technologies, we initially planned to prepare samples that include a quadrant of the spinal cord that correspond to one side of the dorsal horn, comprising ~ 0.6 mm (dorsal-ventral) x 1 mm (medial-lateral) in the lumbar enlargement. Given that the proximal collaterals of Aβ-LTMRs are ~ 1 mm long along the rostral-caudal axis and Aδ- and C-LTMR collaterals are smaller (Kuehn et al., 2019), the final sample dimensions were determined to be ~ 0.6 mm (dorsal-ventral) x 1 mm (medial-lateral) x 1 mm (rostral-caudal). These dimensions are incompatible with genetic EM labeling techniques due to the relatively low penetration depth of DAB staining (Zhang et al., 2019). Multi-beam scanning electron microscopy (MultiSEM) was chosen as the data acquisition technique because of its fast acquisition speed (Kasthuri et al., 2015).

Young adult WT animals (P56-70) were sacrificed and cut using a vibratome to 1 mm-thick transverse sections, which were further trimmed manually to include just one side of the dorsal horn. In order to acquire data as fast as possible because of the large size of the volume, sections must be imaged with short pixel dwell times, and therefore samples need to be heavily impregnated and stained with metals to achieve high signal-to-noise ratios. We chose the rOTO staining protocol devised by Hua et al. (2015) for

its ability to achieve uniform staining in large samples. Before committing to sectioning the samples using automated tape-collecting ultramicrotome (ATUM) (Kasthuri et al., 2015), we first screened the samples using X-ray microtomography (μCT) to observe staining penetration and sample quality. Unfortunately, all samples had regions with low staining intensity at the center (**Fig. 3.2a**), indicating poor staining penetration. However, we noticed that such regions were not in the geometric center of the samples, as one might expect, but were rather close to the dense white matter at the dorsal column (**Fig. 3.2a**). We hypothesized that myelin presents a diffusion barrier for chemicals and/or consumes substantial amounts of heavy metals to cause a drop in the local concentration, and therefore we manually trimmed off both the dorsal column and the lateral tracts before osmication. This modification greatly improved staining penetration and by μCT uniform staining was observed (**Fig. 3.2b**). Nonetheless, upon ultramicrotome sectioning, we noticed many poorly cut sections toward the center, and an examination of sections using single-beam SEM revealed artifacts characteristic of poor epoxy resin infiltration, such as smearing, which are also progressive as one moves farther away from the surface of the sample (data not shown). Estimation of the infiltration depth using these ultrathin sections yielded ~ 100 μm, i.e. only sections with at least one dimension smaller than 200 μm can be fully infiltrated. It is likely that the heavy myelination in the spinal cord in conjunction with the heavy metal impregnation by rOTO reduced the infiltration depth.

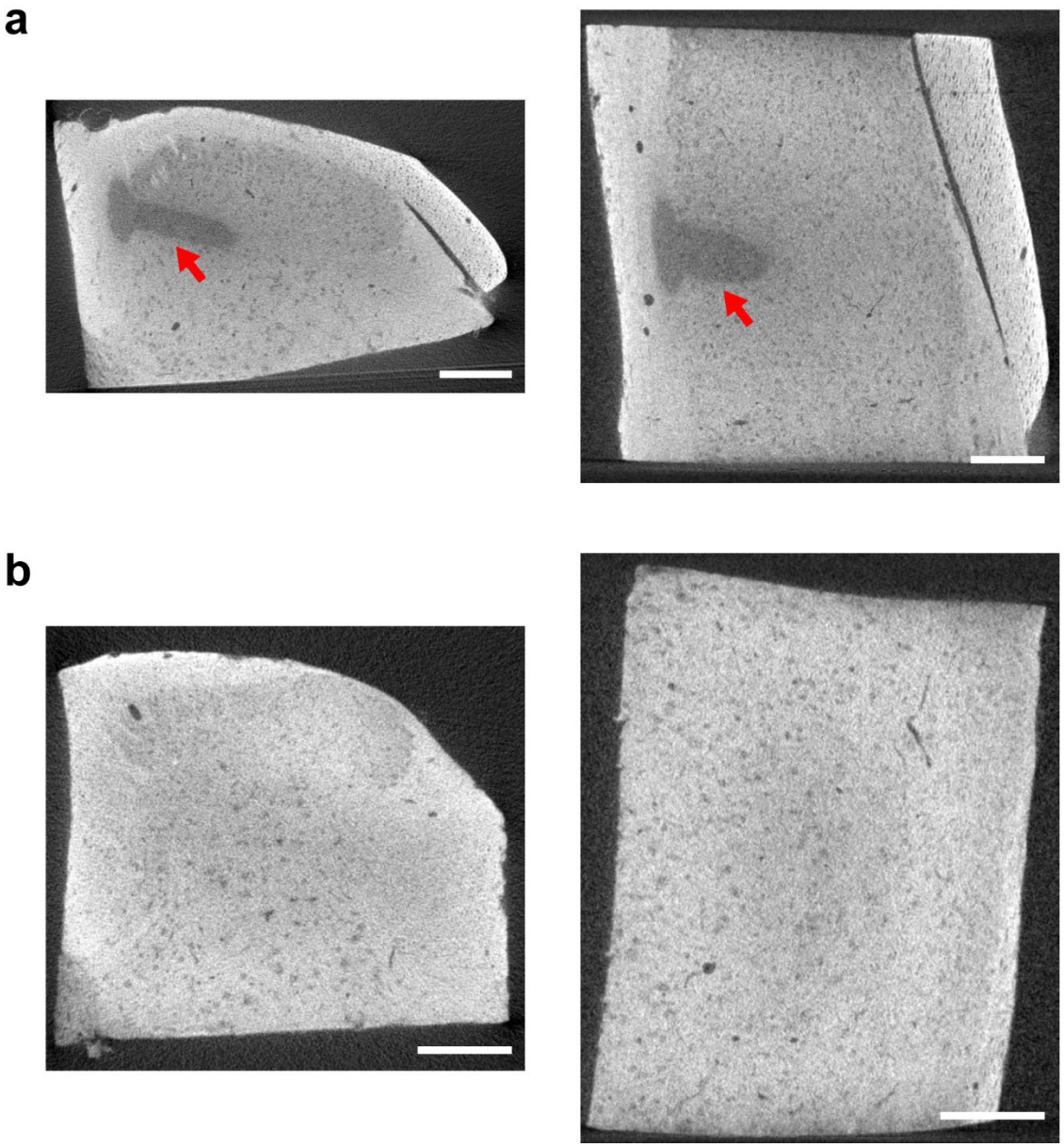

Figure 3.2. Staining optimization for large spinal cord dorsal horn samples

(**a**) Orthogonal µCT sections showing an example of poor heavy metal staining penetration. There was a zone with dramatically lower staining intensity inside the sample with a sharp boundary (arrows). This zone was noticeably closer to the dorsal column compared to the geometric center of the sample, indicating that heavily myelinated white matter acts as a barrier for staining penetration. n = 3 animals and experiments.

(**b**) Orthogonal µCT sections showing mostly uniform staining after dorsal column and lateral tracts were manually trimmed before the EM sample preparation. n = 3 animals and experiments.

Scale bars: 0.2 mm.

Given that we were already using an extended resin infiltration protocol and only ~ 20% of the volumes were well infiltrated, we felt that it is unlikely that we could do better without radically changing the experimental parameters. Therefore, we instead revisited our sample dimensions and noted that most single primary afferents are only ~ 50 µm wide on the medial-lateral axis and arranged in a somatotopic manner (Bai et al., 2015; Kuehn et al., 2019; Li et al., 2011). Making parasagittal sections allowed us to capture a few of these somatotopic primary afferent columns while maintaining a low thickness in the medial-lateral dimension. Therefore, we revised our plan and collected sections that were ~ 0.5 mm (dorsal-ventral) x 0.2 mm (medial-lateral) x 2 mm (rostral-caudal) in dimensions. This additionally allowed us to use genetic labeling, and we double labeled all primary afferents with *Avil*^{Cre}*; ROSA26*$^{LSL\text{-}Matrix\text{-}dAPEX2}$ and corticospinal inputs with AAV1-SV-HRP parenchymal injection into the S1 hindlimb region. We increased the DAB concentration to 0.5 mg/mL to increase the frequency of unique rOTO staining features for Matrix-dAPEX2 (Zhang et al., 2019), confirmed the appropriate staining patterns with LM (**Fig. 3.3a**), and prepared the samples with a modified Hua et al. (2015) rOTO protocol (Zhang et al., 2019). µCT showed uniform staining for all sections (**Fig. 3.3b**). The best sample was then cut on ATUM, tapes laid on wafers, and sections stained with lead citrate and uranyl acetate as previously described (Kasthuri et al., 2015). A total of 56 wafers were made, and wafer 7 to 52 contained large enough dorsal horn ROIs worth overview imaging with single-beam SEM. During overview imaging, we noticed that many wafers on the lateral side had sectioning issues, notably thin-thick cutting and wrinkles in the grey matter (**Fig. 3.4a**). These sectioning problems caused difficulties for image alignment (**Fig. 3.4b**) and rendered a portion of sections unusable. Sections closer to the medial side were unaffected (**Fig. 3.4c, d**). Therefore, it is likely that the different mechanical properties of the grey matter and the white matter caused the more flexible grey matter to be stretched and compressed during sectioning, resulting in wrinkles.

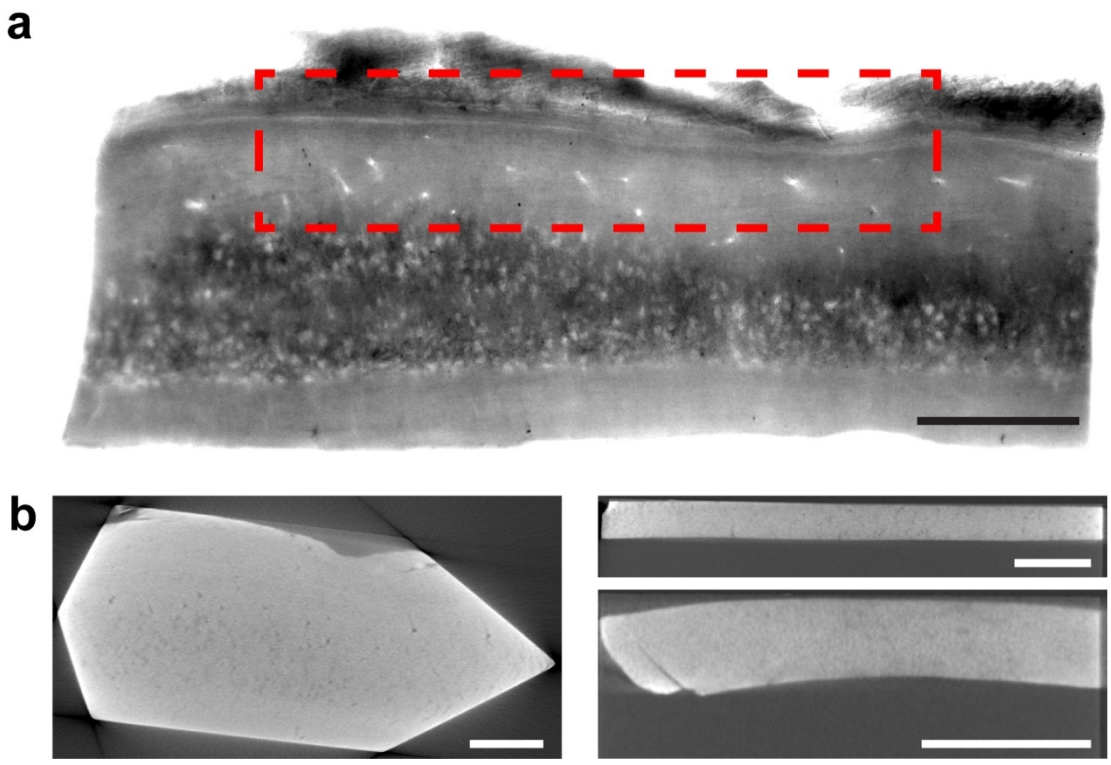

Figure 3.3. Preparation of parasagittal spinal cord sections

(**a**) LM image of a parasagittal section from a P56 *Avil*^{Cre}*; ROSA26*$^{LSL\text{-}Matrix\text{-}dAPEX2}$ animal with AAV1-SV-HRP parenchymal injection into the S1 hindlimb region. Strong DAB labeling could be seen in the grey matter and dorsal roots. Approximate imaging ROI is labeled with red dotted lines. n = 2 animals and experiments.

(**b**) Orthogonal µCT sections of the same sample in **a** showing uniform staining after the EM sample preparation. Slight mechanical deformations were introduced during the vibratome cutting. n = 2 animals and experiments.

Scale bars: 0.5 mm.

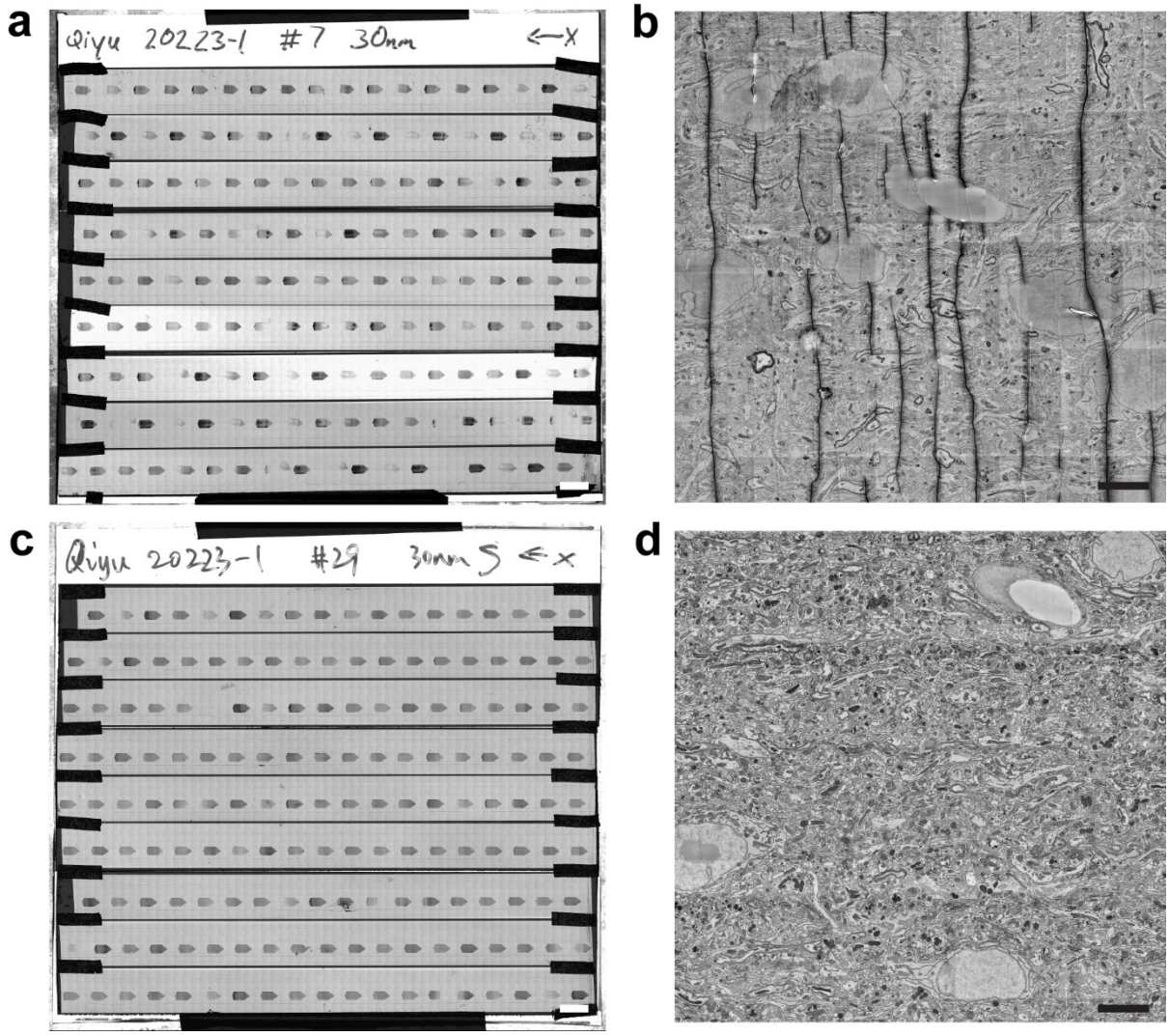

Figure 3.4. Wafer preparation and determination of ultrathin section quality

(**a**) LM image of the whole wafer 7. Prominent thin-thick cutting, indicated by different intensities of the sections along the tapes, was observed in this wafer.

(**b**) Example EM image of one section on wafer 7. While the ultrastructure of the tissue was well preserved, large wrinkles were observed in the grey matter (vertical black lines). These wrinkles interfered with proper alignment of images and therefore rendered these sections unusable.

(**c**) LM image of the whole wafer 7. Section thicknesses were more even in this wafer compared to wafer 7.

(**d**) Example EM image of one section on wafer 29. Almost no wrinkles were observed in this wafer, and images were well aligned in the volume.

Scale bars: **a, c**: 5 mm, **b, d**: 5 µm.

In order to establish that images from the MultiSEM imaging and alignment pipelines are suitable for reconstruction and synapse identification, a test volume from wafer 29 around lamina II_{iv} was imaged and aligned. A labeled primary afferent glomerulus, which is ultrastructurally identified as a type Type IIa glomerulus and therefore likely formed by an Aδ- or C-LTMR, along with a portion of its associated peripheral profiles were manually reconstructed (**Fig. 3.5a**). Synapses between these profiles were also manually identified and annotated (**Fig. 3.5b**). Complex local synaptic interactions were frequently observed in this glomerulus, with profiles participating in numerous dyadic and triadic interactions (**Fig. 3.5c**). Notably, the central axon forms a large number of synapses, sometimes with the same postsynaptic cells, consistent with previous reports (Ribeiro-da-Silva and Coimbra, 1982; Ribeiro-da-Silva et al., 1985). This anatomical arrangement may allow sophisticated local computations and precise control of primary sensory afferent outputs. Additionally, we also found examples where the same inhibitory interneuron form both axoaxonic and axodendritic synapses (**Fig. 3.5d**), suggesting that many inhibitory interneurons likely participate in both forms of inhibition. In all, this pilot experiment showed that the data quality is indeed adequate for 3-D reconstruction and synapse identification.

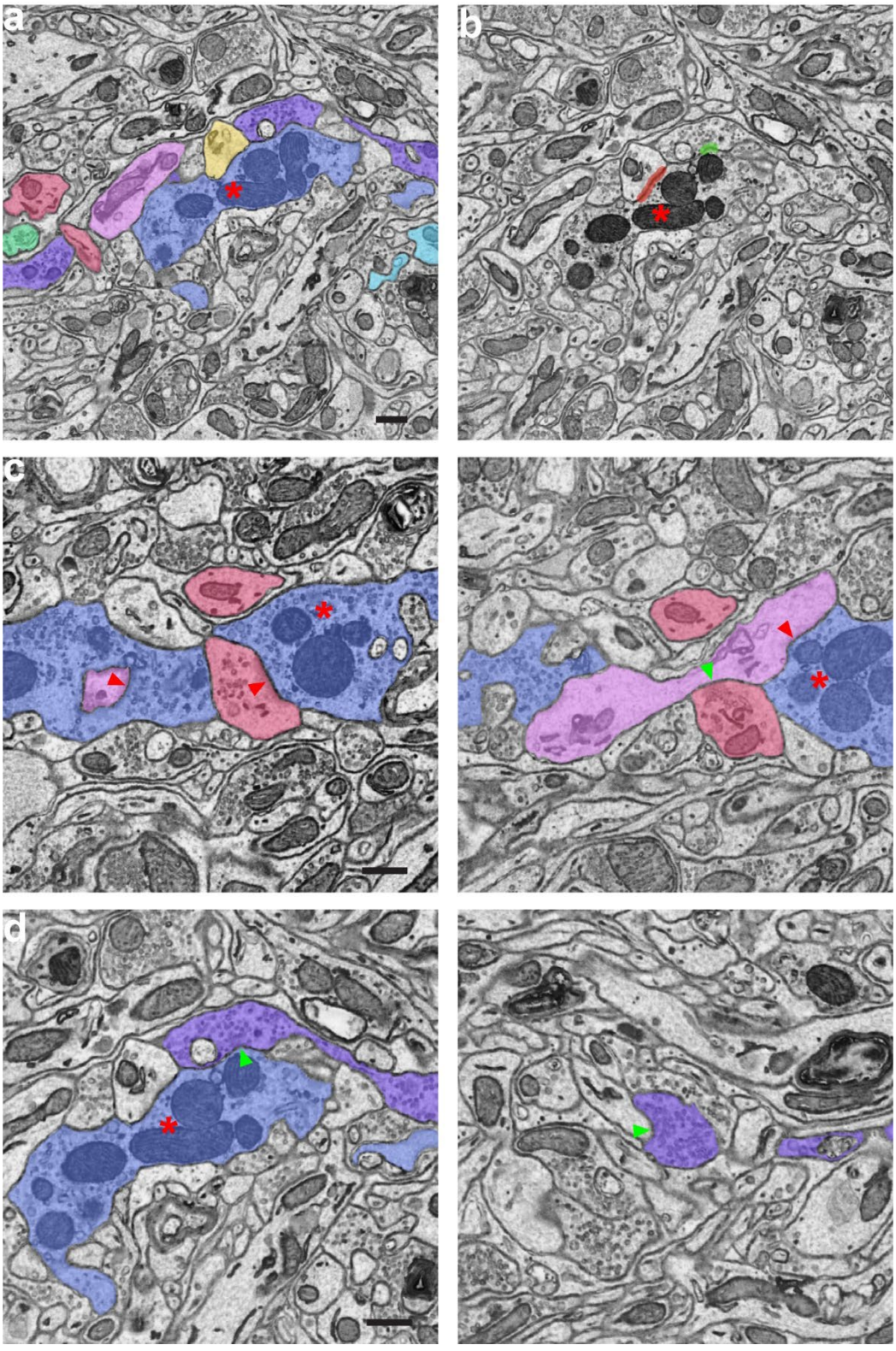

Figure 3.5. Partial reconstruction of a synaptic glomerulus

(**a**) EM image showing the partially reconstructed type Type IIa glomerulus. Asterisk: labeled primary afferent central axon.

(**b**) EM image showing the annotated synapses. Red annotations indicate excitatory synapses and green annotations indicate inhibitory synapses. Asterisk: labeled primary afferent central axon.

(**c**) EM images showing complex local synaptic interactions. (Left) Primary afferent (blue, asterisk) forms axodendritic excitatory synapses (red arrowheads) onto a vesicle-containing dendrite (red) and a plain dendrite (purple). (Right) ~ 100 nm away along the z-axis. Primary afferent (blue, asterisk) forms another axodendritic excitatory synapse (red arrowhead) onto the plain dendrite (purple), and the vesicle-containing dendrite (red) forms a dendrodendritic inhibitory synapse (green arrowhead) onto the same plain dendrite (purple).

(**d**) EM images showing that the same inhibitory interneuron form both (Left) axoaxonic synapses (green arrowhead) and (Right) axodendritic synapses (green arrowhead). Asterisk: labeled primary afferent central axon.

Scale bars: 0.5 µm.

Discussion

While large-scale reconstruction of the dorsal horn is still in its early phases, here we tackled and overcame several technical challenges. Given the complexity of the spinal cord circuitry, we believe that the approach of combining large-scale EM reconstructions with genetically identified neurons will facilitate the analysis and interpretation of the expected vast dataset. Moreover, insights gleaned from the large-scale reconstruction could then be validated functionally using genetically encoded activation and silencing tools, such as channelrhodopsin and tetanus toxin, since the neuronal identities will be known. It is anticipated that this EM dataset will provide the foundation for deciphering the first steps of somatosensory processing in the spinal cord dorsal horn.

Methods

All experiments using animals were conducted according to United States National Institutes of Health guidelines for animal research and were approved by the Institutional Animal Care and Use Committee at Harvard Medical School. All procedures were done at room temperature unless otherwise noted.

Cell culture and transfection, AAV production, Viral injections, Tamoxifen administration

See **Chapter 2 Methods**.

Mice

All mice used in the study are of mixed background.

Th$^{T2A\text{-}CreER}$ (JAX 025614) (Abraira et al., 2017) was used to label C-LTMRs. *Mrgprd*^{Cre} (Rau et al., 2009) was used to label Mrgprd^{+} afferents. *Mrgprb4*^{Cre} (JAX 021077) (Vrontou et al., 2013) was used to label Mrgprb4^{+} afferents. *Slc32a1*$^{IRES\text{-}Cre}$ (JAX 028862) (Vong et al., 2011) was used to label all inhibitory neurons. *Avil*^{Cre} (JAX 032536) (Zhou et al., 2010) and *Avil*^{FlpO} (Choi et al., 2020) were used to label all somatosensory afferents. *Scn10a*^{Cre} (Nassar et al., 2004) was used to label all Na$_V$1.8^{+} neurons.

Animals were sacrificed 2-3 weeks after AAV injections or tamoxifen administration for the C-fiber ultrastructural characterization, whichever came later (median P21, range P21-P35). Animals were sacrificed at P70 or P56 for large-scale reconstruction experiments.

Electron microscopy sample preparation

See **Chapter 2 Methods**. Also see **Appendix 2** for a detailed staining protocol.

X-ray μCT volumes were acquired using a Zeiss Xradia 510 Versa at 60 kV using the 4x objective without any source filter. Number of projections was adjusted so that the imaging time was ~ 1 hour. Reconstruction was done using the built-in automatic reconstruction function.

For samples used for large-scale reconstructions, blocks were cut on ATUM (Kasthuri et al., 2015) at a nominal 30 nm thickness. Wafer making and mapping were done according to Kasthuri et al. (2015). Sections were stained with 4% aqueous uranyl acetate and 3% aqueous lead citrate, 4 minutes each.

MultiSEM imaging and alignment

MultiSEM imaging was done according to Eberle et al. (2015) **Fig. 3**. Pixel dwell time was set to 800 ns.

Images were contrast enhanced using contrast limited adaptive histogram equalization (CLAHE). Alignment was done using the mb_aligner library (https://github.com/adisuissa/mb_aligner), which is based on the method described in Saalfeld et al. (2012).

Manual segmentation

Manual segmentation was done using VAST Lite (Berger et al., 2018) with a Wacom One Pen Display (Wacom). The central primary afferent axon was identified using mitochondrial staining. Synapses were identified using presynaptic vesicles and/or postsynaptic densities. Neuroglancer precomputed volumes and 3-D meshes were generated using Igneous (https://github.com/seung-lab/igneous) and visualized using Neuroglancer (https://github.com/google/neuroglancer).

Chapter 4. Ultrastructural Characterization of Molecularly Distinct Meissner Corpuscle Afferents

This chapter has been previously published as: Neubarth, N. L., Emanuel, A. J., Liu, Y., Springel, M. W., Handler, A., Zhang, Q., Lehnert, B. P., Guo, C., Orefice, L. L., Abdelaziz, A., DeLisle, M. M., Iskols, M., Rhyins, J., Kim, S. J., Cattel, S. J., Regehr, W. G., Harvey, C. D., Drugowitsch, J. & Ginty, D. D. Meissner corpuscles and their spatially intermingled afferents underlie gentle touch perception. *Science* 368, eabb2751 (2020). My contributions to this paper are designing and conducting electron microscopy experiments, and analyzing and interpreting results from these experiments.

Abstract

Meissner corpuscles are mechanosensory end organs that densely occupy mammalian glabrous skin. We generated mice selectively lacking Meissner corpuscles and found them to be deficient in both perceiving the gentlest detectable forces acting on glabrous skin and fine sensorimotor control. We found that Meissner corpuscles are innervated by two mechanoreceptor subtypes that exhibit distinct responses to tactile stimuli. The anatomical receptive fields of these two mechanoreceptor subtypes homotypically tile glabrous skin in a manner that is offset with respect to one another. Electron microscopic analysis of the two Meissner afferents within the corpuscle supports a model in which the extent of lamellar cell wrappings of mechanoreceptor endings determines their force sensitivity thresholds and kinetic properties.

Main Text

The basic anatomy of the Meissner corpuscle and its presumed innervating Aβ Rapidly Adapting Type I (RA1) low-threshold mechanoreceptor (LTMR) have been widely described since its discovery in 1852 (Wagner and Meissner, 1852). However, the Meissner corpuscle's requirement for touch-related behaviors, sensorimotor capabilities, and tactile perception have remained a matter of speculation.

Mice lacking either brain-derived neurotrophic factor (BDNF) or its receptor TrkB die neonatally and notably also have a complete absence of Meissner corpuscles (Gonzalez-Martinez et al., 2005; Gonzalez-Martinez et al., 2004; Perez-Pinera et al., 2008). We thus generated conditional mutant mouse models that are viable in adulthood and selectively lack Meissner corpuscles for addressing their role in tactile perception and sensorimotor behaviors in adult animals. We found that BDNF is expressed in glabrous skin during the period of Meissner corpuscle formation (**Supplementary Fig. 4.1a-c**). Eliminating BDNF expression in epithelial cells of the skin using *K5Cre; BDNF$^{flox/flox}$* mice resulted in a dramatic reduction in the number of Meissner corpuscles (**Supplementary Fig. 4.1f, g, h**). We found no disturbance of Meissner corpuscles in mice lacking BDNF in neurons of the dorsal root ganglia (DRG) or Schwann cells (*Wnt1^{Cre}; BDNF$^{flox/flox}$*; **Supplementary Fig. 4.1d, e, h**), suggesting that skin-derived—and not neuron- or Schwann cell-derived—BDNF is crucial for Meissner corpuscle development. BDNF's cognate receptor, TrkB, is present in a subset of primary sensory neurons of the DRG, and mice that selectively lack TrkB in primary sensory neurons (*Advillin^{Cre}; TrkB$^{flox/flox}$*, hereafter called *TrkB^{cKO}*) (da Silva et al., 2011; Liu et al., 2012), while viable and overtly normal, are also devoid of Meissner corpuscles and their innervating sensory neurons (**Fig. 4.1a, b**, **Supplementary Fig. 4.2**). Mice that lack TrkB in Schwann cells, on the other hand, have a normal complement of Meissner corpuscles (**Supplementary Fig. 4.2h, j**). Although some neurofilament-positive (NFH$^+$) sensory fibers were present in glabrous skin dermal papillae of *TrkB^{cKO}* mice prior to P20, these fibers were absent in adults (**Fig. 4.1a**, **Supplementary Fig. 4.2**). In contrast, Merkel cells and the cutaneous endings of their associated Aβ Slowly Adapting (SA) LTMRs, which are TrkB-negative, were found in comparable numbers in control and *TrkB^{cKO}* adult mice (**Fig. 4.1a, b**). We next did *in vivo* loose-patch electrophysiological recordings (Bai et al., 2015; Ma et al., 2010) of random L4 DRG neurons from adult control and *TrkB^{cKO}* mice. While indentation of hindpaw glabrous skin with gentle force steps evoked both Aβ RA-LTMR and Aβ SA-LTMR physiological responses in control mice, Aβ RA-LTMR responses were absent in *TrkB^{cKO}* mice even at indentation forces as high as 75mN (**Fig. 4.1d-f**). Activation thresholds and firing patterns of Aβ SA-LTMRs in control and *TrkB^{cKO}* mice were indistinguishable (**Fig. 4.1g**). Thus, BDNF and TrkB expressed in glabrous skin epithelial cells and sensory neurons of the DRG, respectively, are essential for development of Meissner corpuscles and the presence of Aβ RA-LTMR responses to indentation of

glabrous skin. In contrast, sensory-neuron TrkB signaling is dispensable for the development and normal response properties of Merkel cells and their associated Aβ SA-LTMRs and, as found previously, the development of Pacinian corpuscles (Gonzalez-Martinez et al., 2005; Gonzalez-Martinez et al., 2004; Luo et al., 2009; Perez-Pinera et al., 2008).

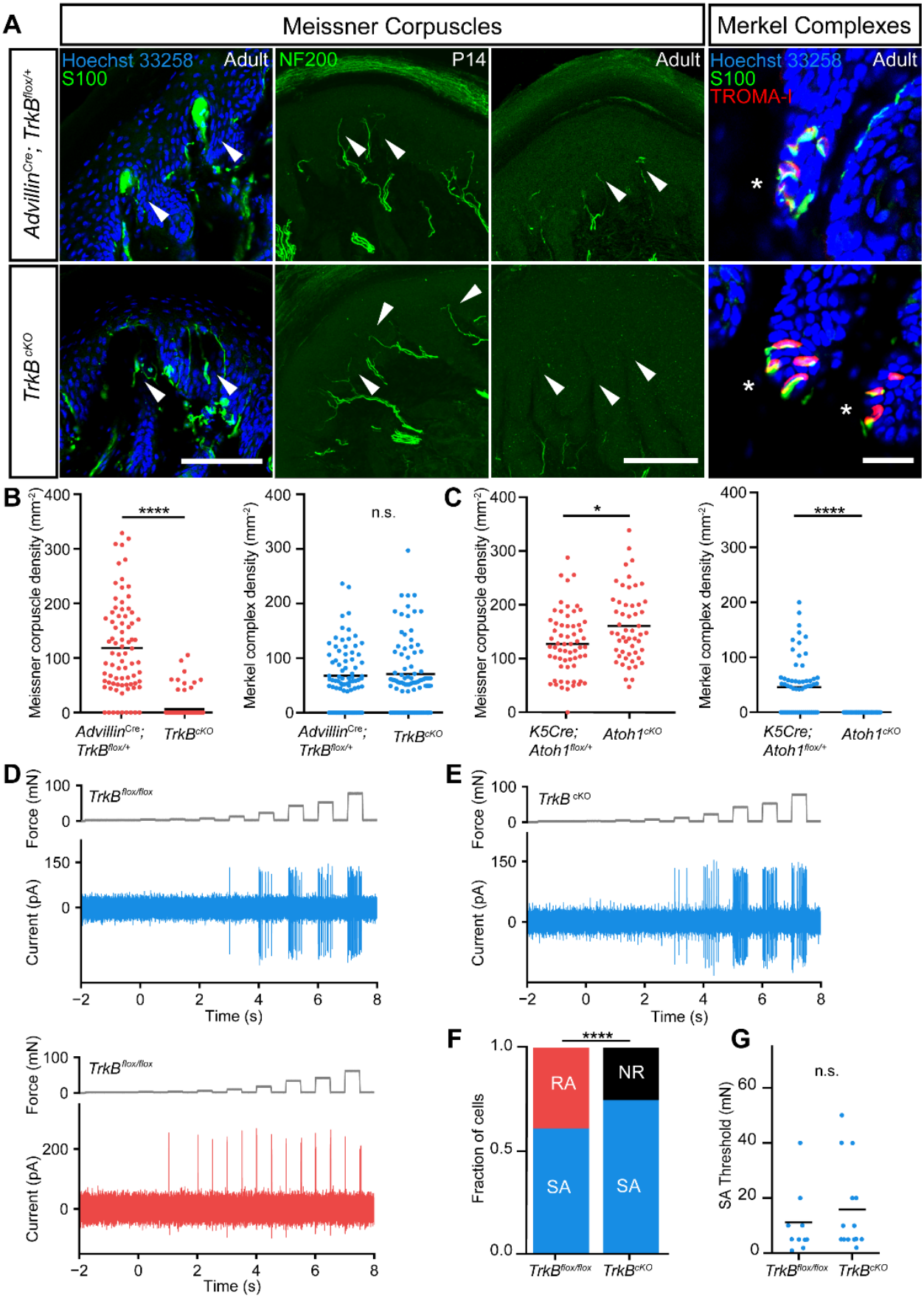
A
Meissner Corpuscles
Merkel Complexes
Advillin Cre; TrkB flox/+
TrkB cKO
Hoechst 33258
S100
Adult
NF200
P14
TROMA-I
B
Meissner corpuscle density (mm-2)
Merkel complex density (mm-2)
****
n.s.
Advillin Cre; TrkB flox/+
TrkB cKO
C
*
K5Cre; Atoh1 flox/+
Atoh1 cKO
D
E
Force (mN)
Current (pA)
Time (s)
TrkB flox/flox
F
Fraction of cells
RA
SA
NR
G
SA Threshold (mN)

Figure 4.1. Meissner corpuscles and their innervating Aβ-LTMRs are absent in *TrkB^{cKO}* mice

(**a**) Digital pad sections from control (upper panels) and *TrkB^{cKO}* mice (lower panels). Arrows and asterisks indicate typical locations of Meissner corpuscles and Merkel complexes, respectively. Meissner corpuscles and their afferents are labeled with S100 or NFH immunostaining in separate sections, respectively (scale bar = 100 μm). Merkel cells and associated nerve terminals are labeled with TROMA-I and S100, respectively (scale bar = 25 μm).

(**b**) Meissner corpuscle and Merkel complex density in glabrous pads of control and *TrkB^{cKO}* mice. Dots represent individual sections, and black bars represent mean. (79 sections from 3 control mice and 81 sections from 3 *TrkB^{cKO}* mice; two-tailed Mann-Whitney test, **** $p < 0.0001$ ($U = 580$), n.s. = not significant ($U = 3163$, $p = 0.9016$)).

(**c**) Meissner corpuscle and Merkel complex density in pads of *K5Cre; Atoh1$^{flox/+}$* and *Atoh1^{cKO}* (*K5Cre; Atoh1$^{flox/flox}$*) mice. Dots represent densities from individual sections and black bars represent means. (62 sections from 2 *K5Cre; Atoh1$^{flox/+}$* animals and 53 sections from 2 *Atoh1^{cKO}* animals; two-tailed Mann-Whitney test, * $p = 0.0113$ ($U = 1193$), **** $p < 0.0001$ ($U = 689$)).

(**d**) *In vivo* recordings of a slowly adapting (SA, top, blue) and a rapidly adapting (RA, bottom, red) Aβ-LTMR from control mice in response to step indentations applied to glabrous hindpaw pedal pads (force records shown in gray).

(**e**) Example recording of an Aβ SA-LTMR from a *TrkB^{cKO}* mouse in response to the same stimulus as in **d**.

(**f**) Proportion of neurons that are SA, RA, and not responsive (NR) to indentation in control (left, n = 18 cells) and *TrkB^{cKO}* mice (right, n = 20 cells). χ^2 test: $\chi^2 = 8.5$, $p = 0.004$.

(**g**) Mean (black bars) and individual (circles) thresholds of Aβ SA-LTMRs in control (left, n = 11 cells) and *TrkB^{cKO}* mice (right, n = 15 cells). Unpaired t-test: $t = -0.81$, $p = 0.42$.

We subjected adult control and *TrkB^{cKO}* mice to behavioral tests of glabrous skin sensitivity, light touch perception, gait analysis, and fine sensorimotor control. First, we measured glabrous hindpaw withdrawal thresholds in *TrkB^{cKO}* and littermate control mice using forces ranging from 0.008 g to 4.0 g applied to the pedal pads of the hindpaw (**Fig. 4.2a**). Wild-type mice withdrew their paws in response to the entire range

of forces presented, rarely reacting to the lowest forces and nearly always reacting to the highest forces. On the contrary, while *TrkB*^{cKO} mice displayed normal hindpaw withdrawal at the high end of this force range, they were unresponsive to the lightest forces (**Fig. 4.2a**). We infer from these behavioral measurements that activation of Merkel cell complexes and Aβ SA-LTMRs does not underlie sensorimotor responses to the lightest detectable forces acting on glabrous skin. To further test whether this deficit was specific to disruption of Meissner corpuscles and not to disturbance of Merkel cell complexes, we measured withdrawal thresholds in mice lacking Merkel cells (*K5Cre*; *Atoh1*$^{flox/flox}$ or *Atoh1*^{cKO}) (Maricich et al., 2012; Maricich et al., 2009; Morrison et al., 2009; Perdigoto et al., 2014; Ramirez et al., 2004; Shroyer et al., 2007; Van Keymeulen et al., 2009). In mice lacking Merkel cells, Meissner corpuscles were present in slightly increased numbers (**Fig. 4.1c**). Behaviorally, mice lacking Merkel cells performed normally on the von Frey paw withdrawal test (**Fig. 4.2b**).

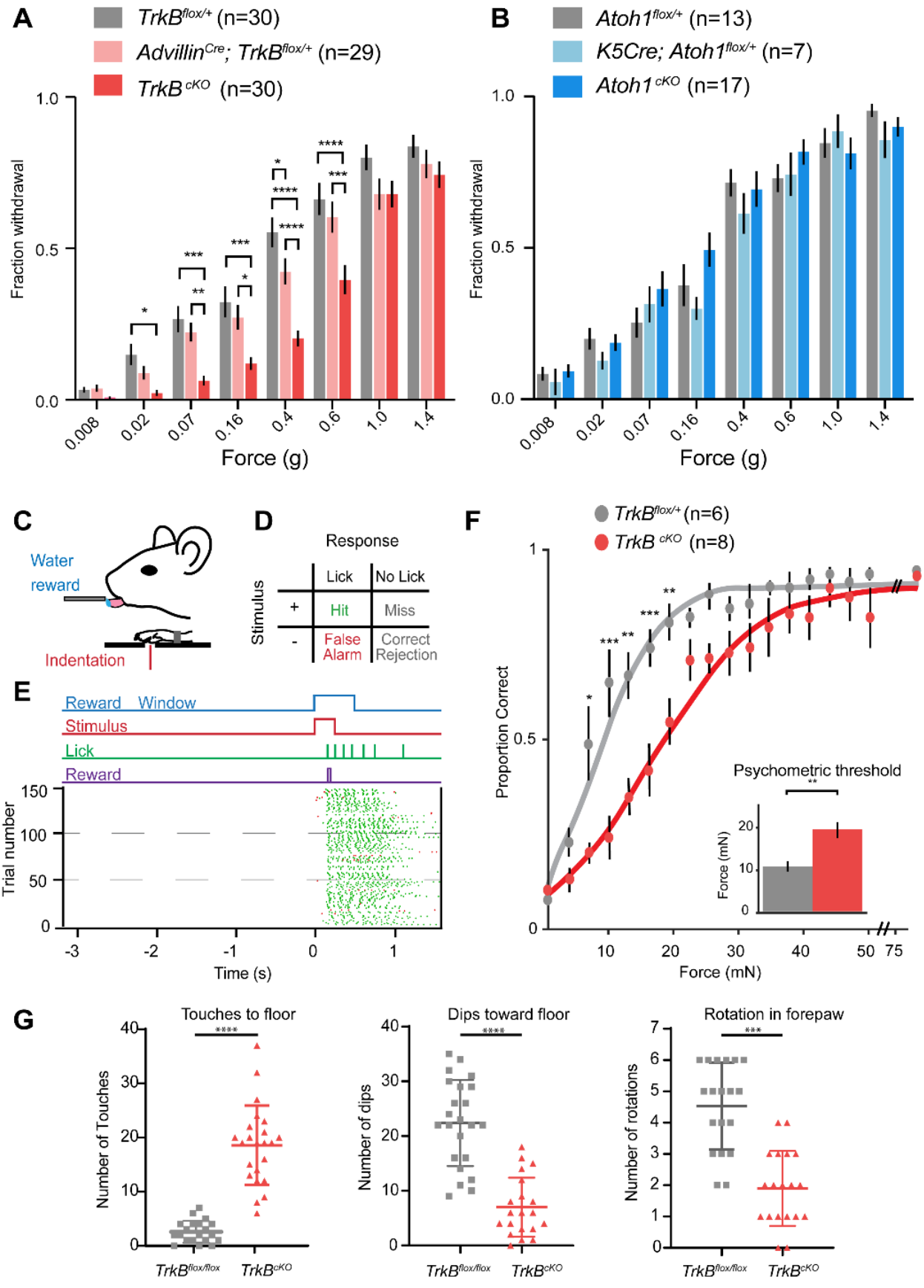
A
TrkB flox/+ (n=30)
Advillin Cre; TrkB flox/+ (n=29)
TrkB cKO (n=30)
Fraction withdrawal
Force (g)
B
Atoh1 flox/+ (n=13)
K5Cre; Atoh1 flox/+ (n=7)
Atoh1 cKO (n=17)
Fraction withdrawal
Force (g)
C
Water reward
Indentation
D
Response
Stimulus
Lick
No Lick
Hit
Miss
False Alarm
Correct Rejection
E
Reward Window
Stimulus
Lick
Reward
Trial number
Time (s)
F
TrkB flox/+ (n=6)
TrkB cKO (n=8)
Proportion Correct
Force (mN)
Psychometric threshold
Force (mN)
G
Touches to floor
Number of Touches
Dips toward floor
Number of dips
Rotation in forepaw
Number of rotations
TrkB flox/flox
TrkB cKO

Figure 4.2. Meissner corpuscles are necessary for light touch perception and fine sensorimotor control

(**a**) Fraction (mean ± s.e.m.) of paw withdrawals to von Frey filament applications for *TrkB*^{cKO} and control mice. RM two-way ANOVA, effect of genotype (F (2,86) = 9.823, p = 0.0001) with post-hoc Tukey's; p-values represent comparisons between genotypes for each filament: * p < .05, ** p < .01, *** p < .001, **** p < .0001.

(**b**) Same as A for *Atoh1*^{cKO} and control mice. RM two-way ANOVA, no effect of genotype: F (2,34) = 0.8258, p = 0.4465

(**c**) Operant conditioning task design.

(**d**) Matrix of possible behavioral outcomes from one trial.

(**e**) Operant conditioning task. (Top) Stimulus paradigm, where animals must withhold for at least 3 seconds before initiation of a new trial. On trials with a stimulus (shown), animal receive rewards only on hit trials. (Bottom) Raster plot of licks. Hit trials shown with green ticks, False alarm trials shown with red ticks.

(**f**) Psychometric functions for the operant conditioning task for *TrkB*^{cKO} and control mice. Error bars represent s.e.m. (Inset shows thresholds; unpaired t-test: t = 2.69, p = 0.002). Two-way ANOVA, effect of genotype (F (1,12) = 8.261, p = 0.0140) with post-hoc Sidak's multiple comparison; p-values represent comparisons between genotypes for each force range: * p < 0.05, ** p < 0.01, *** p < 0.001, **** p < 0.0001.

(**g**) Left, the number of sunflower seed touch-taps when the seed is braced against the floor between forepaws during seed peeling. Middle, the number of times the mouse held the seed in an elevated position and used its incisors to bite into the seed while applying downward force (dips) to expose seed kernel. Right, the number of seed rotations as mice adjusted their grasp. Unpaired student's test, *** p < 0.001 **** p < 0.0001.

Next, we trained water-deprived mice within an operant conditioning behavioral paradigm to report detection of glabrous skin indentation stimuli by lick retrieval of a water reward (**Fig. 4.2c-e**). Mice learned to lick specifically in response to mechanical stimuli within two weeks, at which time we delivered step

indentations ranging between 0 and 75 mN to the forepaw and measured perceptual detection thresholds (force at the midpoint of the psychometric function; **Fig. 4.2f**). While control mice exhibited perceptual detection thresholds of approximately 10 mN, mice lacking Meissner corpuscles had increased perceptual thresholds of approximately 20 mN. In contrast, reactivity to a light air puff applied to back hairy skin was comparable in control and *TrkB*^{cKO} mice (**Supplementary Fig. 4.3**), indicating normal hairy skin sensitivity.

We next tested the requirement of Meissner corpuscles in an innate, fine sensorimotor behavior: forepaw manipulation of sunflower seeds while eating. The amount of time required to deshell and eat the sunflower seed kernel was comparable for control and *TrkB*^{cKO} mice. However, while control mice used their forepaws to hold, elevate, and rotate the sunflower seed, *TrkB*^{cKO} mice typically trapped or braced the seed on the floor while biting and removing the shell to expose the kernel (**Fig. 4.2**; **Supplementary Video 4.1 and 4.2**). *TrkB*^{cKO} mice exhibited fewer forepaw dips to the floor and seed rotations and instead more frequently touched the floor to brace the seed. (**Fig. 4.2g**). In contrast, gait was largely unaltered in *TrkB*^{cKO} mice, although subtle differences in gait were apparent at high velocities (**Supplementary Fig. 4.4**). We observed no other obvious sensorimotor deficits in *TrkB*^{cKO} mice (**Supplementary Fig. 4.3 and 4.4**).

Large-diameter, myelinated sensory neurons innervating Meissner corpuscles express the tyrosine kinase Ret beginning on embryonic day 10.5 (E10.5) (Luo et al., 2009). Consistent with this, *Ret*^{CreER}; *Rosa26*$^{LSL\text{-}tdTomato}$ mice (Luo et al., 2009; Madisen et al., 2010) treated with tamoxifen from E10.5 to E13.5 had tdTomato^{+} sensory fibers that innervate Meissner corpuscles (**Fig. 4.3a**). Because TrkB^{+} sensory neurons are required for Meissner corpuscle formation, we asked whether these Ret^{+} Meissner afferent fibers also express TrkB. TrkB^{+} axon terminals were present in the dermal papillae of glabrous skin during embryonic and early postnatal ages, but TrkB expression was undetectable in Meissner afferent terminals in adult mice (**Supplementary Fig. 4.5**). Therefore, to permanently label TrkB^{+} neurons and visualize their cutaneous endings in glabrous skin of adults, we treated *TrkB*^{CreER}; *Rosa26*$^{LSL\text{-}tdTomato}$ mice (Rutlin et al., 2014) with tamoxifen between E15.5 and P6. We observed that adult *TrkB*^{CreER}; *Rosa26*$^{LSL\text{-}tdTomato}$

mice possess tdTomato$^+$ sensory fibers within Meissner corpuscles (**Fig. 4.3b**). These TrkB$^+$ Meissner corpuscle afferents are distinct from Ret$^+$ Meissner corpuscle afferents. Indeed, using *TrkB^{CreER}*; *Rosa26$^{LSL\text{-}tdTomato}$*; *Ret^{CFP}* compound mice (Uesaka et al., 2008), the TrkB$^+$ and Ret$^+$ sensory neurons were found to be separate populations, with endings of both of these neuronal populations terminating within the majority of corpuscles in both forepaw and hindpaw glabrous skin (**Fig. 4.3c, e**). Dual innervation of corpuscles was also seen using the *Npy2r-GFP* BAC transgenic mouse line, which labels Aβ RA-LTMRs in both hairy and glabrous skin (Li et al., 2011). In *TrkB^{CreER}; Rosa26$^{LSL\text{-}tdTomato}$; Npy2r-GFP* compound mice, all GFP$^+$ fibers in the dermal papillae were tdTomato$^+$ (**Supplementary Fig. 4.5**). On the other hand, in *Ret^{CreER}; Rosa26$^{LSL\text{-}tdTomato}$; Npy2r-GFP* compound mice, tdTomato$^+$ and GFP$^+$ fibers in dermal papillae were distinct and intertwined (**Fig. 4.3d**). Both the Ret$^+$ and TrkB$^+$ Meissner afferents expressed neurofilament, and together these two neuronal populations accounted for most, if not all, NFH$^+$ Meissner corpuscle endings (**Fig. 4.3c**, **Supplementary Fig. 4.5**). Meissner corpuscle lamellar cells, which are specialized terminal Schwann cells, migrated into dermal papillae along Meissner afferent axons during development (**Supplementary Fig. 4.6**), and TrkB$^+$ axons and corpuscle lamellar cells were both absent from dermal papillae of *TrkB^{cKO}* mice. Although axons of Ret$^+$ neurons still projected into dermal papillae in the absence of TrkB$^+$ axons and corpuscle lamellar cells in neonatal *TrkB^{cKO}* mutants, these Ret$^+$ fibers either retracted or degenerated because neither Ret$^+$ nor TrkB$^+$ afferents were present in dermal papillae of adult *TrkB^{cKO}* mice (**Supplementary Fig. 4.2**). Thus, consistent with prior work suggesting multiple, immunohistochemically distinct Meissner corpuscle afferent endings (Abraira and Ginty, 2013), our findings reveal that Meissner corpuscles are co-innervated by a pair of intertwined, molecularly and developmentally distinct populations of sensory neurons, one expressing TrkB and another expressing Ret.

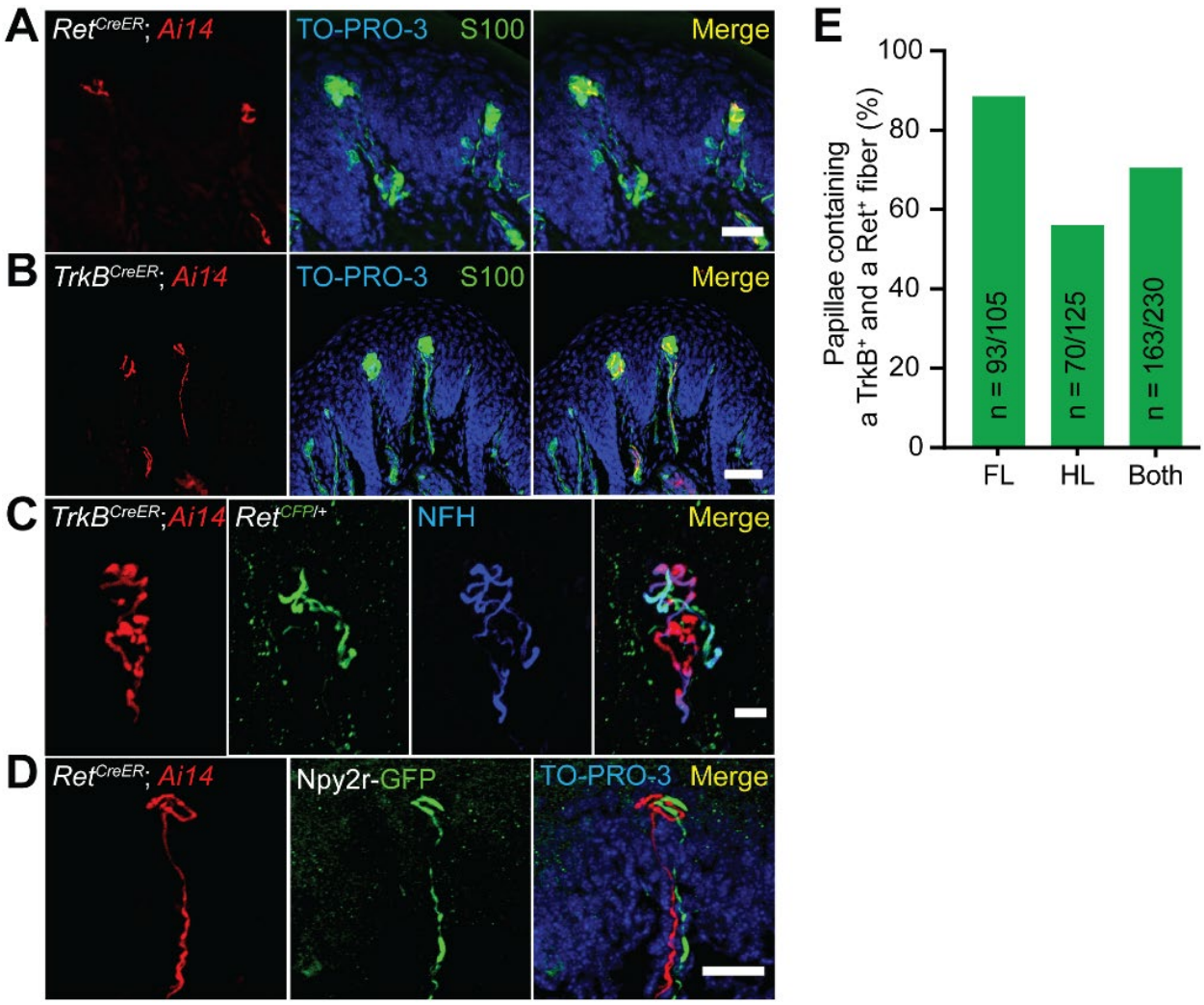

Figure 4.3. Meissner corpuscles are innervated by two molecularly distinct mechanosensory neuron types

(**a**) Forelimb pedal pad section of a P20 *Ret*^{CreER}*; Rosa26*$^{LSL\text{-}tdTomato}$ (*Ai14*) mouse treated with tamoxifen at E10.5-E11.5. Section is immunostained for S100, DsRed, and TO-PRO-3. This experiment was repeated in 3 mice. Scale bar = 25 μm.

(**b**) Hindlimb digital pad section of a P50 *TrkB*^{CreER}*; Rosa26*$^{LSL\text{-}tdTomato}$ (*Ai14*) mouse treated with tamoxifen at E16.5. Section is stained for S100, DsRed, and TO-PRO-3. This experiment was performed in 8 mice with varying dates of tamoxifen administration (E13.5, E16.5, P2, and P6). Scale bar = 50 μm.

(**c**) Hindlimb digital pad section of a P50 *TrkB*^{CreER}*; Ai14; Ret*^{CFP} mouse treated with tamoxifen at P5. Section is immunostained for DsRed, GFP, and NFH. This experiment was repeated in 4 mice with tamoxifen administration at E13.5 or P5. This experiment was repeated in 3 mice. Scale bar = 10 μm.

(**d**) Forelimb pedal pad section of a P20 *Ret^{CreER}; Ai14; Npy2r-GFP* mouse treated with tamoxifen at E10.5. Section is stained with anti-DsRed, anti-GFP, and TO-PRO-3. Scale bar = 25 μm.
(**e**) Percentage of dermal papillae containing both TrkB$^+$ and Ret$^+$ Meissner afferents in forelimb pads, hindlimb pads, and all pads as measured in *TrkB^{CreER}; Ai14; Ret^{CFP}* mice (2 animals). Only papillae containing a tdTomato$^+$ fiber were included in the quantification to eliminate an effect of Cre-lox efficiency on the interpretation of these measurements.

Meissner corpuscles are believed to be innervated by one physiological type of sensory neuron, the Aβ RAI-LTMR (Abraira and Ginty, 2013; Iggo and Ogawa, 1977; Johnson, 2001; Willis and Coggeshall, 2004). Our electrophysiological recordings showed that Aβ RA-LTMR responses to glabrous skin stimulation are lost in *TrkB^{cKO}* mice (**Fig. 4.1f**). Therefore, we hypothesized that the Ret$^+$ and TrkB$^+$ Meissner afferents are previously unrecognized subsets of Aβ RAI-LTMRs. Aβ RA-LTMRs form central collaterals along the rostrocaudal axis of the spinal cord and also extend an axonal branch via the dorsal column to the dorsal column nuclei (DCN) of the brainstem (Brown et al., 1980; Pubols and Pubols, 1973; Shortland and Woolf, 1993). This projection via the direct dorsal column pathway is likely important for tactile perception and discriminative touch (Abraira and Ginty, 2013). We visualized the central projections of both the Ret$^+$ and TrkB$^+$ Meissner afferents. These analyses revealed that both Meissner afferent subtypes display archetypal Aβ LTMR central collateral morphologies and axonal projections to the DCN (**Supplementary Fig. 4.7**) (Brown, 1981; Shortland and Woolf, 1993; Watson, 2003).

We next asked whether either or both Ret$^+$ and TrkB$^+$ Meissner afferents have physiological response properties consistent with those of Aβ RAI-LTMRs. We used the *in vivo* DRG recording preparation for targeted electrophysiological recordings of genetically labeled Ret$^+$ and TrkB$^+$ Meissner afferent populations. All recorded Meissner afferents of both subtypes had small, well-defined receptive fields confined to a single glabrous pad. Both subtypes also had conduction velocities within the Aβ range, although the mean conduction velocity of TrkB$^+$ Meissner afferents was modestly but significantly slower than that of Ret$^+$ Meissner afferents (**Fig. 4.4a**). TrkB$^+$ Meissner afferents responded at both the onset and offset of force-controlled step indentations with high sensitivity, whereas Ret$^+$ Meissner afferents

responded at the onset of step indentations with lower and more varied sensitivity and rarely responded to the offset of step indentations (**Fig. 4.4b-d**). Some (4 of 10) of the Ret$^+$ Meissner afferents responded during the sustained phase of the step indentation (example in **Fig. 4.4e**), indicating Meissner-innervating afferents are not always rapidly adapting. Both TrkB$^+$ and Ret$^+$ Meissner afferents exhibited a wide range of frequency tuning to 2-120 Hz sinusoidal vibrations: Some neurons of both types responded best to high frequencies while others had nearly uniform force thresholds across the tested frequencies (**Supplementary Fig. 4.8**). While frequency tuning did not differ between TrkB$^+$ and Ret$^+$ Meissner afferents, TrkB$^+$ Meissner afferents were more sensitive to vibratory stimuli than Ret$^+$ Meissner afferents (**Supplementary Fig. 4.8**). Altogether, while the response properties of TrkB$^+$ Meissner afferents fit the classic Aβ RAI-LTMR definition, those of most Ret$^+$ Meissner afferents do not.

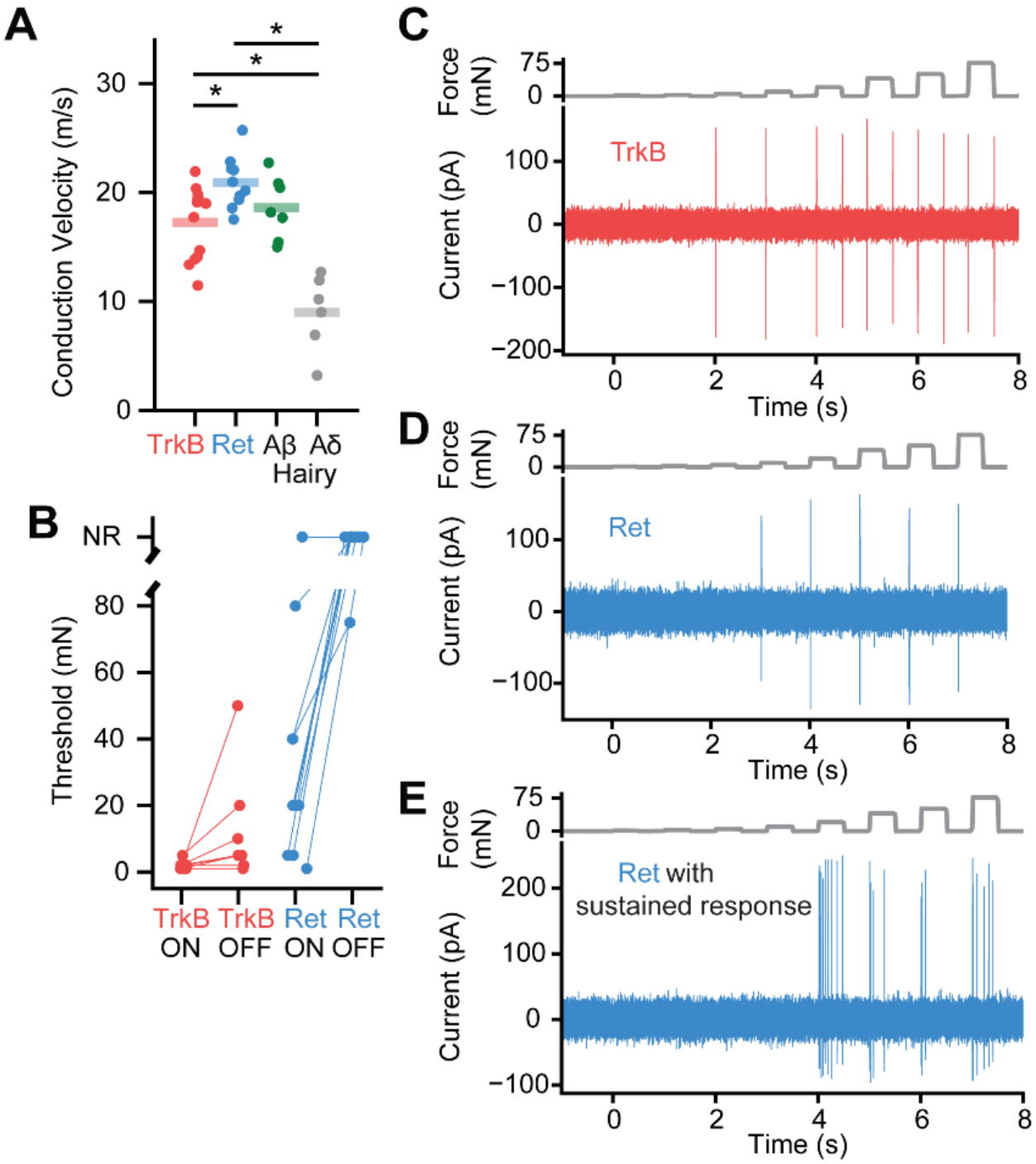

Figure 4.4. Ret⁺ and TrkB⁺ Meissner afferents exhibit distinct physiological response properties

(**a**) Both Meissner afferent subtypes have conduction velocities in the Aβ range as defined by the range of conduction velocities measured from hairy skin Aδ and Aβ LTMRs in the same preparation. The average conduction velocities for TrkB⁺ and Ret⁺ Meissner afferents are significantly different (10 afferents per

type; mean ± s.e.m.: TrkB = 17.3 ± 0.9 m/s, Ret = 20.9 ± 0.8; Mann-Whitney U Test (U = 26.0, p = 0.008). * $p < 0.05$.

(**b**) The minimal force required to produce an action potential at the onset or offset of a step indentation for TrkB$^+$ and Ret$^+$ Meissner afferents.

(**c**) Response of a TrkB$^+$ Meissner Aβ LTMR to a series of step indentations increasing in intensity from 1 to 75 mN.

(**d**) Response of a RA Ret$^+$ Meissner afferent to the same stimuli as in **c**.

(**e**) Response of a SA Ret$^+$ Meissner afferent.

We next investigated the spatial relationships between the cutaneous termination fields of Ret$^+$ and TrkB$^+$ Meissner afferents. Homotypic tiling is a phenomenon in which the anatomical receptive fields of neurons do not spatially overlap with other neurons of their same type. Using whole-mount alkaline phosphatase (AP) staining of sparsely labeled Meissner afferents, we found that the skin innervation areas of individual Ret$^+$ and TrkB$^+$ Meissner afferents are well-demarcated, spatially contiguous, and confined to single glabrous pads (**Supplementary Fig. 4.9**), consistent with the physiological receptive fields being confined to single glabrous pads. Occasionally, two neurons innervating the same toe or pedal pad were labeled (**Fig. 4.5a**). In these cases, TrkB$^+$ afferents were never observed to spatially overlap, and only one out of ten pairs of Ret$^+$ afferents occupying the same pad displayed spatial overlap (**Fig. 4.5c**). For the single overlapped Ret$^+$ afferent pair, the two arborizations shared only one out of twelve total corpuscles, and this corpuscle was on the border of their termination fields. We also used an intersectional genetic labeling strategy to address homotypic tiling. We generated mice harboring either the *TrkB^{CreER}* or *Ret^{CreER}* allele in conjunction with two different Cre-dependent fluorescent reporters, *Rosa26$^{LSL\text{-}YFP}$* and *Rosa26$^{LSL\text{-}tdTomato}$*. We treated these mice with high doses of tamoxifen to randomly and efficiently label individual afferents with one of three possibilities: tdTomato, YFP, or both. Virtually all Meissner corpuscles examined in these mice contained a single-color fiber of a given afferent subtype (**Fig. 4.5b, d**) thus confirming homotypic tiling of the two Meissner afferent types. We also compared the peripheral arborizations of sparsely labeled Ret$^+$ and TrkB$^+$ Meissner corpuscle afferents. These two populations exhibited differences in both their surface area size distributions and the number of Meissner corpuscles

innervated by individual neurons (**Fig. 4.5e, f**; **Supplementary Fig. 4.9**), indicating that the two homotypically tiled Meissner afferent types are heterotypically offset.

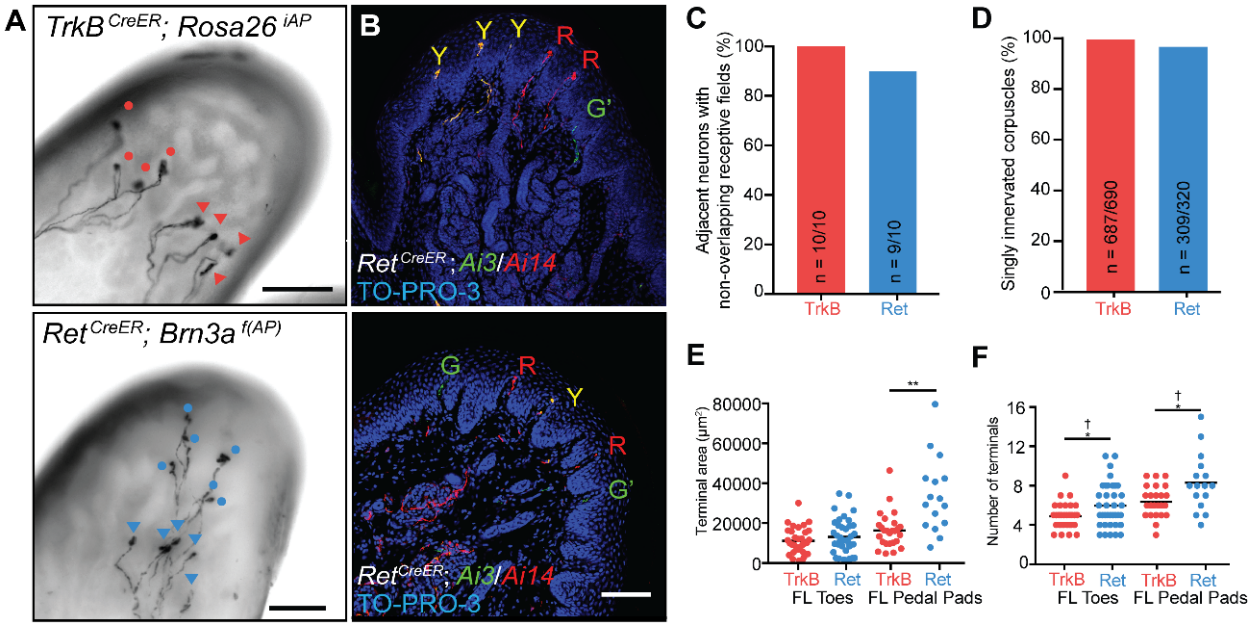

Figure 4.5. Spatial arrangement of Ret⁺ and TrkB⁺ Meissner afferent cutaneous endings

(**a**) Images of whole-mount, AP-stained digital pads of a *TrkB^{CreER}; Rosa26^{iAP}* mouse (top) and a *Ret^{CreER}; Brn3a$^{f(AP)}$* mouse (bottom, Z-projection performed in Fiji) depicting pairs of afferents of the same subtype innervating the same glabrous pad. Tamoxifen doses were titrated to achieve sparse labeling of Meissner afferents. Terminals of one neuron are annotated with circles and terminals of the other with triangles. (scale bars = 100 μm)

(**b**) Digital pad sections of *TrkB^{CreER}; Rosa26$^{LSL\text{-}YFP/LSL\text{-}tdTomato}$* (*Ai3/Ai14*) mice treated with tamoxifen at E12.5 and E13.5 (upper panel) and *Ret^{CreER}; Ai3/Ai14* mice administered tamoxifen at E11.5 and E12.5 (lower panel). Y: fibers express both tdTomato and YFP; R: fibers express tdTomato only; G: fibers express YFP only; G': YFP⁺ fibers without terminals in the sections. Sections were stained with anti-DsRed, anti-GFP, and TO-PRO-3. (scale bar = 100 μm)

(**c**) Percentage of TrkB⁺ and Ret⁺ Meissner afferent pairs innervating the same pad and occupying different spatial territories.

(**d**) Quantification of the percentage of dermal papillae and Meissner corpuscles receiving a single TrkB⁺ fiber (3 animals) and a single Ret⁺ fiber (6 animals).

(**e, f**) Receptive field surface area (**e**) and number of terminal endings (**f**) of TrkB$^+$ and Ret$^+$ Meissner afferents measured in *TrkB^{CreER}; Rosa26^{iAP}* or *TrkB^{CreER}; Brn3a$^{f(AP)}$* mice (N = 21) and *Ret^{CreER}; Rosa26^{iAP}* or *Ret^{CreER}; Brn3a$^{f(AP)}$* mice (N = 21). Individual measurements and mean values (black bar) are plotted for forelimb digital pads and pedal pads. (two-tailed Welch's t-test, mean significantly different: * $p < .05$, ** $p < .01$; F-test of the equality of variances, variance significantly different: † $p < .01$).

One potential advantage of heterotypic overlap of Meissner mechanoreceptors with different force sensitivities is to enable discrimination of a greater range of forces. In this model, spikes emanating from the TrkB$^+$ Meissner Aβ LTMR alone encode the lightest indentation forces whereas spikes from both TrkB$^+$ and Ret$^+$ Meissner mechanoreceptors encode higher forces. Another potential advantage of heterotypic overlap of homotypically tiled Meissner mechanoreceptors is that population responses to forces that co-activate both Meissner afferent types could enable a heightened ability to detect and localize a point stimulus. We modeled the receptive fields of each of the two Meissner afferent subtypes as homotypically tiled grids that are heterotypically offset and simulated measurements of spatial acuity (**Supplementary Fig. 4.10**). Our simulations indicated that, for a single non-overlapping grid, the number of discriminable spatial locations is equal to the number of neurons (**Supplementary Fig. 4.10**). Simulations using two grids that are homotypically tiled but overlapping and maximally offset with respect to each other revealed that the number of distinct spatial locations doubles for the same number of neurons (**Supplementary Fig. 4.10**). This gain arose from a distributed neural representation that an overlapped arrangement facilitates and may enable an enhanced ability to localize a point stimulus without increasing the number of neurons. Therefore, while functional analyses of mice selectively lacking one or the other Meissner afferent subtype will be needed to test our mathematical modeling findings, we speculate that the heterotypic overlap of homotypically tiled Meissner mechanoreceptor subtypes may enable heightened discriminatory capabilities, at a population level, compared to a simpler arrangement of a single homotypically tiled Meissner afferent type.

The different sensitivities and response kinetics of Ret$^+$ and TrkB$^+$ Meissner Aβ mechanoreceptors raised the question of whether these mechanoreceptor types form distinct endings within the corpuscle where

mechanotransduction occurs. We evaluated the ultrastructural properties of the axonal endings of Ret$^+$ and TrkB$^+$ Aβ mechanoreceptors within the Meissner corpuscle using electron microscopy. We crossed *Ret^{CreER}* or *TrkB^{CreER}* mice to reporter mice that express the peroxidase dAPEX2 targeted to the mitochondrial matrix in a recombinase-dependent manner (Zhang et al., 2019), thereby generating an electron-dense label associated with mitochondria and distributed throughout the labeled cells. We could distinguish and characterize the ultrastructural properties of labeled Aβ mechanoreceptors within the Meissner corpuscle. Axons of both Ret$^+$ and TrkB$^+$ mechanoreceptor subtypes terminated within the Meissner corpuscle and both ending types were intimately associated with resident, morphologically complex corpuscle lamellar cells (**Fig. 4.6a, b**). The lamellar cell processes that surround both Meissner mechanoreceptor ending types were periodically discontinuous, thus exposing the naked mechanoreceptor axonal membrane to the extracellular matrix (**Fig. 4.6c**). While Ret$^+$ Meissner axon profiles were usually surrounded by only a few concentrically arranged lamellar cell processes, the lamellar cell processes associated with TrkB$^+$ Meissner profiles were typically much more elaborate. In fact, TrkB$^+$ Meissner afferents have a minimum of five concentric lamellar processes surrounding the axon terminal (range 5-28), and on average twice as many processes compared to Ret$^+$ Meissner afferent terminals (range 3-18; **Fig. 4.6c**). This ultrastructural difference is particularly noteworthy when considering the distinct response kinetics of Ret$^+$ and TrkB$^+$ Meissner afferents together with classical studies of the Pacinian corpuscle suggesting that lamellar wrappings are critical for the Pacinian LTMR's response kinetics (Loewenstein and Mendelson, 1965). For the Pacinian afferent, lamellar cell wrappings are believed to be essential for its high selectivity to vibratory stimuli and for producing a generator potential as force is withdrawn during a step offset. Moreover, "unwrapping" or removing Pacinian lamellar cells converted its generator potential from being transient to sustained (Loewenstein and Mendelson, 1965). Our findings that Ret$^+$ Meissner mechanoreceptors are associated with fewer lamellar cell wrappings compared to the TrkB$^+$ Meissner LTMR, and that they lack responses at indentation step offsets and occasionally display slowly adapting responses, is consistent with these classical theories.

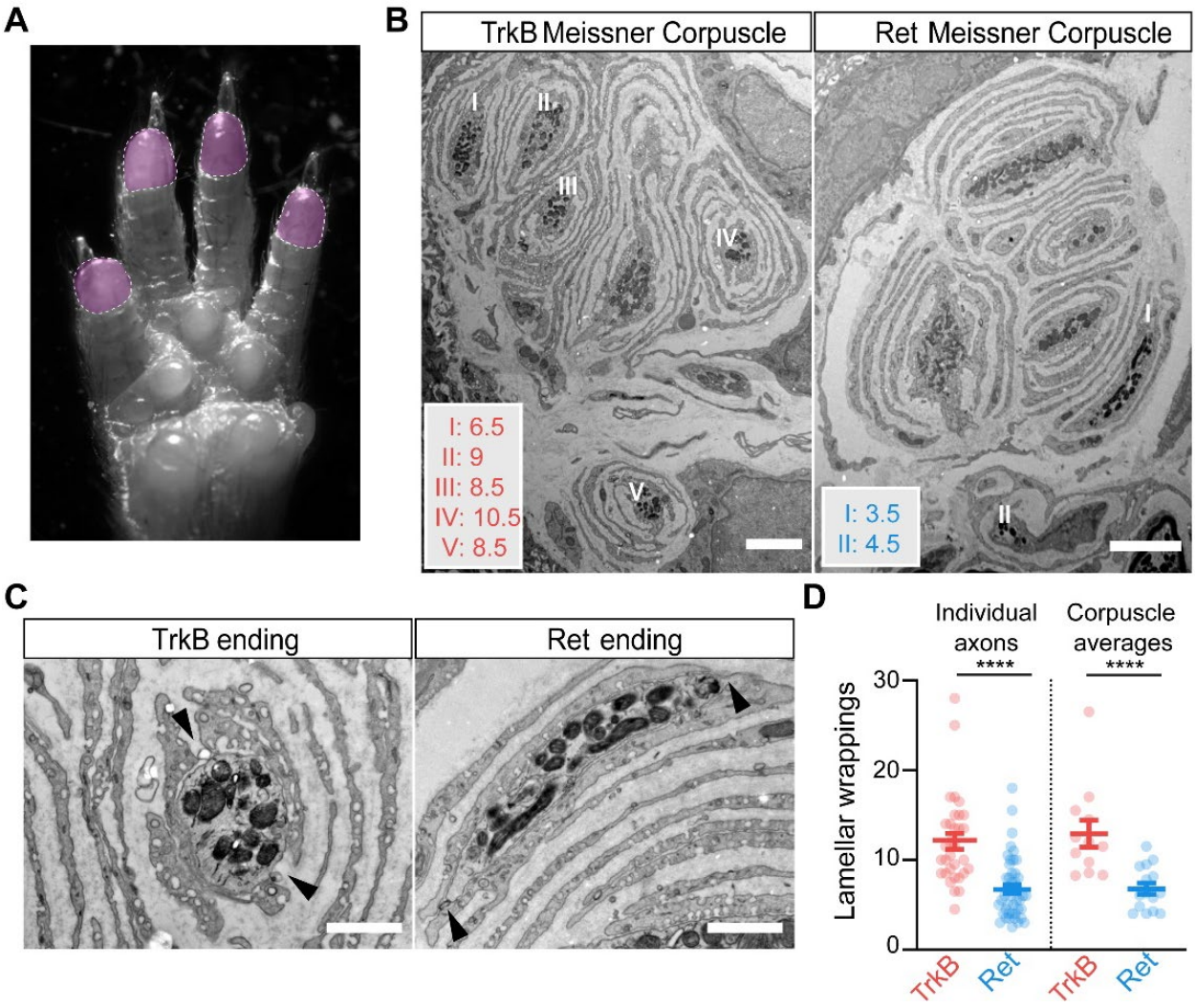

Figure 4.6. TrkB^{+} Meissner Aβ LTMR endings have more lamellar cell wrappings than Ret^{+} Meissner mechanoreceptor endings

(**a**) Image of the paw, with the shaded areas (digit tips) representing regions of high density of Meissner corpuscles used for EM analysis.

(**b**) EM images of Meissner corpuscles from a *TrkB^{CreER}; Advillin^{FlpO}; Rosa26$^{DR\text{-}Matrix\text{-}dAPEX2}$* mouse treated with tamoxifen at P3 (left) and a *Ret^{CreER}; Advillin^{FlpO}; Rosa26$^{DR\text{-}Matrix\text{-}dAPEX2}$* mouse treated with tamoxifen at E11.5 and P10 (right). Scale bar = 3 μm.

(**c**) High magnification images of labeled endings and associated lamellar cells from **b**. Both exhibit openings or areas not directly associated with lamellar cells (black arrowheads). Scale bar = 1 μm.

(**d**) Quantification of the number of lamellar cell wrappings around genetically labeled endings of TrkB and Ret endings. Shown are the number of lamellar wrappings for individual axonal profiles (left panel; n = 32

and 47, respectively) and averages of all axonal profiles within individual corpuscles (right panel; n = 12 and 15, respectively). Mann-Whitney *U* test, **** $p < 0.0001$. N = 2 animals for each LTMR subtype.

Our findings show the Meissner corpuscle to be crucial for perception of the gentlest detectable forces acting on the glabrous skin and for fine sensorimotor control during object manipulation. The corpuscle is endowed with intertwined endings of two molecularly, ultrastructurally, and physiologically distinct mechanoreceptor subtypes whose cutaneous innervation areas are homotypically tiled and heterotypically offset. This arrangement of differentially sensitive Meissner Aβ mechanoreceptors supports a "population coding" model for force intensity. Computational simulations suggest that it may enable higher acuity, at a population level, than would be expected from a simpler arrangement with a single Meissner mechanoreceptor subtype. The organization of the Meissner corpuscle afferents' termination fields thus illustrates a solution to the nervous system's general challenge of localizing stimuli with a limited number of neurons. Our EM findings reveal that the axonal endings of the Ret^+ and $TrkB^+$ Meissner Aβ mechanoreceptor subtypes, and in particular their association with concentrically organized processes of corpuscle lamellar cells, are distinct, supporting a model in which ultrastructural properties of mechanoreceptors within a corpuscle dictate their responses.

Acknowledgements

We thank Emily Kuehn for AAV virus characterization, Wei-Chung Lee for providing access to ultramicrotomy equipment, and Robert LaMotte and Jeff Woodbury for assistance with the *in vivo* physiological recording preparation. We thank Michael Rutlin for preliminary analysis of behavioral deficits in *TrkB* conditional mutant mice, Jessica Barowski for help with figures, David Paul for help with electron microscopy quantification, and Tanya Monteiro for technical assistance. We thank Ofer Mazor and Pavel Gorelik of the HMS Research Instrumentation Core Facility for consultation on operant conditioning design and MATLAB code and Josh Huang for discussing unpublished sunflower seed handling measurements. We thank Matthew Pecot, Soha Ashrafi, Nikhil Sharma, and Gordon Fishell for helpful comments on the manuscript.

Funding

N.L.N., M.W.S., Q.Z. and C.G. were Stuart H.Q. & Victoria Quan Fellows at Harvard Medical School. This work was supported by NIH grants NS97344 (D.D.G.), NS105324 (A.J.E.), NS101843 (M.W.S), MH115554 (J.D.), K99 NS101057 (L.L.O.), NS089521 (C.D.H.), NSF GRFP 2014177995 (M.W.S.), a scholar award by the James S. McDonnell Foundation (J.D.), and the Edward R. and Anne G. Lefler Center for Neurodegenerative Disorders (D.D.G.). D.D.G. is an Investigator of the Howard Hughes Medical Institute.

Author Contributions

N.L.N., Y.L., A.J.E., and D.D.G. conceived the project; N.L.N and Y.L. performed light microscopy experiments with assistance from A.A.; N.L.N., A.J.E., and B.P.L did *in vivo* electrophysiological recordings with guidance from C.D.H.; M.W.S., M.I., J.R., and S.J.K. performed the operant conditioning behavioral experiments; L.L.O. performed the PPI experiments; N.L.N., A.A., and M.M.D. performed all other behavioral experiments; N.L.N. and J.D. performed the modeling; A.H., Q.Z., and S.J.C. did the EM analysis. N.L.N. and D.D.G. wrote the first draft of the paper, with sections subsequently provided by A.J.E.; All authors contributed to the final manuscript draft.

Materials and Methods

Animals

Animals were handled according to protocols approved by the Harvard Standing Committee on Animal Care and are in accordance with Federal guidelines.

Mouse lines

The *TrkB*^{flox}, *Advillin*^{Cre} (JAX 032536), *K5Cre* (MGI 3050065), *Atoh1*^{flox} (JAX 008681), *Ret*^{CreER} (MGI #4437245), *Ai14* (*Rosa26*$^{LSL\text{-}tdTomato}$; JAX 007914), *Ret*^{CFP} (MGI 3777555), *Npy2r-GFP* (MGI 3844094), *Rosa26*^{iAP} (JAX 009253), *Ai3* (*Rosa26*$^{LSL\text{-}YFP}$; JAX 007903), *Ai32* (*Rosa26*$^{LSL\text{-}ChR2(H134R)\text{-}EYFP}$; JAX 024109), *TrkB*^{CreER} (JAX 027214), *Pvalb*$^{2A\text{-}FlpO\text{-}D}$ (JAX 022730), *Ai65* (*Rosa26*$^{FSF\text{-}LSL\text{-}tdTomato}$; JAX 021875), *Rosa26*$^{LSL\text{-}FSF\text{-}ReaChR\text{-}mCitrine}$ (JAX 024846), *Rosa26*$^{DR\text{-}Matrix\text{-}dAPEX2}$ (JAX 032764), *Rosa26*$^{LSL\text{-}Matrix\text{-}dAPEX2}$, *Brn3a*$^{f(AP)}$ (JAX 010558), *BDNF*^{lacZ} (*BDNF*^{flox}; JAX 021055), *Wnt1Cr*e (JAX 022137), and *DhhCre* (JAX 012929) mouse lines have been described previously (Badea et al., 2009a; Badea et al., 2009b; da Silva et al., 2011; Danielian et al., 1998; Gong et al., 2003; Gorski et al., 2003; Hooks et al., 2015; Jaegle et al., 2003; Liu et al., 2012; Luo et al., 2009; Madisen et al., 2015; Madisen et al., 2010; Ramirez et al., 2004; Rutlin et al., 2014; Shroyer et al., 2007; Uesaka et al., 2008; Wu et al., 2012; Zhang et al., 2019). The *Advillin*^{FlpO} mouse line, which was generated by standard gene targeting procedures, enables FlpO-dependent recombination in somatosensory and other peripheral nervous system neurons and will be described in detail elsewhere. All lines were kept on a mixed CD1-C57Bl/6 background.

Tamoxifen treatments

Tamoxifen (Toronto Research Chemicals) was dissolved in 100% ethanol (20mg/mL). The tamoxifen/ethanol mixture was diluted with sunflower seed oil (Sigma) at a 1:2 dilution and vacuum centrifuged for 30-45 minutes until the ethanol evaporated. The resulting solution was stored at -20°C and thawed immediately prior to use. For embryonic tamoxifen treatment, the oil/tamoxifen solution was delivered to pregnant mothers via oral gavage. The Ret^{+} Meissner afferent population was labeled with high efficiency by giving pregnant mother a 2 mg dose of tamoxifen at E11.5 and E12.5. The forelimb was labeled more effectively at E11.5, while the hindlimb was labeled more effectively at E12.5. The TrkB^{+} Meissner afferent population was labeled with high efficiency using intraperitoneal (IP) injection of P4 pups (0.5 mg), but this population was also labeled when pregnant mothers were given tamoxifen any time between E12.5 and E16.5 and when P5 pups were given 0.5 mg of tamoxifen.

Immunohistochemistry

P20 or older mice were euthanized with CO_2 and perfused with Ames Media (Sigma) containing 10 U/mL heparin (Sigma) in PBS, followed by 4% paraformaldehyde (PFA) in PBS. Spinal cords and brainstems were dissected and fixed in 4% PFA at 4 °C overnight. For skin sectioning experiments, glabrous toe and pedal pads were removed from the paw and placed in 4% PFA for 4-6 hours or Zamboni's fixation buffer for 24-48 hours at 4 °C. For whole-mount immunohistochemistry, whole paws were placed in Zamboni's fixation buffer at 4 °C for 24-48 hours. The glabrous skin was then separated from the underlying tissue via fine dissection in PBS. Isolated glabrous paws were fixed in Zamboni's fixation buffer for an additional 1 hour at room temperature. Following fixation, all tissues were rinsed 3x10 minutes in PBS at room temperature. Brainstems and spinal cords with dorsal root ganglia attached were isolated from the vertebral column.

Glabrous pads, spinal cords, and brainstems destined for sectioning were cryoprotected in 30% sucrose in PBS at 4 °C for 24-48 hours. Tissues were embedded in OCT (Tissue Tek) and frozen at -20 °C. Glabrous pads were sectioned at 25 µm, and spinal cords and brainstems were sectioned transversely at 40-50 µm. Sections were dried overnight at room temperature. Glabrous pads were given 1-2 additional days to dry. All sections were rinsed 3x10 minutes with PBS, blocked with 5% normal serum (donkey or goat) in 0.1% PBST (0.1% Triton X-100 in PBS) for 2 hours, and incubated with primary antibody in blocking solution overnight at 4 °C. The following day, sections were rinsed 3x10 minutes with PBST and incubated with secondary antibodies in blocking solution for 2 hours at room temperature or overnight at 4 °C. Sections were then rinsed 1x10 minutes in PBST and 2x10 minutes in PBS and mounted with Fluoromount-G (Southern Biotech). Images were acquired on a Carl Zeiss LSM 700 confocal microscope.

Whole-mount immunohistochemistry of glabrous skin was performed as described previously (Bai et al., 2015). The skin was given several one-hour washes in 0.3-0.5% TritonX-100 in PBS. The skin was then incubated in primary antibodies in blocking solution (5% normal serum (goat or donkey), 75% PBST, 20% DMSO) at room temperature for 72 hours. The skin was washed in PBST for 4-5x1 hour and incubated in

secondary antibodies in blocking solution at room temperature for 48 hours. Tissue was washed several times in PBST then dehydrated in serial methanol dilutions (1 hour each of 25%, 50%, 75%, and 100%), followed by overnight dehydration in 100% methanol at room temperature. The tissue was then cleared in BABB (1 part Benzyl Alcohol: 2 parts Benzyl Benzoate) and imaged.

Primary antibodies were rabbit anti-DsRed (Clontech, Cat. # 632496, 1:500), goat anti-mCherry (Sicgen, Cat. # AB0040-200, 1:500), chicken anti-GFP (Aves Lab, Cat. # GFP-1020, 1:500), rabbit anti-GFP (Invitrogen, Cat. # A-11122, 1:500), goat anti-GFP (US Biological, Cat. # G8965-01E, 1:500), rat anti-MBP (Millipore, Cat. # MAB386, 1:500), rabbit anti-NFH (Sigma, Cat. # N4142, 1:1000), chicken anti-NFH (Aves Lab, Cat. # NFH, 1:500), rabbit anti-S100 (Dako, Cat. # Z031129-2, 1:300), rabbit anti-PKC γ (Santa Cruz, Cat. # SC-211, 1:500), and TROMA-I (rat anti-keratin 8/cytokeratin 18, DSHB, University of Iowa, TROMA-I supernatant, 1:100). The nucleic acid stain TO-PRO-3 (Invitrogen, Cat. # T3605, 1:500), the nonpeptidgeric nociceptor marker IB4 (Isolectin GS-IB_4, conjugated to Alexa Fluor 647, Life Technologies, Cat. # I32450, 1:500), and the nucleic acid stain Hoechst 33258 (Fisher, Cat. # H3569, 1:1000) were applied during secondary antibody incubation.

X-gal staining

Embryos and glabrous skin were fixed with a glutaraldehyde solution (0.2% glutaraldehyde, 2 mM $MgCl_2$ in PBS) overnight at 4 °C. For whole-mount staining, fixed embryos or skin were washed with detergent rinse buffer (0.01% sodium deoxycholate, 0.02% NP40, 2 mM $MgCl_2$ in phosphate buffer, pH 7.4) and stained with staining buffer (0.01% sodium deoxycholate, 0.02% NP40, 2 mM $MgCl_2$, 5mM potassium ferricyanide, 5mM potassium ferrocyanide, 1mg/ml 5-bromo-4-chloro-indolyl-β-D-galactopyranoside in phosphate buffer, pH 7.4) at room temperature. After staining, embryos were dehydrated sequentially with 50% methanol, 80% methanol, and 100% methanol. For staining on sections, 12μm sections were cut and dried for several hours at room temperature. The staining procedure was the same as described for whole-mount staining. After staining, sections were fixed overnight at 4 °C in 4% PFA in PBS, and mounted with Fluoromount-G.

Fluorescent Sparse Labeling

TrkB^{+} Meissner afferents were sparsely labeled by injecting the pedal pads of TrkB^{CreER}; Ai65 mice with a viral vector containing FlpO recombinase, AAV1-hSyn-FlpO (AAV2/1.humanSynapsin1.FlpO.bGH, UPenn Vector Core, titer = 1.23×10^{13} gc/ml). Mice were administered 0.5 mg of tamoxifen at P5 via IP injection. Mice aged P9 were anesthetized via isoflurane (2-3%) delivered from a precision vaporizer. Animals were monitored throughout the 5-10 minute procedure, and the anesthetic dose was adjusted as necessary. AAV1-hSyn-FlpO combined with a small amount of Fast Green dye (Sigma F7252-5G) in 0.9% saline was injected into 1-3 hindlimb or forelimb pedal pads per animal via a beveled glass capillary needle (FHC Inc capillary tubing, FHC 27-30-0). The total volume of AAV/Fast Green mixture injected per pad for sparse labeling was approximately 0.1-0.5 µl. Mice were removed from anesthesia, administered analgesic (Carprofen, 4 mg/kg), and placed on a warm pad for recovery. Animals were given an additional dose of Carprofen after 24 hours and observed to ensure adequate recovery. Mice were perfused 2-9 weeks after injection, and their vertebral columns and glabrous paws were prepared as described above. The viral dose was titrated to achieve labeling of a single neuron per animal, and only mice in which a single cervical or lumbar neuron was observed in the DRG were included in subsequent analyses.

Alkaline Phosphatase Histochemistry

Placental alkaline phosphatase (PLAP) staining was performed as described previously (Liu et al., 2012). Whole paws from P21 mice were fixed in Zamboni's fixation buffer at 4 °C for 24-48 hours. Age was kept consistent to prevent age and size differences from contributing to observed differences between Ret^{+} Meissner afferent and TrkB^{+} Meissner afferent receptive fields. The glabrous skin was then separated from the underlying tissue via fine dissection in PBS. Isolated glabrous paws were fixed in Zamboni's fixation buffer for an additional 1 hour at room temperature. Following fixation, all tissues were rinsed 3x10 minutes in PBS at room temperature and then incubated at 65-68 °C for 2 hours. To detect PLAP signal, tissues were incubated with BCIP/NBT (Roche) solution (diluted in 0.1 M Tris pH 9.5, 0.1 M NaCl,

50 mM $MgCl_2$, 0.1% Tween-20 solution) overnight at room temperature. Tissues were then fixed in 4% PFA in PBS for 1 hour at room temperature, followed by dehydration in ethanol (1 hour 50%, 1 hour 75%, 1 hour 100%, overnight 100%). Finally, tissues were cleared in BABB and imaged.

To sparsely label Ret^+ Meissner afferents, pregnant mice were administered 1 mg tamoxifen at either E11.5 or E12.5. For $TrkB^+$ Meissner afferents, pregnant mice were administered 1 mg tamoxifen at E14.5.

Quantification of Receptive Field Geometries

Images of Meissner afferent terminal arborizations in glabrous pads were analyzed in the Fiji distribution of ImageJ (www.fiji.sc). The perimeter of individual receptive fields (terminal area) was outlined by hand, and the resulting selection was subjected to the Convex Hull function, which replaces a polygon with its convex hull. The area in μm^2 and the aspect ratio (major axis/minor axis) of the convex hull were measured using the measure function. Terminals of afferent arborizations were counted by eye. For some neurons, two fibers from the same neuron could be seen traveling together and terminating in the same corpuscle. In these cases, the two fibers were counted as a single termination. This phenomenon appeared to occur more often for $TrkB^+$ Meissner afferents than for Ret^+ Meissner afferents, but this was not quantified.

In Vivo Electrophysiological Recordings

In vivo dorsal root ganglia (DRG) recordings were made as described previously (Bai et al., 2015) using a preparation modified from that published by Ma, Donnelly and LaMotte (Ma et al., 2010). Ret^{CreER} or $TrkB^{CreER}$ mice with a Cre-dependent YFP, tdTomato, or mCitrine reporter (Ai14, Ai32, or $Rosa26^{LSL\text{-}ReaChR\text{-}mCitrine}$) were administered tamoxifen at the appropriate ages. Since this strategy also labels hairy-skin-innervating neurons, we anterogradely labeled glabrous neurons via subcutaneous injection of cholera toxin subunit B conjugated to Alexa 555 or Alexa 488 (Thermo Fisher; 2 µg/µl in PBS, approximately 0.3 µl per pad) into the left hindlimb toe and pedal pads 2-3 days prior to recording. On the

day of recording, P20-P60 mice were anesthetized with urethane (1 g/kg) via intraperitoneal injection. Anesthesia was maintained with isoflurane (1.5-2% in 100% O_2) for the duration of the surgery and subsequent recording period (SomnoSuite, Kent Scientific). Mouse internal temperature was monitored via a rectal probe and maintained at 35.5-37.5 °C with a temperature controller (TC-344B, Warner Instruments) and thermoelectric heater (C3200-6145, Honeywell) embedded in castable cement (Aremco). The lumbar vertebral column was exposed and secured with custom spinal clamps (Mike's Machine, Attleboro MA). Bone dorsal to the target DRG(s) (L3-L5) was removed with rongeurs. The surgical site was continuously perfused with and immersed in external solution containing (in mM) 140 NaCl, 3.1 KCl, 0.5 KH_2PO_4, 6 glucose, 1.2 $CaCl_2$, 1.2 $MgSO_4$, and 10 HEPES. pH was adjusted to 7.4 with NaOH. The epineurium surrounding the DRG was removed with fine forceps. The DRG was visualized using custom reflective optics on an upright compound microscope (Zeiss). Cell bodies on the surface of the DRG were accessible for recording. Borosilicate glass pipettes (TW150F-4, WPI) were pulled to achieve a 20-30 µm tip diameter. Pipettes were then filled with external solution, and fluorescent cell bodies that were labeled with dye-conjugated CTB were targeted for cell-attached recordings.

Neuron receptive fields (RFs) were localized using a small paintbrush and gentle manual probing. For Meissner afferents, RFs were confined to single toe or pedal pad in the hindlimb. To estimate conduction velocity (CV), an electrical stimulus was delivered to the RF using a bipolar electrode. The delivered current was 2.5 times the threshold at which the neuron fired an action potential. CVs were estimated by dividing the conduction latency (average latency out of 10 trials) by the distance between the DRG and the RF. This distance did not account for the tortuosity of the sensory axon, and, thus, the reported CVs are a lower-bound on the true value. Force-controlled indentation of skin was achieved using an indenter (Model 300 C-I, Aurora Scientific) mounted on two orthogonal linear motorized stages (MTS25/M-Z8E, Thorlabs). The XY position of the indenter was controlled using the stages. The indenter was positioned on top of the RF such that the tip of the indenter was barely touching the surface of the glabrous pad. Sinusoidal force stimuli and low-pass filtered (15 ms boxcar) force steps were synthesized in MATLAB (Mathworks, Natick, MA) and delivered to the skin.

For random recordings of Aβ-LTMRs that innervate glabrous skin (**Fig. 4.1**), the hindpaw glabrous skin pedal pads of *TrkB*$^{flox/flox}$ controls and *TrkB*^{cKO} mice were injected with CTB conjugated to Alexa 488 24-72 hours prior to recording. Neurons with large soma diameters (> 25 μm) that contained CTB 488 were targeted for recording. The receptive fields of the neurons were localized with manual brushing, and force indentations (0.5 s duration, 1-75 mN intensity) were applied to the receptive field. RA neurons were defined as those with spiking responses to indentation at only the onset or offset of the step indentation. SA neurons were defined as those with spikes occurring at the onset and the middle of the step indentation. SA neurons never increased their firing rate in response to the termination of the indentation. Non-responsive (NR) neurons were defined as those that produced action potentials in response to stretching of the foot, but not to the indentation. Extracellular action potentials were recording using a Multiclamp 700A amplifier (Axon Instruments) operating in the voltage-clamp configuration, which was constantly adjusted so that no current was passed by the amplifier. Electrophysiological data was digitized at 40 kHz by a 16-bit A/D converter (USB-6259, National Instruments), low-pass filtered at 10 kHz using the amplifier's internal four-pole Bessel filter, and acquired using pClamp. All electrophysiological data were analyzed using custom Python scripts.

Quantification of Meissner Corpuscle and Merkel Complex Density

Images of serial sections of glabrous pads were sectioned at 25 μm. Images of sections were analyzed in the Fiji distribution of ImageJ (www.fiji.sc). In each section, the number of Meissner corpuscles, visualized via S100 antibody (Meissner corpuscles formed large, ovoid masses in the dermal papillae compared to Schwann cells surrounding neurons, which are also S100^{+}), and the number of Merkel complexes, visualized via TROMA-I antibody, were counted. Then, the length of the surface of the skin was traced and measured in ImageJ and multiplied by the thickness of the sections to obtain a volume in mm^3. Density was calculated by dividing the number of corpuscles or Merkel complexes (clusters of Merkel cells) by the volume of skin.

Behavior

Mice used for behavioral experiments were kept on a reversed light-dark cycle and were tested during the dark phase. Male mice of mixed genetic background (C57BL/6J and CD1) were ear notched for identification and genotyped at approximately P21. Females were not used due to potential effects of the estrous cycle on behavior, and a preliminary observation that female mice have lower von Frey thresholds than male mice. Ear notching was performed using an ear punch device (Kent Scientific). Mice 6-16 weeks of age were subjected to behavioral tests. Mutant animals were compared to control littermates from the same genetic crosses to control for strain/genetic background variability. All behavioral testing was performed by an experimenter blind to genotype.

Von Frey Paw Withdrawal Test

For the von Frey paw withdrawal test, a sheet of wire mesh (9217T52, McMaster-Carr) was attached to an acrylic frame and positioned about 14 inches above a table. Mice were placed in 5x2 inch clear, acrylic chambers, which were taped on top of the mesh. Prior to test date, mice were habituated to the chambers for one hour for two consecutive days. On the test date, withdrawal responses were measured. After allowing the mice to habituate for one hour, von Frey filaments (North Coast Medical) were applied to the left hindpaw. The experimenter applied the filament onto or within close proximity to the pedal pads of the hindpaw. Care was taken to avoid the hairy skin in the middle of the hindpaw. Starting with the lowest force, each filament was applied five times in a row, followed by a brief break. Then, the filament was applied another five times for a total of ten applications. The number of paw withdrawals was recorded for each filament weight.

Operant Conditioning Surgery and Water Restriction

Prior to operant conditioning, control *TrkB*$^{flox/flox}$ and mutant *TrkB*^{cKO} mice were implanted with headplates to in order to restrain them to the operant conditioning behavior apparatus. Adult (>P60) mice were anaesthetized with isoflurance (1.75 - 2% in O2). Following removal of the scalp and periosteum,

MetaBond dental cement was used to secure a lightweight, titanium headplate to the skull. Five days after surgery, mice began water-restriction (40 ml/kg of initial body weight) until they weighed 85% of their pre-restriction weight. Animals were monitored for health conditions every training and testing day using a detailed health assessment adapted for water deprived mice (Guo et al., 2014). Health categories included weight, posture and grooming, activity level, signs of normal eating/waste elimination, and signs of dehydration. The minimum required daily water intake for each animal was 0.8mL during data collection. Any animal that did not receive this much during the assay was supplemented up to the minimum volume.

Operant Conditioning Training

Mice were kept on a reversed light/dark cycle, and behavioral sessions were held daily for each animal. Behavioral paradigm control was performed by a custom written program running within the WaveSurfer application (Howard Hughes Medical Institute) in MATLAB. On the first and second days of training, each animal was given approximately one minute to freely roam the apparatus platform. Mice were then habituated to head restraint for 5-15 minutes with *ad libitum* water from the spout. To minimize the stress and movement of the animal, a three-sided acrylic enclosure was placed over the animal's body. On the third day of training, the right forepaw of each animal was secured over a 3-mm square hole in the apparatus platform, using an elastic strap over the forearm and clear cellophane tape over the back of the forepaw. A fine mechanical stimulator (Model 300 C-I, Aurora Scientific) positioned beneath the platform was used to apply a 75-mN step indentation stimulus to the glabrous skin of the forepaw. This indentation was applied atop a minimal force (< 1 mN) used to hold the arm in position. If the animal licked the spout within 2 s of the stimulus onset, it received a 5-µl water reward. Over the next two weeks of training, the response period was reduced to 0.5 s, and a no-lick window of 3 s was introduced to discourage spurious licks. In the final phase of training, animals were presented with a range of stimulus amplitudes between 0.5 and 50 mN on 60% of trials, with 20% of all trials serving as no-stimulus (catch) trials, and 20% with a salient 75 mN stimulus to maintain task engagement. Within three weeks, animals exhibited stable psychometric functions, with average response rate of 80.5 ± 3.5% and false alarm rate of 17.1 ± 2.5%

(mean ± s.e.m.) for the two days preceding data collection. Mice displayed some differences in overall sensitivity between von Frey and operant conditioning. Differences in stimulus application – including probe diameter, stimulus waveform, and holding force – likely account for these sensitivity differences.

Operant Conditioning Data Collection and Sorting

For all animals, data was collected for six days, following a pattern of two days of testing blocks followed by one day of an easier training paradigm. To exclude data when animals were not engaged in the behavior task, blocks of trials characterized by overall poor performance were omitted from analysis of the detection threshold. We used a d' statistic to identify these blocks of disengagement in the task, calculated using only trials with salient stimuli levels greater than 40 mN (equation 1).

$$\mathrm{d}' = Z(\text{hit rate}) - Z(\text{false alarm rate}) \quad (1)$$

For the first and last 14 trials in a session, d' was calculated over the entire block and the same value was assigned to each of the 14 trials. For all other trials in a session, d' was calculated over blocks of 30 trials and the value was assigned to the middle trial in the block (i.e. the d' value for trial 15 was found using all stimulus trials over 40 mN between trials 1 and 30). Only blocks with at least 15 trials of d' greater than or equal to 1.5 were used in data analysis. Animals with fewer than 750 viable trials were excluded.

To fit psychometric curves to the aggregate data, all stimulus trials were distributed into bins at 3 mN intervals, with the exception of the final bin with the most salient stimulus of 75 mN**.** For each animal, the average response rate during trials within each bin was calculated and averaged across all animals in either the control or *TrkB*^{cKO} group. The MATLAB software package 'psignifit 4' was used to fit a beta-binomial logistic sigmoid curve to each group (equation 2). Psignifit also output a parameter η that scaled the extra variance introduced within the bins of the data, where values near 1 indicated over-dispersed data and values near 0 indicated good binomial dispersion.

$$\psi(x; m, w, \lambda, \gamma) = \gamma + (1 - \lambda - \gamma)\,(11 + e - 2\log(1.05 - 1)\,x - mw) \qquad (2)$$

where *x* is binned stimulus intensity, *m* is the midpoint of the psychometric function, *w* is the width of the curve, *λ* is the upper asymptote, and *γ* is the lower asymptote. Average psychometric threshold for each group was determined by fitting individual mouse response data to a beta-binomial logistic sigmoid curve using Psignifit. For each mouse, the force value at the midpoint of the psychometric function was determined to be its psychometric threshold. This data was then averaged within group.

Horizontal Ladder Assay

For the horizontal ladder assay, a ladder consisting of two parallel acrylic sheets as sides and equally spaced aluminum rods was mounted above a table. An angled mirror was positioned below the ladder to increase visibility of foot position. The lighting in the testing room was dim to eliminate visual input as much as possible. Mice were trained on the ladder during two consecutive habituation days. During habituation, mice were placed on one end of the ladder and were allowed to walk across the ladder towards a cage on the opposite end. Trials in which the mice paused for more than five s, turned around, or walked on the rim of the ladder rather than the rungs were immediately repeated. This continued until mice successfully crossed the ladder three times, but each mouse was subjected to no more than five total trials per day. On the third day, videos of the mice crossing the ladder were recorded, and the number of slips and time to cross the ladder were measured by an experimenter who was blinded to genotype. The average values of three successful trials were obtained for each animal.

Wire Hang Assay

For the wire hang assay, a 35 cm aluminum wire (~2.5 mm in diameter) was hung about 14 inches above a table using two aluminum columns attached to a base. Two paper plates were positioned on each end of the wire to prevent mice from moving to the columns. The mouse was placed in the center of the wire, and a cage with bedding was placed below the mouse to provide a cushioned landing area. For each

mouse, the time from placement on the wire to falling was measured for three successful trials. Mice that remained on the wire for 90 s or longer were removed from the wire, and their time to fall was counted as 90 s. Additionally, trials in which mice fell instantly after placement on the wire were not counted as successful, and the trial was repeated.

Tactile Prepulse Inhibition (PPI) assay

Control and *TrkB*^{cKO} Mice were subjected to the tactile inhibition assay, a measure of hairy skin sensitivity, as described (Orefice et al., 2016).

Sunflower seed handling measurements

Sunflower seed habituation in home cages: One week prior to testing animals were habituated to black oil sunflower seeds, Bio-Serv, S5137-1, Wagner's, 76025, in their home cage by adding one to two tablespoons of seeds to the floor of the cage for five consecutive days. If animals did not recognize seeds as a food source a teaspoon of seeds were cracked before adding to the cage floor.

Behavior chamber habituation and handling two days prior to sunflower seed testing: Animals were habituated to behavior room environment and investigator handling by undergoing tail inking on habituation day 1. To ink the tail, each animal was gently lifted and placed on the cage wire food hopper facing away from investigator. Firmly holding the tail midway from the tail base, a blue permanent soy ink marker was rolled across the tail forming parallel lines to indicate identifying ear notch number. Once inked animals were gently transferred back into the home cage to await test chamber habituation.

The test chamber was constructed of a black matte acrylic wall and three optically clear walls, 10in(l) x 8in(w) x 8in(h), 0.25 in thick, centered on a white matte acrylic floor under diffuse warm white light (2700K). Three digital USB 2.0 CMOS video cameras mounted on camera sliders were positioned on

each clear side of the test chambers. One additional overview camera was mounted directly above the test chamber.

Assay and behavioral measurements: Seeds were withheld from the home cage for two days prior to and during testing to encourage foraging and seed eating in the test chamber. During habituation day 1 and day 2, animals were removed from the home cage and placed in an empty test chamber resting on the white matte acrylic floor. Each animal was given 2-3 seeds while freely exploring the test chamber for 20 minutes. Following the free exploration period animals were returned to their home cages. On testing day 3, animals were transferred from their home cage and placed in the test chamber and allowed to explore the chamber for 5 minutes. Following acclimation, 2-3 seeds were placed on the floor of the test chamber and the seed eating activity was recorded. At the completion of the test, animals were removed from the test chamber and returned to their home cage. Chambers were reset and cleaned with unscented soapy water, wiped down with distilled water, and dried. Animals that failed to eat seeds after 20 minutes were returned to their home cage and the test was rescheduled. This approach was repeated until each animal fully deshelled and consumed multiple seeds. Seeds that were partially shelled, partially consumed, or discarded were not counted. Behaviors were measured by defined seed deshelling/eating actions: 1. Seed peeling/deshelling – the act of grasping/holding the sunflower seed between the forepaws, clamping the upper and lower incisors into the shell surface and applying downward force (dip) that pushed the shell away from the head/teeth towards the floor. This action resulted in a systematic peeling of the shell to expose the seed kernel. Animals unable to maintain a firm grip on or fully grasp the shell would typically adapt by touching, tapping, resting and/or bracing the seed against the floor between the forepaws. Animals also “tucked” the shell against their abdomen, holding the shell between the forepaws, clamping their upper and lower incisors onto the shell surface pulling their heads backwards away from the shell/forepaws to peel off sections of the shell exposing the seed kernel. 2. Touch/Taps - the act of touching and/or holding and/or bracing the seed shell between the forepaws and the floor during seed peeling. 3. Dip – the act of holding the seed shell between forepaws, clamping shell between incisors and applying downward force to peel off sections of shell. 4. Rotate – the act of or ability to change and/or manipulate shell orientation within the forepaws. 5. Rocking – the act of grasping the shell between the

forepaws with shell firmly between incisors, using forepaws to “rock” shell side-to-side between incisors to bite into the shell to peel and expose the seed kernel.

RESOURCES TABLE for Sunflower seed assay

REAGENT or RESOURCE	SOURCE	IDENTIFIER
GRAPHPAD Prism 8	GraphPad Software 7825 Fay Avenue, Suite 230 La Jolla, CA 92037 USA Phone: 858-454-5577 Fax: 858-454-4150 sales@graphpad.com support@graphpad.com	
IC Capture Video Acquisition Software	The Imaging Source, LLC Suite 400 6926 Shannon Willow Rd Charlotte, NC 28226 United States Phone: 704-370-0110 https://www.theimagesource.com/	
Stoelting Digital USB 2.0 CMOS Camera	Stoelting Co. 620 Wheat Lane, Wood Dale, IL 60191 T: 630.860.9700 F: 630.860.9775 E: info@stoeltingco.com	Camera: 60516 Vari-focal, 2.8-12mm Lens: 60528

	www.stoeltingco.com	
Bio-Serv Black Oil Sunflower Seeds	Bio-Serv 3 Foster Lane Flemington, NJ 08822 US Phone: 800-996-9908 https://www.bio-serv.com/	S5137-1
Wagner's Four Season Oil Sunflower Seed	Wagner's, LLC P.O. Box 54 Jericho, N.Y. 11753 Phone: 516-933-6580 Fax: 516-933-6581 info@wagners.com	76025
Sunflower Seed Test Chamber Black Matte, Optically Clear Acrylic 0.25in, 10in(l) x 8in(w) x 8in(h)	Altec Plastics Inc. 116 B Street South Boston, MA 02127 617.269.1400 info@altecplastics.com https://shop.altecplastics.com/	
Sunflower Seed Floor, White Matte Acrylic 0.25in 36in(l) x 26in(w)	Altec Plastics Inc. 116 B Street South Boston, MA 02127 617.269.1400 info@altecplastics.com https://shop.altecplastics.com/	

Gait analysis

A recording setup based on a modified design of LocoMouse (Machado et al., 2015) was built for high speed, automated analysis of mouse locomotion behavior. The dimensions of the transparent corridor used were 64.5 (L) x 4 (W) x 6 (H) cm. Dark enclosures were situated on both ends of the corridor and the animal freely moved between the two ends. Acquisition were triggered by infrared sensors during each epoch of corridor crossing. Two mirrors angled at 48 degrees downward flanked the longitudinal axis of the corridor, which projected the side views of the animal to a camera below. A single high-speed camera (Bonito CL-400B/C 2320 x 700 pixels, Allied Vision, Exton, PA.) captured simultaneous videos of the bottom view and two side views of the animal at 200 fps. Videos of the animal were compressed and analyzed offline using a convolutional neural network for postural tracking written in PyTorch and MATLAB (Mathworks, Natick, MA). Briefly, an hourglass network based on Newell et al. (2016) was trained on 1000 expert annotated frames to simultaneously recognize the following body parts in the bottom and side views: nose, start and end of the tail, forepaws and hind paws. The positions of body parts from all three perspectives were combined to generate a three-dimensional postural time series. A hidden Markov model was used to infer the start and the end of each gait cycle based on paw velocity. The following parameters are measured for each gait cycle: velocity, height, tail elevation, hind paw width, cadence, stride length, paw width, stand duration, vertical and horizontal tail oscillation. A linear mixed effect model of the form Y ~ Intercept + Genotype + Sex + Genotype:Sex+ (1|Name) and ANOVA was used for statistical testing. In the case where velocity is considered as an independent variable, a model of the form Y ~ Intercept + Velocity + Genotype + Sex + Genotype:Sex + Velocity:Genotype + Velocity:Sex + (1|Name) was used instead.

Electron Microscopy

Forepaw toe pads (ages P21-P39) were excised and immersed in a glutaraldehyde/formaldehyde fixative for 1 hour at room temperature, further dissected, and subsequently fixed overnight at 4 °C. Sample preparation was done as previously described (Zhang et al., 2019). Ultrathin sections were cut at 40-60

nm and imaged using a JEOL 1200EX transmission electron microscope at 80 kV accelerating voltage. Images were cropped and adjusted with normalization to enhance contrast using Fiji/ImageJ. For corpuscles that were larger than the imaging field, montage of images was generated using TrakEM2 (Cardona et al., 2012). Only sections close to the center of Meissner corpuscles were included for quantification. Axons that did not have apparent lamellar wrappings were not included. Two researchers, not involved in EM data collection and blind to genotypes, independently counted the number of lamellar wrappings around designated axons. The counts from both researchers were averaged for final analysis. Differences in lamellar wrapping counts per axon between these two researchers ranged from 0 to 5 wrappings.

Modeling

To find the mutual information between point stimulus location and neural population response, we assumed K possible point stimulus locations, denoted s, where each of them is equally likely to occur, that is, $p(s) = 1/K$ for all s. Furthermore, we assumed M ($\leq K$) distinct neural population responses, denoted r, where response $r = m$ corresponds to n_m different point stimulus locations. Some locations might not have tactile receptors, such that $L = \sum_{m=1}^{M} n_m \leq K$. Overall, the set $\{n_1, \dots, n_M\}$ determines the efficiency with which neural population responses encode tactile location.

To find the mutual information between point stimulus location s and neural population response r, we use $\mathrm{MI}(s; r) = \mathrm{H}(s) - \mathrm{H}(s|r)$, where $\mathrm{H}(s)$ is the entropy of stimulus locations, and $\mathrm{H}(s|r)$ is the conditional entropy, conditioned on a particular population response. Due to the uniform stimulus location distribution, we have $\mathrm{H}(s) = \log_2 K$. To find the conditional entropy, we observe that $p(s|r = m) = 1/n_m$ for all locations s that yield population response $r = m$, and $p(s|r = m) = 0$ otherwise. This results in

$$\mathrm{H}(s|r) = -\sum_s p(s) \sum_{m=1}^{M} p(s|r = m) \log_2 p(s|r = m) = -\sum_{m=1}^{M} \frac{n_m}{K} \log_2 \frac{1}{n_m},$$

where we have used the fact that each stimulus location corresponds to at most one population response. Overall, this yields the mutual information:

$$\mathrm{MI}(s;r) = \log_2 K + \sum_{m=1}^{M} \frac{n_m}{K} \log_2 \frac{1}{n_m}.$$

In this expression, n_m/K is the overall fraction of stimulus locations that evoke population response $r = m$, and $1/n_m$ is the probability of each stimulus location given this response.

To find the set $\{n_1, \ldots, n_M\}$ that maximizes the mutual information, we define the column vector $\vec{n} = (n_1, \ldots, n_M)^T$ and write the mutual information in vector form, $\mathrm{MI}(s;r) = \log_2 K + K^{-1}\vec{n}^T \log_2 \ 1/\vec{n}$, where the last division is element-wise. We can then perform a constraint optimization on $\vec{n}$ with constraint $\vec{1}^T\vec{n} = L$, resulting in $n_m^* = L/M$ for all m. Thus, optimal coding (under the above assumptions) distributes the population responses evenly across stimulus locations. Furthermore, the mutual information increases with L, such that it is maximized if all stimulus locations yield a neural response (i.e., there are no gaps in the receptive fields), when $L^* = K$. Under these circumstances, the mutual information becomes $\mathrm{MI}(s;r) = \log_2 M$, providing an upper bound.

For non-overlapped, square receptive fields, the number of distinct population responses M equals the number of neurons N. If these receptive fields tile the whole stimulus space evenly, then the associated mutual information is $\mathrm{MI}(s;r) = \log_2 N$. As the number of discriminable spaces is $2^{MI(s;r)} = N$, the number of efficiently discriminable spaces per neuron is $2^{MI(s;r)}/N = 1$.

For overlapped, square receptive fields, each stimulus location within the receptive field of two distinct neurons results in a distinct neural population response. Two non-overlapped layers with $N/2$ equally sized square receptive fields that are offset against each other result in $4(N/2) = 2N$ distinct population responses (ignoring boundary effects, which become negligible for large N). These responses evenly tile

the stimulus space if the offset is maximized, in which case $\mathrm{MI}(s;r) = \log_2 2N$. This results the number of efficiently discriminable space per neuron to be given by $2^{MI(s;r)}/N = 2$.

The two-point discrimination capability of square receptive fields was modeled by imagining a point stimulus presented to the center of a discriminable space and a circle of points presented at some distance d from the central point. The central point and the shifted point were presented asynchronously. For a given d, the fraction of the circle's circumference that extended outside the central discriminable space into a new discriminable space was considered the percent correct (i.e. the percentage of points unambiguously distinguishable from the central point). For non-overlapped squares with side length s and with a central point presented within a single square:

$$\%\ \text{correct} = \begin{cases} 0, & d \le \frac{s}{2} \\ 100\frac{4}{\pi}\cos^{-1}\frac{s}{2d}, & \frac{s}{2} < d \le \frac{s}{\sqrt{2}} \\ 100, & d < \frac{s}{\sqrt{2}} \end{cases}.$$

For overlapped squares with side length $\sqrt{2}s$ and with a central point presented within a discriminable space:

$$\%\ \text{correct} = \begin{cases} 0, & d \le \frac{s}{2\sqrt{2}} \\ 100\frac{4}{\pi}\cos^{-1}\frac{s}{2\sqrt{2}d}, & \frac{s}{2\sqrt{2}} < d \le \frac{s}{2} \\ 100, & d < \frac{s}{2} \end{cases}.$$

To model irregular and variable receptive fields, images of overlapped and non-overlapped Voronoi tessellations were generated in MATLAB using the voronoi function. The image set consisted of 4000 tessellations seeded with 84-101 random points in a square window. Number of neurons, N, for a single tessellation was the number of seeded points forming Voronoi cells that were within the window. Pairs of tessellations were overlapped to create 2000 overlapped mosaics with number of neurons equal to the

combined number of neurons in the overlaid pairs. Mutual information between neural responses r and stimuli s was defined as above:

$$MI(s;r) = H(s) - H(s|r) = \log_2 K + \sum_{m=1}^{M} \frac{n_m}{K} \log_2 \frac{1}{n_m}$$

where K is the total number of pixels and n_m are the number of pixels per discriminable space. Mutual information was normalized by the number of neurons ($2^{MI}/N$). The difference between overlapped and non-overlapped Voronoi tessellations was determined to be statistically significant using 5000 bootstrap samples, each consisting of a randomly chosen pair from the 2000 overlapped tessellations and 2000 non-overlapped tessellations.

Chapter 5. Ultrastructures of Cutaneous Tactile End Organs and Their Functional Implications

Song Pang and C. Shan Xu performed X-ray μCT and FIB-SEM imaging and aligned the image volumes using SIFT. Harald Hess supervised the collection of the guard hair follicle FIB-SEM image volume. Annie Handler and Stuart Cattel contributed to EM sample preparations, TEM experiments, and manual reconstructions. Tri Nguyen performed the automatic reconstructions of the FIB-SEM volumes. Wei-Chung Lee supervised the automatic reconstruction experiments. Katelyn Comeau and Shan Meltzer performed the plexin D1 immunohistochemistry experiment.

High-resolution 3-D reconstructions of cutaneous tactile end organs revealed conserved ultrastructural features

To comprehensively characterize the ultrastructural features of cutaneous tactile end organs that include guard hair follicles, Meissner corpuscles, and Pacinian corpuscles, we sought to conduct 3-D EM reconstructions of them. Given the relatively small size of these end organs and the intricate ultrastructural features they contain, focused ion beam-scanning electron microscopy (FIB-SEM) is the ideal choice due to its exceptional isotropic resolution and image alignment (Xu et al., 2017).

We chose to characterize the guard hair follicle due to its prominent length and important role in hairy skin somatosensation (Zimmerman et al., 2014). Guard hair follicles from the back hairy skin of P21 animals were isolated by trimming away surrounding hairs, and skin samples that contain single guard hair follicles were cut out and fixed. For the EM preparation, we first started by trying the rOTO protocol described in Hua et al. (2015). While staining appeared to be uniform as determined using μCT (data not shown), upon FIB-SEM imaging prominent artifacts predominantly in mitochondria were observed (**Supplementary Fig. 5.1a**). These artifacts were asymmetric along the z-axis (**Supplementary Fig. 5.1b**) and therefore likely occurred during the FIB milling process. This in addition to the subsequent TEM analysis of the sample (data not shown) led us to hypothesize that these artifacts were caused by poor resin infiltration of the sample, especially due to the existence of the epidermis as a diffusion barrier, the

heavy metal impregnation resulted from rOTO staining, and the high viscosity of the Durcupan resin needed for FIB-SEM imaging (Xu et al., 2017).

Therefore, we instead used a staining protocol that leads to less metal impregnation, a modified Knott et al. (2008) protocol (Xu et al., 2017). With µCT we were able to identify the guard hair by its prominent size, observe both the lanceolate complexes (**Fig. 5.1a**) and the circumferential complexes (**Fig. 5.1b**), and select a precise ROI for FIB-SEM imaging (**Fig. 5.1c**). We then imaged a volume of ~ 80 µm x 80 µm x 78 µm at 6 nm voxel size. The volume was first aligned pairwise using scale-invariant feature transform (SIFT) (Xu et al., 2017), but while images were well aligned locally, a global misalignment existed (**Fig. 5.2a**) when compared with the µCT volume (**Fig. 5.2b**). This is a well-known issue with the SIFT algorithm, which has a bias toward feature-rich regions. On the other hand, global image volume alignment algorithms such as elastix (Klein et al., 2010; Shamonin et al., 2013) have been developed, but they could introduce undesired distortions with imperfect elastic alignments and do not handle large volumes well because full volumes need to be loaded into the memory. Therefore, we devised a pipeline for correcting global alignment errors in SIFT-aligned FIB-SEM volumes. We used µCT volumes as the template and elastix to generate the initial global alignment with downsampled SIFT-aligned FIB-SEM images. Subsequently, the geometric center of each slice in the SIFT-aligned FIB-SEM volume was used to calculate the correct displacement for a translation-only alignment, given the unique advantages of blockface methods. This pipeline generated a locally and globally well aligned volume (**Fig. 5.2c**) without erroneous elastic deformations, and is scalable and generalizable to other blockface methods.

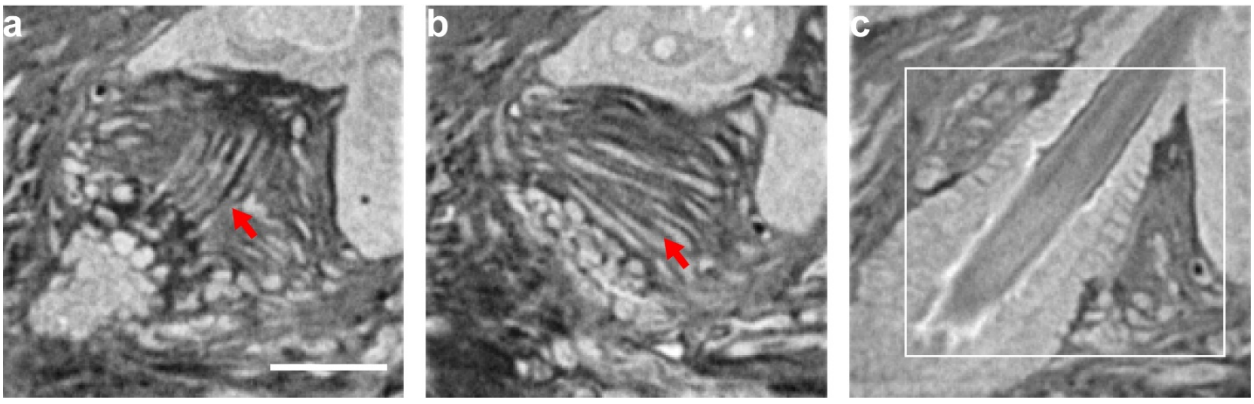

Figure 5.1. µCT volume of the guard hair follicle sample

(**a**) µCT image showing lanceolate complexes (arrow).

(**b**) µCT image showing circumferential complexes (arrow).

(**c**) Imaging ROI for FIB-SEM outlined in white.

Scale bar: 30 µm.

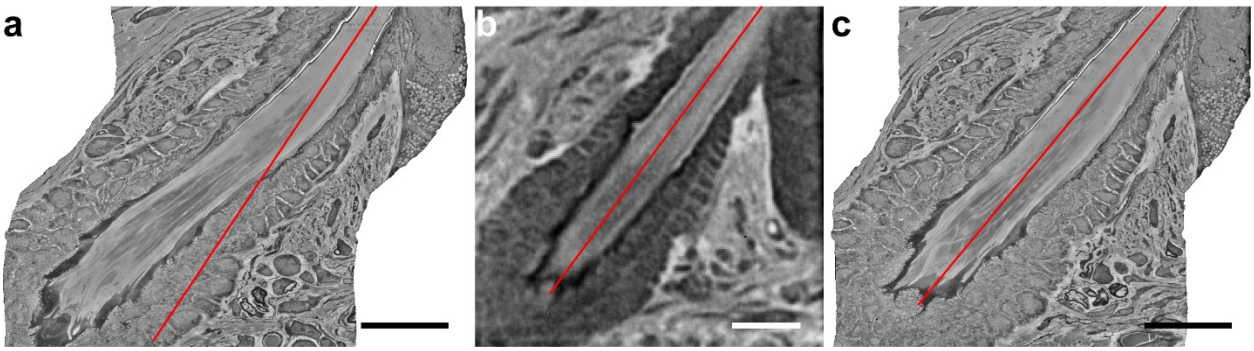

Figure 5.2. Correction of global alignment errors

(**a**) Resliced pairwise SIFT-aligned FIB-SEM volume. While local alignment is accurate, drifts accumulate globally causing noticeable distortion, which can be observed from the erroneously “bent” hair shaft. It is impossible to fully prevent globally accumulated alignment errors with pairwise alignment.

(**b**) µCT section around the same location as the ground truth for global alignment and comparison.

(**c**) Resliced FIB-SEM volume with global alignment correction. Global alignment errors were largely reduced without introducing local alignment errors or elastic distortions.

Lines parallel to the top of the hair shaft in these volumes were added to aid visualization of global alignment quality.

Scale bar: 20 µm.

It has been previously reported only Aβ RA-LTMRs form lanceolate endings around guard hairs (Li et al., 2011). This is further supported by the presence of neurofilaments in these lanceolate endings in the FIB-SEM volume. Upon inspecting the guard hair follicle volume in detail, we made a few striking observations for the lanceolate endings. We noticed that in the terminal Schwann cell (TSC) processes in the lanceolate endings, there were virtually no vesicles and most membrane-enclosed spaces (>95%) at

any given plane were connected with the extracellular space, and were therefore caveolae (**Fig. 5.3a**). These caveolae appeared to be relatively uniform and stable in morphology, suggesting that they were not being actively endocytosed, contrary to what have been reported in other cell types (Andreone et al., 2017; Sadeghian et al., 2018). It is possible that whether caveolae serve endocytic functions depends on the subcellular localization, as we observed more complex morphologies of caveolar networks around the somata of TSCs, with some of them highly suggestive of endocytosis (**Fig. 5.3b**). This result suggests that caveolae may be differentially regulated depending on their subcellular localizations and may serve different functions, such as mechanical buffering in the TSC processes vs. endocytosis in other cell types.

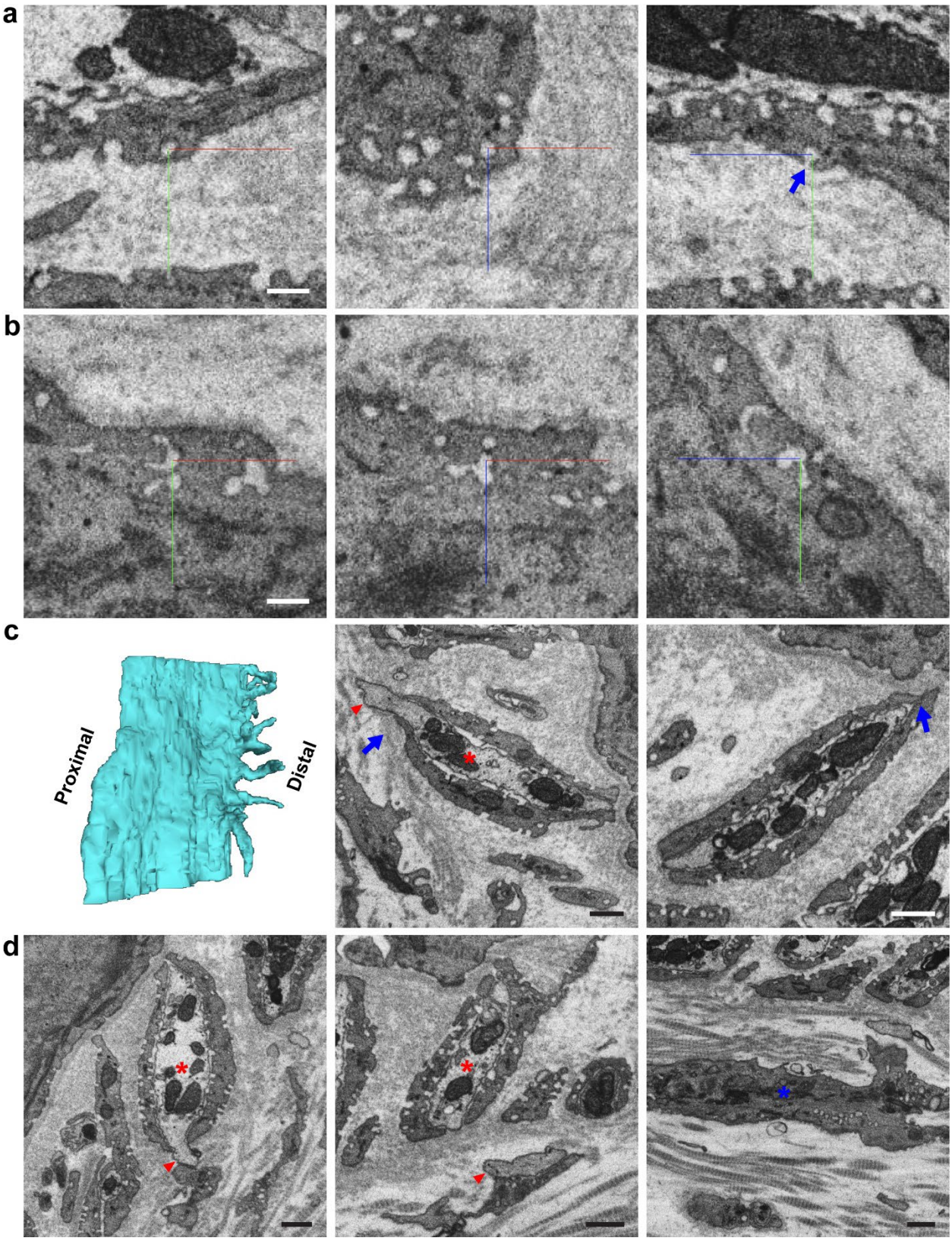

Figure 5.3. Ultrastructural features of lanceolate endings

(**a**) Orthogonal views of a caveola in a TSC process. While it appears to be a membrane-enclosed space when looking at both the xy- and the xz-planes, when looking at the yz-plane it is clear that it opens to the extracellular space (arrow). Based on similar observations, we determined that >95% of other similar-looking profiles in TSCs are also caveolae.
(**b**) Orthogonal views of a caveolar network in a TSC soma. This type of profiles appears to be formed by fusion of multiple caveolae, and they can extend fairly far away from the membrane into the cytoplasm. Caveolar networks were observed much more frequently in TSC somata compared to TSC processes.
(**c**) (Left) 3-D rendering of a stretch of a lanceolate axon, with proximal side to the left and the distal side to the right. Many axonal protrusions are present on the distal side, while none are present on the proximal side. (Middle) Example of an axonal protrusion on the distal side (arrowhead) of a lanceolate ending (asterisk). This axonal protrusion crosses the boundary between the longitudinal collagen fibers and the circumferential collagen fibers (arrow). (Right) Example of a closed gap formed by TSC processes (arrow). These two TSC processes form an open gap in other sections in the volume.
(**d**) (Left and Middle) Examples of axonal protrusions (arrowheads) of lanceolate endings (asterisks) forming contacts with CSCs. This type of contacts can sometimes be fairly extensive, such as the example in the middle panel. (Right) Example of a CSC profile (asterisk). Dark cytoplasm and caveolae are present in CSCs, and they are ultrastructurally indistinguishable from TSCs.
Left panel in **c** is from the test data set shown in **Supplementary Fig. 5.1**.
Scale bars: **a, b**: 0.2 µm, **c, d**: 0.5 µm.

In addition, we noticed numerous long axonal protrusions that extend through the openings of TSC processes on the distal side away from the hair shaft (**Fig. 5.3c**). These axonal protrusions frequently extend into the circumferential collagen region, crossing the boundary between longitudinal and circumferential collagen regions (**Fig. 5.3c**). Given the different collagen fiber orientations, these two regions may filter mechanical forces differently (Bai et al., 2015), and therefore these axonal protrusions may be optimally positioned to sense the shearing stress at the interface between these regions. We hypothesize that these axonal protrusions are sites of activation of mechanosensitive ion channels, such as Piezo2, when mechanical forces are applied to the hairy skin. Interestingly, such axonal protrusions

were not observed on the proximal side, close to the hair shaft (**Fig. 5.3c**), although we did occasionally observe opening and closing of gaps between TSC processes, consistent with a previous report (Li and Ginty, 2014). However, it appears that mouse guard hair afferents have different ultrastructures from rat whisker afferents, where axonal protrusions were seen on both sides (Takahashi-Iwanaga, 2000). Another intriguing feature we noticed is that these axonal protrusions regularly come into contact with non-neuronal cells in the circumferential collagen region (**Fig. 5.3d**). These non-neuronal cells are not the TSCs that surround circumferential axon terminals, although they are ultrastructurally similar to TSCs as they contain dark cytoplasm and an abundance of caveolae (**Fig. 5.3d**). We termed these cells circumferential support cells (CSCs) to reflect the distinction from TSCs. These regular contacts may serve as locations where lanceolate axonal protrusions anchor and receive structural support.

Lastly, we observed that circumferential endings are quite similar to lanceolate endings in a broad sense, except oriented orthogonally. TSCs also ensheathe the circumferential axon fibers, although occasionally large regions of axon terminals naked to the collagen matrix were seen (**Fig. 5.4a**). Axonal protrusions are present, albeit less extensive and at much lower frequency compared to the lanceolate endings (**Fig. 5.4b**). Axon branching can also be seen at certain locations (**Fig. 5.4c**), indicating that some circumferential axons wrap around the hair follicle in a mixed clockwise and counterclockwise manner with no asymmetry.

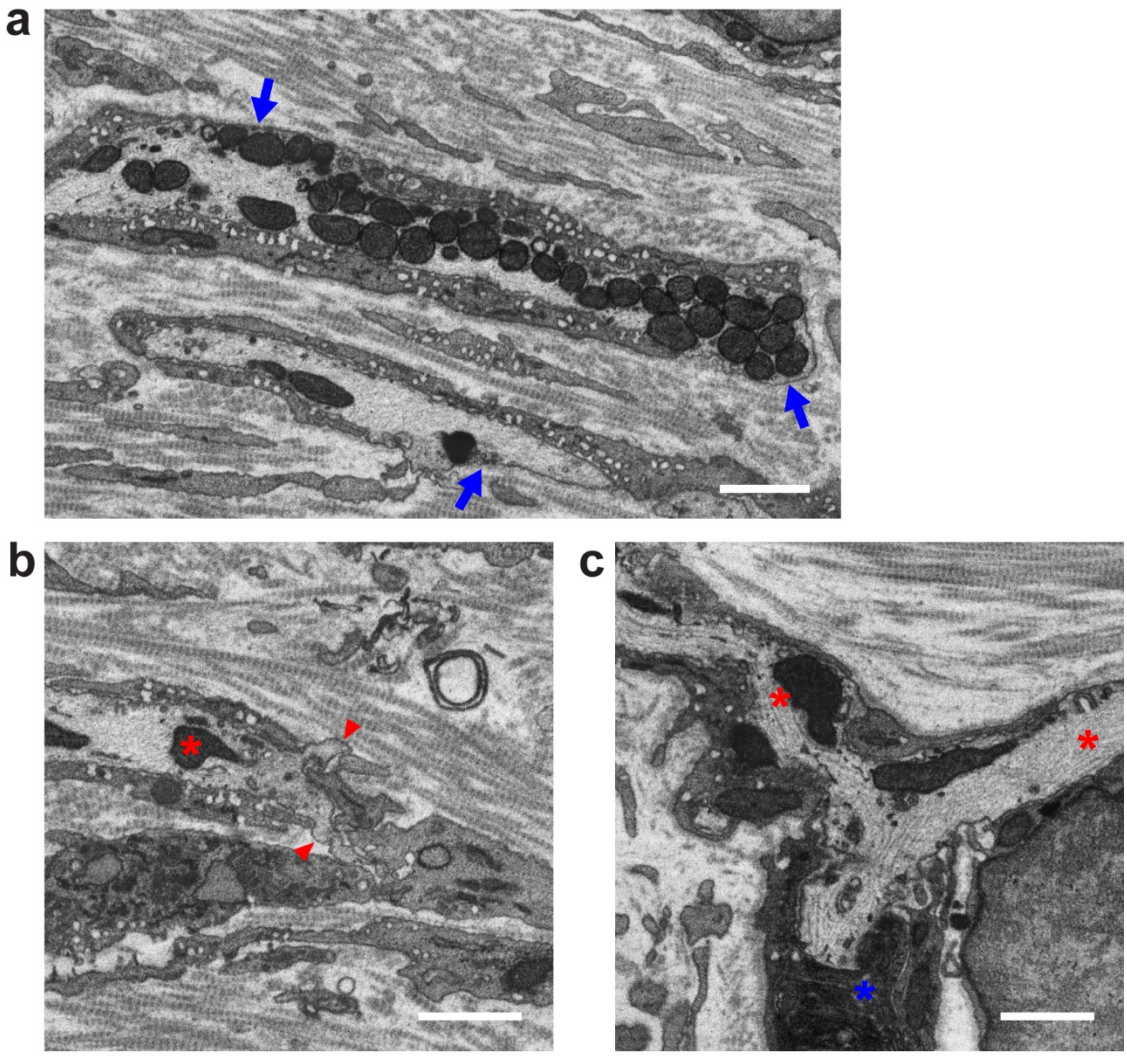

Figure 5.4. Ultrastructural features of circumferential endings

(**a**) EM image of circumferential endings. Circumferential endings are also ensheathed by TSC processes. However, unlike lanceolate endings, large portions of circumferential endings are exposed to the collagen matrix (arrows).

(**b**) Example of axonal protrusions (arrowheads) of a circumferential ending (asterisk). These axonal protrusions are less prominent compared to lanceolate endings, and occur much less frequently.

(**c**) Example of branching of circumferential endings. This myelinated axon sheds its myelin (blue asterisk), and branches in two to wrap around the hair follicle in two opposite directions (red asterisks). Scale bars: 1 μm.

Previous reports suggest that two types circumferential afferents are present around hair follicles: Aβ field-LTMR (Bai et al., 2015) and Aδ Circ-HTMR (Ghitani et al., 2017), and therefore we sought to ultrastructurally identify different cell types using genetic EM labeling (Zhang et al., 2019). We used *Ntrk3*^{CreER}*; ROSA26*$^{LSL\text{-}Matrix\text{-}dAPEX2}$ to label Aβ field-LTMRs (Bai et al., 2015) (**Fig. 5.5a**), and Tg(Calca-Flpe)*; ROSA26*$^{FSF\text{-}Matrix\text{-}dAPEX2}$ to label Aδ Circ-HTMRs (Ghitani et al., 2017) (**Fig. 5.5b**). Two ultrastructural differences were noted: 1) Aβ field-LTMRs have neurofilaments inside their axons (**Fig. 5.5a**), while Aδ Circ-HTMRs do not (**Fig. 5.5b**); 2) Aβ field-LTMRs tend to be larger in diameter than Aδ Circ-HTMRs (**Fig. 5.5**). These two ultrastructural distinctions will hopefully aid identification of these cell types in the FIB-SEM volume.

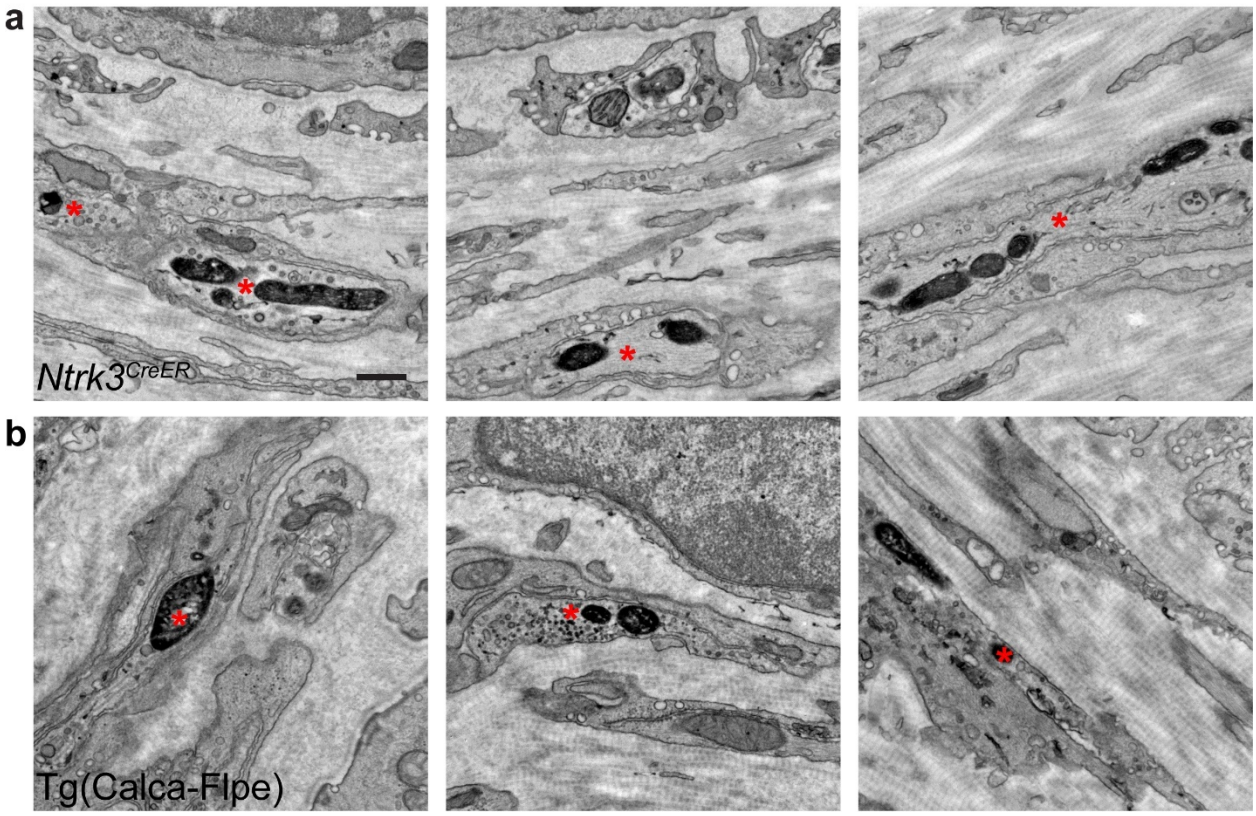

Figure 5.5. Ultrastructural differences between Aβ field-LTMRs and Aδ Circ-HTMRs

(**a**) EM image showing Aβ field-LTMRs (asterisks) from P26 *Ntrk3*^{CreER}*; ROSA26*$^{LSL\text{-}Matrix\text{-}dAPEX2}$ animals treated with 0.5 mg of TAM at P5. Abundant neurofilaments could be frequently observed in these profiles. n = 2 animals.

(**b**) EM image showing Aδ Circ-HTMRs (asterisks) from a P21 Tg(Calca-Flpe)*; ROSA26*$^{FSF\text{-}Matrix\text{-}dAPEX2}$ animal. Neurofilaments were never found in these profiles, and these profiles tend to be smaller in diameter than Aβ field-LTMRs shown in **a**. n = 1 animal.

Scale bar: 0.5 μm.

Additionally, co-staining of S100, which labels Schwann cells, and GFP in Tg(Plxnd1-EGFP)HF78 (Gong et al., 2003) hairy skin tissues revealed two molecularly distinct non-neuronal cell types in the circumferential collagen region (**Fig. 5.6a**), which are likely TSCs and CSCs, respectively. EM labeling with Tg(Plp1-CreER)3*; ROSA26*$^{LSL\text{-}Matrix\text{-}dAPEX2}$ also showed that only TSCs, and not CSCs, were labeled (**Fig. 5.6b**). These results strongly support the idea that TSCs and CSCs are of different developmental lineages, and CSCs may be homologous to capsule cells in Meissner corpuscles and intermediate layer cells in Pacinian corpuscles based on molecular signatures (data not shown) (Cobo et al., 2021).

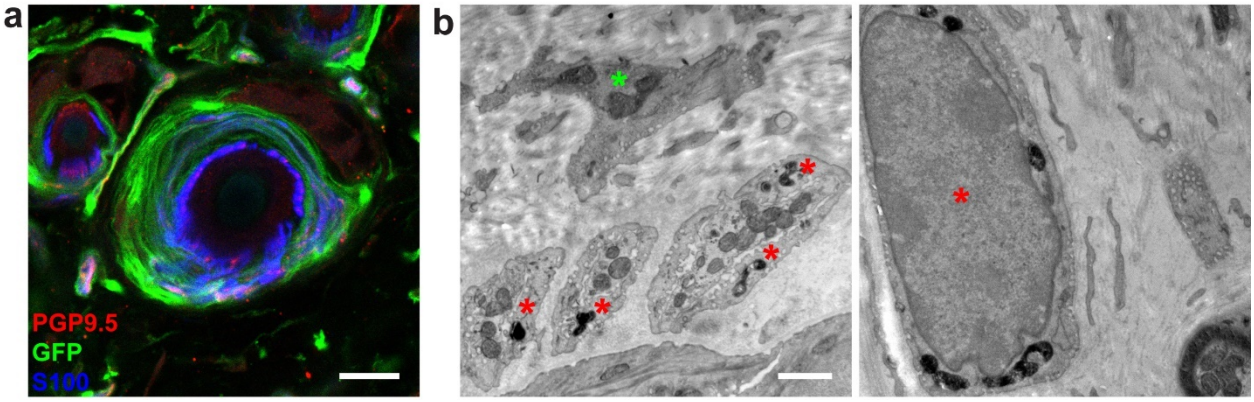

Figure 5.6. CSCs are a distinct cell type from TSCs

(**a**) Confocal image showing hair follicles in a P22 Tg(Plxnd1-EGFP)HF78 animal stained with immunohistochemistry. PGP9.5 labels all axons, GFP labels Plxnd1-EGFP^{+} cells, and S100 labels all Schwann cells, including TSCs. Based on morphology and labeling density, GFP and S100 likely label all non-neuronal cells in the circumferential collagen region. S100 signals are relatively sparse compared to GFP signals, and S100 signals tend to associate with PGP9.5 signals in the circumferential collagen region, suggesting that all S100 signals are from TSCs in this region. In addition, there is no overlap between GFP and S100 signals, indicating that CSCs are different from TSCs. n = 3 animals.

(**b**) EM images showing hair follicles in a P32 Tg(Plp1-CreER)3*; ROSA26*$^{LSL\text{-}Matrix\text{-}dAPEX2}$ animal treated with 1 mg of TAM P12-16. Labeled TSCs (red asterisks) in both the lanceolate collagen region (Left) and the circumferential collagen region (Right) could be observed. On the other hand, unlabeled non-neuronal profiles (green asterisk) in the circumferential collagen region were also frequently observed, which presumably correspond to CSCs. n = 1 animal.
Scale bars: **a**: 20 μm, **b**: 1 μm.

We were encouraged by the hair follicle volume and decided to pursue large-scale reconstruction of other cutaneous end organs. Given our previous results showing that two molecularly distinct Aβ-LTMRs can innervate individual Meissner corpuscles (Neubarth et al., 2020), we collected forepaw toe pad samples and imaged one corpuscle with one myelinated axon (Meissner corpuscle #1, **Fig. 5.7a,b**), and one with two myelinated axons (Meissner corpuscle #2, axon A and B, **Fig. 5.7c,d**) from P21 animals. Although these two corpuscles have different numbers of Aβ afferents, they have similar numbers of lamellar cells and capsule cells (Meissner #1: four lamellar cells, three capsule cells; Meissner #2: five lamellar cells, four capsule cells). Meissner #2 is ~50% larger than Meissner #1, however. Based on our previously characterized ultrastructural features of TrkB$^+$ vs. Ret$^+$ axons (Neubarth et al., 2020), we tentatively identified the Aβ axon in Meissner corpuscle #1 and Aβ axon A in Meissner corpuscle #2 to be TrkB$^+$ axons, and Aβ axon B in Meissner corpuscle #2 to be a Ret$^+$ axon. Presumptive TrkB$^+$ axons have more lamellar wrappings compared to the presumptive Ret$^+$ axon (**Fig. 5.8a,b**) and are located more centrally in the corpuscle, as previously described. Both types of Aβ axons have neurofilaments. In addition, we noticed that individual lamellar cells can form wrappings around both presumptive TrkB$^+$ and presumptive Ret$^+$ axons (**Fig. 5.8c**), indicating that there are no dedicated lamellar cells to each afferent subtype. Strikingly, we observed that these Meissner corpuscle Aβ afferents have prominent axonal protrusions (**Fig. 5.9**), similar to what we saw for lanceolate afferents that associate with the guard hair follicle. However, these Meissner Aβ afferent axonal protrusions can be rather exuberant and branch often, as seen in the presumptive TrkB$^+$ axon in Meissner corpuscle #1 (**Fig. 5.9a**) and the presumptive TrkB$^+$ axon in Meissner corpuscle #2 (**Fig. 5.9b,c**), more so than hair follicle lanceolate afferents. On the other hand, the presumptive Ret$^+$ axon in Meissner corpuscle #2 has protrusions that are somewhat less elaborate

than hair follicle lanceolate afferents (**Fig. 5.9d**). These ultrastructural differences may additionally contribute to the differences in response properties between the two Meissner Aβ afferent subtypes (Neubarth et al., 2020). Moreover, these axonal protrusions frequently extend beyond the initial lamellar wrappings and interact with outer wrappings (**Fig. 5.9e,f**). This suggests a mechanism for Aβ Meissner corpuscle afferents to enhance their vibrational sensitivity.

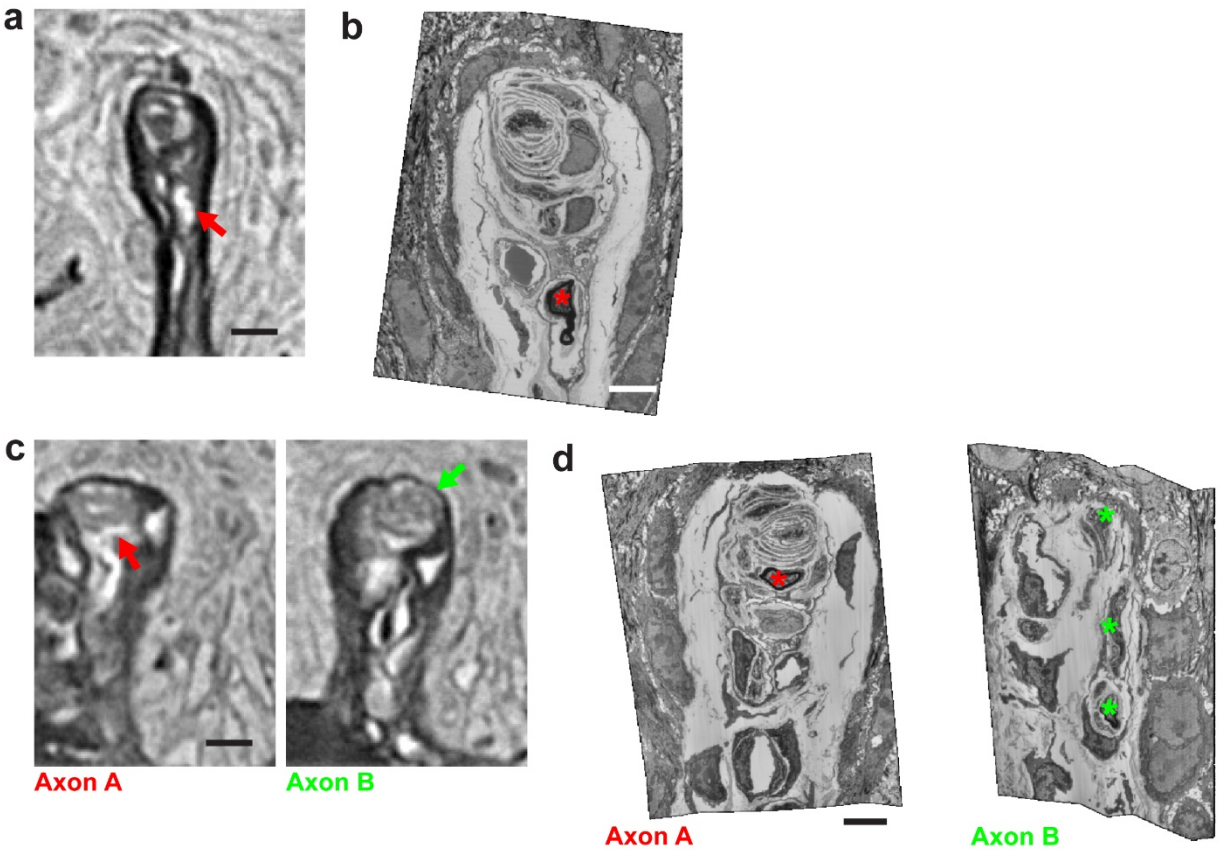

Figure 5.7. Overview of Meissner corpuscle volumes

(**a**) µCT image showing Meissner corpuscle #1. Dermal papilla and corpuscular structures could be clearly seen. The single myelinated axon innervating the corpuscle is labeled with an arrow.

(**b**) FIB-SEM image showing Meissner corpuscle #1. The single myelinated axon innervating the corpuscle is labeled with an asterisk.

(**c**) µCT images showing Meissner corpuscle #2. Two myelinated fibers innervating the corpuscle (axon A and B, red and green arrows, respectively) could be seen.

(**d**) FIB-SEM images showing Meissner corpuscle #2. Axon A and axon B are labeled with red and green asterisks, respectively.

Scale bars: **a, c**: 10 μm, **b, d**: 5 μm.

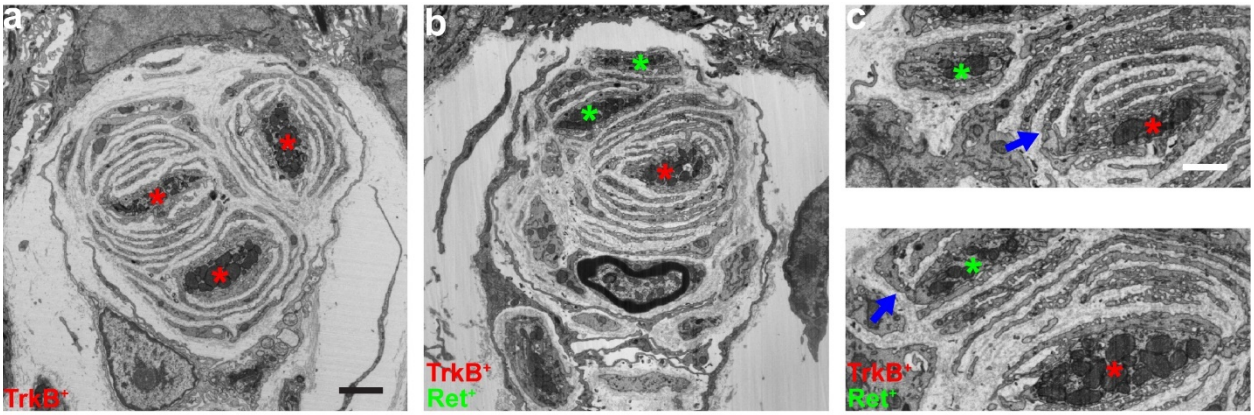

Figure 5.8. Identification of presumptive TrkB$^+$ and presumptive Ret$^+$ Aβ Meissner afferents

(**a**) FIB-SEM image showing Aβ axon terminals (asterisks) in Meissner corpuscle #1. The single Aβ axon has numerous lamellar wrappings, which is characteristic of TrkB$^+$ axons.

(**b**) FIB-SEM image showing Aβ axon terminals (asterisks) in Meissner corpuscle #2. The Aβ axon A (red asterisk) closer to the center has numerous lamellar wrappings, which is characteristic of TrkB$^+$ axons. On the other hand, the Aβ axon B (green asterisks) on the periphery has much fewer lamellar wrappings, which is characteristic of Ret$^+$ axons.

(**c**) FIB-SEM images showing lamellar wrappings around Aβ axon terminals (asterisks) in Meissner corpuscle #2. (Top) One lamellar cell was observed to form wrappings around a presumptive TrkB$^+$ axon terminal (red asterisk) and directly contact it (arrow). (Bottom) The same lamellar cell forms wrappings around a presumptive Ret$^+$ axon terminal (green asterisk) and also directly contacts it (arrow).

Scale bars: **a, b**: 2 μm, **c**: 1 μm.

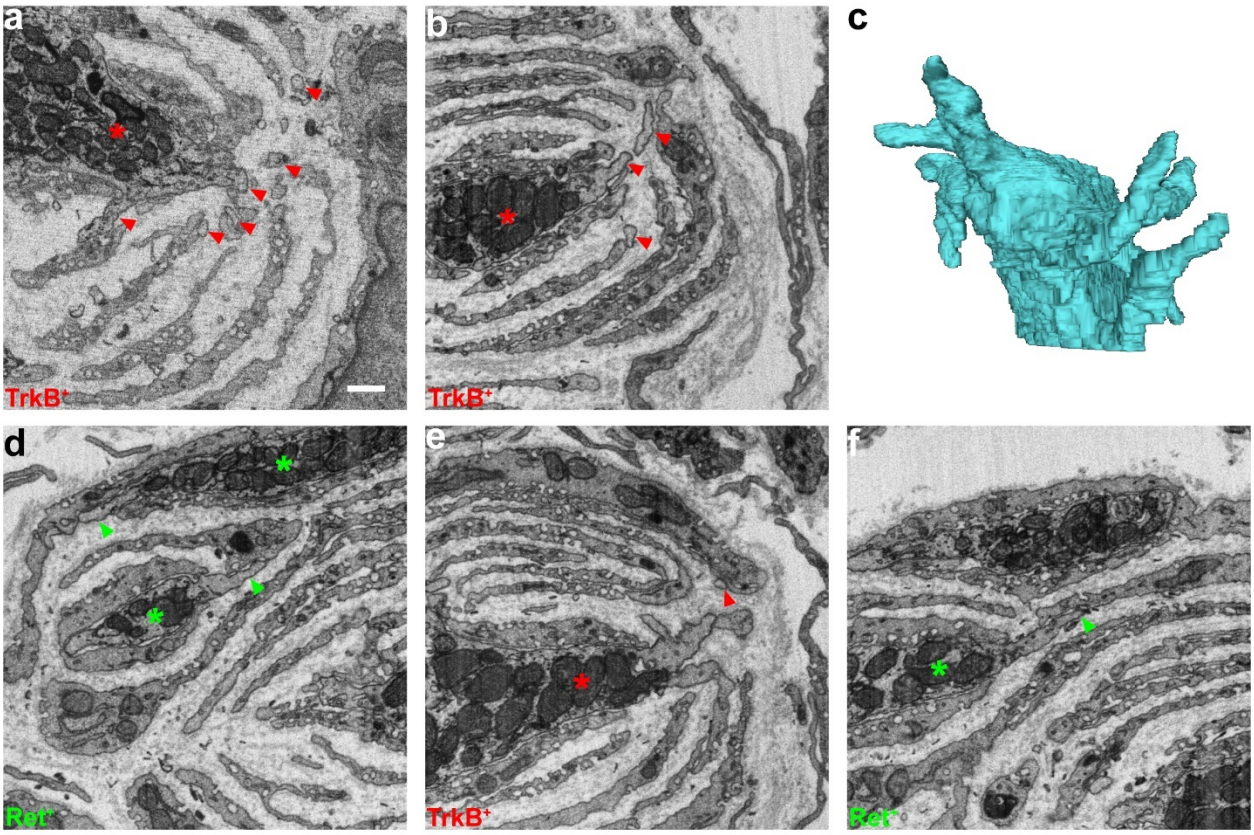

Figure 5.9. Axonal protrusions in presumptive TrkB$^+$ and presumptive Ret$^+$ Aβ Meissner afferents

(**a**) FIB-SEM image showing axonal protrusions (arrowheads) of the presumptive TrkB$^+$ Aβ Meissner afferent (asterisk) in Meissner #1. Many axonal protrusion profiles can be observed in this section, indicating that this axon forms many branches of protrusions.

(**b**) FIB-SEM image showing axonal protrusions (arrowheads) of the presumptive TrkB$^+$ Aβ Meissner afferent (asterisk) in Meissner #2. Similarly complex axonal protrusions are present.

(**c**) 3-D rendering of a portion of axonal protrusions of the presumptive TrkB$^+$ Aβ Meissner afferent in Meissner #2. Elaborate branching patterns can be observed in this axon, which are more complex than hair follicle lanceolate afferents.

(**d**) FIB-SEM image showing axonal protrusions (arrowheads) of the presumptive Ret$^+$ Aβ Meissner afferent (asterisk) in Meissner #2. These axonal protrusions are much simpler and rarely branch in comparison to presumptive TrkB$^+$ Aβ Meissner afferents.

(**e, f**) FIB-SEM image showing axonal protrusions (arrowheads) of the presumptive TrkB$^+$ Aβ Meissner afferent (**e**, asterisk) and the presumptive Ret$^+$ Aβ Meissner afferent (**f**, asterisk) in Meissner #2 forming

contacts with outer lamellar wrappings. These contacts are frequently observed throughout the Meissner corpuscle volumes.

Scale bar: 0.5 μm.

We also noticed that there appear to be dedicated lamellar cells for the heminode regions of Meissner Aβ afferents (**Fig. 5.10**). These lamellar cells have darker cytoplasm and nuclei than the other lamellar cells (**Fig. 5.10a-e**) and associate with the axons immediately after they shed their myelin (**Fig. 5.10f-h**), but do not contribute much if at all to lamellar wrappings in the center of the corpuscle. Therefore, there may be separate subtypes of lamellar cells that play different functional roles. This may be analogous to the previously reported distinction between type I and type II TSCs in hair follicles (Kaidoh and Inoue, 2008; Seguchi et al., 1989). Additionally, heminodes were previously reported to be barriers for Schwann cell growth at neuromuscular junctions and delineate Schwann cell territories (Brill et al., 2011).

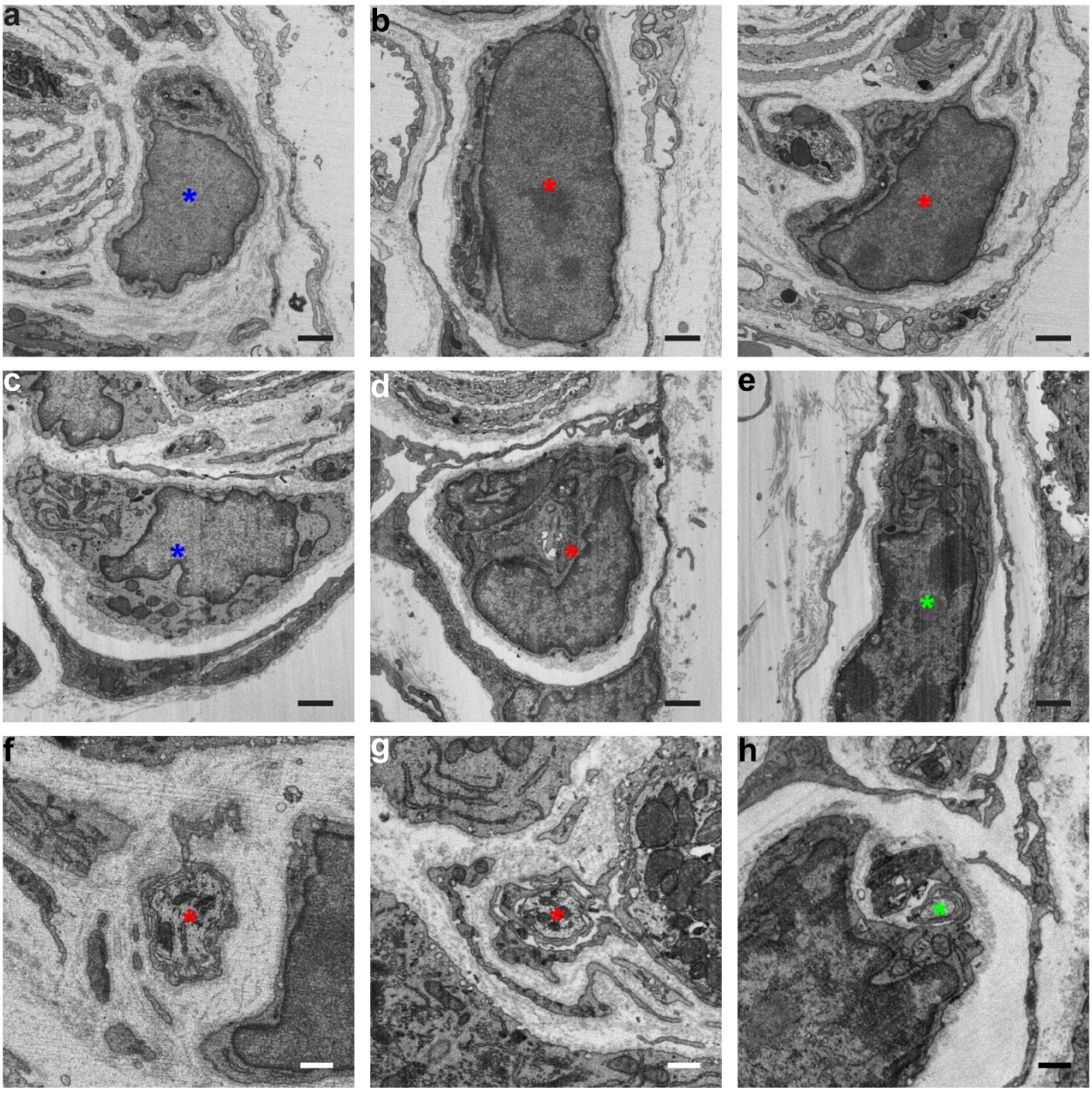

Figure 5.10. Lamellar cells at the heminode regions have distinct ultrastructural features

(**a**) FIB-SEM image showing a lamellar cell (asterisk) in the center of Meissner #1.

(**b**) FIB-SEM images showing two lamellar cells (asterisks) in the heminode region of the presumptive TrkB^{+} Aβ Meissner afferent in Meissner #1. The cytoplasm and nuclei are noticeably darker compared to the cell in **a**.

(**c**) FIB-SEM image showing a lamellar cell (asterisk) in the center of Meissner #2.

(**d**) FIB-SEM image showing the lamellar cell (asterisk) in the heminode region of the presumptive TrkB$^+$ Aβ Meissner afferent in Meissner #2. The cytoplasm and nucleus are noticeably darker compared to the cell in **c**.

(**e**) FIB-SEM image showing the lamellar cell (asterisk) in the heminode region of the presumptive Ret$^+$ Aβ Meissner afferent in Meissner #2. Similarly, the cytoplasm and nucleus are noticeably darker compared to the cell in **c**.

(**f-g**) FIB-SEM images showing Aβ Meissner afferents wrapped by the lamellar cells in **b, d, e** at the heminode regions. This type of lamellar wrapping occurs immediately after the axons lose their association with myelinating Schwann cells.

Scale bars: **a-e**: 1 μm, **f-h**: 0.5 μm.

Aside from Aβ fibers, we also found numerous fibers for which no myelination was observed in the volumes that innervate Meissner corpuscles; these may be Aδ- and/or C-fibers, consistent with a previous report (Pare et al., 2001). These fibers appear to have a variety of morphologies and extend into different regions of the corpuscle (**Fig. 5.11a,b**), in a manner similar to a previous report (Pare et al., 2001). They all associate with lamellar cells in the corpuscle, although lamellar cells do not extensively wrap around these afferents like the identified Aβ fibers (**Fig. 5.11a,b**). Future functional studies of these afferents using genetic tools such as mouse lines described by Sharma et al. (2020) will be of interest to investigate potential nociceptive roles of Meissner corpuscles. There appears to also be one axon for which no myelination was observed in the Meissner #2 volume yet with ultrastructural features highly similar to Ret$^+$ Aβ Meissner afferents, including moderate number of lamellar wrappings, high mitochondrial density, and presence of neurofilaments (**Fig. 5.11c**). In fact, it is not possible to tell this axon apart from the presumptive Ret$^+$ Aβ Meissner afferent discussed above based on local ultrastructural features alone. It may be that this axon sheds its myelin before it enters the volume, and it could even be a branch of the same presumptive Ret$^+$ Aβ Meissner afferent in the volume. Finally, there is one other axon for which no myelination was observed in the Meissner #2 volume with high mitochondrial density and presence of neurofilaments, which are characteristic of Aβ fibers, but this axon does not innervate the center of the Meissner corpuscle and does not have many lamellar wrappings

(**Fig. 5.11d**). This may be one of the Ret$^+$ Aβ afferents that have high thresholds and sustained responses (Neubarth et al., 2020), given its distinct ultrastructure from other Aβ Meissner afferents.

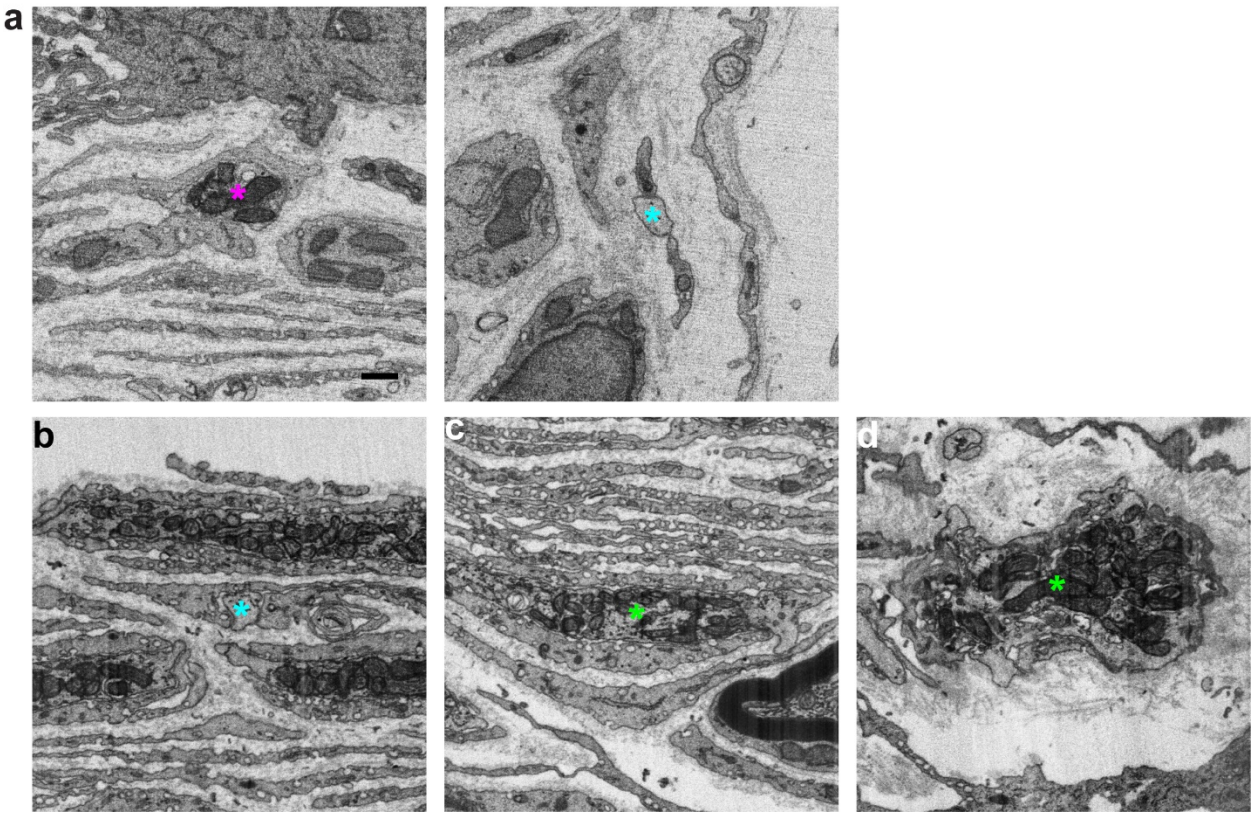

Figure 5.11. Axon fibers with no myelination observed in the volume

(**a**) FIB-SEM images showing two such axon profiles (asterisks) in Meissner #1. (Left) Axon with relatively high density of mitochondria (magenta asterisk), which is characteristic of Aδ-fibers. (Right) Axon with relatively low density of mitochondria and small diameter (cyan asterisk), which are characteristic of C-fibers. These two axon profiles do not have many lamellar wrappings.

(**b**) FIB-SEM image showing one such axon profile (cyan asterisk) in Meissner #2. This axon also has ultrastructural features similar to C-fibers. This axon profile does not have many lamellar wrappings.

(**c**) FIB-SEM image showing another such axon profile (green asterisk) in Meissner #2. This axon has ultrastructural features similar to Ret$^+$ Aβ Meissner afferents, including moderate number of lamellar wrappings, high density of mitochondria, and presence of neurofilaments.

(**d**) FIB-SEM image showing yet another such axon profile (green asterisk) in Meissner #2. This axon has ultrastructural features characteristic of Aβ afferents, including high density of mitochondria and presence of neurofilaments. However, it does not have many lamellar wrappings and does not innervate the center of the corpuscle.

Scale bar: 0.5 μm.

Finally, we have begun sample preparation for Pacinian corpuscles using P80 Tg(Plp1-EGFP)10 animals. We could use this preparation to clearly identify terminal and ultraterminal regions with μCT (**Fig. 5.12a**), and we therefore selected an ROI for FIB-SEM imaging. This sample is now in queue to be imaged. Meanwhile, we manually sectioned and imaged small volumes of the Pacinian corpuscle using TEM. Abundant neurofilaments and densely packed mitochondria were observed in the Pacinian Aβ afferent. Interestingly, while axonal protrusions in the terminal region are structurally simple (**Fig. 5.12b**), similar to those of hair follicle lanceolate afferents and presumptive Ret^+ Meissner afferents, those in the ultraterminal region are elaborate (**Fig. 5.12c**), similar to those of presumptive $TrkB^+$ Meissner afferents. This difference may confer different functional properties to the terminal region vs. the ultraterminal region. Interactions between axonal protrusions and lamellar wrappings were also occasionally seen in Pacinian corpuscles (**Fig. 5.12d**).

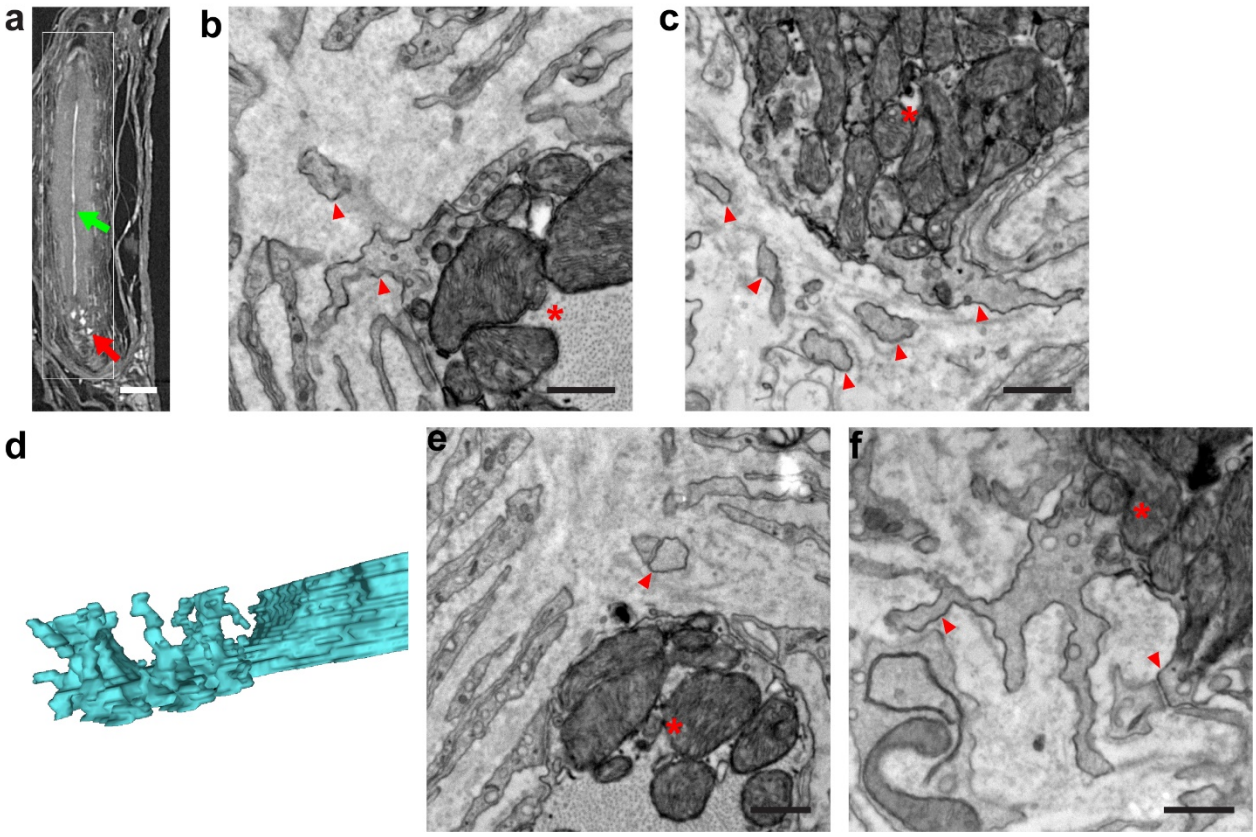

Figure 5.12. Pacinian corpuscle sample and axonal protrusions

(**a**) µCT image showing the Pacinian corpuscle sample. Both the terminal region (green arrow) and the ultraterminal region (red arrow) are clearly visible. Imaging ROI for FIB-SEM is outlined in white.

(**b**) EM image showing axonal protrusions (arrowheads) of the Pacinian axon (asterisk) in the terminal region. They are relatively simple in shape and reminiscent of axonal protrusions of hair follicle lanceolate afferents and presumptive Ret$^+$ Meissner afferents.

(**c**) EM image showing axonal protrusions (arrowheads) of the Pacinian axon (asterisk) in the ultraterminal region. These axonal protrusions are exuberant like those of presumptive TrkB$^+$ Meissner afferents.

(**d**) 3-D rendering of a portion of axonal protrusions of the Pacinian axon in the ultraterminal region. Extensive branching like in **Fig. 5.9c** can be observed.

(**e, f**) EM images showing axonal protrusions (arrowheads) of the Pacinian axon (asterisks) contacting lamellar cells in the terminal (**e**) and the ultraterminal region (**f**).

Scale bars: 0.5 µm.

Investigation of the role of caveolae in cutaneous tactile end organs

The prevalence of caveolae in tactile end organs, especially in non-myelinating Schwann cells, raises the question of what functions, if any, they have in mechanosensation. In order to gain insight into this question, we examined tissues from *Cav1*$^{-/-}$ animals, in which caveolae are largely absent (Razani et al., 2001). We observed a near complete loss of caveolae in both hair follicles (**Fig. 5.13a**) and Meissner corpuscles (**Fig. 5.13b**) of *Cav1*$^{-/-}$ animals. TSC ensheathment and lamellar wrappings remained intact (**Fig. 5.13**), indicating that non-myelinating Schwann cells can still associate with axons without caveolae. This manipulation allows us to study the functions of caveolae in tactile end organs and future electrophysiological recordings from knockout animals will be illuminating.

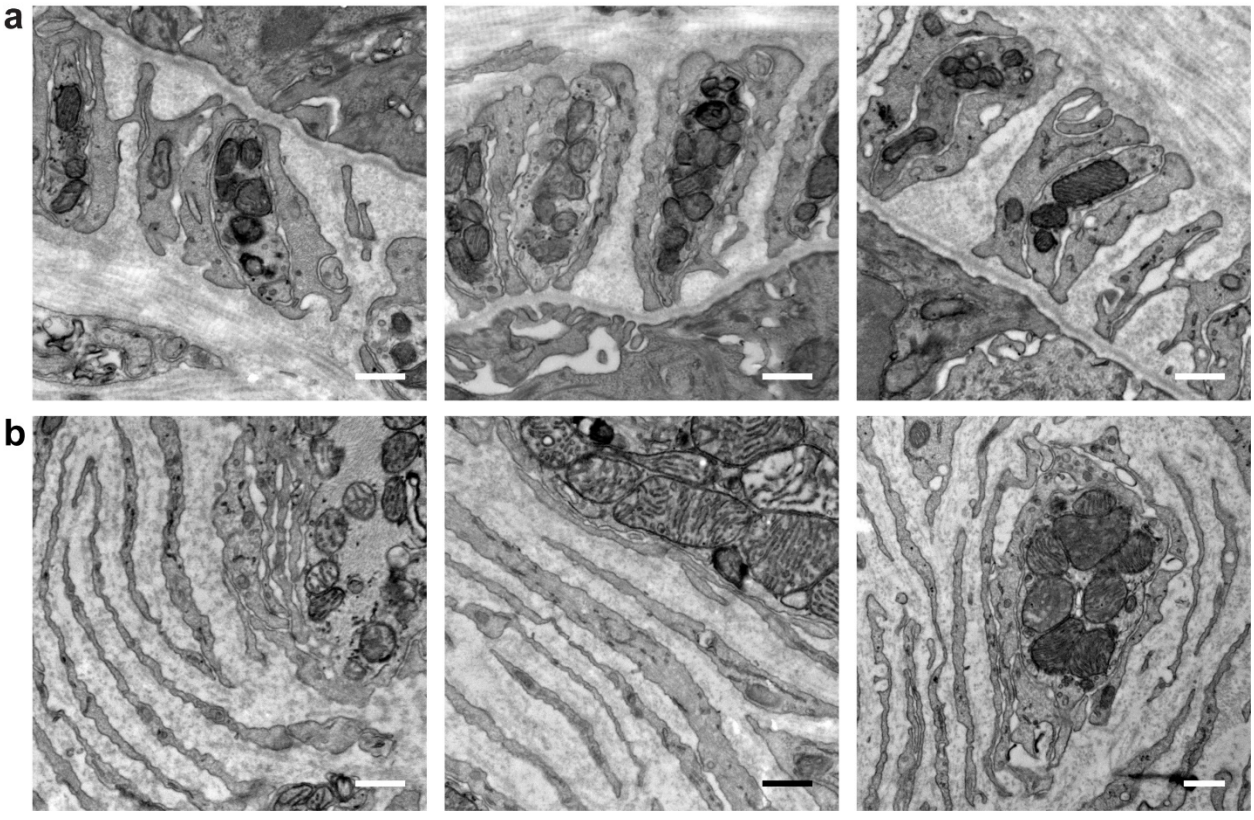

Figure 5.13. Caveolae are greatly reduced in cutaneous tactile end organs in *Cav1*$^{-/-}$ animals

(**a**) EM image showing hair follicles from P21-100 *Cav1*$^{-/-}$ animals. Few caveolae are present in TSCs. Nonetheless, TSCs remain associated with lanceolate axon terminals. n = 3 animals.

(**b**) EM image showing Meissner corpuscles from P21-42 *Cav1*$^{-/-}$ animals. Caveolae are largely ablated in lamellar cells, similar to **a**. Multiple layers of lamellar wrappings are still formed. n = 2 animals. Scale bars: 0.5 µm.

We also examined how Meissner corpuscles deform when external forces are applied during fixation. A 5 g weight was place on top of three dissected forepaw toe pads and the samples were fixed for one hour. Sample preparations were otherwise unchanged. Overt deformations could be seen in these compressed samples, most notably a reduction in extracellular space between lamellar wrappings (**Fig. 5.14a, b**). Additionally, we observed a reduction in caveolae density in lamellar cells (**Fig. 5.14c, d**), suggesting that caveolae can disassemble when forces are applied to the skin. This is consistent with previous *in vitro* studies where caveolae flatten when cells are stretched (Sinha et al., 2011).

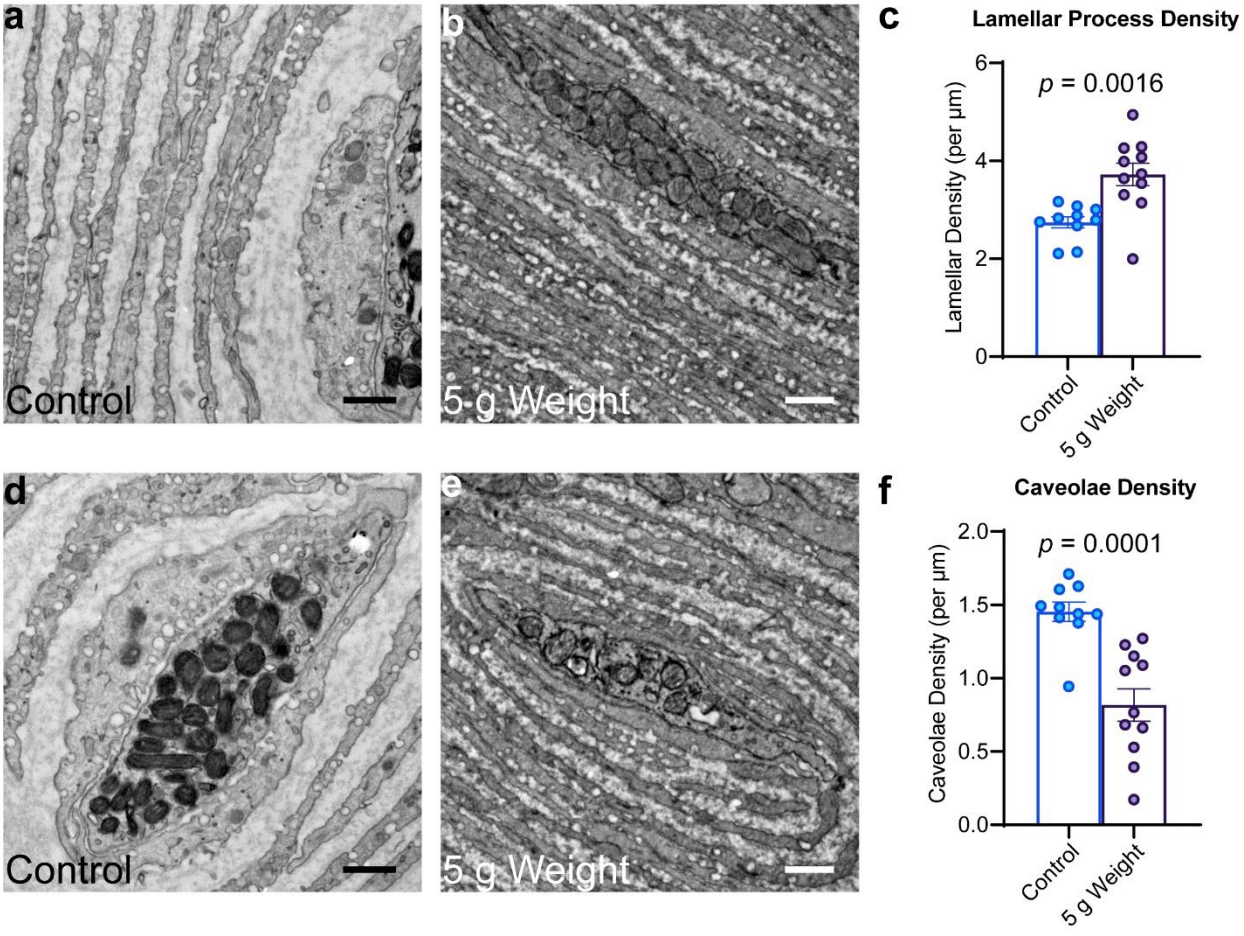

Figure 5.14. Mechanical compression deforms Meissner corpuscles and reduces caveolae density

Control images are from **Fig. 4.6**.

(**a**) EM image showing lamellar wrappings around a Meissner afferent profile in control.

(**b**) EM image showing lamellar wrappings around a Meissner afferent profile after 5 g weight compression (P27 WT). Note the reduced spacing between lamellar wrappings compared to **a**.

(**c**) Quantification of lamellar process density surrounding axon profiles. n = 10 axon profiles (from 2 animals) for control, 11 axon profiles (from 1 animal) for compressed toes.

(**d**) EM image showing caveolae around a Meissner afferent profile in control.

(**e**) EM image showing caveolae around a Meissner afferent profile after 5 g weight compression (P27). Note the reduced caveolae density, especially on the axon-facing side of the first lamellar wrapping, compared to **d**.

(**f**) Quantification of caveolae density on the axon-facing side of the first lamellar wrappings. n = 10 axon profiles (from 2 animals) for control, 11 axon profiles (from 1 animal) for compressed toes.

Scale bars: 0.5 μm.

Cell junctions in cutaneous tactile end organs

Cell-cell junctions and cell-matrix junctions can influence the biophysical properties of axons and associated cells. It has been reported that lanceolate endings can form adherens junctions with TSCs, and N-cadherin is part of these adherens junctions (Kaidoh and Inoue, 2008). After mordanting samples with tannic acid and post-section staining with lead citrate and uranyl acetate, we were able to observe strong electron densities in the cytoplasm of opposing lanceolate endings and TSCs around the mouths of TSC ensheathments (**Fig. 5.15a**), consistent with the previous report. Moreover, in lanceolate TSC processes there are also focal adhesions (**Fig. 5.15b**), which attach TSCs to the surrounding collagen matrix, and occasionally adherens junctions between TSC processes (**Fig. 5.15b**). Similar observations were made in Meissner corpuscles, where adherens junctions were observed between axons and lamellar cells (**Fig. 5.15c**), and occasionally between lamellar processes (**Fig. 5.15d**).

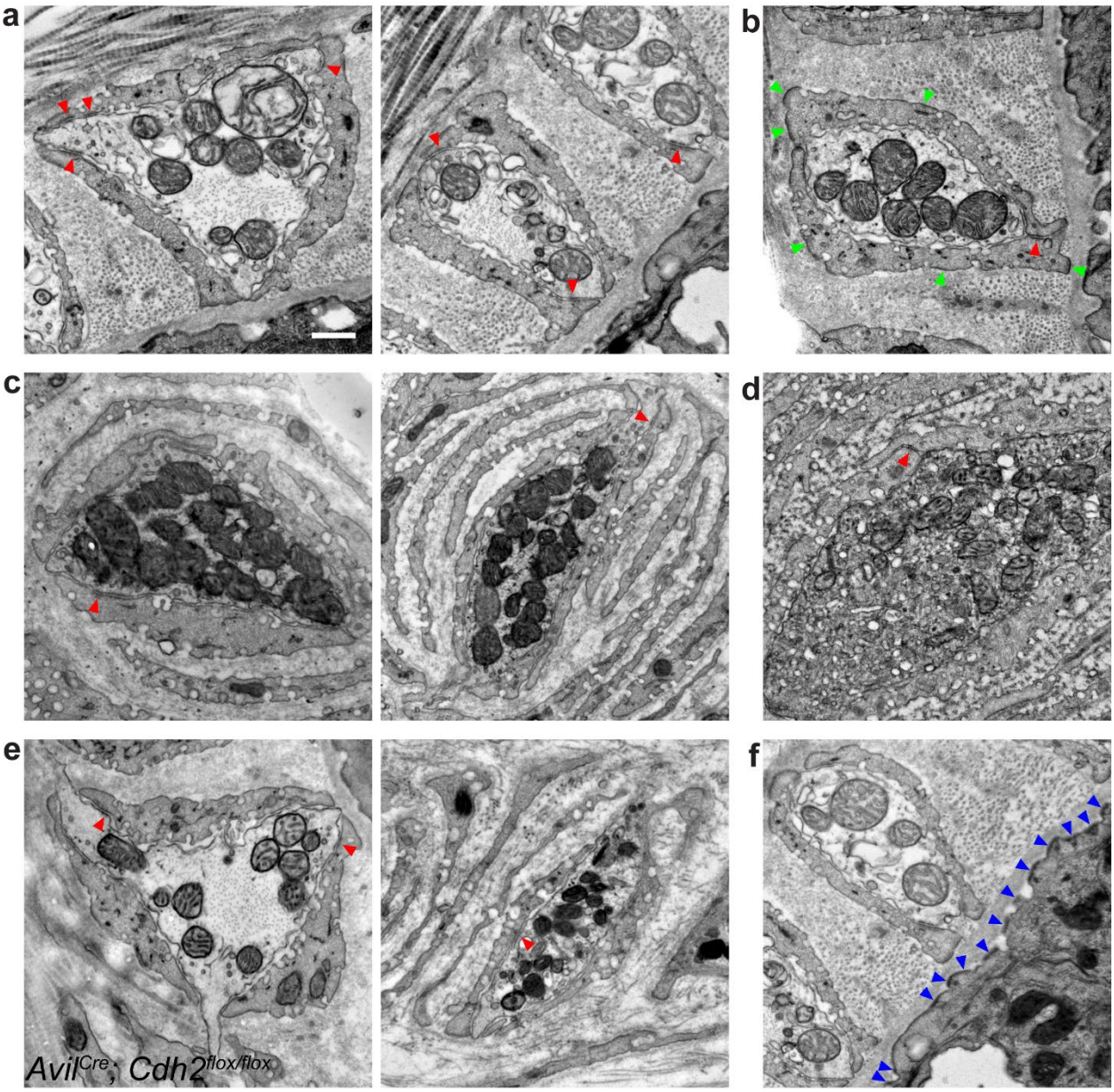

Figure 5.15. Cell junctions are prevalent in tactile end organs

(**a**) EM images showing adherens junctions (red arrowheads) between TSCs and axon terminals in P84 WT hair follicles. Adherens junctions tend to be located closer to the openings between TSC processes. n = 2 animals.

(**b**) EM image showing an adherens junction (red arrowhead) between TSC processes and focal adhesions (green arrowheads) in TSC processes in P84 WT animals. Focal adhesions are somewhat more concentrated on the side facing the basement membrane and the side facing circumferential collagen fibers. n = 2 animals.

(**c**) EM images showing adherens junctions (red arrowheads) between lamellar cells and axon terminals in P84 WT Meissner corpuscles. Similar to **a**, adherens junctions tend to be located closer to the openings between lamellar cell processes. n = 2 animals.
(**d**) EM image showing an adherens junction (red arrowhead) between lamellar processes in P84 WT Meissner corpuscles. n = 2 animals.
(**e**) EM images showing adherens junctions (red arrowheads) between TSCs and axon terminals (Left) and between lamellar cells and axon terminals (Right) in a P21 *Avil*^{Cre}*; Cdh2*$^{flox/flox}$ animal. Adherens junctions are still formed despite the deletion of N-cadherin in axons. n = 1 animal.
(**f**) EM image showing hemidesmosomes (blue arrowheads) in outer root sheath cells in P84 WT hair follicles. These hemidesmosomes are formed densely along the basement membrane. n = 2 animals. Scale bar: 0.5 μm.

We attempted to disrupt these cell junctions with *Avil*^{Cre}*; Cdh2*$^{flox/flox}$, in which N-cadherin is deleted from sensory axons. However, we did not observe any overt differences in either hair follicles or Meissner corpuscles from WT animals, and adherens junctions were still observed (**Fig. 5.15e**). Given that multiple cadherins are expressed in sensory neurons (Sharma et al., 2020; Zheng et al., 2019), in particular E-cadherin, we hypothesize that there may be redundancy in the molecular machinery forming these adherens junctions, and deletion of additional proteins may be required to disrupt them.

Finally, hemidesmosomes were frequently seen in the hair follicle outer root sheath cells which attach these cells to the basement membrane (**Fig. 5.15f**), as previously reported (Li and Ginty, 2014).

Discussion

Many ultrastructural similarities were present across the primary afferents of guard hair follicles, Meissner corpuscles, and Pacinian corpuscles, such as non-myelinating Schwann cell ensheathments, axonal protrusions, caveolae, and adherens junctions, and these may be considered to be “building blocks” for cutaneous tactile end organs. Variations on this theme, such as different orientations, associations with

other structures, additional lamellar wrappings, may endow tuning property differences between individual afferent subtypes. **Fig. 5.16** highlights the similarities and differences between hair follicle lanceolate endings and presumptive TrkB^{+} Meissner afferents.

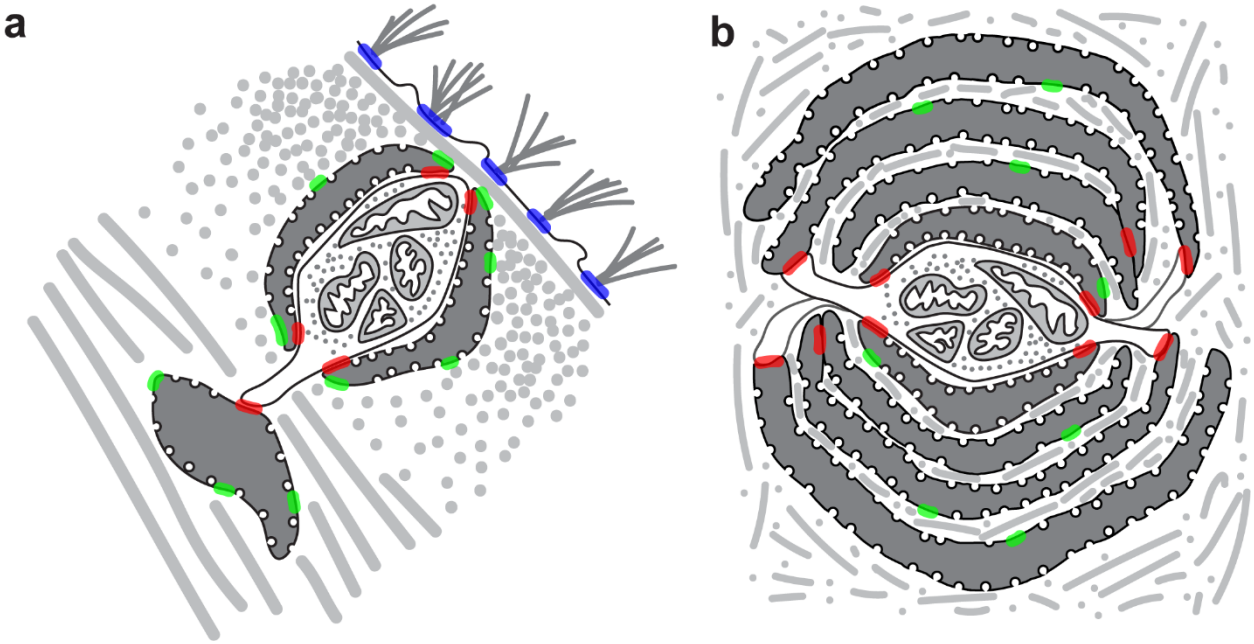

Figure 5.16. Schematics for two types of cutaneous tactile primary afferents

(**a**) Schematic showing components of a lanceolate ending in a hair follicle.

(**b**) Schematic showing components of a presumptive TrkB^{+} ending in a Meissner corpuscle.

Red: adherens junctions, Green: focal adhesions, Blue: hemidesmosomes.

The ultrastructural features across mechanosensory end organs described here allow us to speculate about mechanisms of mechanotransduction. We hypothesize that mechanotransduction in LTMR axons occurs primarily at the axonal protrusions due to their strategic localizations and intimate associations with surrounding cells. Given these ultrastructural findings, one potential model of lanceolate ending activation is as follows: TSCs and CSCs are anchored within longitudinal and circumferential collagen matrix, respectively, and TSCs are additionally anchored to the basement membrane. The basement membrane is also anchored to the outer root sheath cells. On the other hand, the trunks of the lanceolate endings are fixed to the ensheathing TSCs, while their axonal protrusions are attached to CSCs. When

the hair shaft is deflected, the lanceolate ending trunks move together with the hair shaft, while the CSCs remain relatively stationary since they are not as mechanically coupled to the hair shaft. This creates maximum membrane strain in the axonal protrusions, which opens mechanosensitive channels and generate receptor potentials within the axon. This model is summarized in **Fig. 5.17**. Future experiments localizing Piezo2 channels and disrupting cell junctions may support or refute the validity of this model. Completing the full reconstructions of all these cutaneous tactile end organs should also reveal additional ultrastructural and cell biology insights, and biophysical modeling may prove to be a fruitful avenue for elucidating how the unique ultrastructural features of each end organ leads to their distinct physiological properties.

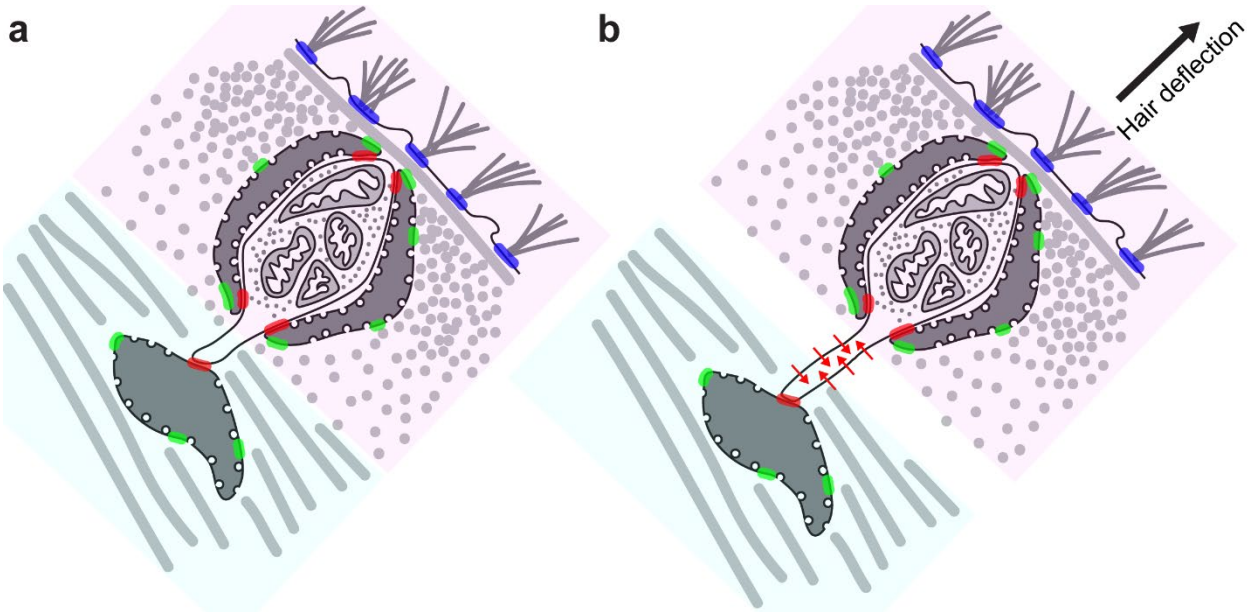

Figure 5.17. Model of lanceolate ending activation

(**a**) Schematic showing components of a lanceolate ending at rest in a hair follicle reproduced from **Fig. 5.16a**. Outer root sheath cells, TSCs, lanceolate axonal trunk, basement membrane, and longitudinal collagen fibers are likely mechanically coupled. On the other hand, CSCs and circumferential collagen fibers are also likely mechanically coupled. The axonal protrusion links these two blocks of materials. (**b**) Schematic showing a model of mechanical activation of the lanceolate ending. Hair deflection causes maximum membrane strain in the axonal protrusion, which in turn activates mechanosensitive Piezo2 channels, and leads to cation influx (red arrows) and depolarization.

Red: adherens junctions, Green: focal adhesions, Blue: hemidesmosomes. Magenta and cyan overlays indicate mechanically coupled regions.

Caveolae have previously been reported to regulate signal transduction, endocytosis, and confer mechanoprotection (Parton, 2018; Parton and del Pozo, 2013). Based on our ultrastructural findings, caveolae in non-myelinating Schwann cell processes do not appear to be involved in endocytosis. It is possible that these caveolae confer different mechanical filtering properties and/or mechanoprotection in cutaneous tactile end organs. Better understanding of their functions require additional insights into functional deficits of end organs lacking caveolae and their disassembly kinetics. *In vivo* electrophysiological recordings and advanced live imaging techniques, respectively, could provide these understandings.

While many anatomical and functional characterizations of primary somatosensory axons were done over the years (Abraira and Ginty, 2013; Zimmerman et al., 2014), comprehensive ultrastructural characterizations have not been accomplished, partially due to the challenges of acquiring and analyzing large-scale EM datasets. EM reconstructions using FIB-SEM are particularly suited for studying cutaneous tactile end organs owing to its unique advantages of high isotropic resolution (voxel size of 6 nm or smaller) and minimal sample distortion. Many obscure ultrastructural features become immediately apparent when viewed with volume reconstructions, which then generates testable hypotheses using molecular biology tools and electrophysiology. This combination of high-throughput EM imaging, molecular biology approaches, and functional recordings will enable the next generation of structure-function studies of the somatosensory system.

Methods

All experiments using animals were conducted according to United States National Institutes of Health guidelines for animal research and were approved by the Institutional Animal Care and Use Committee at Harvard Medical School. All procedures were done at room temperature unless otherwise noted.

Mice

All mice used in the study are of mixed background, except for FIB-SEM guard hair follicle and Meissner corpuscle samples, which are from C57BL6/J WT animals.

Tg(Plp1-EGFP)10 (JAX 033357) (Mallon et al., 2002) and Tg(Plp1-CreER)3 (JAX 005975) (Doerflinger et al., 2003) were used to label Schwann cells. *ROSA26*$^{LSL\text{-}Matrix\text{-}dAPEX2}$ (JAX 032765) and *ROSA26*$^{FSF\text{-}Matrix\text{-}dAPEX2}$ (JAX 032766) were used for genetic EM labeling (Zhang et al., 2019). *Ntrk3*^{CreER} (JAX 030291) (Bai et al., 2015) was used to label Aβ field-LTMRs. Tg(Calca-Flpe) (Choi et al., 2020) was used to label Aδ Circ-HTMRs. Tg(Plxnd1-EGFP)HF78 (Gong et al., 2003) was used to label CSCs. *Cav1*$^{-/-}$ (JAX 007083) (Razani et al., 2001) was used to ablate caveolae. *Cdh2*$^{flox/flox}$ (JAX 007611) (Kostetskii et al., 2005) was used to delete N-caherin in sensory neurons.

Animals were sacrificed at P21 or older (see text for exact ages).

Tamoxifen administration

See **Chapter 2 Methods**.

Electron microscopy sample preparation

See **Chapter 2 and 4 Methods** for TEM sample preparations. Also see **Appendix 2** for a detailed staining protocol.

For FIB-SEM samples, dissected skins were fixed and washed as previously described. Then sections were osmicated in cacodylate buffer containing 1% osmium tetroxide (Electron Microscopy Sciences)/1.5% potassium ferrocyanide (MilliporeSigma) for 1 hour, followed by cacodylate buffer

containing 1% osmium tetroxide for 1 hour. Sections were then washed with ddH_2O, and stained in a solution containing 0.05 M sodium maleate (MilliporeSigma) (pH 5.15), 1% uranyl acetate (Electron Microscopy Sciences), and 2% samarium chloride (MilliporeSigma) at 4°C overnight. After washing with ddH_2O, sections were dehydrated with an ethanol series followed by anhydrous acetone (MilliporeSigma). Sections were then infiltrated with a series of epoxy resin mix (Durcupan, MilliporeSigma) diluted in anhydrous acetone. Finally, sections were embedded in epoxy resin mix and cured at 60°C for 48-72 hours.

X-ray µCT volumes were acquired using Zeiss Xradia 510 Versa at 40 kV using 4x and 20x objectives without any source filter.

Compressed toes were prepared by putting a 5 g weight on three forepaw toes after dissection and during the 1-hour fixation. Afterward, the weight was removed and sample preparation proceeded as previously described.

For tannic acid treatment, samples were incubated in cacodylate buffer containing 1% tannic acid (Electron Microscopy Sciences) for 5 or 20 min or 1% low molecular weight tannic acid for 30 min (Electron Microscopy Sciences) between the osmication step and the uranyl acetate step, with washes preceding and following this treatment.

FIB-SEM Sample Preparation

Three Durcupan embedded mouse end organs samples, one guard hair follicle sample (MH200121-B2K), two Meissner corpuscle samples (200913FPT and 200913FPT2) were each first mounted to the top of a 1 mm copper post which was in contact with the metal-stained sample for belter charge dissipation, as previously described (Xu et al., 2017). Three vertical sample posts were each trimmed to a small block containing region of interest (ROI) with a width perpendicular to the ion beam, and a depth in the direction of the ion beam. The block sizes are 105 µm x 100 µm, 90 µm x 70 µm, and 85 µm x 75 µm for

MH200121-B2K, 200913FPT, and 200913FPT2, respectively. The trimming was guided by X-ray μCT data and optical inspection under a microtome. Thin layers of conductive material of 10-nm gold followed by 100-nm carbon were coated on the trimmed samples using a Gatan 681 High-Resolution Ion Beam Coater. The coating parameters were 6 keV, 200 nA on both argon gas plasma sources, 10 rpm sample rotation with 45-degree tilt.

FIB-SEM 3D large volume imaging

Three FIB-SEM prepared samples, MH200121-B2K, 200913FPT, and 200913FPT2 were imaged sequentially by three customized Zeiss FIB-SEM systems previously described (Xu et al., 2017; Xu et al., 2020). The block face of ROI was imaged by a 1 nA electron beam with 0.9 keV landing energy at 1 MHz scanning rate. The x-y pixel resolution was set at 6 nm. A subsequently applied focused Ga+ beam of 15 nA at 30 keV strafed across the top surface and ablated away 6 nm of the surface. The newly exposed surface was then imaged again. The ablation – imaging cycle continued about once every four minutes for five weeks to complete FIB-SEM imaging MH200121-B2K, and each about once every minute for one week to complete 200913FPT and 200913FPT2. The raw image stacks consist of final isotropic volumes of 80 μm x 80 μm x 80 μm, 40 μm x 30 μm x 50 μm, and 35 μm x 40 μm x 40 μm for MH200121-B2K, 200913FPT, and 200913FPT2, respectively. The voxel size of 6 nm x 6 nm x 6 nm was maintained for each sample throughout entire volumes. 100-200 nm was missing in MH200121-B2K between slice 6483 and slice 6484 due to microscope issues.

Image alignment and processing

Three slices (7597, 7598, 7962) were discarded in MH200121-B2K due to microscope issues, and adjacent slices (7596, 7599, 7961) were copied over. Raw image stacks were first post-processed for image registration and alignment using a SIFT-based algorithm (Xu et al., 2017). The SIFT-aligned FIB-SEM stacks were then downsampled 32x to 192 nm x 192 nm x 192 nm voxel size and adjusted for contrast to reduce illumination unevenness. μCT volumes were cropped to just large enough to fully

include the FIB-SEM ROI. The downsampled FIB-SEM stacks were used as moving images to align to µCT stacks which were fixed images using elastix (Klein et al., 2010; Shamonin et al., 2013). The elastix alignment was done in a manner similar to Phelps et al. (2021) (https://github.com/htem/run_elastix), where an affine alignment was followed by a B-spline elastic alignment. Mutual information (AdvancedMattesMutualInformation) was used as the main metric, and 28 grid spacing and 0 bending weight was used for B-spline alignment to avoid distortions. Corresponding points were added whenever necessary. After satisfactory alignment was achieved, the transform was inverted to allow the mapping of coordinates in the SIFT-aligned FIB-SEM space to the µCT space. In order to align images using only translation, the geometric center of each section was mapped to the µCT space, given that it is rotationally invariant and in general in a well aligned region for elastix alignment. Since the z-axes were nearly identical in direction for the SIFT-aligned FIB-SEM volume and the µCT volume, these transformed coordinates can then be used as displacement vectors to align raw image stacks.

To generate the final volumes, raw FIB-SEM images were first processed to clean up milling artifacts using Fourier transform (Xu et al., 2017), and then contrast enhanced using CLAHE. Images were then placed using displacement vectors generated above into an aligned volume. Volumes were rotated in 3-D space to align their z-axes to major anatomical axes, such as the hair shaft, for the ease of analysis. Neuroglancer precomputed volumes and 3-D meshes were generated using Igneous (https://github.com/seung-lab/igneous) and visualized using Neuroglancer (https://github.com/google/neuroglancer).

Automatic reconstruction

Ground truths for network training were generated through manual segmentation of small image volumes using webKnossos (Boergens et al., 2017). Automatic segmentation was done using the algorithm described in Funke et al. (2019) with parameters described in Kuan et al. (2020).

Immunohistochemistry

Mice were transcardially perfused with Ames' medium (MilliporeSigma) containing heparin (MilliporeSigma) (oxygenated with 95% O_2, 5% CO_2, warmed to 37 °C) to remove blood, and then 4% paraformaldehyde (Electron Microscopy Sciences) in 0.1 M PB (pH 7.4, warmed to 37 °C). Tissues were dissected out and then post-fixed in Zamboni fixative (Newcomer Supply) at 4°C overnight. After washing with PBS, tissues were permeabilized using PBS containing 0.3% Triton X-100 (MilliporeSigma) (0.3 PBST) for 5-8 hours, changing the solution every 30 min. Tissues were then incubated in primary antibodies in 0.3% PBST with 5% Normal Donkey Serum (Jackson ImmunoResearch) and 20% dimethyl sulfoxide (DMSO, MilliporeSigma) for 3-5 days, followed by washes with 0.3% PBST every 30 min for 5-8 hours. Tissues were then incubated in secondary antibodies in 0.3% PBST with 5% Normal Donkey Serum (Jackson ImmunoResearch) and 20% dimethyl sulfoxide (DMSO, MilliporeSigma) for 2-3 days, followed by washes with 0.3% PBST every 30 min for 5-8 hours. After staining, tissues were dehydrated with a methanol (MilliporeSigma) series and cleared with 1:2 benzyl alcohol (MilliporeSigma)/benzyl benzoate (MilliporeSigma) (BABB). Cleared tissues were mounted with BABB and imaged with a Zeiss LSM 700 laser scanning confocal microscope as Z-stacks. Maximum intensity projections were made, and image intensities were adjusted using Fiji/ImageJ.

Primary antibodies used were rabbit anti-S100 beta (1:500, Proteintech, 15146-1-AP), goat anti-GFP (1:500, Sicgen, AB0020-200), and chicken anti-PGP9.5 (1:500, Thermo Fisher, PA1-10011). Secondary antibodies used were donkey anti-Rabbit IgG (H+L) highly cross-adsorbed, Alexa Fluor Plus 405 (1:500, Thermo Fisher, A48258), donkey anti-Goat IgG (H+L) cross-adsorbed, Alexa Fluor 488 (1:500, Thermo Fisher, A-11055), and Alexa Fluor 647 AffiniPure Donkey Anti-Chicken IgY (IgG) (H+L) (1:500, Jackson ImmunoResearch, 703-605-155). All antibodies were validated by manufacturers.

Competing Interest Statement

C.S.X. and H.F.H. are the inventors of a U.S. patent assigned to HHMI for the enhanced FIB-SEM systems used in this work: Xu, C. S., Hayworth, K. J., Hess, H. F. (2020) Enhanced FIB-SEM systems for large-volume 3D imaging. U.S. Patent 10,600,615, 24 Mar 2020.

Appendix 1. Supplementary Figures and Tables

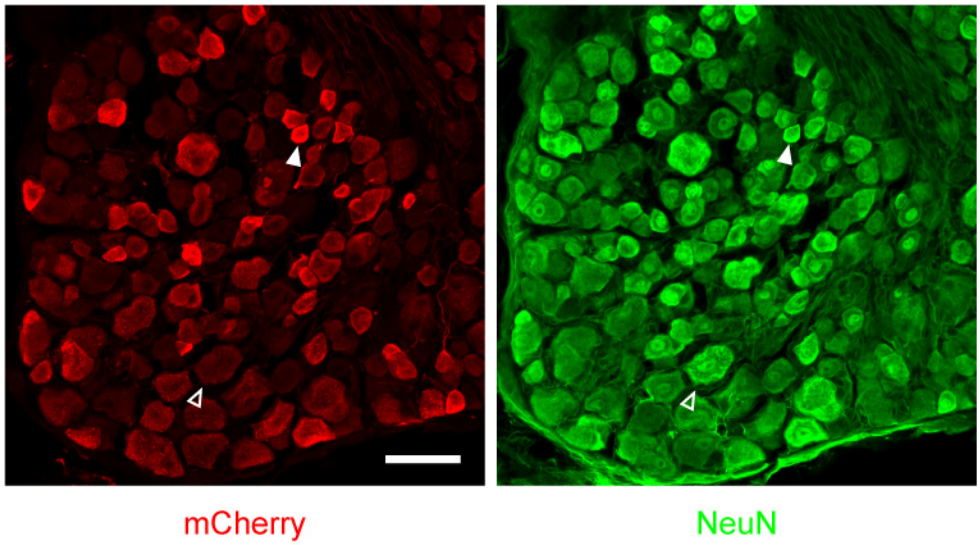

Supplementary Figure 2.1. AAV9 IP injection efficiently transduces DRG neurons

Confocal images showing the transduction efficiency of DRG neurons by neonatal AAV9 IP injections. AAV9-mCherry was used in this experiment. Note the efficient labeling but highly variable expression levels, with small-diameter neurons generally expressing the transgene at higher levels than large-diameter neurons. NeuN was used to label neurons. Solid arrowhead: example small-diameter neuron with high transgene expression level. Open arrowhead: example large-diameter neuron with low transgene expression level. n = 2 animals and experiments.

Scale bar: 50 μm.

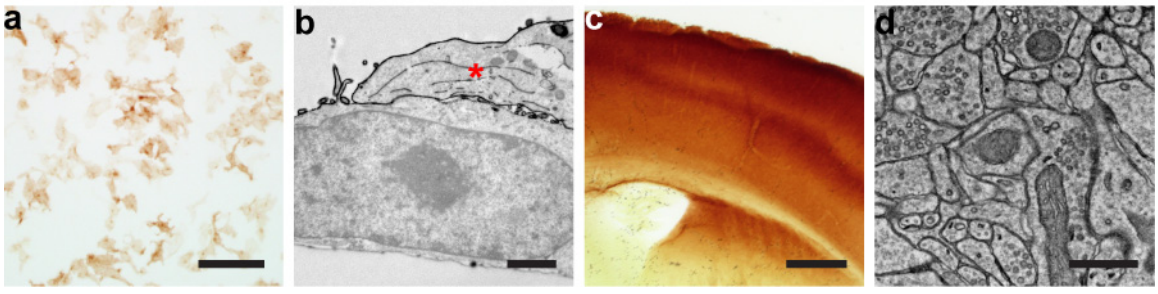

Supplementary Figure 2.2. Insufficient staining using previously reported constructs

(**a**) LM image of HEK293T cells after transfection with HRP-TM. n = 3 experiments.

(**b**) EM image showing plasma membrane labeling in a HEK293T cell transfected with HRP-TM (asterisk). n = 2 experiments.

(**c**) LM image of the cortex after parenchymal injection of AAV1-HRP-TM. Staining could be observed with LM. n = 4 animals and experiments.

(**d**) EM image of the cortex after parenchymal injection of AAV1-HRP-TM. Little if any discernible DAB staining was observed. n = 2 animals and experiments.

Scale bars: **a**: 100 µm, **b**: 2 µm, **c**: 500 µm, **d**: 0.5 µm.

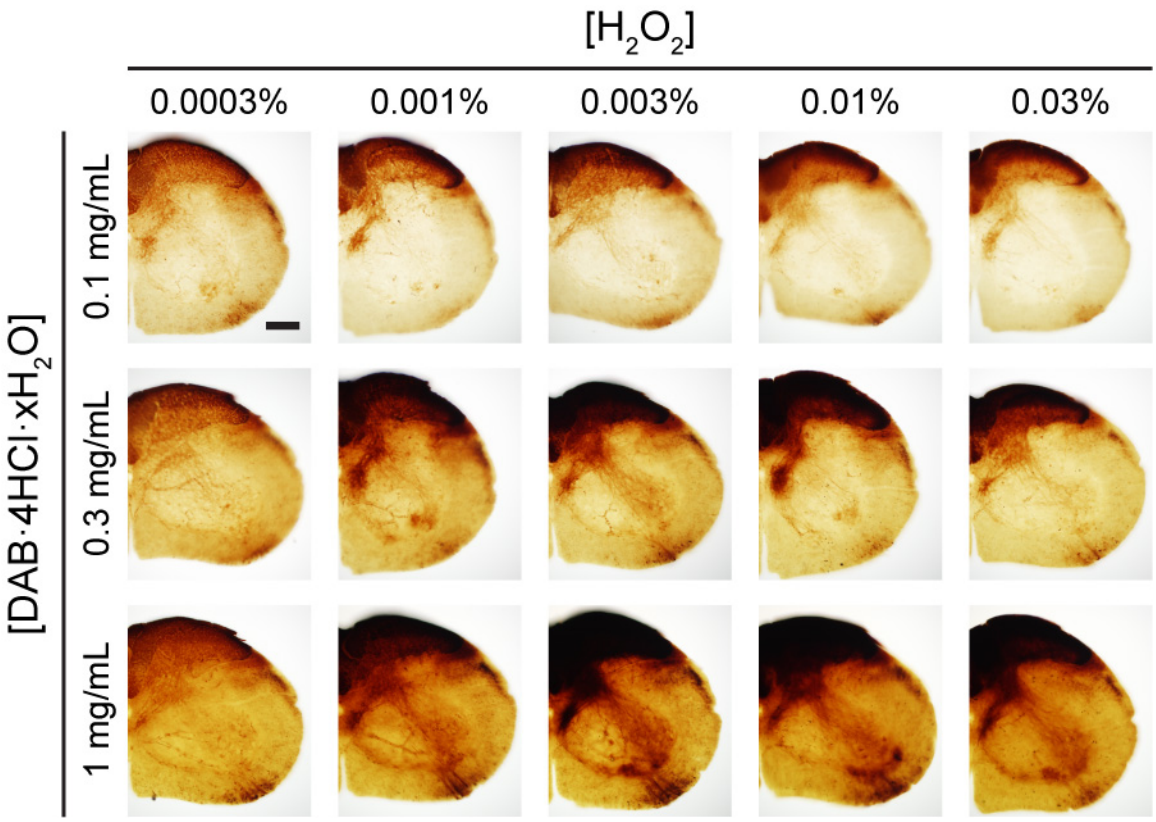

Supplementary Figure 2.3. Comparison of peroxidase staining conditions

LM images of the spinal cord dorsal horn of the same animal after systemic transduction of AAV9-dAPEX2 stained with different conditions. 0.003% hydrogen peroxide gave the highest staining intensity regardless of the DAB concentration. Staining intensity observed under LM was positively correlated with DAB concentration. n = 2 animals and experiments.

Scale bar: 200 µm.

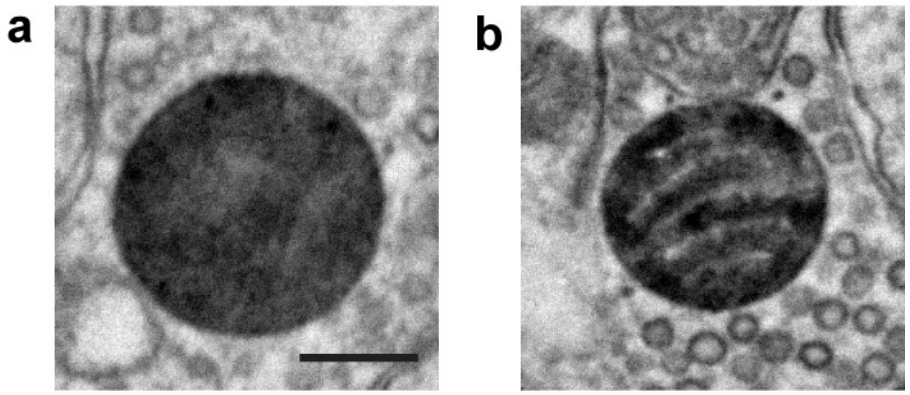

Supplementary Figure 2.4. Excessively high concentrations of DAB could cause staining artifacts

(**a, b**) EM images of the spinal cord dorsal horn of the same animal after systemic transduction of AAV9-Matrix-dAPEX2 stained with 0.003% hydrogen peroxide and 1 mg/mL DAB (**a**) or 0.3 mg/mL DAB (**b**). The ultrastructure of the IMS was better preserved with 0.3 mg/mL DAB staining. n = 2 animals and experiments.

Scale bar: 0.2 μm.

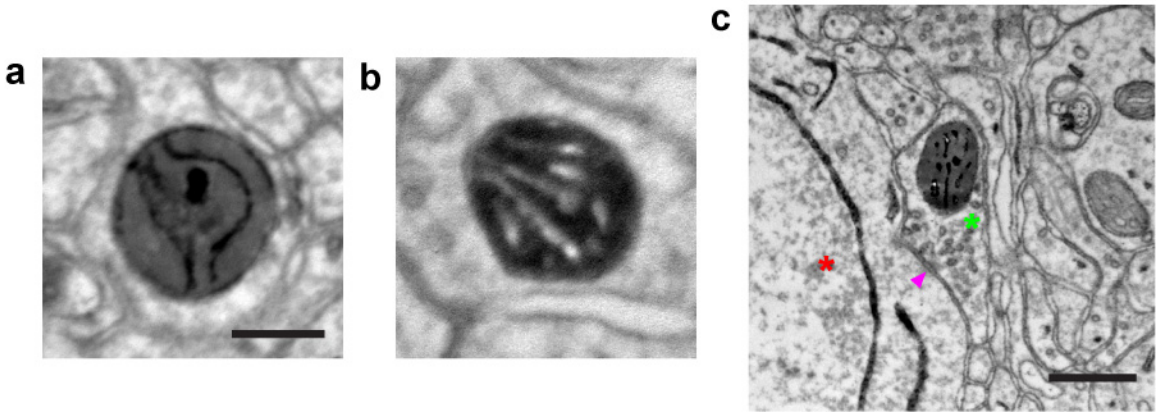

Supplementary Figure 2.5. Excessive osmication could cause staining artifacts

(**a, b**) EM images of the spinal cord dorsal horn of the same *Th*$^{T2A\text{-}CreER}$ animal transduced with AAV9-DIO-Matrix-dAPEX2 and treated with tamoxifen from P14-21 to label C-LTMRs prepared with the rOTO protocol (**a**) or the reduced osmium protocol (**b**). Strong spurious staining was seen in the IMS in the samples prepared with the rOTO protocol. This spurious staining was not seen in unlabeled mitochondria.

Reduced osmium staining preserved the DAB staining while providing sufficient counterstaining contrast. n = 2 animals and experiments.

(**c**) EM images showing a sample prepared with the rOTO protocol with double labeling of cortical layer 5 pyramidal neurons (ER) using Tg(Rbp4-Cre)KL100 and AAV1-DIO-ER-dAPEX2 (red asterisks), and fast-spiking GABAergic interneurons (mitochondrial matrix) using *Pvalb*$^{T2A\text{-}FlpO}$ and AAV1-FDIO-Matrix-dAPEX2 (green asterisks), equivalent to the experiment in **Fig. 3a**. Arrowhead: symmetric perisomatic synapse made by fast-spiking interneurons onto layer 5 pyramidal neurons. Note while spurious staining was present in the IMS, the mitochondrial matrix staining could still be easily distinguished from the ER staining. n = 2 animals and experiments.

Scale bars: **a, b**: 0.2 µm, **c**: 0.5 µm.

Supplementary Table 2.1. List of all constructs tested

Name	Target peptide	Expected staining localization	In vitro (HEK293T) LM observation	In vitro (HEK293T) EM observation	In vivo LM observation	In vivo EM observation	Comments	Source
				Cytosol				
APEX2	None	Cytosol and nucleus	Cytosolic and nuclear staining	Cytosolic and nuclear staining, distribution of staining densities can appear non-uniform	Cytosolic and nuclear staining	Cytosolic and nuclear staining, distribution of staining densities can appear non-uniform		Lam et al., 2015
tdAPEX2	None	Cytosol and nucleus	Cytosolic and nuclear staining	N/A	N/A	N/A	Linker sequence between the two dAPEX2 from Martell et al., 2012	This study
dAPEX2	None	Cytosol and nucleus	Cytosolic and nuclear staining	N/A	Cytosolic and nuclear staining	Cytosolic and nuclear staining, distribution of staining densities can appear non-uniform		This study
				Plasma membrane				
APEX2-CAAX	Prenylation sequence from H-Ras	Inside of plasma membrane and some cytosol	Membrane-associated staining	Staining inside of plasma membrane and some cytosol	Membrane-associated staining	Staining inside of plasma membrane and some cytosol. In small profiles staining appears more similar to cytosolic	Staining pattern depends heavily on profile size and expression level, not ideal for distiguishing from cytosolic staining	Lam et al., 2015
Palmitoyl-APEX2	Palmitoylation sequence from GAP43 (Cimler et al., 1987)	Inside of plasma membrane and some cytosol	Membrane-associated staining	N/A	N/A	N/A	Likely similar to CAAX targeting	This study
HRP-TM	Igκ leader sequence and PDGFR transmembrane domain	Outside of plasma membrane and some ER	Membrane-associated staining	Staining outside of plasma membrane and some ER. Convoluted plasma membrane	AAV1 cortical injection: granular staining in somata and diffuse staining. AAV9 IP injection: no visible staining in spinal cord	AAV1 cortical injection: very little if any staining could be seen. AAV9 IP injection: N/A	Potentially due to insufficient peroxidase activity. All HRP constructs (except VAMP2-HRP) gave lysosomal staining in vivo	Rhee et al., 2013
APEX2-PDGFR	Igκ leader sequence and PDGFR transmembrane domain	Outside of plasma membrane and some ER	Membrane-associated staining with clearly delineated nucleus	Staining mostly in nuclear envelope, some plasma membrane and some ER	N/A	N/A	Mislocalized	This study
PDGFR-APEX2	Igκ leader sequence and PDGFR transmembrane domain	Inside of plasma membrane and some around ER	Cytosolic and nuclear staining	N/A	Cytosolic and nuclear staining	Cytosolic and nuclear staining	Mislocalized	This study

mHRP	wg signal sequence and CD2 transmembrane domain	Outside of plasma membrane and some ER	Diffuse staining	N/A	Granular staining in somata and weak diffuse staining	N/A	Potentially due to insufficient peroxidase activity. All HRP constructs (except VAMP2-HRP) gave lysosomal staining in vivo	Li et al., 2010
HRP-DsRed-GPI	wg signal sequence and dlp GPI-linker	Outside of plasma membrane and some ER	Diffuse staining	N/A	Granular staining in somata and diffuse staining	ER lumenal staining	Potentially due to trafficking issues. All HRP constructs (except VAMP2-HRP) gave lysosomal staining in vivo	Han et al., 2012
dAPEX2-CAAX	Prenylation sequence from H-Ras	Inside of plasma membrane and some cytosol	Membrane-associated staining	N/A	Membrane-associated staining	Staining inside of plasma membrane and some cytosol. In small profiles staining appears more similar to cytosolic	Staining pattern depends heavily on profile size and expression level, not ideal for distiguishing from cytosolic staining	This study
tdAPEX2-CAAX	Prenylation sequence from H-Ras	Inside of plasma membrane and some cytosol	Membrane-associated staining	N/A	Membrane-associated staining	Staining inside of plasma membrane and some cytosol. In small profiles staining appears more similar to cytosolic	Staining pattern depends heavily on profile size and expression level, not ideal for distiguishing from cytosolic staining	This study
Mitochondria								
mito-V5-APEX2	Matrix localization sequence from COX4	Mitochondrial matrix	Granular staining	Staining in mitochondrial matrix	Granular staining in different parts of cells	Staining in mitochondrial matrix		Hung et al., 2016
SMAC-APEX2	Intermembrane space localization sequence from Diablo (Ozawa et al., 2007)	Mitochondrial intermembrane space	Granular staining	Staining in mitochondrial matrix	Granular staining in different parts of cells	Staining in mitochondrial matrix	Mislocalized	This study
IMS-APEX2	Intermembrane space localization sequence from LACTB	Mitochondrial intermembrane space	Small amount of aggregates and granular staining	Staining in mitochondrial intermembrane space	Granular staining in different parts of cells	Staining in mitochondrial intermembrane space	Potentially toxic at high expression levels	Hung et al., 2016
COX4-tdAPEX2	Matrix localization sequence from COX4	Mitochondrial matrix	Granular and cytosolic staining	N/A	N/A	N/A	Mislocalized	This study
LACTB-tdAPEX2	Intermembrane space localization sequence from LACTB	Mitochondrial intermembrane space	Prominent aggregates in cells	N/A	N/A	N/A	Potentially toxic	This study
Matrix-dAPEX2	Matrix localization sequence from COX4	Mitochondrial matrix	Granular staining	N/A	Granular staining in different parts of cells	Staining in mitochondrial matrix		This study

IMS-dAPEX2	Intermembrane space localization sequence from LACTB	Mitochondrial intermembrane space	Some aggregates and granular staining	N/A	Granular staining in different parts of cells	Staining in mitochondrial intermembrane space	No aggregates observed when expression levels are low. Potentially toxic at high expression levels	This study
			Endoplasmic reticulum					
ER-APEX2	Igκ leader sequence and ER retention sequence KDEL	ER lumen	Diffuse staining	ER lumenal staining	Diffuse staining mostly in soma	ER lumenal staining	Largely absent in long axons	This study
CALR-APEX2-KDEL	ER signal sequence from calreticulin (Wu et al., 2014) and ER retention sequence KDEL	ER lumen	Cytosolic and nuclear staining	N/A	N/A	N/A	Mislocalized	This study
IGK-tdAPEX2-KDEL	Igκ leader sequence and ER retention sequence KDEL	ER lumen	Prominent aggregates in cells	N/A	Diffuse staining mostly in soma. Somatic staining lighter than ER-APEX2	N/A	Linker sequence between the two dAPEX2 from Martell et al., 2012. Potentially toxic	This study
IGK-tdAPEX2-40aa-KDEL	Igκ leader sequence and ER retention sequence KDEL	ER lumen	Prominent aggregates in cells	N/A	N/A	N/A	Potentially toxic. Linker sequence between the two dAPEX2 is 40 aa long. Second dAPEX2 is codon optimized	This study
ER-dAPEX2	Igκ leader sequence and ER retention sequence KDEL	ER lumen	Diffuse staining	N/A	Diffuse staining mostly in soma	ER lumenal staining	Largely absent in long axons	This study
			Synaptic vesicles					
VAMP2-HRP	SNARE complex protein VAMP2, HRP at C-terminus	Synaptic vesicle lumen	Membrane-associated staining	N/A	AAV1 cortical injection: weak diffuse staining. AAV9 IP injection: animals dead after injections in two separate experiments	AAV1 cortical injection: infrequently one or two synaptic vesicles per bouton. AAV9 IP injection: N/A	Not tested using the originally reported fixation and staining conditions	Atasoy et al., 2014
VAMP2-APEX2	SNARE complex protein VAMP2, APEX2 at C-terminus	Synaptic vesicle lumen	Mostly cytosolic staining	N/A	Mostly cytosolic staining	N/A		This study
VAMP2-dAPEX2	SNARE complex protein VAMP2, dAPEX2 at C-terminus	Synaptic vesicle lumen	Mostly cytosolic staining	N/A	N/A	N/A	Likely similar to VAMP2-APEX2	This study
SYP-dAPEX2	Synaptophysin, dAPEX2 between TM3 and 4	Synaptic vesicle lumen	Membrane-associated and cytosolic staining	N/A	Weak staining	Little if any staining	Mislocalized or not tolerated	This study

SYP-dAPEX2-Cytosolic	Synaptophysin, dAPEX2 at C-terminus	Cytosolic side of synaptic vesicles	Aggregates and membrane-associated staining	N/A	AAV1 cortical injection: Intermediate-sized granular staining, sometimes aggregates in cell bodies. AAV9 IP injection: Intermediate-sized granular staining	Strong staining is similar to cytosolic, and weak staining is around vesicles but not very discernible. Aggregates are large collections of vesicle-like structures	Variable staining pattern depending on expression level. Potentially toxic	This study
APEX2-VAMP2	SNARE complex protein VAMP2, dAPEX2 at N-terminus	Cytosolic side of synaptic vesicles	Aggregates and membrane-associated staining	N/A	N/A	N/A	In vitro LM appearance not different from dAPEX2-VAMP2 and SYP-dAPEX2-Cytosolic	This study
dAPEX2-VAMP2	SNARE complex protein VAMP2, dAPEX2 at N-terminus	Cytosolic side of synaptic vesicles	Aggregates and membrane-associated staining	N/A	N/A	N/A	In vitro LM appearance not different from APEX2-VAMP2 and SYP-dAPEX2-Cytosolic	This study
SV-HRP	Synaptophysin, HRP between TM3 and 4	Synaptic vesicle lumen	No staining	N/A	Granular staining in somata and diffuse staining	Multiple synaptic vesicles per bouton	All HRP constructs (except VAMP2-HRP) gave lysosomal staining in vivo	This study
				Microtubules				
TAU-APEX2	Microtubule-associated protein tau	Microtubules	Cytosolic staining	Cytosolic staining	Cytosolic staining, somewhat more staining in axons compared to untagged	Staining at microtubules and in cytosol	Difficult to differentiate from cytosolic staining	This study
				Peroxisomes				
dAPEX2-PTS1	Peroxisomal targeting signal 1 SKL	Peroxisomes	Cytosolic and nuclear staining	N/A	N/A	N/A	Mislocalized	This study

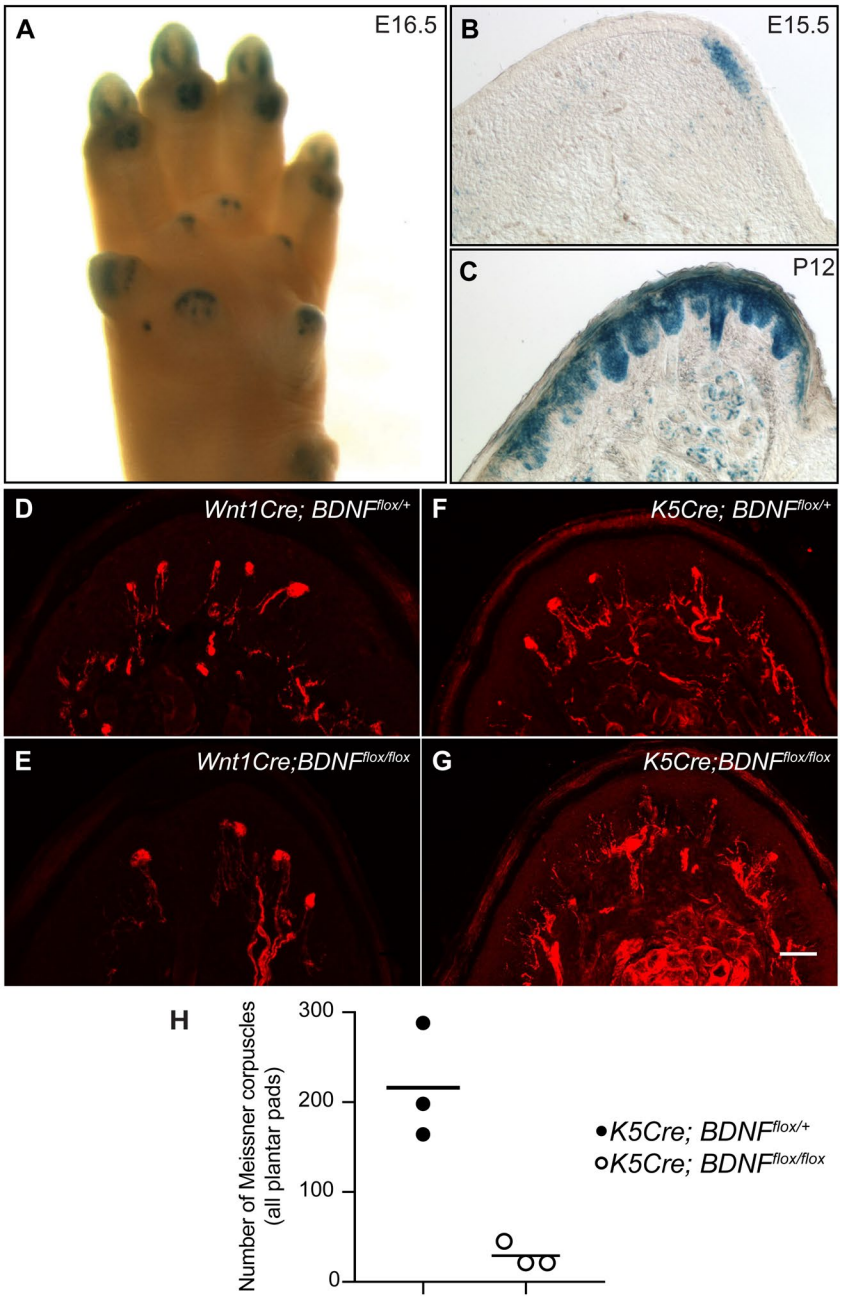

Supplementary Figure 4.1. BDNF expressed in epithelial cells, but not in neural crest-derived sensory neurons or Schwann cells, is essential for Meissner corpuscle formation

(**a**) Whole forelimb of an E16.5 *BDNF^{lacZ}* embryo stained using X-gal.

(**b, c**) Forelimb palmar pad sections of *BDNF^{lacZ}* mice at E15.5 and P12 stained with X-gal.

(**d-g**) Hindlimb plantar pad sections were stained with anti-S100 to reveal Meissner corpuscles in *Wnt1Cre; BDNF$^{flox/flox}$* mice, in which BDNF expression is eliminated in DRG sensory neurons and

Schwann cells, and control mice. The number of Meissner corpuscles in glabrous skin of control and *Wnt1Cre; BDNF$^{flox/flox}$* mice are comparable, and this comparison was done with two pairs of control (105 and 133 corpuscles in two hindlimb pedal pads per mouse) and *Wnt1Cre; BDNF$^{flox/flox}$* mice (119 and 89 corpuscles in two hindlimb pedal pads per mouse). (scale bar = 50 μm)

(**h**) Quantifications of the number of Meissner corpuscles in all hindlimb plantar pads of *K5Cre; BDNF$^{flox/flox}$* mice, in which BDNF expression is eliminated in skin epithelial cells, and control mice at P20 (3 mice for each genotype, 6 hindlimb pedal pads per mouse). Black bars represent means. Serial sections were cut throughout the whole plantar region and Meissner corpuscles were identified by S100 staining and counted across all sections.

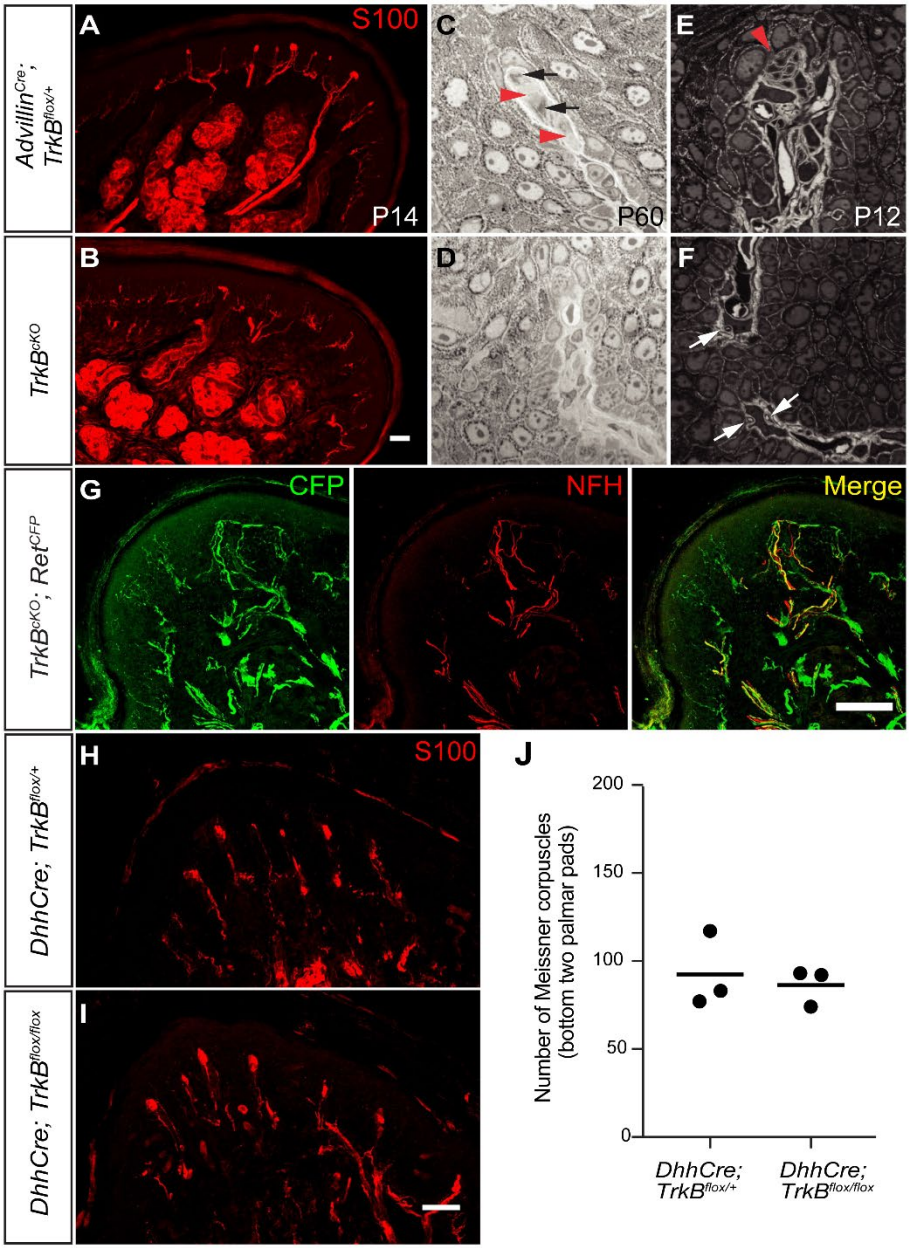

Supplementary Figure 4.2. TrkB is required in sensory neurons, but not glia cells, for the formation of Meissner corpuscles and their innervating sensory neurons

(**a, b**) Hindlimb plantar pad sections of control and *TrkB*^{cKO} mice at P14 stained with anti-S100 antibody. (scale bar = 50 μm)

(**c-f**) To exclude the possibility that in sensory-neuron-specific *TrkB*^{cKO} mice Meissner corpuscles are formed but fail to express S100 protein, we performed toluidine/methylene blue staining on semi-thin sections of the glabrous skin. Semi-thin sections (0.5 μm) of hindlimb plantar pads of control and *TrkB*^{cKO}

mice were cut parallel to the skin surface. In **c** and **d**, mice were sacrificed at P60, and staining was done with methylene blue. Red arrowheads: cytoplasmic processes of lamellar cells; black arrows: nerve terminals (densely stained). In **e** and **f**, mice were sacrificed at P12, and staining was performed with toluidine blue. Red arrowheads: pre-mature corpuscle, white arrows: large caliber nerve fibers. No Schwann cells were observed in the dermal papillae of adult or P12 *TrkB*^{cKO} mice. These experiments were performed in 2 animals per age with similar results.

(**g**) A forelimb palmar pad section of a P14 *TrkB*^{cKO}*; Ret*^{CFP} mouse stained with anti-GFP and anti-NFH antibodies. The majority of the NFH^{+} fibers present in glabrous skin dermal papillae at P14 are CFP^{+}. This experiment was performed in 2 mice with similar results. (scale bar = 50 μm)

(**h, i**) Hindlimb plantar pad sections of control and *DhhCre; TrkB*$^{flox/flox}$ mice at P20 stained with anti-S100 antibody. *DhhCre* mice express Cre recombinase in all Schwann cells. (scale bar = 50 μm)

(**j**) Quantification of the number of Meissner corpuscles in control and *DhhCre; TrkB*$^{flox/flox}$ mice at P20. Meissner corpuscles in the bottom two palmar pads of each forelimb were counted (3 mice for each genotype). Black bars represent means.

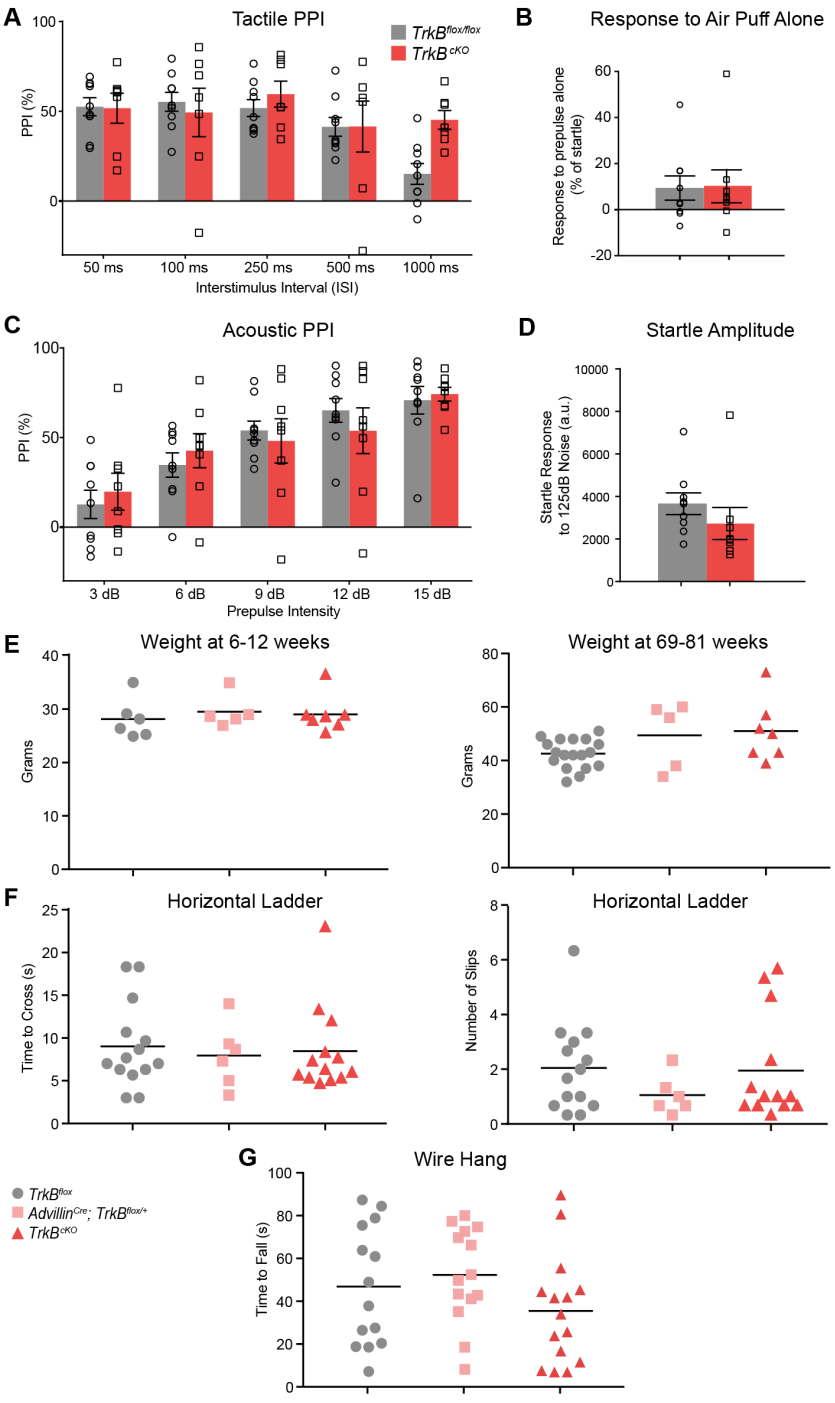

Supplementary Figure 4.3. *TrkB*^{cKO} mice have normal hairy skin sensitivity and are overtly normal

(**a**) Percent inhibition of the startle response to a 125-dB noise (pulse), when the startle noise was preceded by a light air puff (prepulse, 0.9 PSI, 50 ms) applied to the back hairy skin at multiple inter-stimulus intervals (ISIs) between the prepulse and the pulse, for *TrkB*^{cKO} mutant mice and control littermates. Repeated measures, two-way ANOVA: no significant differences between genotypes.

(**b**) Response to a light air puff (0.9 PSI, 50 ms) applied to the back hairy skin, for *TrkB*^{cKO} mutant mice and control littermates. Responses are expressed as a percent of startle response to a 125-dB noise. Student's t-test, not significant. N= 9 (control littermates) and 8 (*TrkB*^{cKO} mutants).

(**c**) Percent inhibition of the startle response to a 125-dB noise (pulse), when the startle noise is preceded by a non-startling tone prepulse (80 dB for 20 ms, with a 100 ms ISI) in *TrkB*^{cKO} mutant mice and control littermates. Repeated measures, two-way ANOVA: no significant differences between genotypes.

(**d**) Magnitude of startle response to a 125-dB noise in *TrkB*^{cKO} mutant mice and control littermates. Student's t-test, not significant.

(**e**) Left: Weights of adult (6-12 weeks old) male control and *TrkB*^{cKO} mice are similar. Right: Weights of aged adult (69-81 weeks old) control and *TrkB*^{cKO} mice are also similar. Black bars represent means.

(**f**) *TrkB*^{cKO} mice performed similarly to controls when crossing a horizontal ladder. Each point represents the average of three trials for each animal, and black bars represent means.

(**g**) *TrkB*^{cKO} mice performed similarly to controls when hanging from a suspended wire. Each point represents the average of three trials for each animal, and black bars represent means.

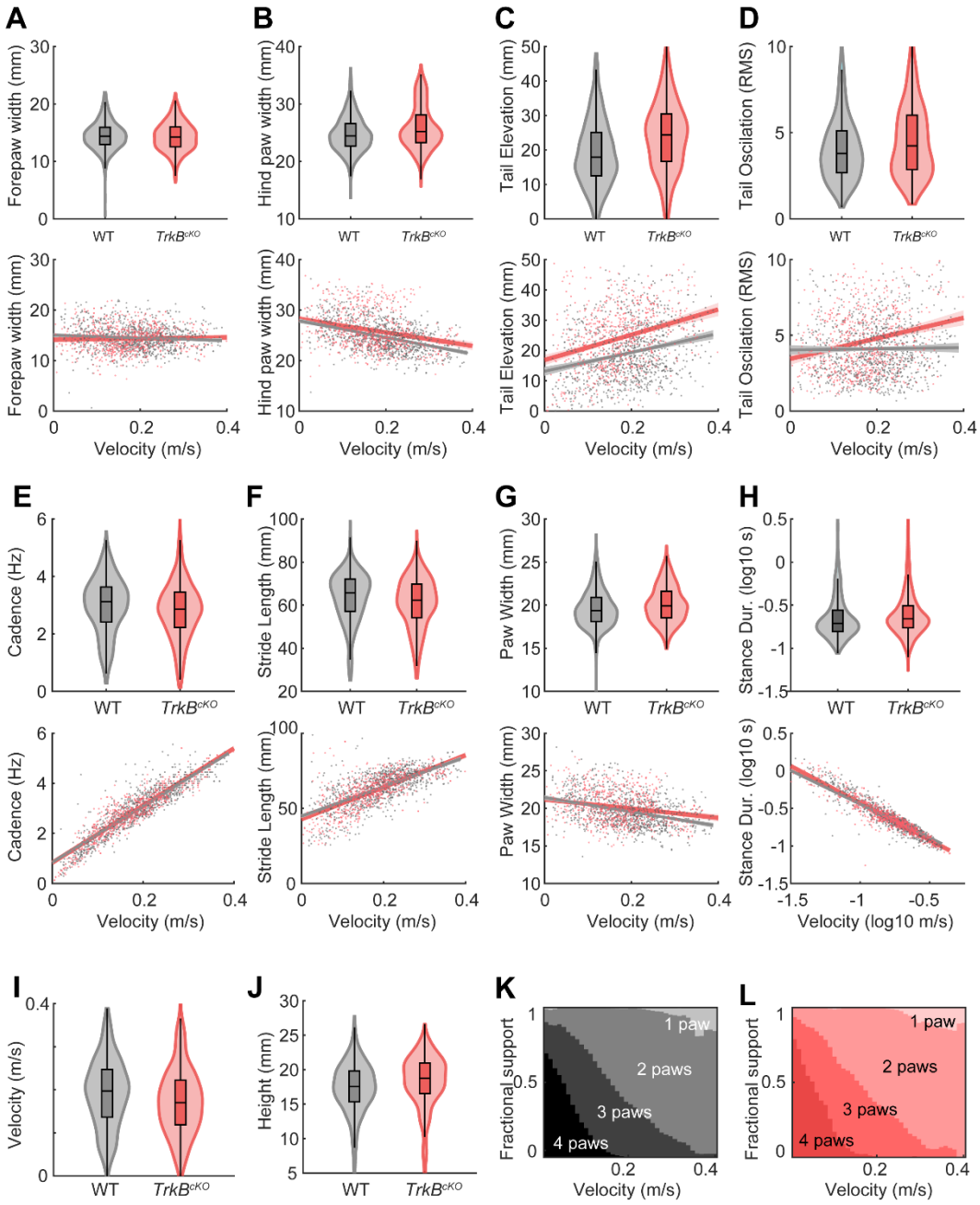

Supplementary Figure 4.4. *TrkB*^{cKO} mice have normal gait but more tail oscillation is observed at higher velocity

(**a-h**) Violin plots (top) and regression analyses with velocity as an independent variable (bottom) for animal forepaw width (**a**), hindpaw width (**b**), tail elevation (**c**), tail oscillation (**d**), cadence (**e**), stride length (**f**), paw width (contralateral forepaw to hindpaw) (**g**), average stance duration (**h**) for control mice in grey and *TrkB*^{cKO} mice in red.

(**i, j**) Violin plots for velocity (**i**) and height (**j**).

(**k, l**) Fraction of time during a single gait cycle for a given velocity when the subject had four (darkest) to one (lightest) paws on the floor for support. Control mice in grey and *TrkB*^{cKO} mice in red.

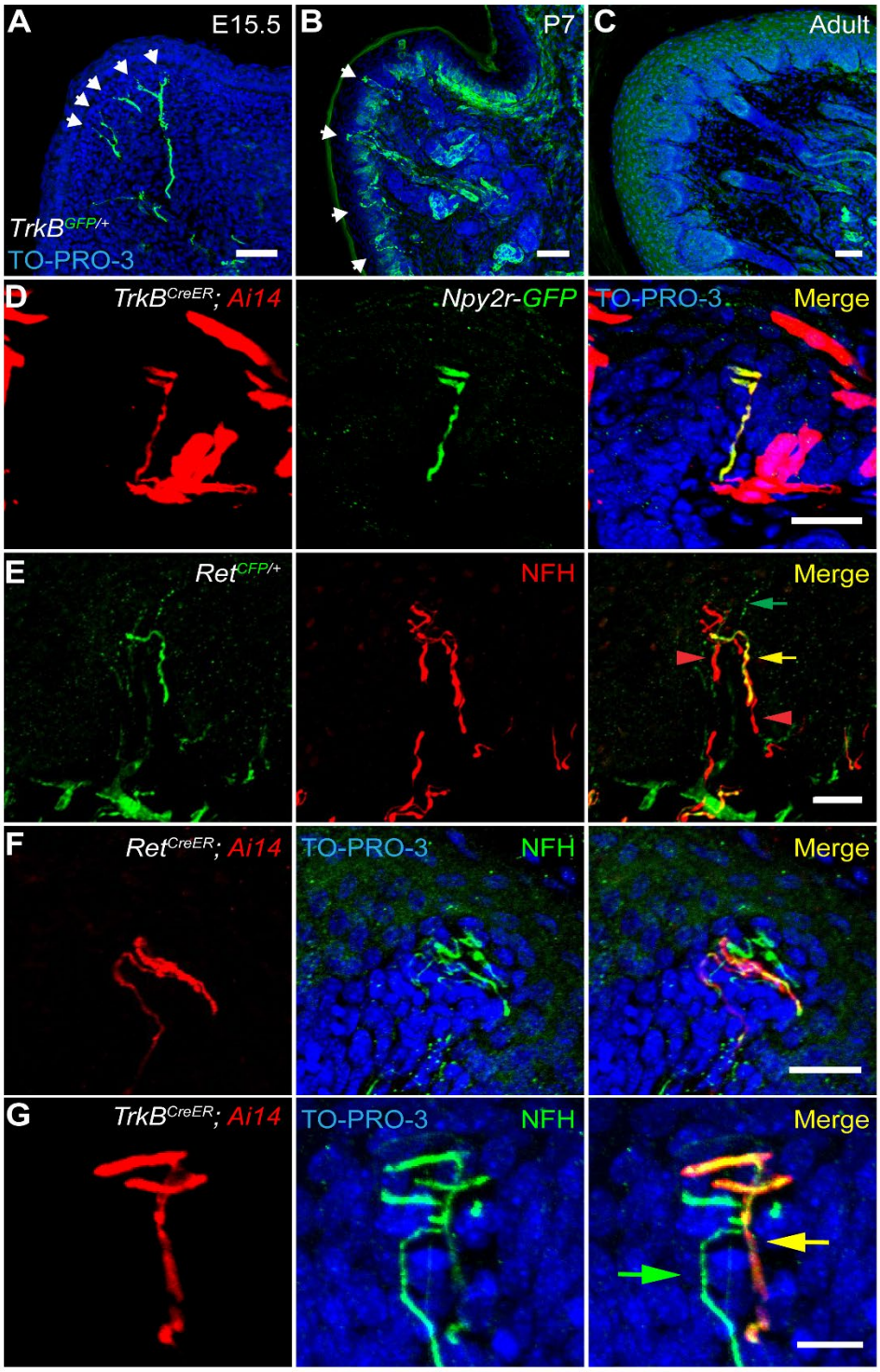

Supplementary Figure 4.5. TrkB$^+$ and Ret$^+$ neurons innervating Meissner corpuscles are distinct populations of neurofilament-positive afferents

(**a-c**) Forelimb palmar pad sections of *TrkB^{GFP}* mice at different developmental stages stained with anti-GFP and TO-PRO-3. Note that GFP is expressed in Meissner corpuscle afferents at an early age (P7), but not in adults. These experiments were performed in multiple animals with similar results (**a**: 2 mice, **b**: 4 mice, **c**: 2 mice). (scale bar = 50 μm)

(**d**) Glabrous skin section of a P20 *TrkB^{CreER}; Ai14; Npy2r-GFP* mouse treated with tamoxifen at P5 to permanently label early TrkB$^+$ neurons. Section was stained with anti-DsRed, anti-GFP, and TO-PRO-3. Result observed in 6 corpuscles of 1 mouse. (scale bar = 25 μm)

(**e**) A hindlimb digital pad section of a P50 *Ret^{CFP}* mouse stained with anti-GFP and anti-NFH antibodies. This experiment was performed in 3 mice with similar results. Yellow arrow: CFP$^+$/NFH$^+$ Ret fiber. Green arrow: CFP$^+$/NFH$^-$ nonpeptidergic C-fiber. Red arrowheads: NFH$^+$/CFP$^-$ fibers. (scale bar = 25 μm)

(**f**) Forelimb pedal pad section of a P20 *Ret^{CreER}; Ai14* mouse treated with tamoxifen at E10.5-E11.5. Section was stained with anti-NFH antibody and TO-PRO-3. This experiment was performed in 2 mice with similar results. (scale bar = 25 μm)

(**g**) A hindlimb digital pad section of a P50 *TrkB^{CreER}; Ai14* mouse treated with tamoxifen at E16.5 (same mouse as used in **Fig. 4.3b**). Section was stained with anti-DsRed, anti-NFH, and TO-PRO-3. This experiment was performed in 3 mice with similar results. (scale bar = 12.5 μm).

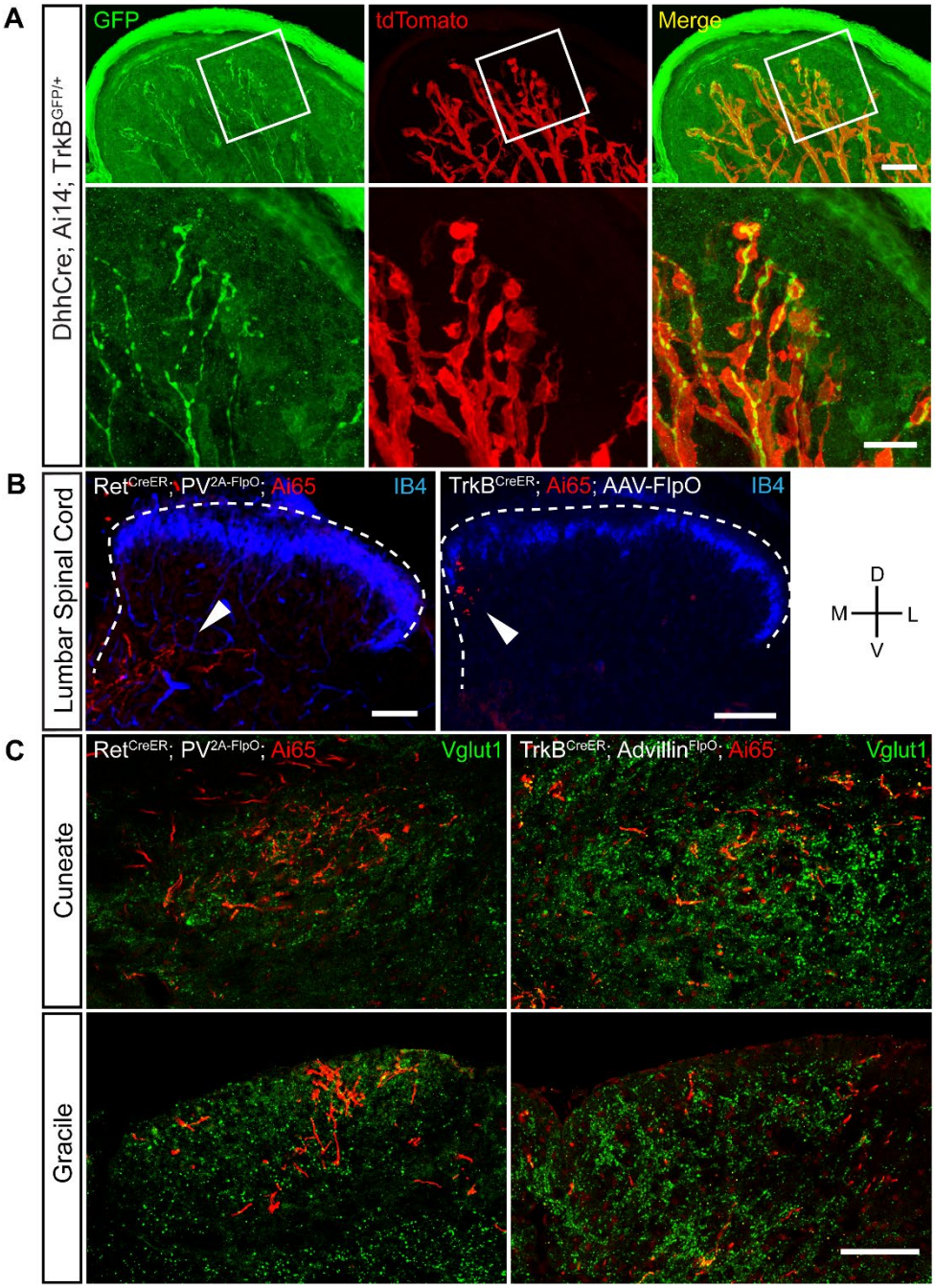

Supplementary Figure 4.6. Schwann cells are associated with TrkB-expressing fibers in dermal papillae during development and both TrkB⁺ and Ret⁺ Meissner corpuscle afferents form projections in the spinal cord and DCN

(**a**) Upper panels: A forelimb palmar pad section of a P5 *DhhCre; TrkB^{GFP}; Ai14* mouse stained with anti-GFP antibody. Schwann cells have not yet differentiated into lamellar cells at this age. TdTomato, which is expressed in Schwann cells, was detected via direct fluorescence. For each GFP⁺ fiber in dermal

papillae, there are Schwann cell(s) associated with its tip. Lower panels: enlarged views of the region cropped in upper panels. This experiment was performed in 3 mice with similar results. (scale bars = 50 μm)

(**b**) Transverse sections of lumbar spinal cords. Left panel is from a P21 *Ret^{CreER}; PV$^{2A\text{-}FlpO}$; Rosa26$^{LSL\text{-}FSF\text{-}tdTomato}$* (*Ai65)* mouse treated with tamoxifen at E11.5 and E12.5 (similar results were observed in three mice), and right panel is from an adult *TrkB^{CreER}; Ai65* mouse treated with tamoxifen at P5 and given an injection of AAV-FlpO to a glabrous hindlimb pedal pad to achieve labeling of a single TrkB^{+} Meissner afferent (a second section from this animal and sections from the other three animals are in **Supplementary Fig. 4.6**). Both sections were stained with anti-DsRed antibody and IB4. Arrowheads indicate dorsal horn collaterals. (scale bars = 100 μm, D = dorsal, V = ventral, M = medial, L = lateral)

(**c**) Transverse sections of the medulla at the level of the cuneate and gracile nuclei of the DCN. Left panels are from a P21 *Ret^{CreER}; PV$^{2A\text{-}FlpO}$; Ai65* mouse treated with tamoxifen at E11.5 and E12.5 (DCN innervation observed in 3/3 mice), and right panels are from a P23 *TrkB^{CreER}; Advillin^{FlpO}; Ai65* mouse treated with tamoxifen at E13.5 and E14.5 (DCN innervation observed in this mouse and another adult mouse given tamoxifen at P4). All sections were stained with anti-Vglut1 and anti-DsRed antibodies. (scale bar = 100 μm; D = dorsal, V = ventral, M = medial, L = lateral)

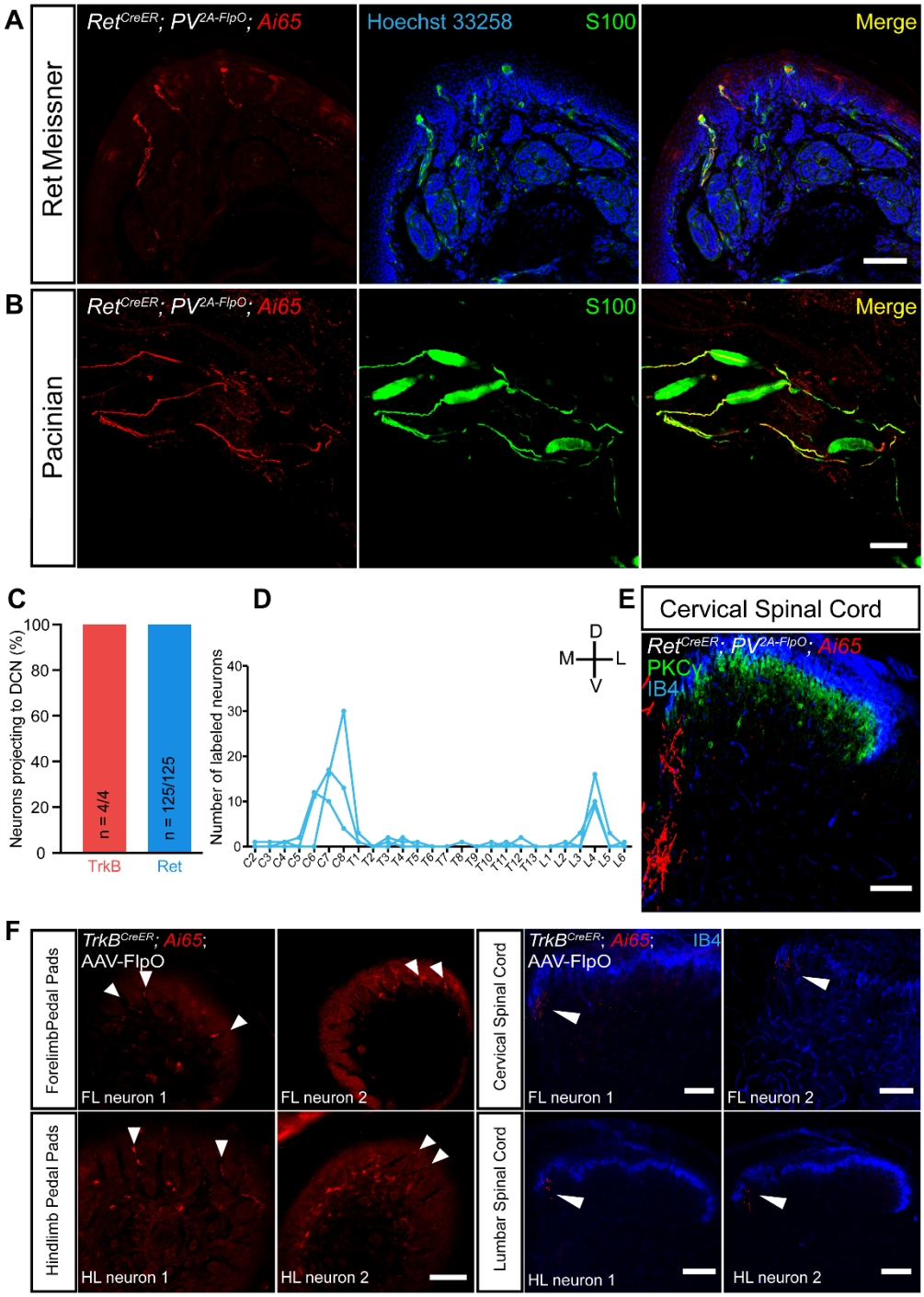

Supplementary Figure 4.7. TrkB⁺ and Ret⁺ Meissner corpuscle afferents display typical Aβ-LTMR morphology in the central nervous system

(**a, b**) A Ret-parvalbumin intersectional genetic strategy predominantly labels Ret⁺ neurons innervating Meissner and Pacinian corpuscles. No tdTomato⁺ neurons were observed in back and hindlimb hairy skin or in proprioceptors of the anterior tibialis muscle. **a** is a digital pad section from a P21 *Ret^{CreER}; PV$^{2A-FlpO}$;*

Ai65 mouse treated with tamoxifen at E11.5 and E12.5. Anti-S100 antibody labels Meissner corpuscles in the dermal papillae and Schwann cells surrounding the innervating sensory neurons. **b** is whole-mount immunostaining of Pacinian corpuscles located in the periosteum of the fibula from a *Ret^{CreER}; PV$^{2A\text{-}FlpO}$; Ai65* mouse. Anti-S100 antibody labels Pacinian corpuscles and Schwann cells surrounding the innervating sensory neurons. Skin sections and whole-mount Pacinian corpuscles were stained with anti-DsRed antibody. This experiment was performed in 3 mice with similar results. (scale bars = 100 μm).

(**c**) Percentage of TrkB^{+} pedal pad Meissner neurons traveling to the DCN via the dorsal columns at the transition between cervical spinal levels and the medulla (4/4 neurons from 4 *TrkB^{CreER}; Ai65* mice with AAV-FlpO injection into the pedal pads, 2 hindlimb and 2 forelimb), and percentage of Ret^{+}/PV^{+} neurons (Pacinian and Meissner afferents, see **Supplementary Fig. 4.6**) traveling to the DCN (number of neurons in the dorsal column at the medulla was compared to number of fluorescent neurons in the DRG, 2 *Ret^{CreER}; PV$^{2A\text{-}FlpO}$; Ai65* mice, 76/76 and 49/49 neurons labeled in the DRG, respectively). Note that the dual genetic/paw virus injection strategy has a low labeling efficiency and marks few neurons per animal.

(**d**) Number of tdTomato^{+} neurons in the DRG per spinal segment in three *Ret^{CreERT2}; PV$^{2A\text{-}FlpO}$; Ai65* mice. This is consistent with the finding that the Ret-PV intersectional strategy predominantly labels limb-level Pacinian afferents and Meissner afferents innervating glabrous skin.

(**e**) Transverse section of cervical spinal cord from a P21 *Ret^{CreER}; PV$^{2A\text{-}FlpO}$; Ai65* mouse treated with tamoxifen at E11.5 and E12.5. Section was stained with anti-DsRed, anti-PKCγ, and IB4. This experiment was performed in 3 mice with similar results. (scale bar = 100 μm; D = dorsal, V = ventral, M = medial, L = lateral)

(**f**) Peripheral terminations in the glabrous skin (arrowheads, left panels) and example spinal cord collateral morphologies (arrowheads, right panels) for single forelimb (FL) and hindlimb (HL) pedal pad neurons in adult *TrkB^{CreER}; Ai65* mice treated with tamoxifen at P5 and given an injection of AAV-FlpO to a glabrous pedal pad in order to achieve sparse labeling of a single neuron per animal. Whole-mount pedal pads were stained with anti-dsRed. Spinal cord sections were cut transversely and stained with IB4 and anti-dsRed. Another spinal cord section from HL neuron 1 is depicted in **Supplementary Fig. 4.5**. (scale bars = 100 μm; D = dorsal, V = ventral, M = medial, L = lateral)

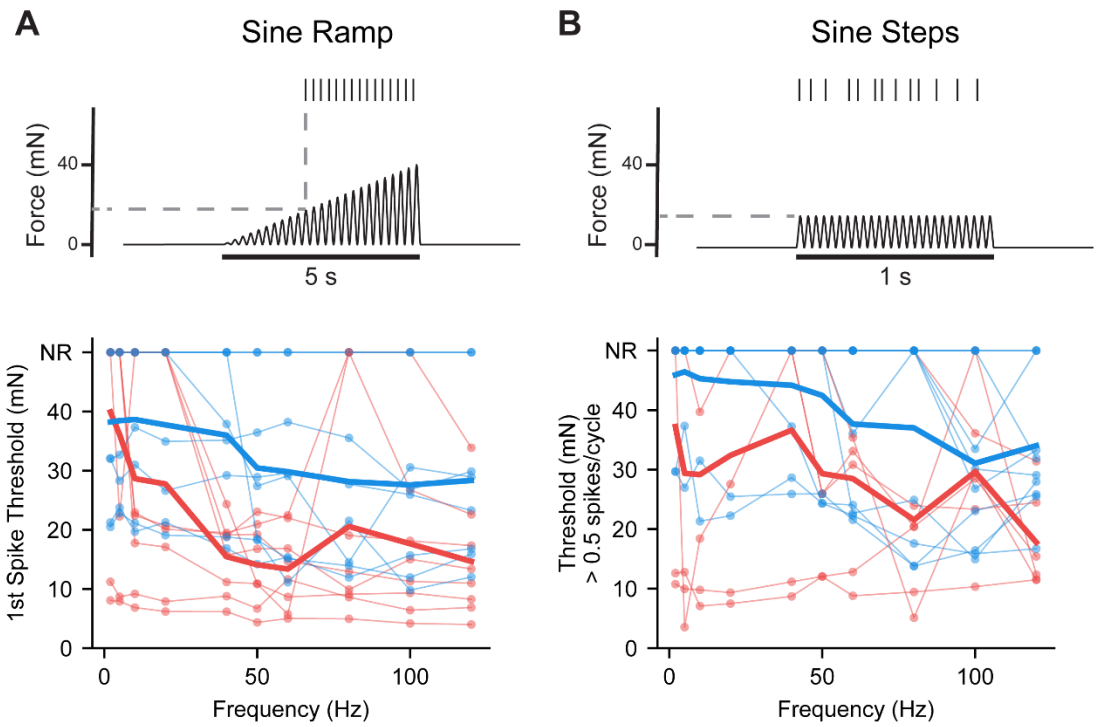

Supplementary Figure 4.8. TrkB$^+$ and Ret$^+$ Meissner afferents exhibit a wide range of frequency tuning to 2-120 Hz sinusoidal vibrations

(**a**) Top: Schematic of threshold determination to intensity-ramping sine stimuli. The threshold was measured as the force of the sine envelope at the time of the first action potential. Bottom: thresholds for individual (connected points) and mean (thick line) TrkB$^+$ (blue) and Ret$^+$ (red) Meissner afferents. NR: no response.

(**b**) Top: Schematic of threshold determination to a sine-step protocol. Intensities and frequencies were drawn at random, and the intensity at which the Meissner afferent fired greater than 0.5 spikes/cycle was considered the threshold for each frequency. Bottom: thresholds for individual (connected points) and mean (thick line) TrkB+ (blue) and Ret+ (red) Meissner afferents. NR: no response.

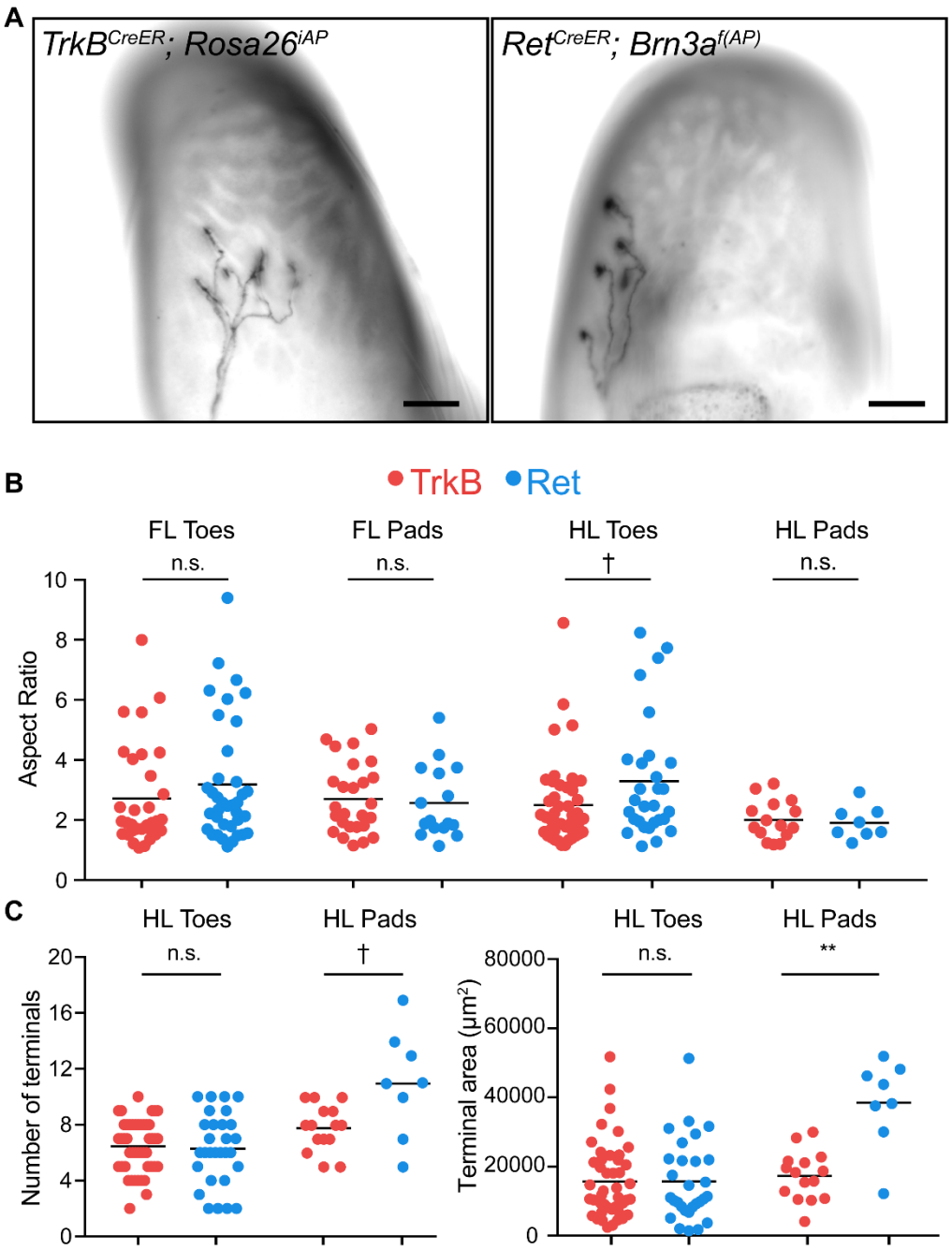

Supplementary Figure 4.9. Measurements of TrkB⁺ and Ret⁺ Meissner afferent morphological receptive fields

(**a**) Representative images of whole-mount, AP-stained digital pads of a *TrkB^{CreER}; Rosa26^{iAP}* mouse (left) and a *Ret^{CreER}; Brn3a$^{f(AP)}$* mouse (right), in which TrkB⁺ and Ret⁺ Meissner afferents were sparsely labeled using a low dose of tamoxifen, respectively. Images depict individual Meissner corpuscle afferents innervating glabrous digital pads. Analysis includes a total 119 individual TrkB⁺ afferent receptive fields

(58 forelimb and 61 hindlimb) from 21 mice for and a total of 90 individual Ret^{+} afferent receptive fields (53 forelimb and 37 hindlimb) from 21 mice. (scale bars = 100 μm)

(**b, c**) Aspect ratios (**b**, major axis/minor axis), number of terminal endings (**c**, left), and surface areas (**c**, right) of TrkB^{+} and Ret^{+} Meissner afferent morphological receptive fields measured in *TrkB^{CreER}; Rosa26^{iAP}* or *TrkB^{CreER}; Brn3a$^{f(AP)}$* mice and *Ret^{CreER}; Rosa26^{iAP}* or *Ret^{CreER}; Brn3a$^{f(AP)}$* mice. Individual measurements and mean values (black bar) are plotted for each group. Receptive field quantification plotted here and in **Fig. 4.3** includes data from 119 individual TrkB^{+} afferent receptive fields (58 forelimb and 61 hindlimb) from 21 mice and from 90 individual Ret^{+} afferent receptive fields (37 hindlimb and 53 forelimb) from 21 mice. (two-tailed Welch's t-test, mean significantly different: ** $p < .01$; F-test of the equality of variances, variance significantly different: † $p < .05$).

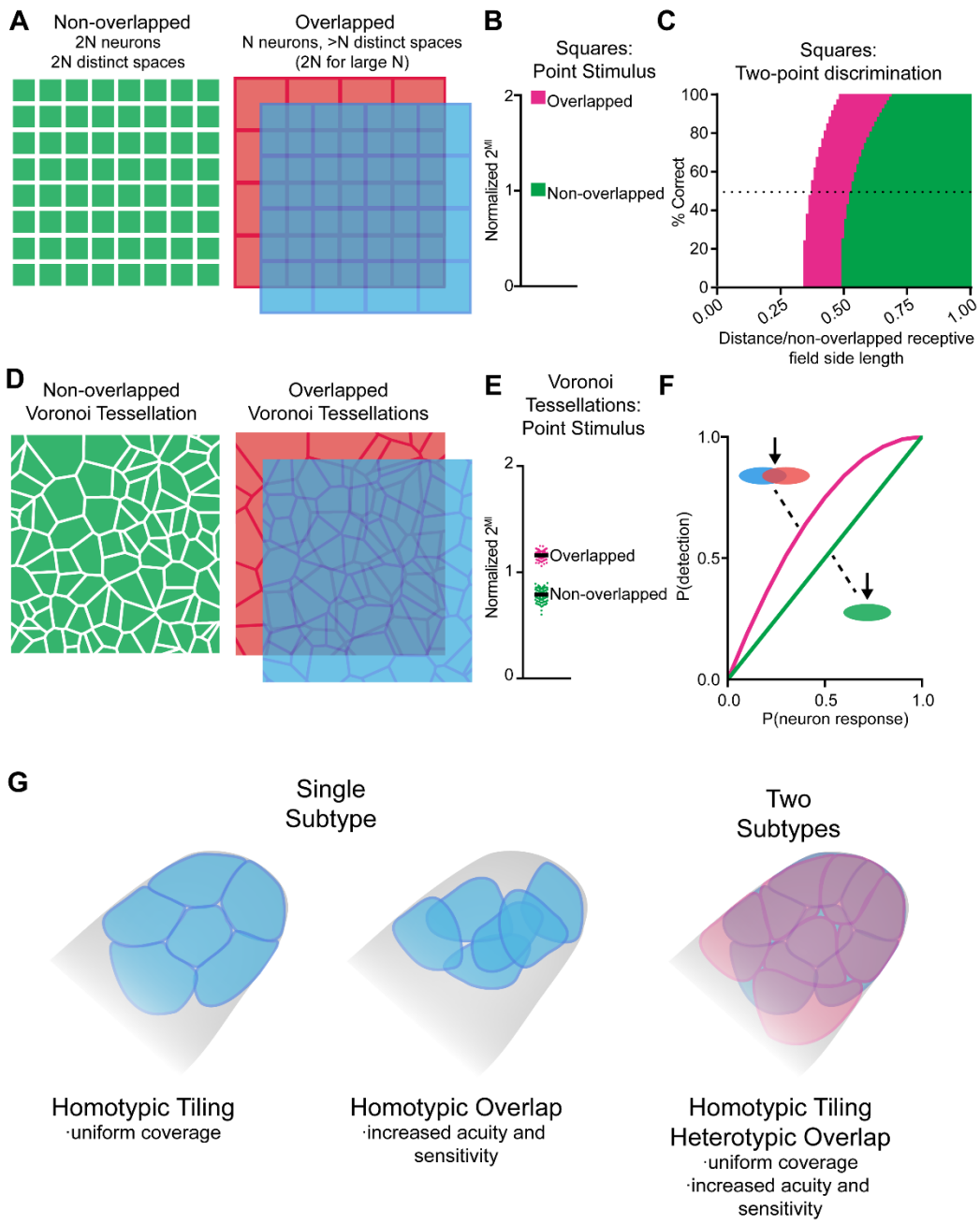

Supplementary Figure 4.10. Computational modeling suggests that heterotypic overlap of homotypically tiled mosaics, like that observed in Meissner corpuscle afferents, enables both uniform skin coverage and enhanced acuity

(**a**) Schematic demonstrating overlapped grids of homotypically tiled uniform squares (blue and red) and their equivalent non-overlapped grids (green). Overlapped receptive fields provide greater than N discriminable spaces (approaching 2N for large numbers of neurons), while non-overlapped receptive

fields would require more neurons with smaller receptive fields to achieve the same resolution (see Methods).

(**b**) Mutual information (MI) between a single pixel stimulus and the responses of simulated grids of uniform squares with overlapped and non-overlapped arrangements. Mutual information was normalized by the number of neurons ($2^{MI}/N$) such that perfect performance of a non-overlapped arrangement should be equal to 1 and perfect performance for an overlapped arrangement should be 2 (see Methods).

(**c**) Two-point discrimination ability of overlapped vs. non-overlapped grids. The two stimuli were 1) a central point and 2) a point shifted by some distance from the central point. For each distance, the point was positioned at all angles between 0 and 2π radians. The percentage of points in which the representation of the central point and the representation of the shifted point were different are plotted for each distance relative to the side lengths of the square neurons of the non-overlapped arrangement (see Methods). For a fair comparison, modeled receptive fields for the overlapped arrangement are larger than for the non-overlapped arrangement to achieve the same total number of neurons.

(**d**) Schematic of non-overlapped (left) and overlapped (right) Voronoi tessellations.

(**e**) Mutual information ($2^{MI}/N$) between a single point stimulus and the responses of overlapped and non-overlapped Voronoi tessellations generated in MATLAB (see Methods for details). Using 4000 generated tessellations, pairs of tessellations were overlapped to create 2000 overlapped mosaics. The number of neurons, N, was the number of randomly seeded points per arrangement, and MI was normalized by N to allow comparison between arrangements with different numbers of neurons. A random subset of these results is plotted: The pink circles represent the normalized MI for 100 examples of overlapped tessellations, and the green circles represent the normalized MI for 100 examples of non-overlapped tessellations. Black bars in both cases represent the overall mean.

(**f**) Probability of detection (the probability that at least one neuron responds) plotted as a function of the probability of a single neuron responding to a stimulus within its receptive field. The green line depicts the probability of detection for a single-layered arrangement of homotypically tiled neurons (P(neuron responds)). The pink line indicates the probability of detection for a double-layered arrangement of overlapping neurons assuming the neurons are independent $(1-(1-P(\text{neuron responds}))^2)$. The probability of detection is greater for an overlapping arrangement at all probabilities between 0 and 1, exclusive.

(**g**) Homotypic tiling of a single subtype of Meissner tactile afferents ensures uniform and complete coverage of the skin surface (left). On the other hand, homotypic overlap can provide higher sensitivity and acuity, but this arrangement comes at the expense of the uniformity and completeness of skin coverage ensured by a tiling mechanism (center). Combining both homotypic tiling and non-redundant heterotypic overlap through the existence of two molecularly distinct subtypes of tactile afferents ensures uniform and complete coverage of the skin while also enabling high acuity and sensitivity, using the fewest neurons (right).

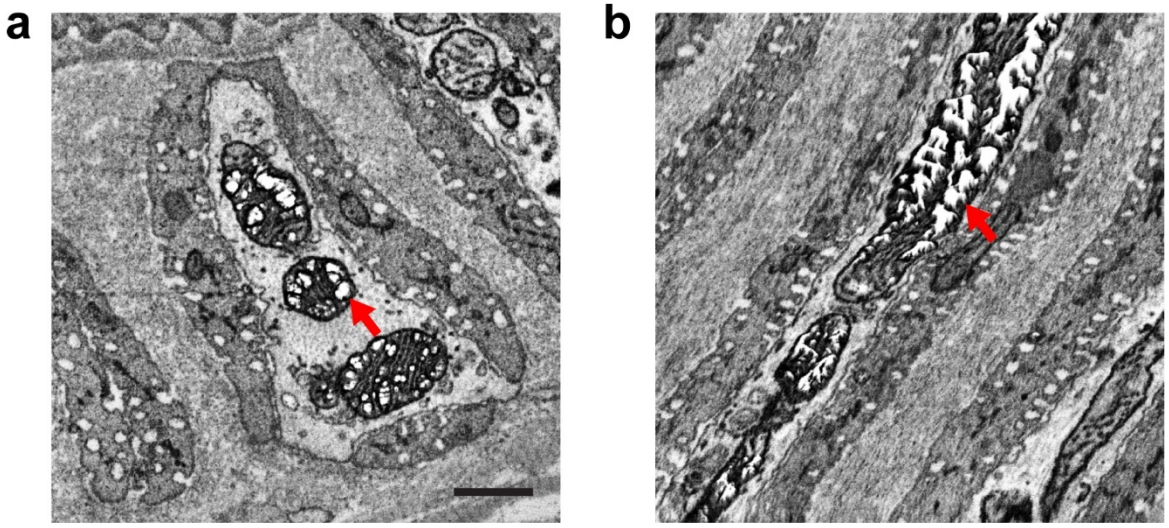

Supplementary Figure 5.1. FIB-SEM artifacts in poorly infiltrated samples

(**a**) FIB-SEM image showing prominent artifacts inside axonal mitochondria (arrow).

(**b**) FIB-SEM image showing an orthogonal plane (z-axis is vertical in this image). There is asymmetry in the z-axis in these artifacts (arrow), suggesting that they are related to the FIB milling process.

Scale bar: 0.5 µm.

Appendix 2. Detailed Electron Microscopy Staining Protocol

Treat all samples and solutions as light-sensitive (especially the ones indicated in the list of reagents) and cover plates and vials with aluminum foils at all times. Most organic reagents are moisture sensitive and therefore containers should be kept closed as much as possible and in desiccators. Most reagents used in this protocol are highly toxic, and therefore appropriate personal protective equipment should be worn at all times and exposures should be minimized by using a fume hood.

DAB staining:

All steps are done at room temperature (r.t.) unless otherwise specified.

1. Sacrifice the animal 2-3 weeks after AAV injection by transcardial perfusion with warm (37 °C) Ames' medium with heparin (equilibrated with carbogen: 95% O_2, 5% CO_2) to clear blood, followed by warm (37 °C) 2.5% glutaraldehyde, 2% paraformaldehyde in cacodylate buffer. Post-fix the sample using the same fixative at 4 °C overnight. If transcardial perfusion is known to not fix your particular type of samples well, fix your samples with an alternative protocol, but use the fixative described above. Note if no blood clearing is done you will see strong endogenous peroxidase labeling of red blood cells, which may interfere with the observation of peroxidase staining in LM but does not usually cause any issue in EM analysis.
2. Wash the sample with cacodylate buffer, and section the sample with a vibratome at 100-200 µm in cacodylate buffer. Use low melting point agarose for embedding if possible to minimize thermal denaturation of the enzyme. Trim the sections to include only the area expected to have staining. This and the following DAB staining steps should be done as soon as the post-fixation is done, as we have noticed loss of enzyme activity over time in storage.
3. Use a shaker or rotator for all staining steps to ensure even staining. Place one section per well in 12-well or 24-well plates. Wash the sections for 2×10 min with 50 mM glycine in cacodylate buffer to quench aldehyde fixatives, and then wash the sections for 1×10 min with cacodylate buffer.

4. Incubate the sections in 1 mL of 0.3 mg/mL 3,3'-diaminobenzidine tetrahydrochloride hydrate (DAB, corresponds to ~ 0.16 mg/mL of the free base, assuming 9.5% water content) in cacodylate buffer for 30 min. Add 10 µL of 0.3% H_2O_2 in cacodylate buffer directly into the DAB solution (to a final H_2O_2 concentration of 0.003%) and mix well to initiate the peroxidase staining reaction. Allow the reaction to proceed for 1 hr. If higher staining solution volume is needed, scale up volumes of reagents proportionally.
5. Wash the sections with cacodylate buffer for 4×10 min. Post-fix in 3% glutaraldehyde in cacodylate buffer at 4 °C overnight.
6. Wash sections in cacodylate buffer for 1×10 min, and then in 50 mM glycine in cacodylate buffer for 1×10 min, and finally in cacodylate buffer for 2×10 min. Samples can be stored at 4 °C for a few days before further processing without apparent issues.

EM sample preparation:

Use a shaker or rotator for all staining steps to ensure even staining. Use glass scintillation vials for EM preparation.

For typical TEM applications, ***1) Normal-contrast TEM protocol*** is recommended. If high sample electron contrast is required, such as imaging using SEM or certain TEM platforms, follow ***2) SEM or High-contrast TEM protocol***.

1) Normal-contrast TEM protocol:

Day 1:

1. Stain in 1% osmium tetroxide/1.5% potassium ferrocyanide in cacodylate buffer at r.t. for 1 hr. Place filter paper and weights on top of sections for the first 15 min to flatten the sections if necessary.

2. Wash sections in ddH_2O for 4×5 min.
3. Stain in 1% uranyl acetate in 0.05 M maleate buffer at 4 °C overnight.

Day 2:

1. Wash sections in ddH_2O for 4×5 min.
2. Dehydrate the sections with 50 % EtOH at 4 °C for 5 min.
3. Dehydrate the sections with 70 % EtOH at 4 °C for 5 min.
4. Dehydrate the sections with 90 % EtOH at 4 °C for 5 min.
5. Dehydrate the sections with 95 % EtOH for 3×10 min, with the first wash warm to r.t. from 4 °C, and second and third washes at r.t.
6. Dehydrate the sections with 100 % EtOH at r.t. for 3×20 min.
7. Exchange the sections into propylene oxide for 2×30 min.
8. Infiltrate the sections with 20% resin mix in propylene oxide for 1 hr.
9. Infiltrate the sections with 40% resin mix in propylene oxide for 1 hr.
10. Infiltrate the sections with 50% resin mix in propylene oxide overnight.

Day 3:

1. Infiltrate the sections with 60% resin mix in propylene oxide for 1 hr.
2. Infiltrate the sections with 80% resin mix in propylene oxide for 1 hr.
3. Infiltrate the sections with 100% resin mix for 1 hr.
4. De-gas the samples under vacuum for 1 hr.
5. Embed the sections in 100% resin mix and cure at 60 °C for 48-72 hrs. Samples can be stored indefinitely at r.t. after curing.

Sample imaging considerations:

1. Section at 30-40 nm for best resolution.
2. We pick up sections on Formvar or Pioloform films coated with carbon. Other types of sample support may work but may have different properties under the electron beam.
3. Do not stain with lead citrate or uranyl acetate on ultrathin sections, as extra staining could obscure the DAB signal. Samples should have sufficient contrast when imaged with a digital camera.

2) SEM or High-contrast TEM protocol (modified from Hua et al. (2015)):

Day 1:

1. Stain in 2% osmium tetroxide in cacodylate buffer at r.t. for 1 hr. Place filter paper and weights on top of sections for the first 15 min to flatten the sections if necessary.
2. Stain in 2.5% potassium ferrocyanide in cacodylate buffer at r.t. for 1 hr.
3. Wash sections in ddH_2O for 4×5 min.
4. Stain in 1% thiocarbohydrazide in ddH_2O at 40 °C for 15 min.
5. Wash sections in ddH_2O for 4×5 min.
6. Stain in 2% osmium tetroxide in ddH_2O at r.t. for 1 hr.
7. Wash sections in ddH_2O for 4×5 min.
8. Stain in 1% uranyl acetate in 0.05 M maleate buffer at 4 °C overnight.

Day 2:

1. Heat sections in uranyl acetate solution to 50 °C for 2 hrs.
2. Wash sections in ddH_2O for 4×5 min.
3. Dehydrate the sections with 50 % EtOH at 4 °C for 5 min.
4. Dehydrate the sections with 70 % EtOH at 4 °C for 5 min.
5. Dehydrate the sections with 90 % EtOH at 4 °C for 5 min.

6. Dehydrate the sections with 95 % EtOH for 3×10 min, with the first wash warm to r.t. from 4 °C, and second and third washes at r.t.
7. Dehydrate the sections with 100 % EtOH at r.t. for 3×20 min.
8. Exchange the sections into propylene oxide for 2×30 min.
9. Infiltrate the sections with 20% resin mix in propylene oxide for 1 hr.
10. Infiltrate the sections with 40% resin mix in propylene oxide for 1 hr.
11. Infiltrate the sections with 50% resin mix in propylene oxide overnight.

Day 3:

1. Infiltrate the sections with 60% resin mix in propylene oxide for 1 hr.
2. Infiltrate the sections with 80% resin mix in propylene oxide for 1 hr.
3. Infiltrate the sections with 100% resin mix for 1 hr.
4. De-gas the samples under vacuum for 1 hr.
5. Embed the sections in 100% resin mix and cure at 60 °C for 48-72 hrs. Samples can be stored indefinitely at r.t. after curing.

Special considerations for using Matrix-dAPEX2 and IMS-dAPEX2:

1. This protocol leads to strong staining in the IMS for mitochondria labeled with Matrix-dAPEX2 (see **Supplementary Fig. 2.5**). This is preferred because this IMS staining pattern is usually not obscured with heavy counterstaining required for SEM. Do not use IMS-dAPEX2 with this protocol, as it has a smaller range of optimal expression level than Matrix-dAPEX2 and often not distinguishable from Matrix-dAPEX2 under this staining condition.

2. Consider examining ultrathin sections with TEM first to determine the percentage of mitochondria with IMS staining when using Matrix-dAPEX2 with SEM. If the percentage is too low, you can increase the DAB concentration to 0.5 mg/mL and see if IMS staining becomes more prevalent.

Sample imaging considerations:

1. Section at 30-40 nm for best resolution. We use the same sectioning and pickup setup as in Kasthuri *et al.*, 2014.
2. Stain with lead citrate and uranyl acetate on sections to increase contrast.
3. Ultrathin sections can be imaged with SEM using either backscattered electrons or secondary electrons. Postsynaptic densities tend to be more prominent using backscattered electrons, but imaging using secondary electrons can be substantially faster.

Catalog numbers for reagents:

Please check expiration dates and stability of chemicals and avoid using degraded chemicals.

Ames' medium: Sigma A1420

Sodium bicarbonate: Sigma-Aldrich 792519

Heparin: Sigma-Aldrich H3393

Glutaraldehyde: Electron Microscopy Sciences 16316

Paraformaldehyde: Electron Microscopy Sciences 15712

Sodium cacodylate: Electron Microscopy Sciences 12310

Hydrochloric acid: Fisher A144SI-212

Calcium chloride: Sigma-Aldrich 793639

Magnesium chloride hexahydrate: Sigma-Aldrich M9272

Glycine: Sigma-Aldrich 410225

3,3'-diaminobenzidine tetrahydrochloride hydrate: Sigma D5637, **light sensitive**

Hydrogen peroxide: Sigma-Aldrich 216763, **light sensitive**

Osmium tetroxide: Electron Microscopy Sciences 19190, **light sensitive**

Potassium ferrocyanide: Sigma-Aldrich P3289, **light sensitive**

Uranyl acetate: Electron Microscopy Sciences 22400, **light sensitive**, **radioactive**

Maleic acid: Sigma-Aldrich M0375

Sodium hydroxide: Fisher SS266-1

Ethanol: Sigma-Aldrich 459836

Propylene oxide: Electron Microscopy Sciences 20411

LX-112: Ladd Research 21310

DDSA: Electron Microscopy Sciences 13710

NMA: Electron Microscopy Sciences 19000

DMP-30: Electron Microscopy Sciences 13600

SEM or High-contrast TEM protocol only:

Thiocarbohydrazide: Electron Microscopy Sciences 21900, **light sensitive**

Protocols for solution preparation:

Ames' medium with heparin (10 U/mL)

Dissolve the Ames' medium powder in appropriate amounts of ddH_2O. Gas the solution with 100% CO_2, and then slowly add sodium bicarbonate at 1.9 g/L. Make sure no precipitates are formed. Dissolve heparin in ddH_2O to make a 10 kU/mL solution. Add 1 mL of 10 kU/mL heparin solution per 1 L of Ames' medium. Filter the solution with a 0.22 μm filter and store at 4 °C.

Cacodylate buffer (0.15 M sodium cacodylate, 4 mM $CaCl_2$, 4 mM $MgCl_2$, pH 7.4)

Dissolve sodium cacodylate (64.21 g for 1 L), calcium chloride (0.89 g for 1 L) and magnesium chloride hexahydrate (1.63 g for 1 L) in ddH_2O to make a 0.3 M sodium cacodylate, 8 mM calcium chloride, 8 mM magnesium chloride solution. Adjust pH to 7.4 with 12 M hydrochloric acid. Filter the solution with a 0.22

μm filter and store at 4 °C. Mix equal volumes of 0.3 M sodium cacodylate, 8 mM calcium chloride, 8 mM magnesium chloride solution (pH 7.4) and ddH_2O to make cacodylate buffer. Store at 4 °C.

DAB stock solution

Dissolve 3,3'-diaminobenzidine tetrahydrochloride hydrate in ddH_2O to make a 50 mg/mL solution. Aliquot and store the solution at -20 °C. Thaw the solution just before use and vortex to dissolve all solids. The solution can be refrozen for repeated uses but should be discarded when significant color appears in the solution.

1% uranyl acetate in 0.05 M maleate buffer (pH 5.15)

Dissolve 11.6 g of maleic acid with 100 mL 1 N sodium hydroxide solution and bring up the volume to 500 mL with ddH_2O to make a 0.2 M sodium maleate solution. Combine 100 mL of 0.2 M sodium maleate solution, 10.76 mL 1 N sodium hydroxide solution, bring up the volume to 400 mL with ddH_2O and verify that pH is 6.0, and then add 4 g of uranyl acetate to make 1% uranyl acetate in 0.05 M maleate buffer. Filter the solution with a 0.22 μm filter and store at 4 °C.

Resin mix

	~ 60 g total	~ 30 g total
Resin (WPE = 143)	30.00 g	15.00 g
DDSA	16.38 g	8.19 g
NMA	15.21 g	7.61 g
DMP-30	0.78 g	0.39 g

Mix the first three components together thoroughly for 5 min by hand. Then add DMP-30 and mix for another 5 min. Use the freshly prepared resin mix immediately for infiltration and do not store and reuse

the resin mix, as polymerization occurs immediately after all the components are mixed in leading to increasing viscosity, even at r.t.

This resin mix is equivalent to the 5 mL/5 mL Mixture A/Mixture B combination in Luft, 1961. We used LX-112 as the resin. We have not tried other types of resins, but they may also give comparable results. Different infiltration/embedding schedules may need to be used if using other types of resins or processing hard to infiltrate sample types.

For consistent results, adjust the amounts of components using the WPE specific to your batch of resin. To calculate the amounts of components, multiply the amounts of DDSA and NMA in the table above by 143 / WPE. Then, for each gram of increase/decrease of total anhydrides (DDSA + NMA), increase/decrease the amount of DMP-30 by 0.0132 g. For example, if the WPE of your resin is 160, then for 30.00 g of resin, you will need 16.38 * 143 / 160 = 14.64 g of DDSA, 15.21 * 143 / 160 = 13.59 g of NMA, and 0.78 - (1.74 + 1.62) * 0.0132 = 0.74 g of DMP-30.

Normal-contrast TEM protocol only:

1% osmium tetroxide/1.5% potassium ferrocyanide in cacodylate buffer

Mix equal volumes of 4% osmium tetroxide and ddH_2O to make a 2% osmium tetroxide solution. Dissolve potassium ferrocyanide in 0.3 M sodium cacodylate, 8 mM calcium chloride, 8 mM magnesium chloride solution (pH 7.4) to make a 3% potassium ferrocyanide solution. Add equal volumes of the 3% potassium ferrocyanide solution dropwise to the 2% osmium tetroxide solution, and then mix well to make 1% osmium tetroxide/1.5% potassium ferrocyanide in cacodylate buffer.

SEM or High-contrast TEM protocol only:

2% osmium tetroxide in cacodylate buffer

Mix equal volumes of 4% osmium tetroxide and 0.3 M sodium cacodylate, 8 mM calcium chloride, 8 mM magnesium chloride solution (pH 7.4) to make 2% osmium tetroxide in cacodylate buffer.

2.5% potassium ferrocyanide in cacodylate buffer

Dissolve potassium ferrocyanide in cacodylate buffer to make 2.5% potassium ferrocyanide in cacodylate buffer.

1% thiocarbohydrazide solution

This solution needs to be freshly made every time. Add thiocarbohydrazide to ddH_2O for a 1% solution. Warm up the mixture to 60 °C and vortex to dissolve thiocarbohydrazide, then cool it down to 40 °C and filter it with a 0.22 μm filter before use.

Troubleshooting:

1) Low staining intensity observed in light microscopy

1. Inadequate enzyme expression level: check virus injection quality, virus concentration, suitability of viral delivery route, recombinase activity, etc.
2. Degraded enzyme: conduct DAB staining immediately after post-fixation and do not store the samples, avoid exposing tissues to high temperatures.
3. Degraded chemicals: replace chemical stocks, especially hydrogen peroxide and DAB.
4. Insufficient/inappropriate mixing of chemicals: mix chemicals well.
5. Using SV-HRP construct: this construct does not usually give strong staining observable in light microscopy, proceed to conduct electron microscopy.

2) Low staining intensity observed in electron microscopy

1. Check issues and solutions in ***1)***.
2. Lead citrate and uranyl acetate staining used on ultrathin sections with ***Normal-contrast TEM protocol***: do not use additional staining.
3. Poor ultrathin section: image other ultrathin sections from the same sample.
4. Insufficient staining penetration in the center of the sample: reduce sample thickness.

3) Abnormal organelle ultrastructure

1. Excessive enzyme expression level: most typically seen with IMS-dAPEX2, reduce virus volume and/or concentration.

4) Poor tissue ultrastructure

1. Poor fixation: prepare new samples with better fixation.
2. Physical injury from virus injections: use finer needles, inject more slowly, inject lower volumes, etc.

References

Abraira, V.E., and Ginty, D.D. (2013). The sensory neurons of touch. Neuron *79*, 618-639.

Abraira, V.E., Kuehn, E.D., Chirila, A.M., Springel, M.W., Toliver, A.A., Zimmerman, A.L., Orefice, L.L., Boyle, K.A., Bai, L., Song, B.J.*, et al.* (2017). The Cellular and Synaptic Architecture of the Mechanosensory Dorsal Horn. Cell *168*, 295-310 e219.

Adams, S.R., Mackey, M.R., Ramachandra, R., Palida Lemieux, S.F., Steinbach, P., Bushong, E.A., Butko, M.T., Giepmans, B.N.G., Ellisman, M.H., and Tsien, R.Y. (2016). Multicolor Electron Microscopy for Simultaneous Visualization of Multiple Molecular Species. Cell Chem Biol *23*, 1417-1427.

Alvarez, F.J., Kavookjian, A.M., and Light, A.R. (1993). Ultrastructural morphology, synaptic relationships, and CGRP immunoreactivity of physiologically identified C-fiber terminals in the monkey spinal cord. J Comp Neurol *329*, 472-490.

Andreone, B.J., Chow, B.W., Tata, A., Lacoste, B., Ben-Zvi, A., Bullock, K., Deik, A.A., Ginty, D.D., Clish, C.B., and Gu, C. (2017). Blood-Brain Barrier Permeability Is Regulated by Lipid Transport-Dependent Suppression of Caveolae-Mediated Transcytosis. Neuron *94*, 581-594 e585.

Atasoy, D., Betley, J.N., Li, W.P., Su, H.H., Sertel, S.M., Scheffer, L.K., Simpson, J.H., Fetter, R.D., and Sternson, S.M. (2014). A genetically specified connectomics approach applied to long-range feeding regulatory circuits. Nat Neurosci *17*, 1830-1839.

Badea, T.C., Cahill, H., Ecker, J., Hattar, S., and Nathans, J. (2009a). Distinct roles of transcription factors brn3a and brn3b in controlling the development, morphology, and function of retinal ganglion cells. Neuron *61*, 852-864.

Badea, T.C., Hua, Z.L., Smallwood, P.M., Williams, J., Rotolo, T., Ye, X., and Nathans, J. (2009b). New mouse lines for the analysis of neuronal morphology using CreER(T)/loxP-directed sparse labeling. PLoS One *4*, e7859.

Bai, L., Lehnert, B.P., Liu, J., Neubarth, N.L., Dickendesher, T.L., Nwe, P.H., Cassidy, C., Woodbury, C.J., and Ginty, D.D. (2015). Genetic Identification of an Expansive Mechanoreceptor Sensitive to Skin Stroking. Cell *163*, 1783-1795.

Bannatyne, B.A., Maxwell, D.J., and Brown, A.G. (1987). Fine structure of synapses associated with characterized postsynaptic dorsal column neurons in the cat. Neuroscience *23*, 597-612.

Basbaum, A.I., Bautista, D.M., Scherrer, G., and Julius, D. (2009). Cellular and molecular mechanisms of pain. Cell *139*, 267-284.

Berger, D.R., Seung, H.S., and Lichtman, J.W. (2018). VAST (Volume Annotation and Segmentation Tool): Efficient Manual and Semi-Automatic Labeling of Large 3D Image Stacks. Front Neural Circuits *12*, 88.

Berning, M., Boergens, K.M., and Helmstaedter, M. (2015). SegEM: Efficient Image Analysis for High-Resolution Connectomics. Neuron *87*, 1193-1206.

Bock, D.D., Lee, W.C., Kerlin, A.M., Andermann, M.L., Hood, G., Wetzel, A.W., Yurgenson, S., Soucy, E.R., Kim, H.S., and Reid, R.C. (2011). Network anatomy and in vivo physiology of visual cortical neurons. Nature *471*, 177-182.

Boergens, K.M., Berning, M., Bocklisch, T., Braunlein, D., Drawitsch, F., Frohnhofen, J., Herold, T., Otto, P., Rzepka, N., Werkmeister, T.*, et al.* (2017). webKnossos: efficient online 3D data annotation for connectomics. Nat Methods *14*, 691-694.

Boyle, K.A., Gradwell, M.A., Yasaka, T., Dickie, A.C., Polgar, E., Ganley, R.P., Orr, D.P.H., Watanabe, M., Abraira, V.E., Kuehn, E.D.*, et al.* (2019). Defining a Spinal Microcircuit that Gates Myelinated Afferent Input: Implications for Tactile Allodynia. Cell Rep *28*, 526-540 e526.

Briggman, K.L., Helmstaedter, M., and Denk, W. (2011). Wiring specificity in the direction-selectivity circuit of the retina. Nature *471*, 183-188.

Brill, M.S., Lichtman, J.W., Thompson, W., Zuo, Y., and Misgeld, T. (2011). Spatial constraints dictate glial territories at murine neuromuscular junctions. J Cell Biol *195*, 293-305.

Brown, A.G. (1981). Organization in the spinal cord : the anatomy and physiology of identified neurones (Berlin, New York: Springer-Verlag).

Brown, A.G., Fyffe, R.E., and Noble, R. (1980). Projections from Pacinian corpuscles and rapidly adapting mechanoreceptors of glabrous skin to the cat's spinal cord. J Physiol *307*, 385-400.

Browne, T.J., Smith, K.M., Gradwell, M.A., Iredale, J.A., Dayas, C.V., Callister, R.J., Hughes, D.I., and Graham, B.A. (2019). Spinoparabrachial projection neurons form distinct classes in the mouse dorsal horn. Pain.

Byers, M.R. (1985). Sensory innervation of periodontal ligament of rat molars consists of unencapsulated Ruffini-like mechanoreceptors and free nerve endings. J Comp Neurol *231*, 500-518.

Cardona, A., Saalfeld, S., Schindelin, J., Arganda-Carreras, I., Preibisch, S., Longair, M., Tomancak, P., Hartenstein, V., and Douglas, R.J. (2012). TrakEM2 software for neural circuit reconstruction. PLoS One *7*, e38011.

Castle, M.J., Turunen, H.T., Vandenberghe, L.H., and Wolfe, J.H. (2016). Controlling AAV Tropism in the Nervous System with Natural and Engineered Capsids. Methods Mol Biol *1382*, 133-149.

Chalfie, M., Sulston, J.E., White, J.G., Southgate, E., Thomson, J.N., and Brenner, S. (1985). The neural circuit for touch sensitivity in Caenorhabditis elegans. J Neurosci *5*, 956-964.

Chang, W., Kanda, H., Ikeda, R., Ling, J., DeBerry, J.J., and Gu, J.G. (2016). Merkel disc is a serotonergic synapse in the epidermis for transmitting tactile signals in mammals. Proc Natl Acad Sci U S A *113*, E5491-5500.

Choi, S., Hachisuka, J., Brett, M.A., Magee, A.R., Omori, Y., Iqbal, N.U., Zhang, D., DeLisle, M.M., Wolfson, R.L., Bai, L.*, et al.* (2020). Parallel ascending spinal pathways for affective touch and pain. Nature *587*, 258-263.

Cobo, R., Garcia-Piqueras, J., Cobo, J., and Vega, J.A. (2021). The Human Cutaneous Sensory Corpuscles: An Update. J Clin Med *10*.

Cox, J.J., Reimann, F., Nicholas, A.K., Thornton, G., Roberts, E., Springell, K., Karbani, G., Jafri, H., Mannan, J., Raashid, Y.*, et al.* (2006). An SCN9A channelopathy causes congenital inability to experience pain. Nature *444*, 894-898.

Cruz, F., Lima, D., Zieglgansberger, W., and Coimbra, A. (1991). Fine structure and synaptic architecture of HRP-labelled primary afferent terminations in lamina IIi of the rat dorsal horn. J Comp Neurol *305*, 3-16.

Cui, Z., Gerfen, C.R., and Young, W.S., 3rd (2013). Hypothalamic and other connections with dorsal CA2 area of the mouse hippocampus. J Comp Neurol *521*, 1844-1866.

da Silva, S., Hasegawa, H., Scott, A., Zhou, X., Wagner, A.K., Han, B.X., and Wang, F. (2011). Proper formation of whisker barrelettes requires periphery-derived Smad4-dependent TGF-beta signaling. Proc Natl Acad Sci U S A *108*, 3395-3400.

Daigle, T.L., Madisen, L., Hage, T.A., Valley, M.T., Knoblich, U., Larsen, R.S., Takeno, M.M., Huang, L., Gu, H., Larsen, R.*, et al.* (2018). A Suite of Transgenic Driver and Reporter Mouse Lines with Enhanced Brain-Cell-Type Targeting and Functionality. Cell *174*, 465-480 e422.

Dani, A., Huang, B., Bergan, J., Dulac, C., and Zhuang, X. (2010). Superresolution imaging of chemical synapses in the brain. Neuron *68*, 843-856.

Danielian, P.S., Muccino, D., Rowitch, D.H., Michael, S.K., and McMahon, A.P. (1998). Modification of gene activity in mouse embryos in utero by a tamoxifen-inducible form of Cre recombinase. Curr Biol *8*, 1323-1326.

Deverman, B.E., Pravdo, P.L., Simpson, B.P., Kumar, S.R., Chan, K.Y., Banerjee, A., Wu, W.L., Yang, B., Huber, N., Pasca, S.P.*, et al.* (2016). Cre-dependent selection yields AAV variants for widespread gene transfer to the adult brain. Nat Biotechnol *34*, 204-209.

Doerflinger, N.H., Macklin, W.B., and Popko, B. (2003). Inducible site-specific recombination in myelinating cells. Genesis *35*, 63-72.

Drawitsch, F., Karimi, A., Boergens, K.M., and Helmstaedter, M. (2018). FluoEM, virtual labeling of axons in three-dimensional electron microscopy data for long-range connectomics. Elife *7*.

Duncan, D., and Morales, R. (1978). Relative numbers of several types of synaptic connections in the substantia gelatinosa of the cat spinal cord. J Comp Neurol *182*, 601-610.

Eberle, A.L., Mikula, S., Schalek, R., Lichtman, J., Tate, M.L.K., and Zeidler, D. (2015). High-resolution, high-throughput imaging with a multibeam scanning electron microscope. J Microsc *259*, 114-120.

Fang, T., Lu, X., Berger, D., Gmeiner, C., Cho, J., Schalek, R., Ploegh, H., and Lichtman, J. (2018). Nanobody immunostaining for correlated light and electron microscopy with preservation of ultrastructure. Nat Methods *15*, 1029-1032.

Feinberg, E.H., Vanhoven, M.K., Bendesky, A., Wang, G., Fetter, R.D., Shen, K., and Bargmann, C.I. (2008). GFP Reconstitution Across Synaptic Partners (GRASP) defines cell contacts and synapses in living nervous systems. Neuron *57*, 353-363.

Funke, J., Tschopp, F., Grisaitis, W., Sheridan, A., Singh, C., Saalfeld, S., and Turaga, S.C. (2019). Large Scale Image Segmentation with Structured Loss Based Deep Learning for Connectome Reconstruction. IEEE Trans Pattern Anal Mach Intell *41*, 1669-1680.

Gerfen, C.R., Paletzki, R., and Heintz, N. (2013). GENSAT BAC cre-recombinase driver lines to study the functional organization of cerebral cortical and basal ganglia circuits. Neuron *80*, 1368-1383.

Gerke, M.B., and Plenderleith, M.B. (2004). Ultrastructural analysis of the central terminals of primary sensory neurones labelled by transganglionic transport of bandeiraea simplicifolia I-isolectin B4. Neuroscience *127*, 165-175.

Ghitani, N., Barik, A., Szczot, M., Thompson, J.H., Li, C., Le Pichon, C.E., Krashes, M.J., and Chesler, A.T. (2017). Specialized Mechanosensory Nociceptors Mediating Rapid Responses to Hair Pull. Neuron *95*, 944-954 e944.

Gibson, S.J., Polak, J.M., Bloom, S.R., and Wall, P.D. (1981). The distribution of nine peptides in rat spinal cord with special emphasis on the substantia gelatinosa and on the area around the central canal (lamina X). J Comp Neurol *201*, 65-79.

Gong, S., Zheng, C., Doughty, M.L., Losos, K., Didkovsky, N., Schambra, U.B., Nowak, N.J., Joyner, A., Leblanc, G., Hatten, M.E.*, et al.* (2003). A gene expression atlas of the central nervous system based on bacterial artificial chromosomes. Nature *425*, 917-925.

Gonzalez-Martinez, T., Farinas, I., Del Valle, M.E., Feito, J., Germana, G., Cobo, J., and Vega, J.A. (2005). BDNF, but not NT-4, is necessary for normal development of Meissner corpuscles. Neurosci Lett *377*, 12-15.

Gonzalez-Martinez, T., Germana, G.P., Monjil, D.F., Silos-Santiago, I., de Carlos, F., Germana, G., Cobo, J., and Vega, J.A. (2004). Absence of Meissner corpuscles in the digital pads of mice lacking functional TrkB. Brain Res *1002*, 120-128.

Gorski, J.A., Zeiler, S.R., Tamowski, S., and Jones, K.R. (2003). Brain-derived neurotrophic factor is required for the maintenance of cortical dendrites. J Neurosci *23*, 6856-6865.

Graham, B.A., and Hughes, D.I. (2020). Defining populations of dorsal horn interneurons. Pain *161*, 2434-2436.

Gray, E.G. (1959). Electron microscopy of synaptic contacts on dendrite spines of the cerebral cortex. Nature *183*, 1592-1593.

Grudt, T.J., and Perl, E.R. (2002). Correlations between neuronal morphology and electrophysiological features in the rodent superficial dorsal horn. J Physiol *540*, 189-207.

Guo, Z.V., Li, N., Huber, D., Ophir, E., Gutnisky, D., Ting, J.T., Feng, G., and Svoboda, K. (2014). Flow of cortical activity underlying a tactile decision in mice. Neuron *81*, 179-194.

Han, C., Wang, D., Soba, P., Zhu, S., Lin, X., Jan, L.Y., and Jan, Y.N. (2012). Integrins regulate repulsion-mediated dendritic patterning of drosophila sensory neurons by restricting dendrites in a 2D space. Neuron *73*, 64-78.

Hildebrand, D.G.C., Cicconet, M., Torres, R.M., Choi, W., Quan, T.M., Moon, J., Wetzel, A.W., Scott Champion, A., Graham, B.J., Randlett, O.*, et al.* (2017). Whole-brain serial-section electron microscopy in larval zebrafish. Nature *545*, 345-349.

Hochman, S., Shreckengost, J., Kimura, H., and Quevedo, J. (2010). Presynaptic inhibition of primary afferents by depolarization: observations supporting nontraditional mechanisms. Ann N Y Acad Sci *1198*, 140-152.

Hoffman, B.U., Baba, Y., Griffith, T.N., Mosharov, E.V., Woo, S.H., Roybal, D.D., Karsenty, G., Patapoutian, A., Sulzer, D., and Lumpkin, E.A. (2018). Merkel Cells Activate Sensory Neural Pathways through Adrenergic Synapses. Neuron *100*, 1401-1413 e1406.

Hooks, B.M., Lin, J.Y., Guo, C., and Svoboda, K. (2015). Dual-channel circuit mapping reveals sensorimotor convergence in the primary motor cortex. J Neurosci *35*, 4418-4426.

Hu, H., Gan, J., and Jonas, P. (2014). Interneurons. Fast-spiking, parvalbumin(+) GABAergic interneurons: from cellular design to microcircuit function. Science *345*, 1255263.

Hua, Y., Laserstein, P., and Helmstaedter, M. (2015). Large-volume en-bloc staining for electron microscopy-based connectomics. Nat Commun *6*, 7923.

Hughes, D.I., Sikander, S., Kinnon, C.M., Boyle, K.A., Watanabe, M., Callister, R.J., and Graham, B.A. (2012). Morphological, neurochemical and electrophysiological features of parvalbumin-expressing cells: a likely source of axo-axonic inputs in the mouse spinal dorsal horn. J Physiol *590*, 3927-3951.

Hung, V., Udeshi, N.D., Lam, S.S., Loh, K.H., Cox, K.J., Pedram, K., Carr, S.A., and Ting, A.Y. (2016). Spatially resolved proteomic mapping in living cells with the engineered peroxidase APEX2. Nat Protoc *11*, 456-475.

Ide, C. (1976). The fine structure of the digital corpuscle of the mouse toe pad, with special reference to nerve fibers. Am J Anat *147*, 329-355.

Iggo, A., and Muir, A.R. (1969). The structure and function of a slowly adapting touch corpuscle in hairy skin. J Physiol *200*, 763-796.

Iggo, A., and Ogawa, H. (1977). Correlative physiological and morphological studies of rapidly adapting mechanoreceptors in cat's glabrous skin. J Physiol *266*, 275-296.

Jaegle, M., Ghazvini, M., Mandemakers, W., Piirsoo, M., Driegen, S., Levavasseur, F., Raghoenath, S., Grosveld, F., and Meijer, D. (2003). The POU proteins Brn-2 and Oct-6 share important functions in Schwann cell development. Genes Dev *17*, 1380-1391.

Januszewski, M., Kornfeld, J., Li, P.H., Pope, A., Blakely, T., Lindsey, L., Maitin-Shepard, J., Tyka, M., Denk, W., and Jain, V. (2018). High-precision automated reconstruction of neurons with flood-filling networks. Nat Methods *15*, 605-610.

Jarrell, T.A., Wang, Y., Bloniarz, A.E., Brittin, C.A., Xu, M., Thomson, J.N., Albertson, D.G., Hall, D.H., and Emmons, S.W. (2012). The connectome of a decision-making neural network. Science *337*, 437-444.

Joesch, M., Mankus, D., Yamagata, M., Shahbazi, A., Schalek, R., Suissa-Peleg, A., Meister, M., Lichtman, J.W., Scheirer, W.J., and Sanes, J.R. (2016). Reconstruction of genetically identified neurons imaged by serial-section electron microscopy. Elife *5*.

Johnson, K.O. (2001). The roles and functions of cutaneous mechanoreceptors. Curr Opin Neurobiol *11*, 455-461.

Kaidoh, T., and Inoue, T. (2008). N-cadherin expression in palisade nerve endings of rat vellus hairs. J Comp Neurol *506*, 525-534.

Kambrun, C., Roca-Lapirot, O., Salio, C., Landry, M., Moqrich, A., and Le Feuvre, Y. (2018). TAFA4 Reverses Mechanical Allodynia through Activation of GABAergic Transmission and Microglial Process Retraction. Cell Rep *22*, 2886-2897.

Karagiannis, E.D., and Boyden, E.S. (2018). Expansion microscopy: development and neuroscience applications. Curr Opin Neurobiol *50*, 56-63.

Kasthuri, N., Hayworth, K.J., Berger, D.R., Schalek, R.L., Conchello, J.A., Knowles-Barley, S., Lee, D., Vazquez-Reina, A., Kaynig, V., Jones, T.R.*, et al.* (2015). Saturated Reconstruction of a Volume of Neocortex. Cell *162*, 648-661.

Klein, S., Staring, M., Murphy, K., Viergever, M.A., and Pluim, J.P. (2010). elastix: a toolbox for intensity-based medical image registration. IEEE Trans Med Imaging *29*, 196-205.

Knott, G., Marchman, H., Wall, D., and Lich, B. (2008). Serial section scanning electron microscopy of adult brain tissue using focused ion beam milling. J Neurosci *28*, 2959-2964.

Koch, S.C., Tochiki, K.K., Hirschberg, S., and Fitzgerald, M. (2012). C-fiber activity-dependent maturation of glycinergic inhibition in the spinal dorsal horn of the postnatal rat. Proc Natl Acad Sci U S A *109*, 12201-12206.

Kostetskii, I., Li, J., Xiong, Y., Zhou, R., Ferrari, V.A., Patel, V.V., Molkentin, J.D., and Radice, G.L. (2005). Induced deletion of the N-cadherin gene in the heart leads to dissolution of the intercalated disc structure. Circ Res *96*, 346-354.

Kuan, A.T., Phelps, J.S., Thomas, L.A., Nguyen, T.M., Han, J., Chen, C.L., Azevedo, A.W., Tuthill, J.C., Funke, J., Cloetens, P.*, et al.* (2020). Dense neuronal reconstruction through X-ray holographic nano-tomography. Nat Neurosci *23*, 1637-1643.

Kuehn, E.D., Meltzer, S., Abraira, V.E., Ho, C.Y., and Ginty, D.D. (2019). Tiling and somatotopic alignment of mammalian low-threshold mechanoreceptors. Proc Natl Acad Sci U S A *116*, 9168-9177.

Lakso, M., Pichel, J.G., Gorman, J.R., Sauer, B., Okamoto, Y., Lee, E., Alt, F.W., and Westphal, H. (1996). Efficient in vivo manipulation of mouse genomic sequences at the zygote stage. Proc Natl Acad Sci U S A *93*, 5860-5865.

Lam, S.S., Martell, J.D., Kamer, K.J., Deerinck, T.J., Ellisman, M.H., Mootha, V.K., and Ting, A.Y. (2015). Directed evolution of APEX2 for electron microscopy and proximity labeling. Nat Methods *12*, 51-54.

Larsson, M., and Broman, J. (2019). Synaptic Organization of VGLUT3 Expressing Low-Threshold Mechanosensitive C Fiber Terminals in the Rodent Spinal Cord. eNeuro *6*.

Leal-Ortiz, S., Waites, C.L., Terry-Lorenzo, R., Zamorano, P., Gundelfinger, E.D., and Garner, C.C. (2008). Piccolo modulation of Synapsin1a dynamics regulates synaptic vesicle exocytosis. J Cell Biol *181*, 831-846.

Lee, W.C., Bonin, V., Reed, M., Graham, B.J., Hood, G., Glattfelder, K., and Reid, R.C. (2016). Anatomy and function of an excitatory network in the visual cortex. Nature *532*, 370-374.

Li, J., Wang, Y., Chiu, S.L., and Cline, H.T. (2010). Membrane targeted horseradish peroxidase as a marker for correlative fluorescence and electron microscopy studies. Front Neural Circuits *4*, 6.

Li, L., and Ginty, D.D. (2014). The structure and organization of lanceolate mechanosensory complexes at mouse hair follicles. Elife *3*, e01901.

Li, L., Rutlin, M., Abraira, V.E., Cassidy, C., Kus, L., Gong, S., Jankowski, M.P., Luo, W., Heintz, N., Koerber, H.R.*, et al.* (2011). The functional organization of cutaneous low-threshold mechanosensory neurons. Cell *147*, 1615-1627.

Light, A.R., and Perl, E.R. (1979a). Reexamination of the dorsal root projection to the spinal dorsal horn including observations on the differential termination of coarse and fine fibers. J Comp Neurol *186*, 117-131.

Light, A.R., and Perl, E.R. (1979b). Spinal termination of functionally identified primary afferent neurons with slowly conducting myelinated fibers. J Comp Neurol *186*, 133-150.

Lin, T.Y., Luo, J., Shinomiya, K., Ting, C.Y., Lu, Z., Meinertzhagen, I.A., and Lee, C.H. (2016). Mapping chromatic pathways in the Drosophila visual system. J Comp Neurol *524*, 213-227.

Linden, R.W., Millar, B.J., and Halata, Z. (1994). A comparative physiological and morphological study of periodontal ligament mechanoreceptors represented in the trigeminal ganglion and the mesencephalic nucleus of the cat. Anat Embryol (Berl) *190*, 127-135.

Liu, Y., Rutlin, M., Huang, S., Barrick, C.A., Wang, F., Jones, K.R., Tessarollo, L., and Ginty, D.D. (2012). Sexually dimorphic BDNF signaling directs sensory innervation of the mammary gland. Science *338*, 1357-1360.

Loewenstein, W.R., and Mendelson, M. (1965). Components of Receptor Adaptation in a Pacinian Corpuscle. J Physiol *177*, 377-397.

Lu, Y., and Perl, E.R. (2005). Modular organization of excitatory circuits between neurons of the spinal superficial dorsal horn (laminae I and II). J Neurosci *25*, 3900-3907.

Luo, W., Enomoto, H., Rice, F.L., Milbrandt, J., and Ginty, D.D. (2009). Molecular identification of rapidly adapting mechanoreceptors and their developmental dependence on ret signaling. Neuron *64*, 841-856.

Ma, C., Donnelly, D.F., and LaMotte, R.H. (2010). In vivo visualization and functional characterization of primary somatic neurons. J Neurosci Methods *191*, 60-65.

Ma, Q. (2010). Labeled lines meet and talk: population coding of somatic sensations. J Clin Invest *120*, 3773-3778.

Machado, A.S., Darmohray, D.M., Fayad, J., Marques, H.G., and Carey, M.R. (2015). A quantitative framework for whole-body coordination reveals specific deficits in freely walking ataxic mice. Elife *4*.

Machida, A., Kuwahara, H., Mayra, A., Kubodera, T., Hirai, T., Sunaga, F., Tajiri, M., Hirai, Y., Shimada, T., Mizusawa, H.*, et al.* (2013). Intraperitoneal administration of AAV9-shRNA inhibits target gene expression in the dorsal root ganglia of neonatal mice. Mol Pain *9*, 36.

Madisen, L., Garner, A.R., Shimaoka, D., Chuong, A.S., Klapoetke, N.C., Li, L., van der Bourg, A., Niino, Y., Egolf, L., Monetti, C.*, et al.* (2015). Transgenic mice for intersectional targeting of neural sensors and effectors with high specificity and performance. Neuron *85*, 942-958.

Madisen, L., Zwingman, T.A., Sunkin, S.M., Oh, S.W., Zariwala, H.A., Gu, H., Ng, L.L., Palmiter, R.D., Hawrylycz, M.J., Jones, A.R.*, et al.* (2010). A robust and high-throughput Cre reporting and characterization system for the whole mouse brain. Nat Neurosci *13*, 133-140.

Mallon, B.S., Shick, H.E., Kidd, G.J., and Macklin, W.B. (2002). Proteolipid promoter activity distinguishes two populations of NG2-positive cells throughout neonatal cortical development. J Neurosci *22*, 876-885.

Malmberg, A.B., Chen, C., Tonegawa, S., and Basbaum, A.I. (1997). Preserved acute pain and reduced neuropathic pain in mice lacking PKCgamma. Science *278*, 279-283.

Maricich, S.M., Morrison, K.M., Mathes, E.L., and Brewer, B.M. (2012). Rodents rely on Merkel cells for texture discrimination tasks. J Neurosci *32*, 3296-3300.

Maricich, S.M., Wellnitz, S.A., Nelson, A.M., Lesniak, D.R., Gerling, G.J., Lumpkin, E.A., and Zoghbi, H.Y. (2009). Merkel cells are essential for light-touch responses. Science *324*, 1580-1582.

Marshall, A.G., and McGlone, F.P. (2020). Affective Touch: The Enigmatic Spinal Pathway of the C-Tactile Afferent. Neurosci Insights *15*, 2633105520925072.

Marshall, A.G., Sharma, M.L., Marley, K., Olausson, H., and McGlone, F.P. (2019). Spinal signalling of C-fiber mediated pleasant touch in humans. Elife *8*.

Martell, J.D., Deerinck, T.J., Lam, S.S., Ellisman, M.H., and Ting, A.Y. (2017). Electron microscopy using the genetically encoded APEX2 tag in cultured mammalian cells. Nat Protoc *12*, 1792-1816.

Martell, J.D., Deerinck, T.J., Sancak, Y., Poulos, T.L., Mootha, V.K., Sosinsky, G.E., Ellisman, M.H., and Ting, A.Y. (2012). Engineered ascorbate peroxidase as a genetically encoded reporter for electron microscopy. Nat Biotechnol *30*, 1143-1148.

Martell, J.D., Yamagata, M., Deerinck, T.J., Phan, S., Kwa, C.G., Ellisman, M.H., Sanes, J.R., and Ting, A.Y. (2016). A split horseradish peroxidase for the detection of intercellular protein-protein interactions and sensitive visualization of synapses. Nat Biotechnol *34*, 774-780.

Maxwell, D.J., Koerber, H.R., and Bannatyne, B.A. (1985). Light and electron microscopy of contacts between primary afferent fibres and neurones with axons ascending the dorsal columns of the feline spinal cord. Neuroscience *16*, 375-394.

Maxwell, D.J., Ottersen, O.P., and Storm-Mathisen, J. (1995). Synaptic organization of excitatory and inhibitory boutons associated with spinal neurons which project through the dorsal columns of the cat. Brain Res *676*, 103-112.

Maxwell, D.J., and Réthelyi, M. (1987). Ultrastructure and synaptic connections of cutaneous afferent fibres in the spinal cord. Trends in Neurosciences *10*, 117-123.

McGlone, F., Wessberg, J., and Olausson, H. (2014). Discriminative and affective touch: sensing and feeling. Neuron *82*, 737-755.

Melzack, R., and Wall, P.D. (1965). Pain mechanisms: a new theory. Science *150*, 971-979.

Millar, B.J., Halata, Z., and Linden, R.W. (1989). The structure of physiologically located periodontal ligament mechanoreceptors of the cat canine tooth. J Anat *167*, 117-127.

Morgan, J.L., Berger, D.R., Wetzel, A.W., and Lichtman, J.W. (2016). The Fuzzy Logic of Network Connectivity in Mouse Visual Thalamus. Cell *165*, 192-206.

Morrison, K.M., Miesegaes, G.R., Lumpkin, E.A., and Maricich, S.M. (2009). Mammalian Merkel cells are descended from the epidermal lineage. Dev Biol *336*, 76-83.

Motta, A., Berning, M., Boergens, K.M., Staffler, B., Beining, M., Loomba, S., Hennig, P., Wissler, H., and Helmstaedter, M. (2019). Dense connectomic reconstruction in layer 4 of the somatosensory cortex. Science *366*.

Naim, M.M., Shehab, S.A., and Todd, A.J. (1998). Cells in laminae III and IV of the rat spinal cord which possess the neurokinin-1 receptor receive monosynaptic input from myelinated primary afferents. Eur J Neurosci *10*, 3012-3019.

Nassar, M.A., Stirling, L.C., Forlani, G., Baker, M.D., Matthews, E.A., Dickenson, A.H., and Wood, J.N. (2004). Nociceptor-specific gene deletion reveals a major role for Nav1.7 (PN1) in acute and inflammatory pain. Proc Natl Acad Sci U S A *101*, 12706-12711.

Neubarth, N.L., Emanuel, A.J., Liu, Y., Springel, M.W., Handler, A., Zhang, Q., Lehnert, B.P., Guo, C., Orefice, L.L., Abdelaziz, A.*, et al.* (2020). Meissner corpuscles and their spatially intermingled afferents underlie gentle touch perception. Science *368*.

Neumann, S., Braz, J.M., Skinner, K., Llewellyn-Smith, I.J., and Basbaum, A.I. (2008). Innocuous, not noxious, input activates PKCgamma interneurons of the spinal dorsal horn via myelinated afferent fibers. J Neurosci *28*, 7936-7944.

Newell, A., Yang, K., and Deng, J. (2016). Stacked Hourglass Networks for Human Pose Estimation. arXiv, 1603.06937.

Ng, J., Browning, A., Lechner, L., Terada, M., Howard, G., and Jefferis, G. (2016). Genetically targeted 3D visualisation of Drosophila neurons under Electron Microscopy and X-Ray Microscopy using miniSOG. Sci Rep *6*, 38863.

Orefice, L.L., Zimmerman, A.L., Chirila, A.M., Sleboda, S.J., Head, J.P., and Ginty, D.D. (2016). Peripheral Mechanosensory Neuron Dysfunction Underlies Tactile and Behavioral Deficits in Mouse Models of ASDs. Cell *166*, 299-313.

Owens, D.M., and Lumpkin, E.A. (2014). Diversification and specialization of touch receptors in skin. Cold Spring Harb Perspect Med *4*.

Pare, M., Elde, R., Mazurkiewicz, J.E., Smith, A.M., and Rice, F.L. (2001). The Meissner corpuscle revised: a multiafferented mechanoreceptor with nociceptor immunochemical properties. J Neurosci *21*, 7236-7246.

Parton, R.G. (2018). Caveolae: Structure, Function, and Relationship to Disease. Annu Rev Cell Dev Biol *34*, 111-136.

Parton, R.G., and del Pozo, M.A. (2013). Caveolae as plasma membrane sensors, protectors and organizers. Nat Rev Mol Cell Biol *14*, 98-112.

Pease, D.C., and Quilliam, T.A. (1957). Electron microscopy of the pacinian corpuscle. J Biophys Biochem Cytol *3*, 331-342.

Perdigoto, C.N., Bardot, E.S., Valdes, V.J., Santoriello, F.J., and Ezhkova, E. (2014). Embryonic maturation of epidermal Merkel cells is controlled by a redundant transcription factor network. Development *141*, 4690-4696.

Perez-Pinera, P., Garcia-Suarez, O., Germana, A., Diaz-Esnal, B., de Carlos, F., Silos-Santiago, I., del Valle, M.E., Cobo, J., and Vega, J.A. (2008). Characterization of sensory deficits in TrkB knockout mice. Neurosci Lett *433*, 43-47.

Peters, A., Palay, S.L., and Webster, H.d.F. (1991). The Fine Structure of the Nervous System: Neurons and Their Supporting Cells, 3rd edn (New York: Oxford University Press).

Phelps, J.S., Hildebrand, D.G.C., Graham, B.J., Kuan, A.T., Thomas, L.A., Nguyen, T.M., Buhmann, J., Azevedo, A.W., Sustar, A., Agrawal, S*., et al.* (2021). Reconstruction of motor control circuits in adult Drosophila using automated transmission electron microscopy. Cell *184*, 759-774 e718.

Polgar, E., Durrieux, C., Hughes, D.I., and Todd, A.J. (2013). A quantitative study of inhibitory interneurons in laminae I-III of the mouse spinal dorsal horn. PLoS One *8*, e78309.

Pubols, L.M., and Pubols, B.H., Jr. (1973). Modality composition and functional characteristics of dorsal column mechanoreceptive afferent fibers innervating the raccoon's forepaw. J Neurophysiol *36*, 1023-1037.

Ralston, H.J., 3rd, Light, A.R., Ralston, D.D., and Perl, E.R. (1984). Morphology and synaptic relationships of physiologically identified low-threshold dorsal root axons stained with intra-axonal horseradish peroxidase in the cat and monkey. J Neurophysiol *51*, 777-792.

Ralston, H.J., 3rd, and Ralston, D.D. (1979). The distribution of dorsal root axons in laminae I, II and III of the macaque spinal cord: a quantitative electron microscope study. J Comp Neurol *184*, 643-684.

Ramirez, A., Page, A., Gandarillas, A., Zanet, J., Pibre, S., Vidal, M., Tusell, L., Genesca, A., Whitaker, D.A., Melton, D.W.*, et al.* (2004). A keratin K5Cre transgenic line appropriate for tissue-specific or generalized Cre-mediated recombination. Genesis *39*, 52-57.

Ranade, S.S., Syeda, R., and Patapoutian, A. (2015). Mechanically Activated Ion Channels. Neuron *87*, 1162-1179.

Ranade, S.S., Woo, S.H., Dubin, A.E., Moshourab, R.A., Wetzel, C., Petrus, M., Mathur, J., Begay, V., Coste, B., Mainquist, J.*, et al.* (2014). Piezo2 is the major transducer of mechanical forces for touch sensation in mice. Nature *516*, 121-125.

Rau, K.K., McIlwrath, S.L., Wang, H., Lawson, J.J., Jankowski, M.P., Zylka, M.J., Anderson, D.J., and Koerber, H.R. (2009). Mrgprd enhances excitability in specific populations of cutaneous murine polymodal nociceptors. J Neurosci *29*, 8612-8619.

Razani, B., Engelman, J.A., Wang, X.B., Schubert, W., Zhang, X.L., Marks, C.B., Macaluso, F., Russell, R.G., Li, M., Pestell, R.G.*, et al.* (2001). Caveolin-1 null mice are viable but show evidence of hyperproliferative and vascular abnormalities. J Biol Chem *276*, 38121-38138.

Rethelyi, M., Light, A.R., and Perl, E.R. (1982). Synaptic complexes formed by functionally defined primary afferent units with fine myelinated fibers. J Comp Neurol *207*, 381-393.

Rexed, B. (1952). The cytoarchitectonic organization of the spinal cord in the cat. J Comp Neurol *96*, 414-495.

Rhee, H.W., Zou, P., Udeshi, N.D., Martell, J.D., Mootha, V.K., Carr, S.A., and Ting, A.Y. (2013). Proteomic mapping of mitochondria in living cells via spatially restricted enzymatic tagging. Science *339*, 1328-1331.

Ribeiro-da-Silva, A. (2004). Substantia Gelatinosa of the Spinal Cord. In The Rat Nervous System, G. Paxinos, ed. (Burlington: Academic Press), pp. 129-148.

Ribeiro-da-Silva, A., and Coimbra, A. (1982). Two types of synaptic glomeruli and their distribution in laminae I-III of the rat spinal cord. J Comp Neurol *209*, 176-186.

Ribeiro-da-Silva, A., Pignatelli, D., and Coimbra, A. (1985). Synaptic architecture of glomeruli in superficial dorsal horn of rat spinal cord, as shown in serial reconstructions. J Neurocytol *14*, 203-220.

Ribeiro-da-Silva, A., Tagari, P., and Cuello, A.C. (1989). Morphological characterization of substance P-like immunoreactive glomeruli in the superficial dorsal horn of the rat spinal cord and trigeminal subnucleus caudalis: a quantitative study. J Comp Neurol *281*, 497-415.

Rodriguez, C.I., Buchholz, F., Galloway, J., Sequerra, R., Kasper, J., Ayala, R., Stewart, A.F., and Dymecki, S.M. (2000). High-efficiency deleter mice show that FLPe is an alternative to Cre-loxP. Nat Genet *25*, 139-140.

Rudomin, P., and Schmidt, R.F. (1999). Presynaptic inhibition in the vertebrate spinal cord revisited. Exp Brain Res *129*, 1-37.

Rutlin, M., Ho, C.Y., Abraira, V.E., Cassidy, C., Bai, L., Woodbury, C.J., and Ginty, D.D. (2014). The cellular and molecular basis of direction selectivity of Adelta-LTMRs. Cell *159*, 1640-1651.

Saalfeld, S., Cardona, A., Hartenstein, V., and Tomancak, P. (2010). As-rigid-as-possible mosaicking and serial section registration of large ssTEM datasets. Bioinformatics *26*, i57-63.

Saalfeld, S., Fetter, R., Cardona, A., and Tomancak, P. (2012). Elastic volume reconstruction from series of ultra-thin microscopy sections. Nat Methods *9*, 717-720.

Sadeghian, H., Lacoste, B., Qin, T., Toussay, X., Rosa, R., Oka, F., Chung, D.Y., Takizawa, T., Gu, C., and Ayata, C. (2018). Spreading depolarizations trigger caveolin-1-dependent endothelial transcytosis. Ann Neurol *84*, 409-423.

Salio, C., Aimar, P., Malapert, P., Moqrich, A., and Merighi, A. (2021). Neurochemical and Ultrastructural Characterization of Unmyelinated Non-peptidergic C-Nociceptors and C-Low Threshold Mechanoreceptors Projecting to Lamina II of the Mouse Spinal Cord. Cell Mol Neurobiol *41*, 247-262.

Scheffer, L.K., Xu, C.S., Januszewski, M., Lu, Z., Takemura, S.Y., Hayworth, K.J., Huang, G.B., Shinomiya, K., Maitlin-Shepard, J., Berg, S.*, et al.* (2020). A connectome and analysis of the adult Drosophila central brain. Elife *9*.

Scheibel, M.E., and Scheibel, A.B. (1969). Terminal patterns in cat spinal cord. 3. Primary afferent collaterals. Brain Res *13*, 417-443.

Schikorski, T., Young, S.M., Jr., and Hu, Y. (2007). Horseradish peroxidase cDNA as a marker for electron microscopy in neurons. J Neurosci Methods *165*, 210-215.

Seguchi, H., Yagyu, Y., and Kobayashi, T. (1989). Three dimensional observations of the palisade-shaped nerve endings of normal hair of rat's snout. Anat Anz *169*, 225-234.

Sewards, T.V., and Sewards, M. (2002). Separate, parallel sensory and hedonic pathways in the mammalian somatosensory system. Brain Res Bull *58*, 243-260.

Shamonin, D.P., Bron, E.E., Lelieveldt, B.P., Smits, M., Klein, S., Staring, M., and Alzheimer's Disease Neuroimaging, I. (2013). Fast parallel image registration on CPU and GPU for diagnostic classification of Alzheimer's disease. Front Neuroinform *7*, 50.

Sharma, N., Flaherty, K., Lezgiyeva, K., Wagner, D.E., Klein, A.M., and Ginty, D.D. (2020). The emergence of transcriptional identity in somatosensory neurons. Nature *577*, 392-398.

Shields, S.D., Ahn, H.S., Yang, Y., Han, C., Seal, R.P., Wood, J.N., Waxman, S.G., and Dib-Hajj, S.D. (2012). Nav1.8 expression is not restricted to nociceptors in mouse peripheral nervous system. Pain *153*, 2017-2030.

Shortland, P., and Woolf, C.J. (1993). Morphology and somatotopy of the central arborizations of rapidly adapting glabrous skin afferents in the rat lumbar spinal cord. J Comp Neurol *329*, 491-511.

Shroyer, N.F., Helmrath, M.A., Wang, V.Y., Antalffy, B., Henning, S.J., and Zoghbi, H.Y. (2007). Intestine-specific ablation of mouse atonal homolog 1 (Math1) reveals a role in cellular homeostasis. Gastroenterology *132*, 2478-2488.

Shu, X., Lev-Ram, V., Deerinck, T.J., Qi, Y., Ramko, E.B., Davidson, M.W., Jin, Y., Ellisman, M.H., and Tsien, R.Y. (2011). A genetically encoded tag for correlated light and electron microscopy of intact cells, tissues, and organisms. PLoS Biol *9*, e1001041.

Sinha, B., Koster, D., Ruez, R., Gonnord, P., Bastiani, M., Abankwa, D., Stan, R.V., Butler-Browne, G., Vedie, B., Johannes, L.*, et al.* (2011). Cells respond to mechanical stress by rapid disassembly of caveolae. Cell *144*, 402-413.

Smith, E.S., and Lewin, G.R. (2009). Nociceptors: a phylogenetic view. J Comp Physiol A Neuroethol Sens Neural Behav Physiol *195*, 1089-1106.

Spencer, P.S., and Schaumburg, H.H. (1973). An ultrastructural study of the inner core of the Pacinian corpuscle. J Neurocytol *2*, 217-235.

Sugiura, Y., Lee, C.L., and Perl, E.R. (1986). Central projections of identified, unmyelinated (C) afferent fibers innervating mammalian skin. Science *234*, 358-361.

Takahashi-Iwanaga, H. (2000). Three-dimensional microanatomy of longitudinal lanceolate endings in rat vibrissae. J Comp Neurol *426*, 259-269.

Takahashi-Iwanaga, H., Maeda, T., and Abe, K. (1997). Scanning and transmission electron microscopy of Ruffini endings in the periodontal ligament of rat incisors. J Comp Neurol *389*, 177-184.

Todd, A.J. (1996). GABA and glycine in synaptic glomeruli of the rat spinal dorsal horn. Eur J Neurosci *8*, 2492-2498.

Todd, A.J. (2010). Neuronal circuitry for pain processing in the dorsal horn. Nat Rev Neurosci *11*, 823-836.

Todd, A.J., and Sullivan, A.C. (1990). Light microscope study of the coexistence of GABA-like and glycine-like immunoreactivities in the spinal cord of the rat. J Comp Neurol *296*, 496-505.

Uddenberg, N. (1968). Functional organization of long, second-order afferents in the dorsal funiculus. Exp Brain Res *4*, 377-382.

Uesaka, T., Nagashimada, M., Yonemura, S., and Enomoto, H. (2008). Diminished Ret expression compromises neuronal survival in the colon and causes intestinal aganglionosis in mice. J Clin Invest *118*, 1890-1898.

Valtschanoff, J.G., Weinberg, R.J., and Rustioni, A. (1993). Amino acid immunoreactivity in corticospinal terminals. Exp Brain Res *93*, 95-103.

Van Keymeulen, A., Mascre, G., Youseff, K.K., Harel, I., Michaux, C., De Geest, N., Szpalski, C., Achouri, Y., Bloch, W., Hassan, B.A.*, et al.* (2009). Epidermal progenitors give rise to Merkel cells during embryonic development and adult homeostasis. J Cell Biol *187*, 91-100.

Vong, L., Ye, C., Yang, Z., Choi, B., Chua, S., Jr., and Lowell, B.B. (2011). Leptin action on GABAergic neurons prevents obesity and reduces inhibitory tone to POMC neurons. Neuron *71*, 142-154.

Vrontou, S., Wong, A.M., Rau, K.K., Koerber, H.R., and Anderson, D.J. (2013). Genetic identification of C fibres that detect massage-like stroking of hairy skin in vivo. Nature *493*, 669-673.

Wagner, R., and Meissner, G. (1852). Ueber das Vorhandensein bisher unbekannter eigentümlicher Tastkörperchen (Corpuscula tactus) in den Gefühlswärzchen der menschlichen Haut, und über die Endausbreitung sensitiver Nerven [On the presence of previously unknown peculiar corpuscles (Corpuscula tactus) in the sensory cusps of the human skin, and on the end propagation of sensitive nerves]. Nachrichten von der Georg-Augusts-Universität und der Königlichen Gesellschaft der Wissenschaften *2*, 17-30.

Wall, P.D., Freeman, J., and Major, D. (1967). Dorsal horn cells in spinal and in freely moving rats. Exp Neurol *19*, 519-529.

Watkins, R.H., Dione, M., Ackerley, R., Backlund Wasling, H., Wessberg, J., and Loken, L.S. (2021). Evidence for sparse C-tactile afferent innervation of glabrous human hand skin. J Neurophysiol *125*, 232-237.

Watson, A.H. (2003). GABA- and glycine-like immunoreactivity in axons and dendrites contacting the central terminals of rapidly adapting glabrous skin afferents in rat spinal cord. J Comp Neurol *464*, 497-510.

Watson, A.H., Hughes, D.I., and Bazzaz, A.A. (2002). Synaptic relationships between hair follicle afferents and neurones expressing GABA and glycine-like immunoreactivity in the spinal cord of the rat. J Comp Neurol *452*, 367-380.

White, J.G., Southgate, E., Thomson, J.N., and Brenner, S. (1986). The structure of the nervous system of the nematode Caenorhabditis elegans. Philos Trans R Soc Lond B Biol Sci *314*, 1-340.

Willis, W.D., and Coggeshall, R.E. (2004). Sensory mechanisms of the spinal cord, Vol 1, 3rd edn (New York: Kluwer Academic/Plenum Publishers).

Woo, S.H., Ranade, S., Weyer, A.D., Dubin, A.E., Baba, Y., Qiu, Z., Petrus, M., Miyamoto, T., Reddy, K., Lumpkin, E.A*., et al.* (2014). Piezo2 is required for Merkel-cell mechanotransduction. Nature *509*, 622-626.

Woolf, C.J., and King, A.E. (1990). Dynamic alterations in the cutaneous mechanoreceptive fields of dorsal horn neurons in the rat spinal cord. J Neurosci *10*, 2717-2726.

Wu, H., Williams, J., and Nathans, J. (2012). Morphologic diversity of cutaneous sensory afferents revealed by genetically directed sparse labeling. Elife *1*, e00181.

Xu, C.S., Hayworth, K.J., Lu, Z., Grob, P., Hassan, A.M., Garcia-Cerdan, J.G., Niyogi, K.K., Nogales, E., Weinberg, R.J., and Hess, H.F. (2017). Enhanced FIB-SEM systems for large-volume 3D imaging. Elife *6*.

Xu, C.S., Pang, S., Hayworth, K.J., and Hess, H.F. (2020). Transforming FIB-SEM Systems for Large-Volume and. In Volume Microscopy, I. Wacker, E. Hummel, S. Burgold, and R. Schröder, eds. (New York, NY: Springer US), pp. 221-243.

Yasaka, T., Tiong, S.Y.X., Hughes, D.I., Riddell, J.S., and Todd, A.J. (2010). Populations of inhibitory and excitatory interneurons in lamina II of the adult rat spinal dorsal horn revealed by a combined electrophysiological and anatomical approach. Pain *151*, 475-488.

Zhang, Q., Lee, W.A., Paul, D.L., and Ginty, D.D. (2019). Multiplexed peroxidase-based electron microscopy labeling enables simultaneous visualization of multiple cell types. Nat Neurosci *22*, 828-839.

Zheng, Y., Liu, P., Bai, L., Trimmer, J.S., Bean, B.P., and Ginty, D.D. (2019). Deep Sequencing of Somatosensory Neurons Reveals Molecular Determinants of Intrinsic Physiological Properties. Neuron *103*, 598-616 e597.

Zheng, Z., Lauritzen, J.S., Perlman, E., Robinson, C.G., Nichols, M., Milkie, D., Torrens, O., Price, J., Fisher, C.B., Sharifi, N*., et al.* (2018). A Complete Electron Microscopy Volume of the Brain of Adult Drosophila melanogaster. Cell *174*, 730-743 e722.

Zhou, X., Wang, L., Hasegawa, H., Amin, P., Han, B.X., Kaneko, S., He, Y., and Wang, F. (2010). Deletion of PIK3C3/Vps34 in sensory neurons causes rapid neurodegeneration by disrupting the endosomal but not the autophagic pathway. Proc Natl Acad Sci U S A *107*, 9424-9429.

Zhu, F., Cizeron, M., Qiu, Z., Benavides-Piccione, R., Kopanitsa, M.V., Skene, N.G., Koniaris, B., DeFelipe, J., Fransen, E., Komiyama, N.H*., et al.* (2018). Architecture of the Mouse Brain Synaptome. Neuron *99*, 781-799 e710.

Zimmerman, A., Bai, L., and Ginty, D.D. (2014). The gentle touch receptors of mammalian skin. Science *346*, 950-954.

Zimmerman, A.L., Kovatsis, E.M., Pozsgai, R.Y., Tasnim, A., Zhang, Q., and Ginty, D.D. (2019). Distinct Modes of Presynaptic Inhibition of Cutaneous Afferents and Their Functions in Behavior. Neuron *102*, 420-434 e428.

Zylka, M.J., Rice, F.L., and Anderson, D.J. (2005). Topographically distinct epidermal nociceptive circuits revealed by axonal tracers targeted to Mrgprd. Neuron *45*, 17-25.